OCS Study MMS 2009-049

Surface Circulation Radar Mapping in Alaskan Coastal Waters: Beaufort Sea and Cook Inlet

Rachel A Potter and Thomas J Weingartner
School of Fisheries and Ocean Sciences
University of Alaska, Fairbanks

Final Report
March 2010

Prepared under MMS Contract No.1435-01-04-CT-35579,
M04PC00002, M08PC20006

US Department of the Interior
Minerals Management Service (MMS)
Alaska OCS Region
Anchorage, Alaska

OCS Study MMS 2009-049

Surface Circulation Radar Mapping in Alaskan Coastal Waters: Beaufort Sea and Cook Inlet

Rachel A Potter and Thomas J Weingartner
School of Fisheries and Ocean Sciences
University of Alaska, Fairbanks

Final Report
March 2010

Prepared under MMS Contract No.1435-01-04-CT-35579,
M04PC00002, M08PC20006

US Department of the Interior
Minerals Management Service (MMS)
Alaska OCS Region
Anchorage, Alaska

This study was funded by the U.S. Department of the Interior, Minerals Management Service (MMS), Alaska Outer Continental Shelf Region, Anchorage, Alaska, under Contract No. 1435-01-04-CT-35579 as part of the MMS Alaska Environmental Studies Program

Executive Summary

A high-frequency radar (HFR) system used to map surface currents from shore was installed on the Beaufort Sea during the open water seasons of 2005 and 2006 and in southern Cook Inlet from November 2006 through November 2007. We used a switchable-frequency HFR system that operates at 25 or 13 MHz. The system maps ocean currents in real-time over a broad area (40 and 60 km offshore range, depending upon frequency) on a grid with a 1 to 3 km resolution. The surface current data can be used for spill response planning, search and rescue, marine navigation, and marine ecosystem studies. The objectives of this study included assessing the viability of HFR in the presence of partially ice-covered waters and to obtain background information on currents on the inner shelf of the Beaufort Sea and Cook Inlet in order to improve spill trajectory models.

The Beaufort Sea deployment took place in the vicinity of Prudhoe Bay. Technical difficulties with equipment and siting precluded obtaining a comprehensive data set in 2005, but a complete season of surface current data was collected in 2006 beginning with ice break-up in early July and continuing through freeze-up in October. The data underscore the importance of the winds in forcing the Alaskan Beaufort shelf circulation. Statistical analyses show that for all ice conditions (including ice-free waters) and in both 2005 and 2006 most of the current variance (~90%) is oriented in the along-shore and that along-shore winds account for ~75% of the along-shore current variance. HFR data was validated by comparing it to a current meter deployed in the area. Linear regressions were used to compare the along- and cross-shore velocity components derived from the current meter and HFR. The results are statistically significant for both components with 93% (and 70%) of the current meter along-shore (cross-shore) velocity variance captured by the HFR. Our results suggest that strong storm winds can rapidly replace Beaufort Sea shelf waters. For example, we estimate that the entire volume of the inner shelf of the Beaufort Sea was replaced in about 25 days in fall 2006. This study has extended the utility of HFR surface current mapping to high-latitude, partially ice-covered seas.

The HFR deployment in Lower Cook Inlet occurred from November 2006 through November 2007. Tidal currents dominate the circulation in Lower Cook Inlet, accounting for at least 67% the current variability and, in many locations, more than 85% of the variance, due to the fact that Cook Inlet is nearly resonant with semi-diurnal tides. The annual mean, non-tidal, surface current circulation indicates generally southward flow over most of Lower Cook Inlet, which connects with the westward-flowing Alaska Coastal Current at the Inlet's mouth. The southward flow is swiftest along the western side of the Inlet and over the bank separating two deeper troughs in the center of Lower Cook Inlet. There is, in addition, a weak counter-clockwise eddy near the mouth of Kachemak Bay in Lower Cook Inlet and a northward (up-Inlet) flow offshore of Anchor Point that is likely fed by an outflow along the north coast of Kachemak Bay. The net southward flow in Lower Cook Inlet implies that there must be inflow at depth to maintain mass balance. This inflow from the Gulf of Alaska shelf probably feeds the counter-clockwise eddy and is likely concentrated in the two deep troughs in Lower Cook Inlet. Weekly maps of the non-tidal, surface flow indicate large synoptic variability. These variations are uncorrelated with the winds over Lower Cook Inlet.

TABLE OF CONTENTS

Page

Executive Summary ... iii

LIST OF FIGURES ... vii
LIST OF TABLES ... xv

CHAPTER ONE - Beaufort Sea ... 1

1.0 Introduction ... 1
  1.1 Beaufort Sea Regional Setting ... 2

2.0 Methods ... 6
  2.1 Defining First Order Regions (reprinted with permission from CODAR Ocean Sensors) .. 9
  2.2 Defining Beaufort Sea Spectra ... 11
  2.3 Antenna Pattern Measurement ... 18
  2.4 Empirical Orthogonal Functions ... 19

3.0 Results ... 20
  3.1 Wind ... 21
  3.2 Ice ... 23
  3.3 Salinity ... 29
  3.4 Currents ... 29
    3.4.1 Regime One: Open Water out to 15 to 20 km Offshore ... 32
    3.4.2 Regime Two: Band of Fragmented Ice 20 to 30 km Offshore ... 39
    3.4.3 Regime Three: Ice-Free Waters ... 49
    3.4.4 Regime Four: Early Landfast Ice Formation ... 60
  3.5 Data Validation ... 67

4.0 Discussion ... 69

5.0 Future Work ... 71

CHAPTER TWO - Cook Inlet ... 72

1.0 Introduction ... 72
  1.1 Cook Inlet Regional Setting ... 72

2.0 Methods ... 77
  2.1 Defining Cook Inlet Spectra ... 79
  2.2 Antenna Pattern Measurement ... 80

3.0 Results ... 81
  3.1 Winds ... 83

3.2 Ice 83
3.4 Tidal Variability 85
3.5 Subtidal Variability 85

4.0 Discussion 115

5.0 Future Work 119

List of References 121

Acknowledgements 125

APPENDIX A 127

APPENDIX B 137

LIST OF FIGURES

Page

Figure 1. Map of the Alaskan Beaufort Sea and North Slope with subdivisions indicated above the figure. 2

Figure 2. Mean monthly statistics on upwelling and downwelling derived from the 1945 - 2005 Barrow wind record. 3

Figure 3. Daily runoff for a) Kuparuk and b) Sagavanirktok rivers from 2003-2007.. 5

Figure 4. Stars show locations of the HFR sites in Prudhoe Bay. The westernmost site was located on the West Dock Causeway, and the easternmost site was located on the northernmost tip of the Endicott Causeway. 6

Figure 5. Top photo: HFR system components deployed at Endicott, including the transmit antenna, receive antenna, and instrument hut, as well as the Starband satellite dish used for remote communications. Bottom photo: View of the inside of the instrument hut, which housed the laptop computer, the transmit and receive electronics, back-up battery power, tools, and spare parts. 7

Figure 6. Typical two-dimensional coverage in the Beaufort Sea during open water. 8

Figure 7. Typical radar spectra from ocean sea-echo, with the dominant first-order region (dark shading) surrounded by the second-order region (lighter shading), superimposed on a noise floor. 10

Figure 8. First-order peaks falling to the noise floor. Due to the absence of long ocean waves, there is no second-order echo. 12

Figure 9. Radar spectrum showing ionospheric echo superimposed on the sea-echo spectrum. The first-order peaks are just visible above the ionospheric echo. 12

Figure 10. Examples of radar spectra when there are strong currents. The first-order region has spread over the surrounding higher order structure. 13

Figure 11. An example of a saturated spectrum. First-order spectrum cannot be isolated as it is merged with the higher-order echo. 13

Figure 12. Example spectra when ice exists offshore. Positive returns on the right side of the plot are a split first-order peak. 14

Figure 13. Range cells are overlaid on SAR imagery. 14

Figure 14. Sample spectra shows a split first order peak on the positive side of the returns. Gray-shaded area shows the first order definitions with the default CODAR software settings (a) and after the first order line settings are corrected to capture the split first order peak. 15

Figure 15. Range Cell 10 is highlighted with green showing the area included in the first order energy and red showing the excluded area. 16

Figure 16. Spectral plot defining both the Bragg peaks used to determine surface current velocities as well as the baseline peak, which is defined by moving ice. 17

Figure 17. Spectra for all West Dock range cells on October 9, 2006, are depicted on the left, with a cross section of Range Cell 8 shown on the right. 17

Figure 18. Antenna pattern measurements for a)2005 and b)2006. 18

Figure 19. 2005 and 2006 operational timeline for both West Dock (WEST) and Endicott (ENDI) field sites. 21

Figure 20. Time series plot of the antenna signal to noise ratio and wind speed showing a direct correlation between the two time series...22

Figure 21. Linear regression of the along-shore wind component of meteorological stations in our study area for July 2005 and 2006..23

Figure 22. Time series of wind speed for June 2005 and 2006. Wind speeds in 2005 were higher in magnitude earlier than 2006 winds. 24

Figure 23. Monthly averages of the ice edge along the North Slope of Alaska from AMSR-E for A) July, B) August, C) September, and D) October 2005 and 2006. 25

Figure 24. SAR imagery from July 1 and July 5, 2006, depicts the ice conditions near Prudhoe Bay. 26

Figure 25. Bi-weekly SAR imagery from 2005 and 2006. 27-28

Figure 26. Salinity vs Offshore Radar Range for a 25 MHz and 13 MHz CODAR HFR system. There is a direct relationship between salinity and radar range. 29

Figure 27. SAR imagery from July 18, 2006, shows an example of Regime One, when open water was within 15 to 20 km of shore and ice covered the rest of the HFR field-of-view 30

Figure 28. SAR imagery from September 8, 2006, shows an example of Regime Two, when there was a persistent band of fragmented ice 20 to 30 km offshore. 30

Figure 29. SAR imagery from October 14, 2005, shows an example of Regime Four, when landfast ice was beginning to form from the shoreline seaward. 31

Figure 30. SAR imagery from July 5, 2006. An example of Endicott one-dimensional data return locations when ice floes were present between shore and the ice edge under westward winds of ~7 m/s..32

Figure 31. Percent coverage through time of two-dimensional HFR data returns during regime one for July 5-19 and August 5-14, 2006. 33

Figure 32. Average current and wind vectors from August 5-14, 2006. 32

Figure 33. Principal axes for currents measured from August 5-14, 2006. Current variations variations are predominantly in the along-shore direction with little to no cross-shore flow. 33

Figure 34. Time series plot of EOF mode 1 and the along-shore wind speed for August 6-14. 35

Figure 35. July 8, 2006, one-dimensional HFR returns overlaid on SAR imagery..................36

Figure 36. July 15, 2006, one-dimensional HFR returns overlaid on SAR imagery................37

Figure 37. August 7, 2006, one-dimensional HFR returns overlaid on SAR imagery. 37

Figure 38. August 8, 2006, one-dimensional HFR returns overlaid on SAR imagery. 38

Figure 39. August 7, 2006, two-dimensional HFR returns overlaid on SAR imagery. 38

Figure 40. August 8, 2006, two-dimensional HFR returns overlaid on SAR imagery. 39

Figure 41. Percent coverage through time of two-dimensional HFR current returns from August 26 - September 3, 2005, and August 25 - September 26, 2006. 40

Figure 42. Mean currents and wind speeds from August 26 - September 3, 2005, and August 25 - September 26, 2006..41

Figure 43. Principal axes from August 26 - September 3, 2005, and August 25 - September 26, 2006. 43

Figure 44. Time series of EOF mode 1 and wind speed from August 26 - September 3, 2005, and August 25 - September 26, 2006. 44

Figure 45. August 26, 2005, two-dimensional HFR returns overlaid on SAR imagery. 45

Figure 46. August 29, 2005, two-dimensional HFR returns overlaid on SAR imagery. 45

Figure 47. August 30, 2005, two-dimensional HFR returns overlaid on SAR imagery. 46

Figure 48. September 3, 2005, two-dimensional HFR returns overlaid on SAR imagery. 46

Figure 49. Two-dimensional surface currents overlaid on SAR imagery for a) September 8, 2006, and b) September 11, 2006. Time series of wind direction and magnitude for September 7-11 is shown as a stick plot. 47

Figure 49. Two-dimensional surface currents overlaid on SAR imagery for c) September 17, 2006, and d) September 21, 2006. Time series of wind direction and magnitude for September 16-22 is shown as a stick plot. 48

Figure 50. Percent coverage through time of two-dimensional HFR current returns from September 16 - October 10, 2005, and October 2 - 20, 2006. 50

Figure 51. Mean currents and wind speeds from September 16 - October 10, 2005, and October 2 - 20, 2006. 51

Figure 52. Principal axes from September 16 - October 10, 2005, and October 2 - 20, 2006. .52

Figure 53. Time series of EOF mode 1 and wind speed from September 16 - October 10, 2005, and October 2 - 20, 2006..53

Figure 54. Time series of along-shore surface currents and winds..54

Figure 55. Time series of the u and v components of surface currents and wind speeds. 55

Figure 56. Principal axes for September 24-30, with variations predominantly in the along-shore direction. Wind vector time series. Averaged surface current vectors for the same time frame. 56

Figure 57. Principal axes for October 1-7, with variations predominantly in the along-shore direction. Wind vector time series. Averaged surface currents vectors for the same time frame. 57

Figure 58. Principal axes for October 8-14, with variations predominantly in the along-shore direction. Wind vector time series. Averaged surface current vectors for the same time frame. 58

Figure 59. 24-hour surface current trajectories from October 10 – 11, 2006, when winds reversed from blowing to the west to blowing toward the east. Dots on the trajectories depict locations at one hour intervals. 59

Figure 60. 24-hour surface current trajectories from October 14, 2006. During this time, winds reversed from blowing to the east to blowing toward the west. Dots on the trajectories depict locations at one hour intervals. 59

Figure 61. Percent coverage through time of two-dimensional HFR current returns from October 19 - 20, 2006. 60

Figure 62. Mean currents and wind speeds from October 19 - 20, 2006....61

Figure 63. Time series of wind direction and magnitude for October 19 - 20, 2006. 61

Figure 64. October 10, 2005, SAR image showing open water in the HFR coverage area....62

Figure 65. 03:00 UTC, October 13, 2005, SAR image. Yellow circles represent HFR data returns....63

Figure 66. 17:00 UTC, October 13, 2005, SAR image. Yellow circles represent HFR data returns....63

Figure 67. October 12, 2006, SAR image with HFR data returns. Grease ice is present along barrier islands and causeways....64

Figure 68. October 15, 2006, SAR image with HFR data returns. Nearshore area inside of the barrier islands is covered with grease ice. 65

Figure 69. October 18, 2006, SAR image with HFR data returns. Nearshore area inside of the barrier islands is covered with grease ice. 65

Figure 70. October 19, 2006, SAR image with HFR data returns. Landfast ice edge has entered the HFR coverage area....66

Figure 71. October 22, 2006, SAR image with HFR data returns. HFR area is completely ice covered. 66

Figure 72. Location of moored upward-looking ADCP and the nearest HFR gridpoint which were compared for data validation....67

Figure 73. Time series of along-shore and cross-shore current components collected from the HFR and an upward-looking ADCP located near Cross Island....68

Figure 74. Linear regressions of the along-shore and cross-shore components of the HFR and ADCP, excluding data from the storm on October 9, 2006. 68

Figure 75. Bathymetric map of Cook Inlet and adjacent Gulf of Alaska. 73

Figure 76. Mean daily discharge from January 1, 2006, through October 31, 2007, for several of the major rivers emptying into Cook Inlet and the mean monthly discharge for the Susitna River at the head of Knik Arms for the period 1975-1993. 74

Figure 77. May 19, 2007, MODIS visible satellite image. Notice the brown suspended sediment in the Upper Inlet that is transported southward along the western side of the Lower inlet. 74

Figure 78. Summer Circulation in Lower Cook Inlet (Muench et al. 1978). 75

Figure 79. Surface Circulation in Lower Cook Inlet (Burbank 1977). 76

Figure 80. Bathymetric map of Lower Cook Inlet. 77

Figure 81. Black stars show locations of the HFR sites in Cook Inlet, Alaska. The northern site was located in Anchor Point, and the southern site was located in the Alaska Native village of Nanwalek. 78

Figure 82. Onsite housing for electornics at Anchor Point. 79

Figure 83. Typical two-dimensional coverage of the HFR in Lower Cook Inlet at 13 MHz. ...79

Figure 84. Results of the 13 MHz antenna pattern measurements performed in Cook Inlet for Anchor Point and Nanwalek. 80

Figure 85. Operational timelines for Anchor Point and Nanwalek field sites. 82

Figure 86. Percent coverage through time of two-dimensional HFR current returns from November 12, 2006, through November 10, 2007. 83

Figure 87. Satellite imagery from March 2007 showing grease ice presence in Lower Cook Inlet 84

Figure 88. M_2 tidal ellipses for points with >50% data coverage. 86

Figure 89. S_2 tidal ellipses for points with >50% data coverage. 86

Figure 90. K_1 tidal ellipses for points with >50% data coverage. 87

Figure 91. Representative locations displayed in Tables 1 and 2 overlaid on M_2 tidal ellipses. 87

Figure 92. Subtidal mean currents derived from HFR in Lower Cook Inlet from November 12, 2006, through November 10, 2007, overlaid on bathymetry contours. 90

Figure 93. Subtidal principle axes derived from HFR in Lower Cook Inlet from November 12, 2006, through November 10, 2007, overlaid on bathymetry contours. 90

Figure 94. Weekly mean current and wind vectors overlaid on bathymetry contours for November 26 - December 2, 2006, with placenames. 91

Figure 95. Weekly mean current and wind vectors overlaid on bathymetry contours for December 3 - 9, 2006. 91

Figure 96. Weekly mean current and wind vectors overlaid on bathymetry contours for December 10 - 16, 2006. 92

Figure 97. Weekly mean current and wind vectors overlaid on bathymetry contours for December 17 - 23, 2006. 92

Figure 98. Weekly mean current and wind vectors overlaid on bathymetry contours for December 24 - 30, 2006. 94

Figure 99. Weekly mean current and wind vectors overlaid on bathymetry contours for December 31 - January 6, 2007. 94

Figure 100. Weekly mean current and wind vectors overlaid on bathymetry contours for January 7 - 13, 2007.....95

Figure 101. Weekly mean current and wind vectors overlaid on bathymetry contours for January 14 - 20, 2007.....95

Figure 102. Weekly mean current and wind vectors overlaid on bathymetry contours for January 21 - 27, 2007.....96

Figure 103. Weekly mean current and wind vectors overlaid on bathymetry contours for January 28 - February 3, 2007. 96

Figure 104. Weekly mean current and wind vectors overlaid on bathymetry contours for February 4 - 10, 2007.....97

Figure 105. Weekly mean current and wind vectors overlaid on bathymetry contours for February 11 - 17, 2007.....97

Figure 106. Weekly mean current and wind vectors overlaid on bathymetry contours for February 18 - 24, 2007.....98

Figure 107. Weekly mean current and wind vectors overlaid on bathymetry contours for February 25 - March 3, 2007. 98

Figure 108. Weekly mean current and wind vectors overlaid on bathymetry contours for March 4 - 10, 2007.....99

Figure 109. Weekly mean current and wind vectors overlaid on bathymetry contours for March 11 - 17, 2007.....99

Figure 110. Weekly mean current and wind vectors overlaid on bathymetry contours for April 1 - 7, 2007.....100

Figure 111. Weekly mean current and wind vectors overlaid on bathymetry contours for April 8 - 14, 2007.....100

Figure 112. Weekly mean current and wind vectors overlaid on bathymetry contours for April 15 - 21, 2007.....102

Figure 113. Weekly mean current and wind vectors overlaid on bathymetry contours for April 22 - 28, 2007.....102

Figure 114. Weekly mean current and wind vectors overlaid on bathymetry contours for April 29 - May 5, 2007. 103

Figure 115. Weekly mean current and wind vectors overlaid on bathymetry contours for May 6 - 12, 2007.....103

Figure 116. Weekly mean current and wind vectors overlaid on bathymetry contours for May 13 - 19, 2007.....104

Figure 117. Weekly mean current and wind vectors overlaid on bathymetry contours for May 20 - 26, 2007.....104

Figure 118. Weekly mean current and wind vectors overlaid on bathymetry contours for May 27 - June 2, 2007.....105

Figure 119. Weekly mean current and wind vectors overlaid on bathymetry contours for June 3 - 9, 2007.....105

Figure 120. Weekly mean current and wind vectors overlaid on bathymetry contours for June 10 - 16, 2007. 106

Figure 121. Weekly mean current and wind vectors overlaid on bathymetry contours for June 17 - 23, 2007. 106

Figure 122. Weekly mean current and wind vectors overlaid on bathymetry contours for June 24 - 30, 2007. 107

Figure 123. Weekly mean current and wind vectors overlaid on bathymetry contours for July 1 - 7, 2007....107

Figure 124. Weekly mean current and wind vectors overlaid on bathymetry contours for July 8 - 14, 2007....108

Figure 125. Weekly mean current and wind vectors overlaid on bathymetry contours for July 15 - 21, 2007....108

Figure 126. Weekly mean current and wind vectors overlaid on bathymetry contours for July 22 - 28, 2007....110

Figure 127. Weekly mean current and wind vectors overlaid on bathymetry contours for July 29 - August 4, 2007. 110

Figure 128. Weekly mean current and wind vectors overlaid on bathymetry contours for August 5 - 11, 2007....111

Figure 129. Weekly mean current and wind vectors overlaid on bathymetry contours for August 12 - 18, 2007....111

Figure 130. Weekly mean current and wind vectors overlaid on bathymetry contours for August 19 - 25, 2007....112

Figure 131. Weekly mean current and wind vectors overlaid on bathymetry contours for August 26 - September 1, 2007....112

Figure 132. Weekly mean current and wind vectors overlaid on bathymetry contours for September 2 - 8, 2007. 113

Figure 133. Weekly mean current and wind vectors overlaid on bathymetry contours for September 9 - 15, 2007. 113

Figure 134. Weekly mean current and wind vectors overlaid on bathymetry contours for September 16 - 22, 2007. 114

Figure 135. Weekly mean current and wind vectors overlaid on bathymetry contours for September 23 - 29, 2007. 114

Figure 136. Weekly mean current and wind vectors overlaid on bathymetry contours for September 30 - October 6, 2007. 116

Figure 137. Weekly mean current and wind vectors overlaid on bathymetry contours for October 7 - 13, 2007. 116

Figure 138. Weekly mean current and wind vectors overlaid on bathymetry contours for October 14 - 20, 2007. 117

Figure 139. Weekly mean current and wind vectors overlaid on bathymetry contours for October 21 - 27, 2007. 117

Figure 140. Weekly mean current and wind vectors overlaid on bathymetry contours for October 28 - November 3, 2007. 118

Figure 141. Weekly mean current and wind vectors overlaid on bathymetry contours for November 4 - 10, 2007. 118

LIST OF TABLES

Page

Table 1. Tidal ellipse hodograph properties for locations shown in Figure 91. 88

Table 2. Tidal, non-tidal, and total current variances for the east-west and north-south current components at the seven grid points shown in Figure 91. 89

Table 3. Field log listing frequency switches, notes, and significant events for the 2005 Endicott field season. 126

Table 4. Field log listing frequency switches, notes, and significant events for the 2005 West Dock field season. 127

Table 5. Field log listing frequency switches, notes, and significant events for the 2006 Endicott field season. 129

Table 6. Field log listing frequency switches, notes, and significant events for the 2006 West Dock field season. 131

CHAPTER ONE - Beaufort Sea

This study was designed to collect and map surface currents utilizing High Frequency Radar (HFR) in both the Arctic Beaufort Sea, where ice was present in varying concentrations, and in Cook Inlet, where strong tides were an important environmental factor in the collection and analysis of surface currents. HFR data provides a real-time synoptic view of surface currents, rather than the point source data available subsequent to recovery of oceanographic instrumentation, such as that provided by a mooring. Having high temporal and spatial resolution surface current data is critical for successful forecasting of contaminant spill trajectories and conducting search and rescue operations.

Chapter one of this report addresses the 2005 and 2006 Beaufort Sea field seasons of the U.S. Minerals Management Service Outer Continental Shelf program Contract #1435-01-04-CT-35579, Surface Circulation Radar Mapping in Alaskan Coastal Waters: Beaufort Sea and Cook Inlet including 1. introduction, including regional setting; 2. methods, including how to process radar data in the presence of ice; 3. results for winds, ice, and currents; 4. discussion of the data; and 5. recommendations for future work. Cook Inlet data collected from November 2006 through November 2007 is covered in chapter two. This study is the result of a U.S. Minerals Management Service research sponsorship meeting conducted under Contract #1435-01-02-CT-31150.

1.0 Introduction

Mapping surface currents in partially sea-ice covered waters using HFR has received limited effort to date. An HFR system manufactured by Costal Ocean Dynamics Applications Radar (CODAR) Ocean Sensors was deployed in Prudhoe Bay, Alaska, during ice breakup in July 1984 to investigate the prospect of using HFR to observe ice and water velocities as well as ice cover (Lipa et al. 1986). Gulf Oil was interested in using these observations to make operating decisions regarding floating platforms. They found that the CODAR HFR system was indeed able to observe both ice and water velocities as well as the ice edge, but shortly after these initial tests, Gulf Oil merged with Standard Oil, and the HFR systems were never utilized. Since then, applications of HFR in Arctic environments have been scarce and limited to examining the operational issues associated with ship-mounted systems (Gurgel and Essen 2000). This is in contrast to the shore-based HFR in this report, where emphasis is placed on data quality under varying ice conditions.

Operating an HFR system in the presence of varying sea ice conditions is challenging with respect to both field and data processing stages. Field equipment needs to be set up before ice breakup but after enough snow melt that the equipment can be anchored to the ground. Environmental conditions are harsh with freezing temperatures and powerful storms. When there is ice present in the field-of-view, default processing settings for converting raw data into surface currents fail. In Prudhoe Bay, HFR operations require permission from BP to access the oil fields; this involves training and safety courses required by BP.

University of Alaska Fairbanks (UAF) personnel deployed and maintained two HFR systems on the Beaufort Sea coast in Prudhoe Bay during the open water seasons of 2005 and 2006. The ice conditions as well as number and intensity of storms varied greatly between the two years. Both of these factors have a direct effect on the quality of the data as well as how the data is processed, which proved to be an intensive, time consuming effort. This report addresses the two field seasons and covers the analysis performed based on the project objectives.

1.1 Beaufort Sea Regional Setting

The Alaskan Beaufort Sea shelf (Figure 1) extends ~500 km eastward from Point Barrow to the Mackenzie River portion of the Beaufort Sea shelf in Canadian waters. The shelf width is ~80 km as measured from the coast to the 200 m isobath. Shelf depths grade smoothly offshore with bottom slopes typically being ~10^{-3} inshore of the 100 m isobath. There appears to be little along-shelf variation in the bathymetry, with the exceptions of Barrow Canyon along the western margin of the shelf and Mackenzie Canyon at the eastern boundary.

Sea ice can cover the shelf year-round, although more typically the inner shelf (and in recent years the entire shelf) is ice-free during the summer months. Landfast ice begins to form in mid- to late October and extends 20 – 40 km offshore through mid-June (Weingartner et al. 2009). The outer shelf may remain ice-free longer, although by late November ice typically covers the entire shelf.

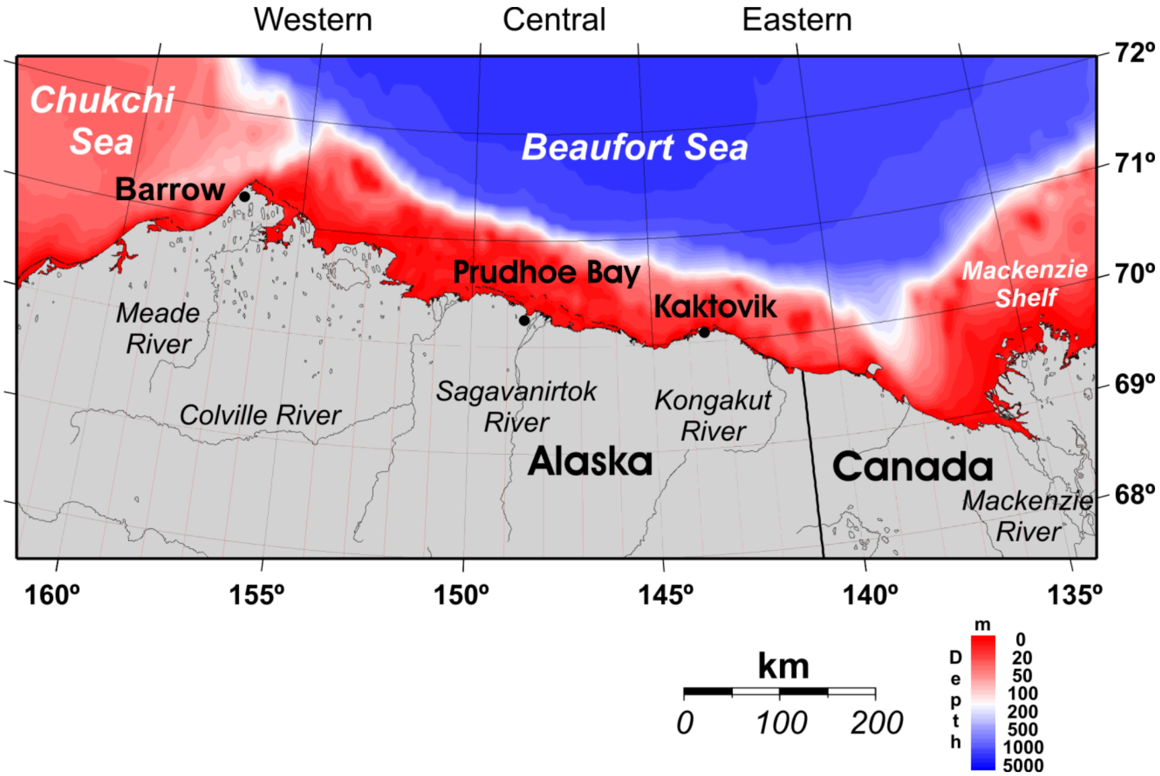

Figure 1. Map of the Alaskan Beaufort Sea and North Slope with subdivisions indicated above the figure.

Ocean circulation during the open water season is strongly influenced by the wind field. Winds from the northeast blow throughout the year, so that on average the prevailing along-shelf winds are westward and upwelling favorable. However, based on the climatological analysis of the Barrow wind record by Taylor and Weingartner (2007), winds vary seasonally (Figure 2). Upwelling favorable winds occur 55% or more of the time in all months and exceed 70% of the time in spring and fall, while downwelling winds are most frequent in July and August. The wind stress magnitude also varies seasonally. Wind stress (up- or downwelling) is a minimum from May through July and a maximum from October through January.

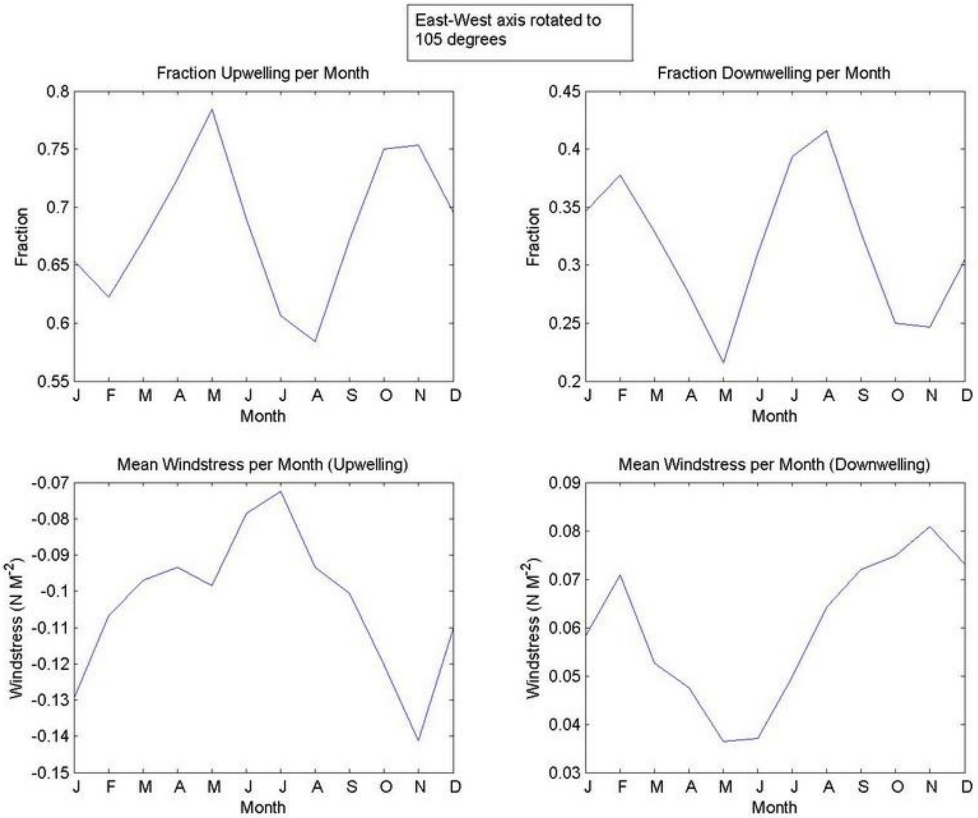

Figure 2. Mean monthly statistics on upwelling and downwelling derived from the 1945 - 2005 Barrow wind record by Taylor and Weingartner (2007). The upper panels show the fraction of upwelling (left) and downwelling (right) days in a month. The lower panel shows the mean monthly upwelling (left) and downwelling (right) wind stress.

Seasonally varying mesoscale winds may also influence the local winds over the shelf. For example, a persistent summer sea breeze enhances the mean westward winds within ~25 km of the coast (Kozo 1982a; Kozo 1982b). From October through April, mountain barrier baroclinicity (Kozo 1980; Kozo 2984) can produce along-shore divergence in the wind field. This effect occurs when the southward flow of low-level cold air from the Arctic Ocean is blocked along the northern flank of the Brooks Range. (There is relatively little relief along

Alaska's North Slope, with elevations climbing only gradually inland to the foothills of the Brooks Range.) The resulting isopycnal slopes induce eastward surface winds on the order of 15 m/s over a horizontal width scale of 200 – 300 km. The western Beaufort coast is rarely influenced by the mountain barrier effect because it lies more than 300 km north of the Brooks Range, but the eastern Beaufort coast lies within 60 km of the mountains. Consequently, winds can be westward over the western Beaufort coast but eastward along the eastern coast. Kozo (1984) estimated that the mountain barrier baroclinicity effect occurs ~20% of the time during winter.

Three distinct oceanic regimes bound the Alaskan Beaufort Sea. To the west, waters of Pacific Ocean origin flow northward from Bering Strait and across the Chukchi shelf. While this flow divides along three main branches across the Chukchi shelf, the one most relevant for the Beaufort shelf is the outflow through Barrow Canyon in the northeast Chukchi Sea (Mountain et al. 1976; Aagaard and Roach 1990; Weingartner et al. 1998; Weingartner et al. 2005; Pickart et al. 2005). Variability in the canyon outflow is large, especially in fall and winter, and mainly due to fluctuations in the regional winds (Weingartner et al. 1998; Weingartner et al. 2005; Woodgate et al. 2005). Part of the Barrow Canyon outflow continues eastward as a subsurface current (or slope undercurrent) along the Beaufort shelfbreak and slope, where it forms the upper halocline waters of the Canada Basin (Mountain et al. 1976; Aagaard 1984; Pickart 2004; Pickart et al. 2005), and part of the water rounds Pt. Barrow and continues onto the inner portion of the western Beaufort shelf (Okkonen et al. 2009); although no year-round measurements have been made to examine the frequency of this intrusion.

The outer shelf and continental slope provide the offshore boundary for the Alaskan Beaufort Sea. In the upper ~50 m the flow is westward and part of the southern limb of the wind-driven Beaufort Gyre. This flow can occasionally be reversed by strong winds from the east and/or by occasional shelfbreak upwelling that advects eastward momentum from the slope undercurrent onto the shelf as far inshore as the 50 m isobath (Aagaard 1984; Pickart 2004).

The Mackenzie shelf joins the Alaskan Beaufort shelf to the east, and it is apparent in satellite imagery that the eastern Beaufort shelf is influenced by year-round discharge from the Mackenzie River (Carmack et al. 1989; Macdonald et al. 1989; Macdonald and Carmack 1991). Mackenzie shelf water has been detected throughout much of the Canada basin, including the continental slope of the Chukchi and western Beaufort Sea as far as 160°W (Guay and Falkner 1998; Macdonald et al. 1999). Therefore, it seems likely that wind-driven currents also transport Mackenzie shelf waters onto the Alaskan Beaufort shelf. In this regard, we note that the migratory behavior of arctic cisco provide indirect evidence for the intrusion of Mackenzie River waters onto the inner shelf of the Alaskan Beaufort Sea. These fish apparently require a nearshore band of low-salinity water in order to complete their annual migration between the Mackenzie and Colville rivers each summer (Colonell and Galloway 1997). The migratory corridor is presumably maintained by the westward drift of low-salinity water from the Mackenzie shelf. In addition to the Mackenzie River, a large number of smaller rivers discharge into the Alaskan Beaufort Sea (Figure 1). These are asymmetrically distributed with most of them discharging into the central and eastern portions of the shelf. This asymmetric discharge, along with the influence of the Mackenzie, might establish an along-shelf density gradient that gives rise to an along-shelf baroclinic pressure gradient.

Our measurements were made in the vicinity of Prudhoe Bay, which lies approximately midway along the Alaskan Beaufort coast. Although a number of smaller streams empty into this area the three major rivers (and their watershed areas) that discharge into the study region are: the Sagavanirktok River (14900 km^2), the Kuparuk River (8100 km^2), and the Colville River (53,500 km^2). Only the first two of these are routinely gauged, and only seasonally, because the gauges are installed at ice breakup and removed in fall prior to freezeup. Typical discharge time series for these gauged rivers are shown in Figure 3. The annual discharge cycle is characterized by a rapid initiation and increase in runoff in late May or June that lasts about two weeks, during

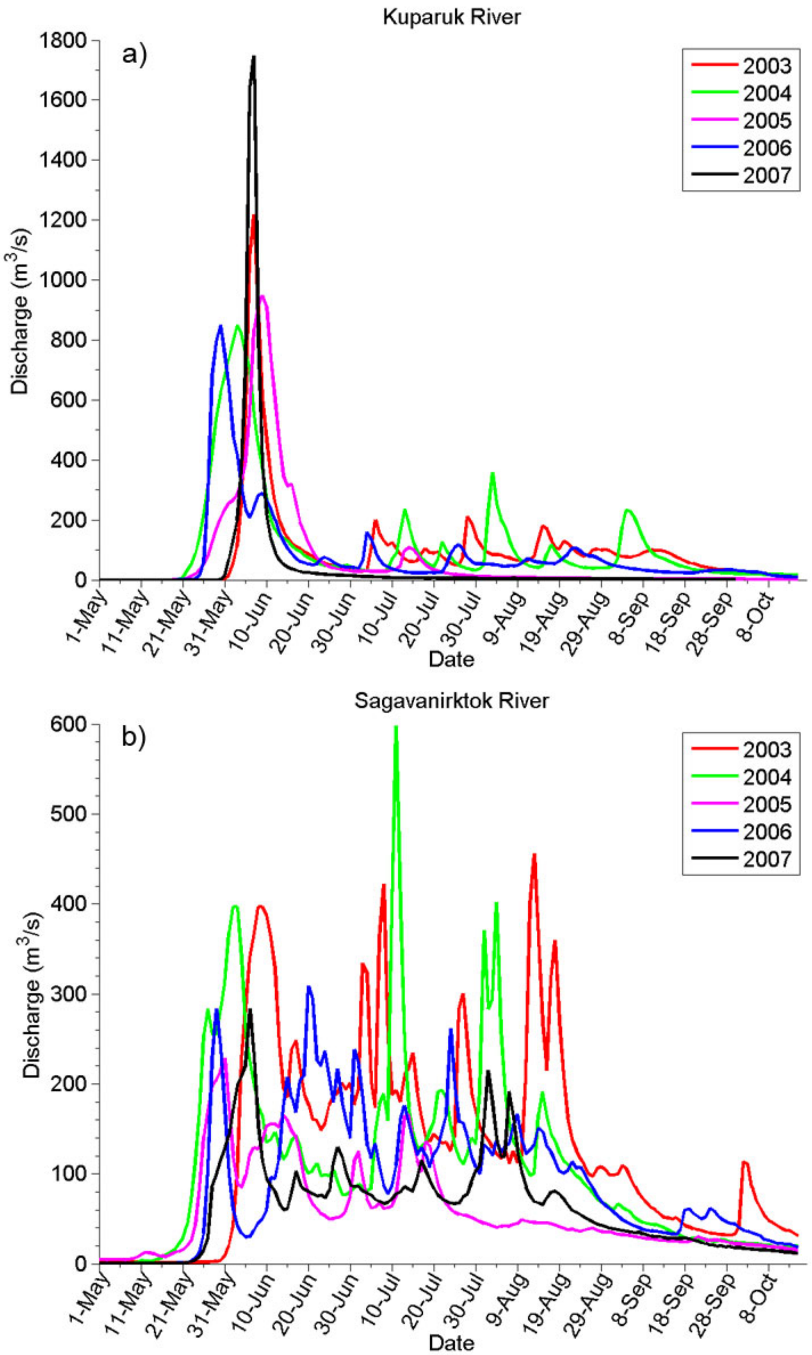

Figure 3. Daily runoff for a) Kuparuk and b) Sagavanirktok rivers from 2003-2007. The Sagavanirktok River gauge is located about 140 km inland, so the discharge at the coast is probably greater than that measured by the gauge.

which time nearly 90% of the annual discharge occurs. Following this spring freshet, the discharge is small and gradually decays to negligible values by October, although the decay can be punctuated by smaller, short-lived and sporadic discharge events following summer rain storms. The Colville River has a similar seasonal cycle, although the discharge is substantially larger because of its larger drainage area. Unlike the Mackenzie and other large Arctic rivers, there is no measurable winter discharge from any North Slope rivers, as most freeze to the bottom and all have watersheds lying entirely within drainages underlain by permafrost.

2.0 Methods

In June 2005 and 2006, while the Beaufort Sea was still ice covered, CODAR HFR systems with switchable frequencies (13/25 MHz) were installed at the end of the West Dock Causeway, north of the Seawater Treatment Plant, and north of the Endicott Production Facility (at the tip of Endeavor Island) to measure ocean surface currents at a high spatial and temporal frequency (Figure 4). Each site consisted of a transmit antenna, receive antenna, Starband satellite dish for remote communications, and an electronics hut, which housed the SeaSonde (i.e. the receive/transmit electronics), laptop, and backup battery power, as well as spare parts (Figure 5).

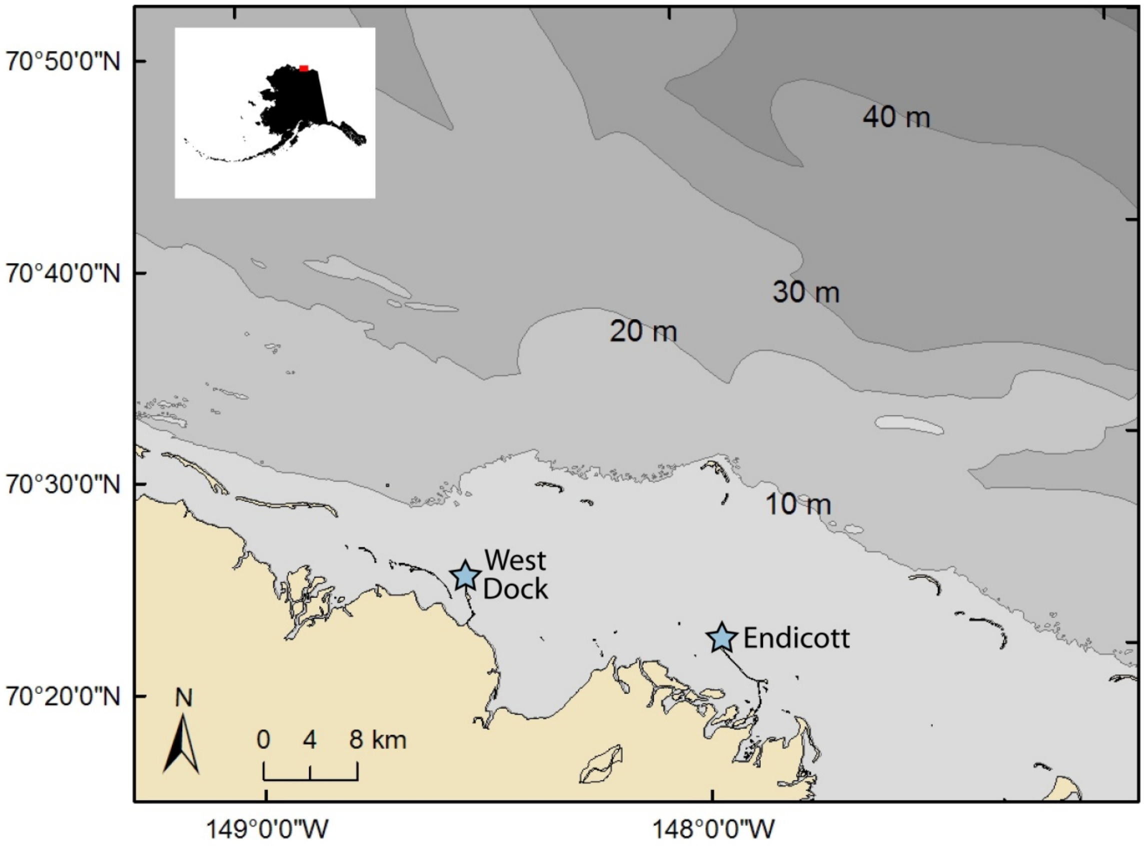

Figure 4. Stars show the locations of the HFR sites in Prudhoe Bay, Alaska. The westernmost site was located on the West Dock Causeway, and the easternmost site was located on the northernmost tip of the Endicott Causeway. Gray shading represents bathymetry contours in meters.

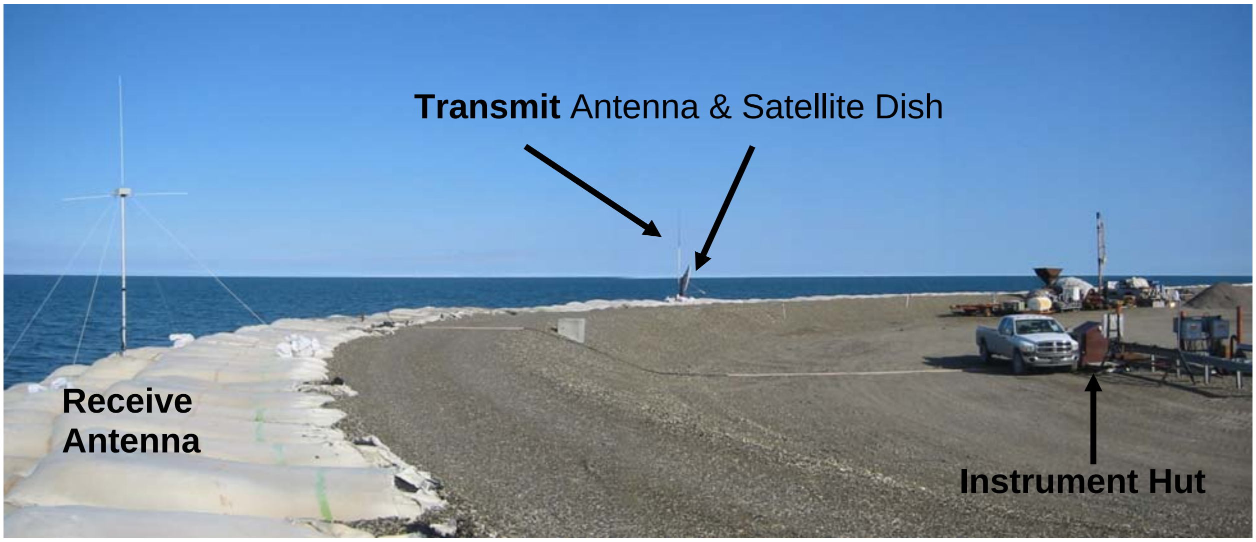

Figure 5. Top photo: HFR system components deployed at Endicott, including the transmit antenna, receive antenna, instrument hut, and the Starband satellite dish used for remote communications. Bottom photo: View of the inside of the instrument hut, which housed the laptop computer, the transmit and receive SeaSonde electronics, back-up battery power, tools, and spare parts.

The offshore coverage area of the systems is primarily dependent on frequency. At 25MHz the radar mask extends ~40 km offshore, while at 13 MHz radar wave propagation increases and coverage can extend ~60 km offshore (Figure 6). These distances are dependent on environmental conditions such as winds, wave field, sea surface salinity, presence of sea ice, and ambient radio noise sources. The 25 MHz frequency receives energy from a 6 m ocean wave, while the 13 MHz receives energy from 12.5 m ocean waves.

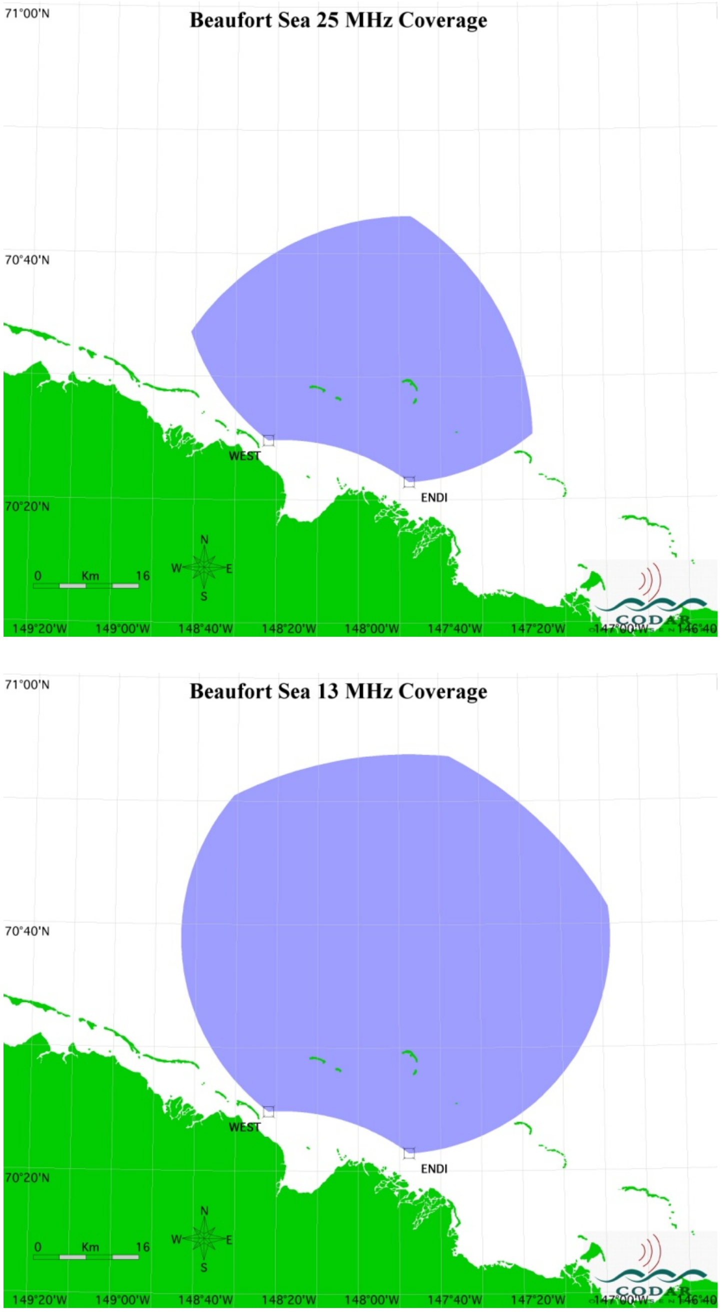

Figure 6. Typical two-dimensional coverage in the Beaufort Sea during open water conditions. The map on the top shows coverage for the 25 MHz setting, and the map on the bottom shows the coverage area when the system was running at 13 MHz.

The switchable frequency system is a relatively new feature for CODAR products and was essential for achieving our project objectives of collecting data and determining how well the HFR performs in variable ice/open water conditions. The switchable frequency option had been used once before in a Santa Cruz, California, deployment where it worked continuously for about 1.5 years. However, there were several problems associated with this hardware in our study, which in 2005, lead to poorer data quality and quantity than anticipated. These problems were subsequently resolved, and the dual-frequency system worked flawlessly in 2006.

The hardware complications in 2005 prevented useful data from being collected until after August 21, when the system ran at 25 MHz from August 22 to September 29 and then was switched to 13 MHz until the end of the 2005 field season in October. A high wind event on October 10 caused a break in the power line supplying the West Dock field site, but the Endicott field site continued operating through October 26. Although the Endicott field site remained operational longer than the West Dock site, October 13 was the last date of data returns due to landfast ice formation.

In 2006, we initially transmitted at 25 MHz when the ice edge was within ~40 km of the shoreline and when winds were low or the fetch was short (e.g. during mixed ice/open water). In order to optimize the system during variable environmental conditions, technicians at UAF and CODAR headquarters in Mountain View, California, were able to remotely switch the operating frequency by executing a simple computer program. System frequency was switched numerous times during the first half of the 2006 field season to ensure that the optimal operating frequency, given particular environmental conditions, was used (Appendix A). The systems remained in place until landfast ice formation ended data returns on October 22, 2006.

2.1 Defining First Order Regions (reprinted with permission from CODAR Ocean Sensors)

Surface currents are determined from the HFR by analyzing and processing the Doppler spectrum of the backscattered radar waves (Barrick et al. 1985). HFR backscatter cross spectra have a characteristic appearance. Dominant first-order peaks, which are used to calculate the current speeds, occur due to Bragg scattering from ocean waves with a wavelength one half the radar wavelength. In the absence of ambient noise and ocean currents the backscattered signal would appear as delta functions in the spectra. Spectral broadening occurs due to currents in the field-of-view of the radar.

Figure 7 shows typical sea-echo spectra. The first-order peaks are surrounded by a higher order continuum, predominantly caused by the interaction of the radar wave with pairs of ocean waves, one of which has a wavelength approximately equal to the first-order Bragg wave, the other being a longer wave with significant energy. Near the Bragg frequency, the second wave in the pair is the longest wave present on the ocean surface. Further away in frequency, the second wave diminishes in length so that eventually the radar echo falls beneath the noise floor.

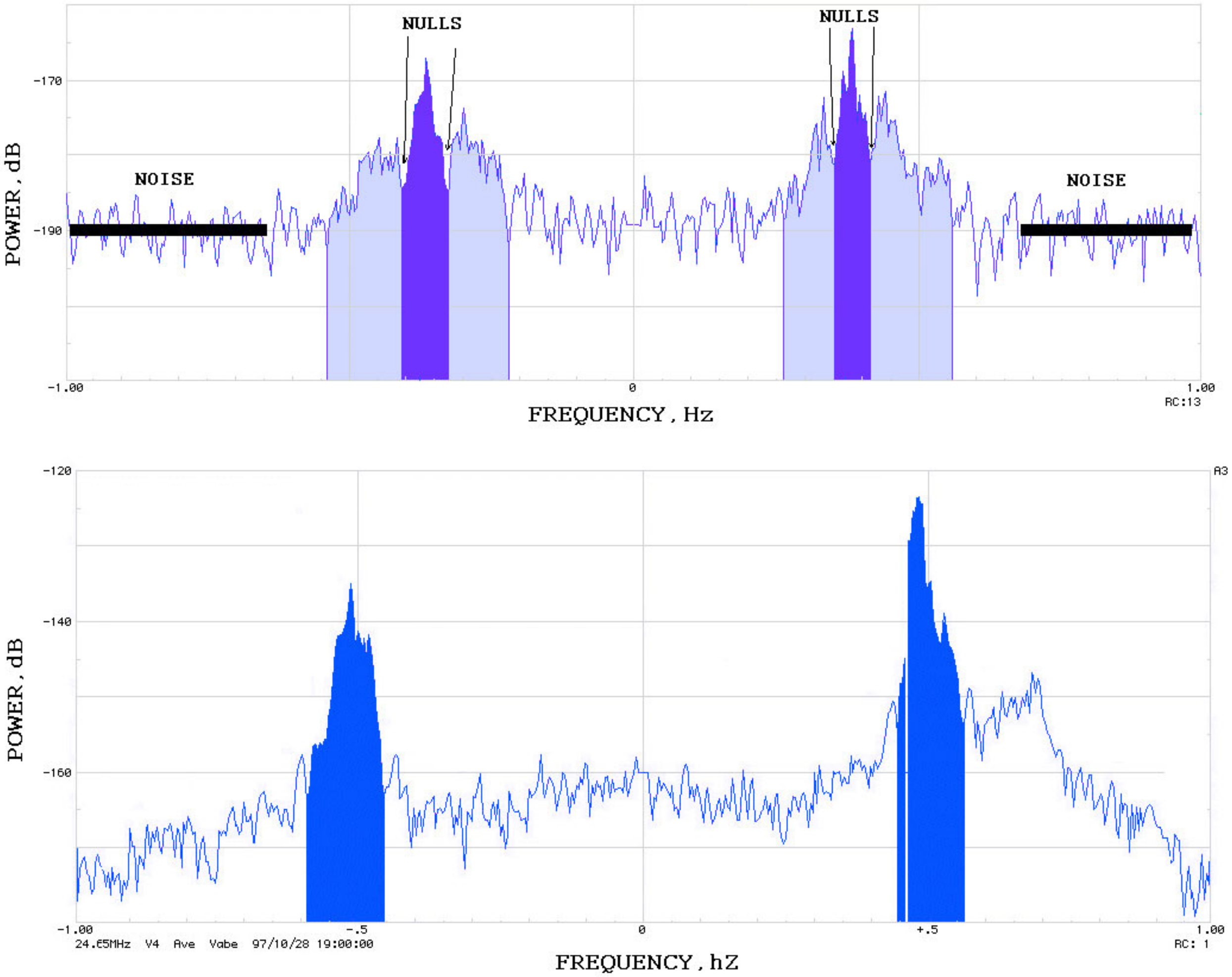

Figure 7. Typical radar spectra from ocean sea-echo, with the dominant first-order region (dark shading) surrounded by the second-order region (lighter shading), superimposed on a noise floor. In the top plot, the dominant ocean waves have a long period; hence the second-order peaks are close to the first-order region. In the bottom plot, the dominant waves are shorter, and the second-order structure is further displaced from the first.

We can use the following features to distinguish between first and second-order regions of the spectrum:

1. Power in the second-order peaks is typically halfway between the noise floor and the first-order peak.
2. Second-order peaks surround first-order peaks.
3. Second-order frequencies are approximately symmetric about the Bragg frequency.

However there are cases when the features listed are not definable:

1. No second-order echo: Where there are no long waves, there is negligible second-order echo (e.g. in ports, rivers, fetch-limited conditions). The first-order region falls straight to the noise floor (Figure 8).
2. Contamination by ionospheric echoes or radar interference from other sources: radar echo from another source is superimposed on the sea-echo signal (Figure 9). A comparison of noise in the Beaufort Sea spectra with auroral activity indices did not show any correlation between the two suggesting that this measure of ionospheric noise did not affect our data.
3. Extremely strong currents that spread the first-order region over the surrounding higher-order spectrum (Figure 10).
4. Saturated radar spectra: When the ocean wave amplitudes are large, the radar spectrum becomes saturated, resulting in the breakdown of the perturbation expansion on which the analysis is based. The expansion is in terms of h/l where l is the radar wavelength and h is the significant wave height. For the expansion to converge, h/l must be less than 0.5 (approximately), so the spectrum becomes saturated when the wave height exceeds one half the wavelength. When this saturation occurs, first and second order spectra merge so that there is no clear separation between them (Figure 11). The current vectors derived from such spectra can be inaccurate and imprecise.

2.2 Defining Beaufort Sea Spectra

Processing cross spectra files from the Beaufort Sea region proved challenging. The default parameters used to process cross spectra are not optimal in a partially ice-covered environment. Without getting the proper first order definition, gaps can begin to appear in the data, and the quality of the returned current magnitudes and direction suffer. When ice is present the first order peak can split, which causes the default processing settings to fail; hence, only part of the first order energy is resolved, which causes the resultant radial currents to be incomplete. An example of this is shown in Figure 12, where the positive first order peak is split into two different, but viable, peaks. Using the default processing settings, the taller peak on the monopole is recognized as first order, while the slightly shorter peak is discarded as second order. This, however, is not the case because both peaks are in fact first order but split due to the presence of ice in the study area.

The radar parses collected data into range cells, which are consistent radial distances from the receive antennae (Figure 13). The estimated spectra from each sample are determined for each range cell. A split first-order peak indicates that ice occurs somewhere within the range cell. For example, as one begins at the coast and traces along one of the more offshore range rings in Figure 13, one finds open water, ice, and then open water again. It is the ice in the middle of the range cell that causes the first order peak to be split. When spectra are collected by the receive antenna, the CODAR processing algorithms attempt to define the first order peak. The default settings resolve only the higher peak (Figure 14a); however, when the default settings are optimized for the sea ice environment, all of the first order energy is captured (Figure 14b). This

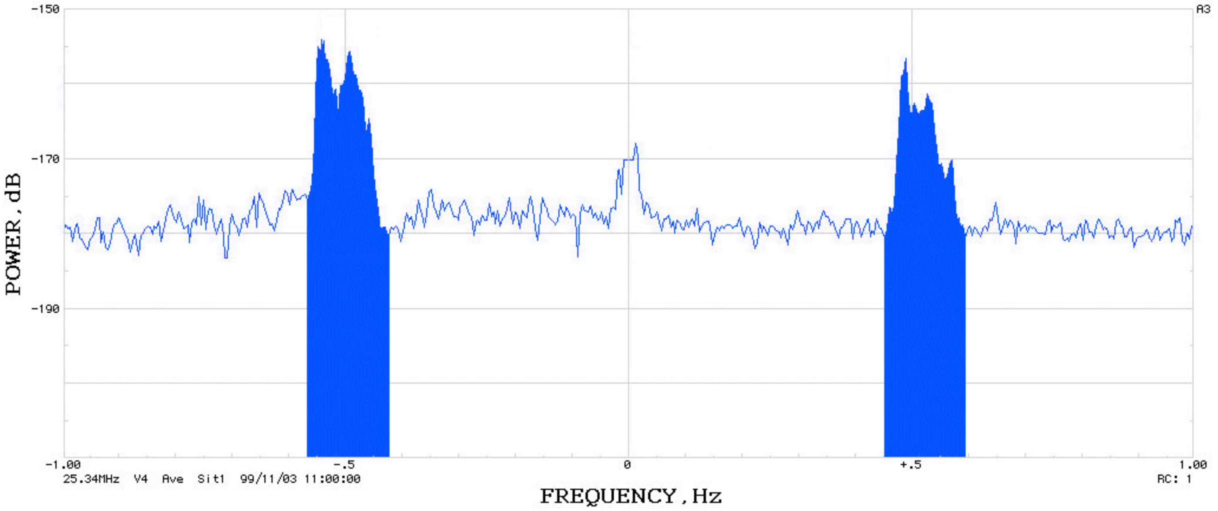

Figure 8. First-order peaks falling to the noise floor. Due to the absence of long ocean waves, there is no second-order echo.

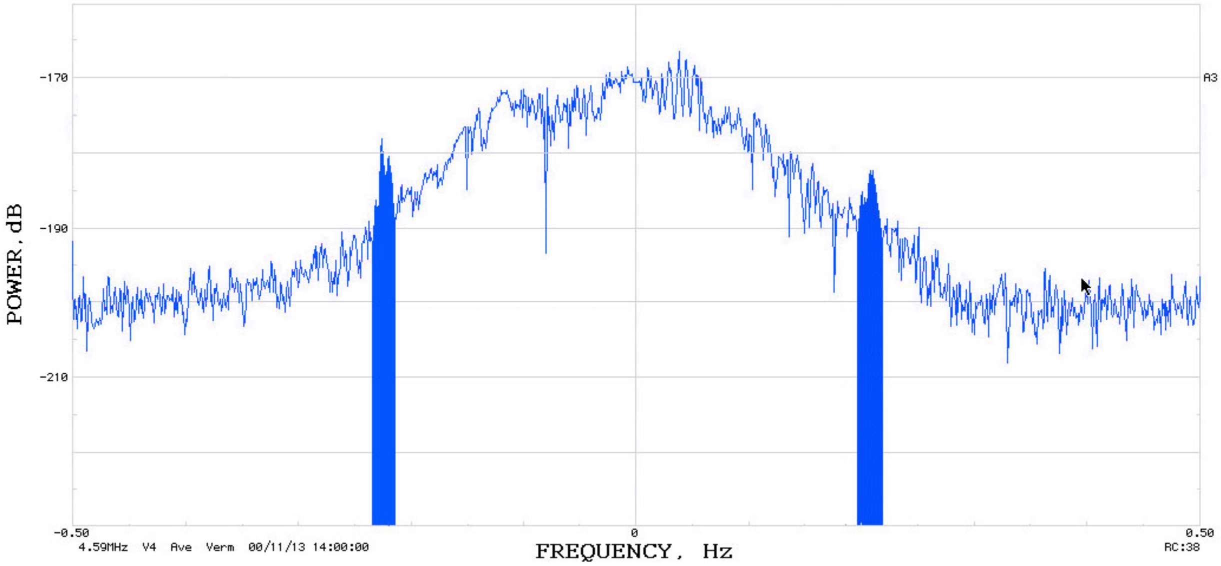

Figure 9. Radar spectrum showing ionospheric echo superimposed on the sea-echo spectrum. The first-order peaks are just visible above the ionospheric echo.

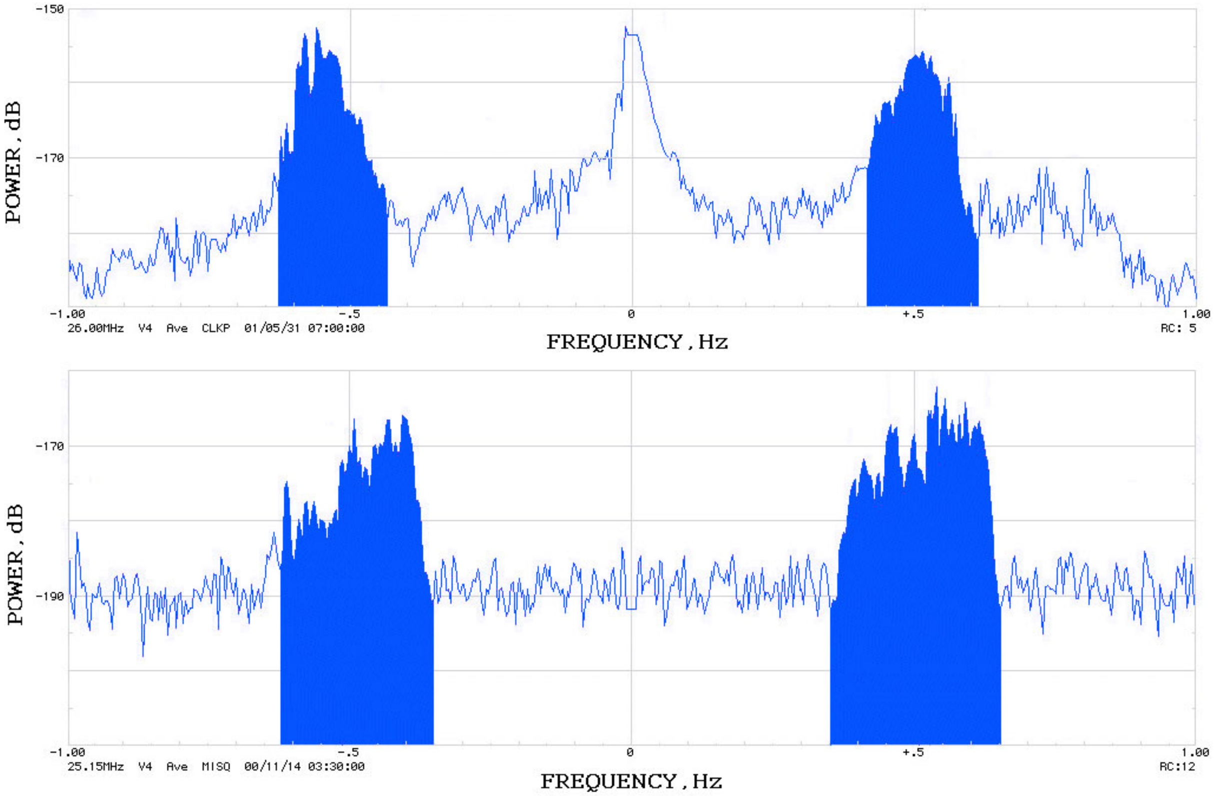

Figure 10. Examples of radar spectra when there are strong currents. The first-order region has spread over the surrounding higher order structure.

Figure 11. An example of a saturated spectrum. First-order spectrum cannot be isolated as it is merged with the higher-order echo.

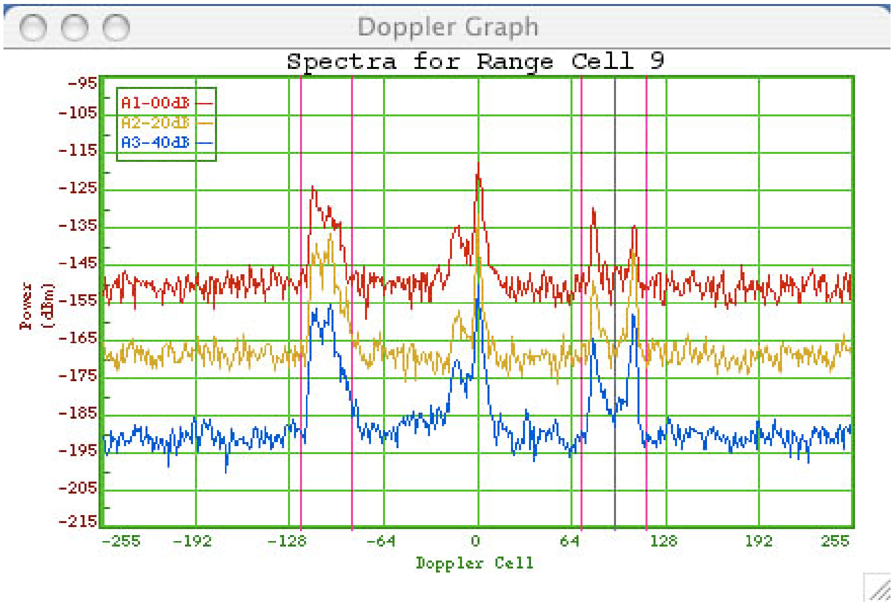

Figure 12. Example spectra when ice exists offshore. Positive returns on the right side of the plot are a split first-order peak (located between the two vertical pink lines).

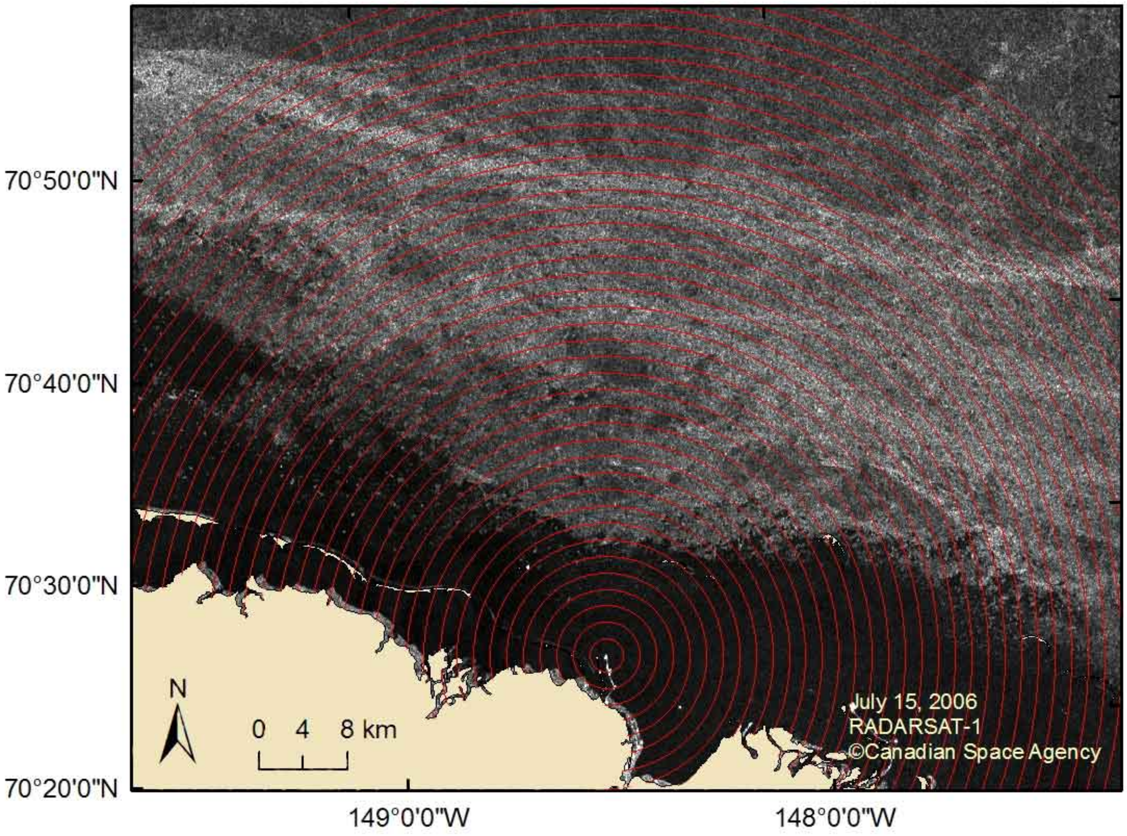

July 15, 2006
RADARSAT-1
©Canadian Space Agency

Figure 13. Range cells are overlaid on SAR imagery. The gray shaded area descending from the top is sea ice. Each red circle is considered a range cell, numbered with Range Cell 1 closest to the antenna location (center of the bullseye). Range Cells 1-6 include only open water, but range cells numbered greater than 6 include both open water and ice.

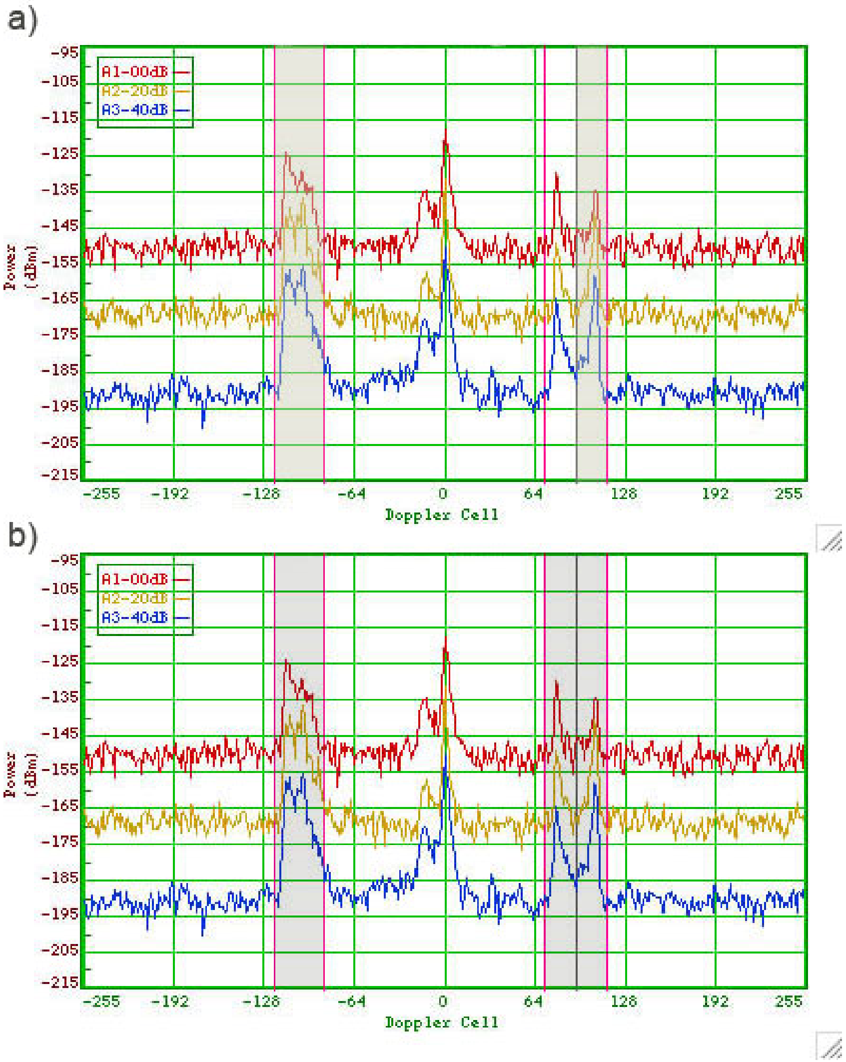

Figure 14. Sample spectra shows a split first order peak on the positive side of the returns. Gray-shaded area shows the first order definitions with the default CODAR software settings (a) and after the first order line settings are corrected to capture the split first order peak (b).

is shown diagrammatically by tracing a range cell in Figure 15. Before changing the processing parameters, only the open water energy to the east was captured, but after changing the settings to include the second peak, first order energy both west and east of the antenna was captured.

The most important settings to change when defining a split first order peak are the smoothing value applied for a running mean and the “factor down” value, which defines the power range in which to look for the boundary between the first and second order returns. In the Beaufort Sea, settings were changed to capture the highest peak as well as any nearby peaks between the highest peak and zero Hz. Normally, any peak lower than the highest peak is considered a second order return, but by capturing all of the peaks, all of the energy in a split peak is captured. Changing the settings to capture both peaks is dependent on there not being any second order

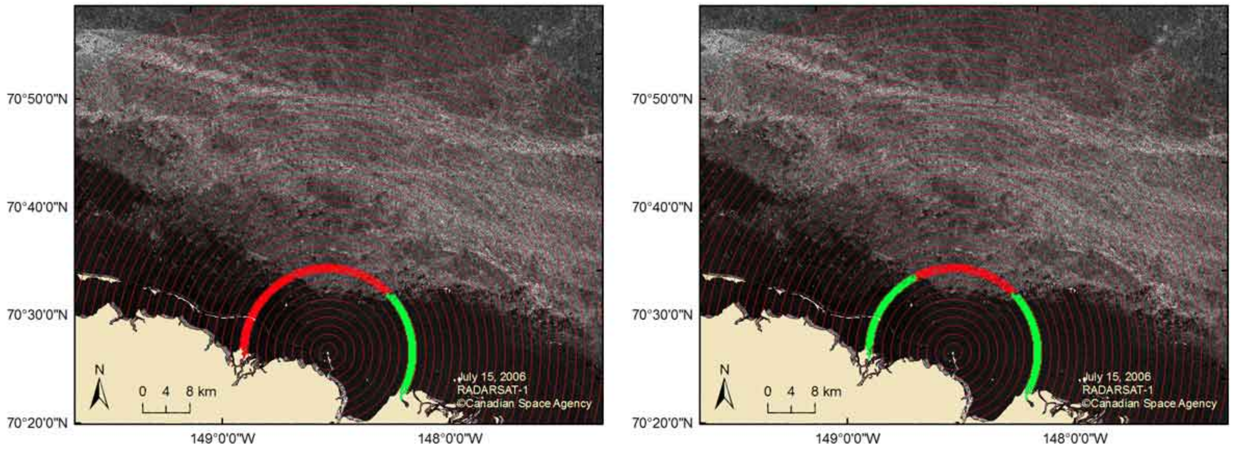

Figure 15. Range Cell 10 is highlighted with green showing the area included in the first order energy and red showing the excluded area. The plot on the left shows data analyzed before changing the processing settings, whereas the plot on the right shows the data analyzed after the change.

peaks present, so if second order energy is present, this method cannot be used. However, when ice is present in the field-of-view, fetch is usually limited, which tends to eliminate second order energy. Visual inspection of the individual spectrum and environmental data (e.g. winds, ice cover, etc.) pertinent to each spectrum ensures that the best fit settings are applied.

All of the range rings for one radar sweep are present in the same file. Unfortunately, there is no presently existing method to apply differing settings to different range rings. One setting is applied to the entire spectra file, so if there is ice nearshore without any second order energy, but offshore there is open water with second order energy, there is no way to optimize the settings to correctly define both scenarios. When such situations occurred in this study, settings were optimized for range cells with ice present rather those containing open water with second order energy so that we could assess how well the HFR works in the presence of ice.

In addition to surface currents, ice velocities can also be obtained using the HFR. Ice echo in the cross spectra is centered on the zero frequency line (Figure 16). As it is an echo from a hard target, it is confined to the area surrounding the zero-Doppler region. The location of the ice can be retrieved from the range cell within which the peak lies. By processing each Doppler bin within the ice peak (each bin corresponds to a known radial velocity), the bearing of the ice radial velocity is determined.

Currents are calculated from the classic "Bragg peaks" that appear at the corresponding phase velocity of waves half the radar wavelength. The Bragg peak spreading occurs for exactly the same reason as spectral spreading at the zero frequency region corresponding to ice, e.g. the radial current velocities transporting the Bragg waves differ from one part of the range cell to another. As one can see from the spectral plot shown (Figure 16), the Bragg echo peaks used for currents and the peaks coming from ice are nicely and unambiguously separated, so they can be analyzed for velocities simultaneously and unequivocally.

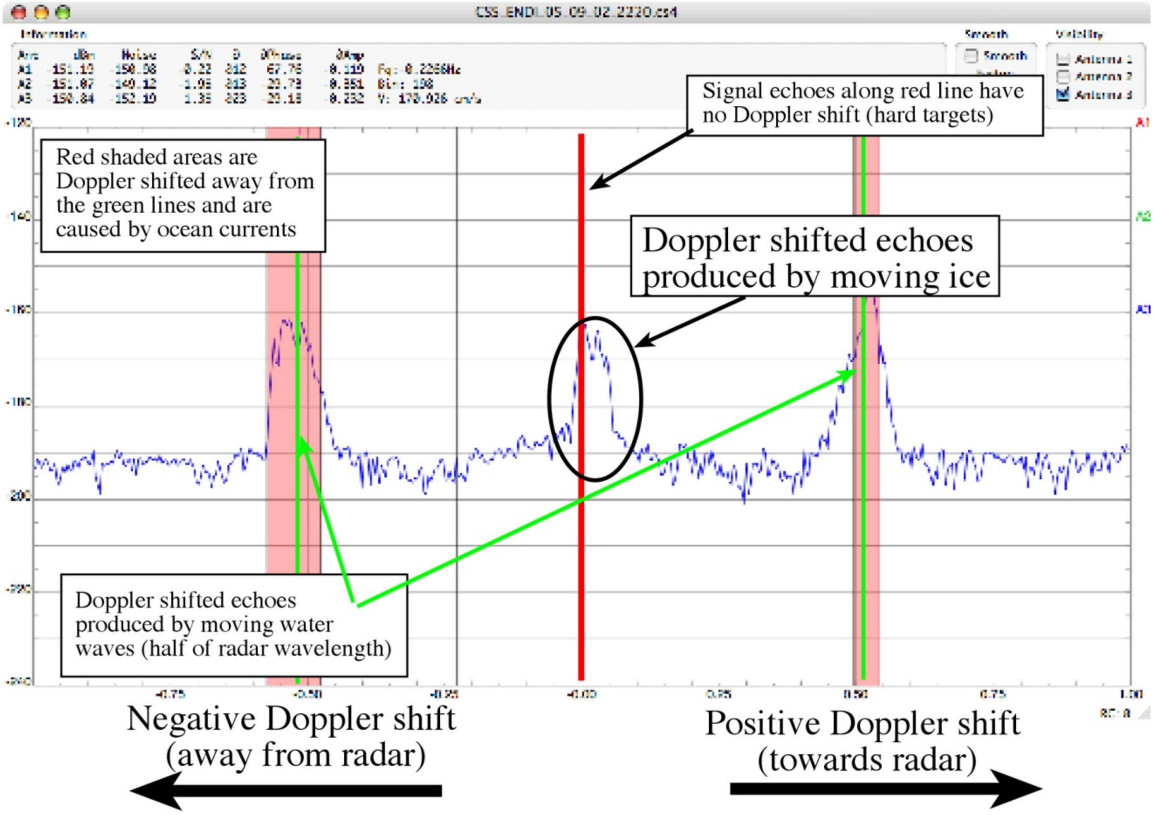

Figure 16. Spectral plot defining Bragg peaks used to determine surface current velocities as well as the baseline peak, which is defined by moving ice.

Saturated spectra were collected from West Dock and Endicott during a strong October 2006 storm. An example of saturated spectra from West Dock is shown in Figure 17. Note the similarity Figure 17 and the example saturated spectrum in Figure 11.

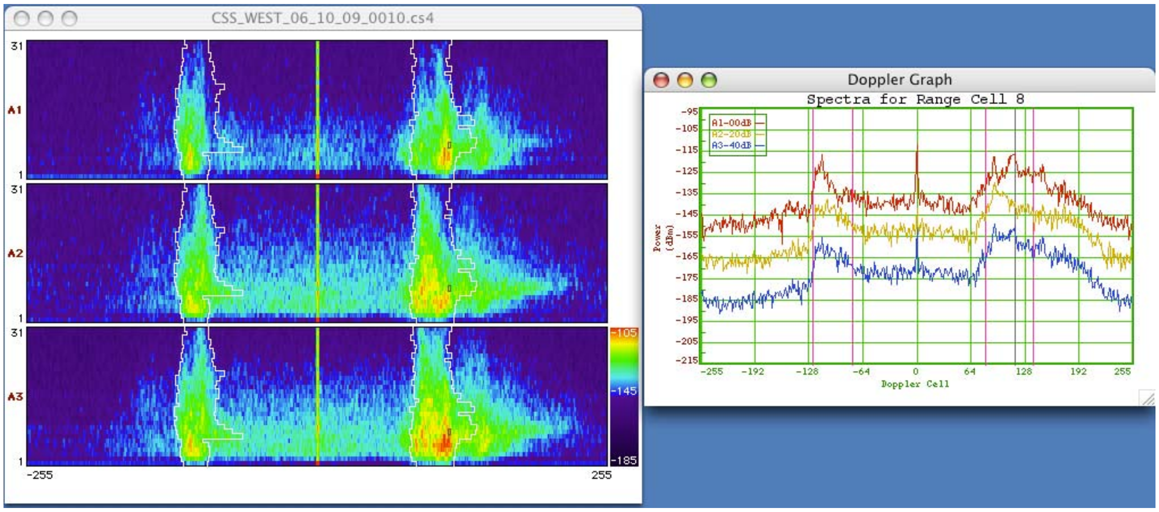

Figure 17. Spectra for all West Dock range cells on October 9, 2006, are depicted on the left, with a cross section of Range Cell 8 shown on the right.

2.3 Antenna Pattern Measurement

The first step to ensuring quality data from a field site is to perform an antenna pattern measurement (Barrick and Lipa 1986). This is a calibration that accounts for any conducting objects in the field area that interfere with a clean frequency return from surface waves. Figure 18 shows antenna pattern measurements at both sites and for both frequencies.

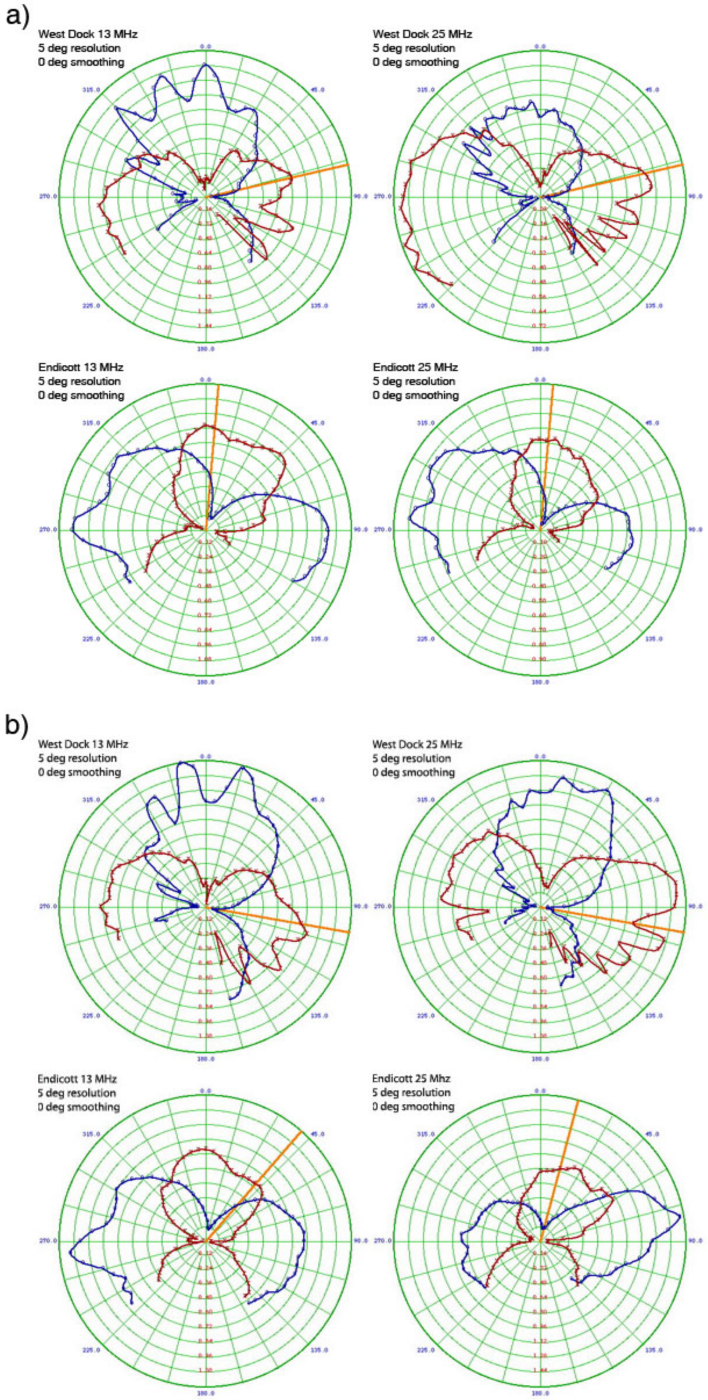

Figure 18. Antenna pattern measurements for a) 2005 and b) 2006. West Dock results are in the top row, and Endicott results are in the bottom row, with 13 MHz results on the left and 25 MHz results on the right.

In an ideal environment without any conductive interference, each of the colored 'loops' in the figure would be a perfect circle. This is not the case at West Dock nor Endicott because each site included multiple metal structures. In addition, at West Dock there was interference due to a pipeline buried offshore, evident by the noisier returns when compared with Endicott. Deviation in these patterns from a true circle can lead to problems in data quality. The antenna patterns were measured at one time to get a baseline noise floor. While there can be temporal variation in these patterns due to traffic in the area, our patterns were determined on a day with little activity or anomalous interference, and thus represent what we believe is the constant background calibration pattern.

Inconsistent noise sources can induce periods of poor data quality that cannot be accounted for by measuring the antenna pattern. These include ship traffic at West Dock, a crane used for a restoration project at Endicott, and, in 2006, persistent daily background noise at Endicott around 10:00 UTC. These are all human sources, but nature can interfere with data quality as well. A strong storm on October 9, 2006, blew down the transmit antenna at West Dock. Conversely, calm days resulted in no waves, and therefore no energy is reflected back to the antennae giving little to no data return. Power outages were experienced at both locations, causing temporal data gaps. Lastly, hardware failure can also plague an HFR field site, as was the case in early 2005 with the switcable frequency systems, a failed hard drive in the West Dock laptop in 2006, and the receive antenna at West Dock which began to fail shortly before the end of the 2006 field season leaving a persistent spatial gap for the last couple weeks of data collection. Luckily, these times of interference were minimal when compared to times with no interference.

2.4 Empirical Orthogonal Functions

Our description of the spatio-temporal structure of the currents is based on empirical orthogonal functions (EOFs). This technique partitions the variance of the spatially-distributed HFR currents into linear, coherent, and independent (orthogonal) functions or modes. While there are as many modes resolved as there are data points, the EOF procedure generally indicates that only a few modes are needed to provide an adequate description of the data. Hence the procedure enables a compact description of a spatially distributed, time-varying data set.

The EOFs partition the variance into linear modes, each of which may vary spatially and temporally. While the modes may be linked to physical mechanisms, such connections do not necessarily exist, since the EOFs derive from statistical properties of the data rather than a fit to a dynamical model. The EOFs are determined from the eigenvalues and eigenfunctions of the correlation matrix, which is constructed from the correlations (at zero lag) for all gridpoints used in the calculation. This procedure insures all grids receive equal weighting. The sum of the eigenvalues of the correlation matrix equals the total variance of the data set. Thus, each eigenvalue provides the fractional contribution that its mode (eigenvector and its associated time amplitude function) makes to the total variance. The modes are ordered such that the lowest modes account for most of the variance in the data. Emery and Thomson (1997) offer a more detailed description of the procedure, and North et al. (1982) discuss the statistical significance of the modes.

3.0 Results

The 2006 field season was far more successful than the 2005 field season. For the first half of the 2005 field season, unreliable satellite communications made it difficult to troubleshoot and anticipate potential problems, the switchable frequency antennas were not operating optimally, and, prior to August, a poor antenna location at the West Dock field site introduced nearly insurmountable interference from buried pipelines.

Upon initial field installation in 2005, CODAR was not finished manufacturing the switchable frequency receiver circuit controller boards for the radar electronics; however they were completed and retrofitted by a UAF technician in late June prior to breakup. By mid-July there were reports of breakup and open water conditions, but no Bragg peaks were detected in the data returns. Troubleshooting revealed a problem in the CODAR software, which needed to be upgraded to work with the newly installed switchable frequency circuit boards. Also discovered was a hardware malfunction in the transmit/receive module, which caused an occasional drop in transmit power due to a digital to analog convert, which controls the radar attenuation levels. This power drop was resolved by issuing a reset command once a day.

On August 21, 2005, a second hardware malfunction was discovered, this time with the dual frequency transmit antenna. The transmit antenna has horizontal whip elements which create a ground plane. Normally the length of the installed whips vary with frequency, but this is not possible with a switchable frequency system. A ‘trap’, consisting of a capacitor and inductor in parallel, on the transmit antenna allows the system to work at either 12 or 25 MHz. When operating at a frequency lower than the resonance of the trap, the inductor has low enough impedance that it appears (electrically) that the horizontal antenna elements are longer than the actual size at 13 MHz. The trap at 25 MHz is at the resonance frequency, and the capacitor/inductor generate a very high impedance which electrically removes the top half of the transmit antenna. Although this was the same design that was successfully used in Santa Cruz, the cable runs in Prudhoe Bay were less than half those of Santa Cruz. Hence the peak voltage was 30 to 40% greater than the original design plan. This difference exceeded the voltage limits of the capacitors and overheated one of them to the point of failure. Over the next few weeks, troubleshooting was performed at CODAR using three times the expected power necessary for Prudhoe Bay operations until the system passed all tests. During this testing, the malfunction was temporarily remedied in the field by removing the dual-frequency capabilities of the transmit antenna and installing a fixed antenna with only one frequency. On September 29, 2005, UAF technicians installed the repaired dual-frequency transmit antenna. The original capacitor was replaced with one that could withstand a voltage 10 times greater than the expected peak voltage. In the post-processing of this data set, we have decided to only include data collected after August 21, as we feel that this data is free of contamination from all sources of equipment malfunctions.

In 2005, West Dock had 79% runtime, and Endicott had 91% runtime. Having all hardware problems remedied for the 2006 deployment, the runtime for both sites increased to 87% and 99% respectively (Figure 19). Were it not for a hard drive failure at West Dock for approximately two weeks in late July/early August, which was not immediately diagnosed, both sites would have been 99% operational for the 2006 field season.

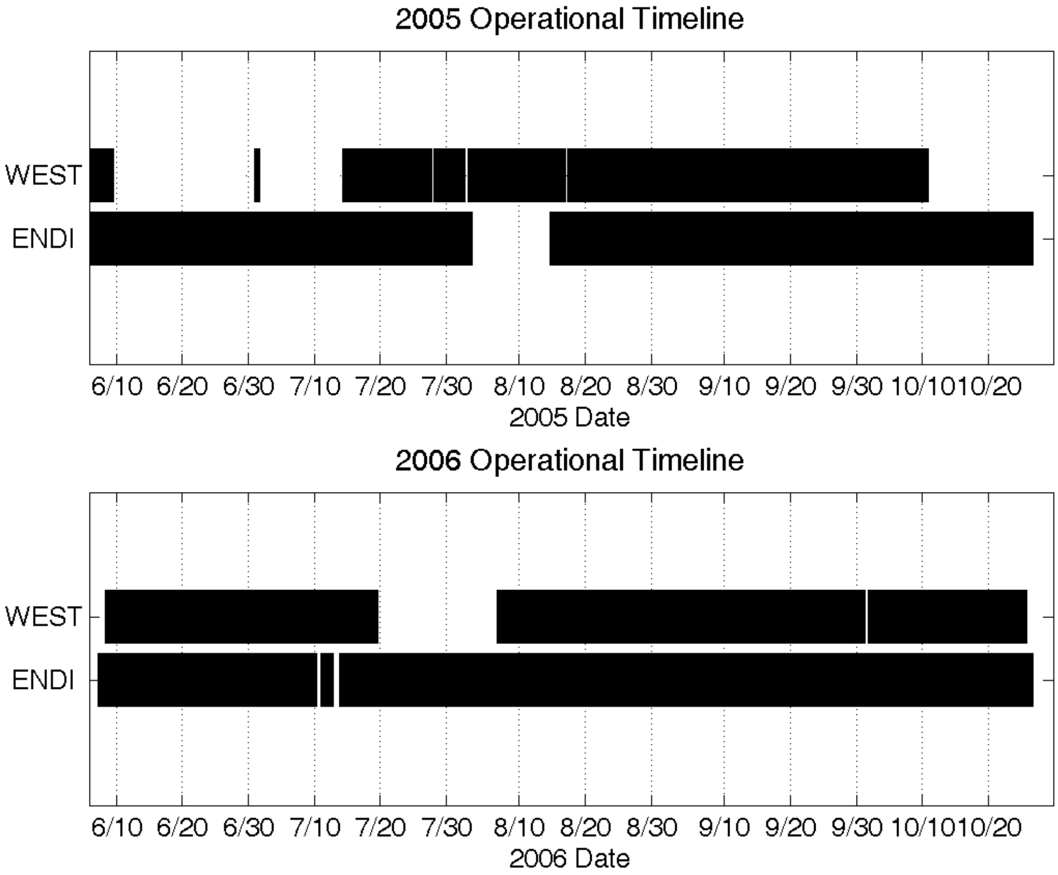

Figure 19. 2005 and 2006 operational timeline for both West Dock (WEST) and Endicott (ENDI) field sites. Where the black bar is filled, the systems were operational, and where there are gaps, the system was not operational. Please see Appendix A for details on downtimes.

One-dimensional radial current data from each site was transferred hourly to UAF in Fairbanks, Alaska, where they were processed into two-dimensional surface current files. Figures in "jpg" format were created from the data and posted in near real-time on the World Wide Web.

3.1 Wind

In the Alaskan Beaufort Sea, HFR signal strength is often directly related to the local wind magnitude, fetch, and duration (Figure 20). Meteorological station locations in our study area included North Star Production Island and Endicott (Veltkamp and Wilcox 2007), as well as a National Oceanic and Atmospheric Administration Center for Operational Oceanographic Products and Services (NOAA CO-OPS) station at West Dock. A comparison of monthly winds from 2005 and 2006 amongst all three stations show no

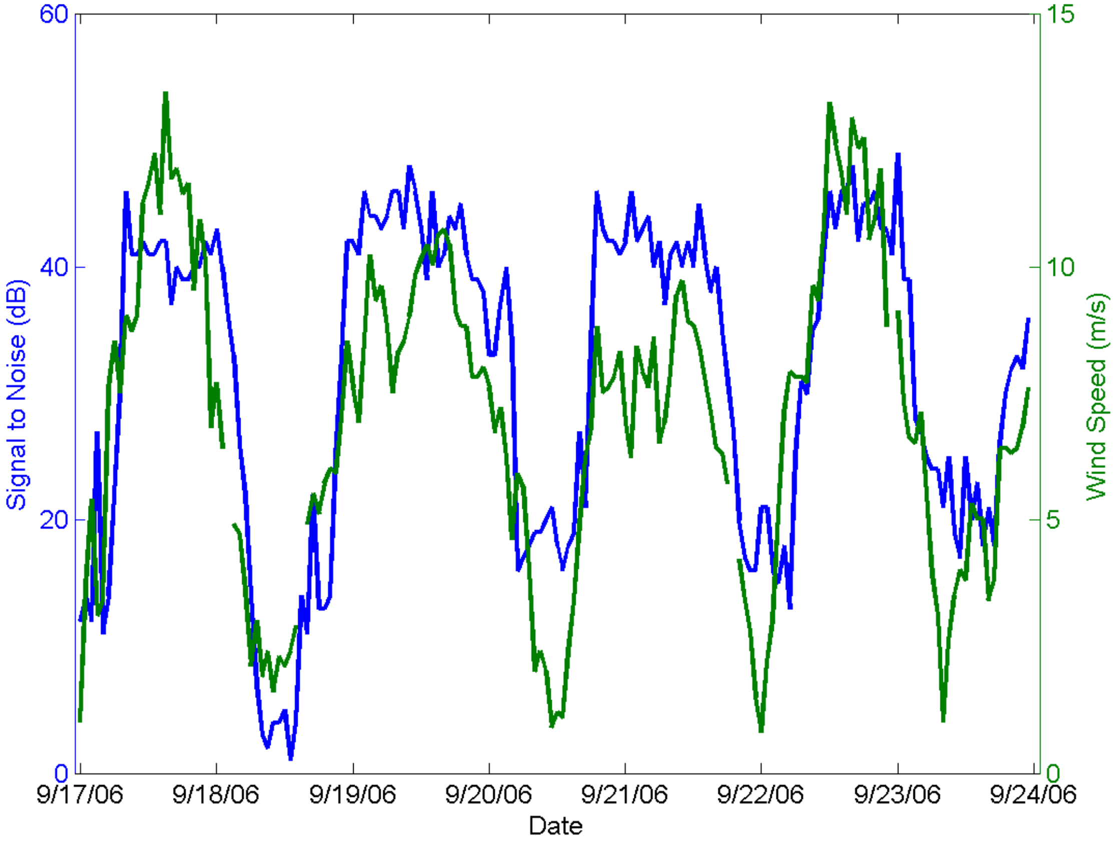

Figure 20. Time series plot of the antenna signal to noise ratio (blue) and wind speed (green) showing a direct correlation between the two time series.

statistically significant variations among the locations as determined from regressions of the along-shore winds (Figure 21). The meteorological station at Endicott had the fewest data gaps in 2005, and the meteorological station at West Dock had the fewest data gaps during the 2006 field season. Thus, wind data used in this report for 2005 are from Endicott and for 2006 are from West Dock. In accordance with oceanographic convention, wind direction is reported herein as the direction toward which the wind is blowing.

From June through October during 2005 and 2006, winds speeds averaged 6.6 m/s and were predominantly westward in direction (Appendix B). In June 2005 and 2006, landfast ice covered the HFR coverage area and local winds were primarily westward with speeds less than 7 m/s (6.3 and 5.7 m/s respectively). From early to mid-July 2005 and 2006, landfast ice began to breakup after overflooding by river runoff. July winds were slightly more variable than in June but continued to be predominantly westward in direction with wind speeds averaging 5.9 m/s in 2005 and 6.3 m/s in 2006. In both years, August winds shifted to a more west-southwest

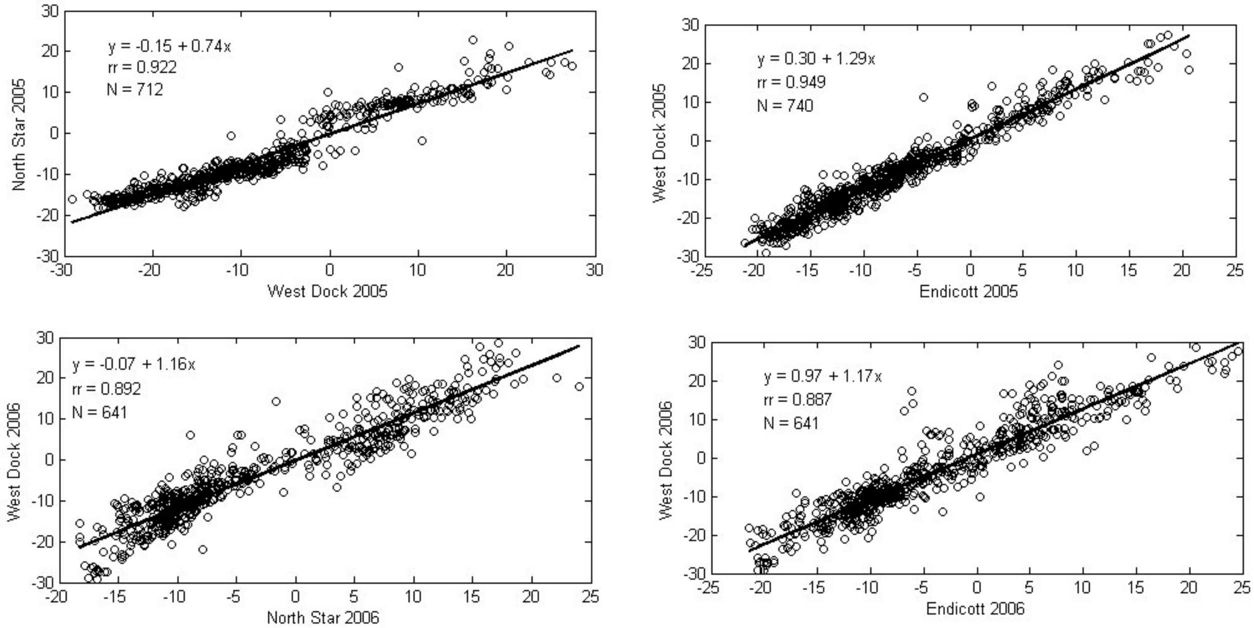

Figure 21. Linear regressions of the along-shore wind component of meteorological stations in our study area for July 2005 and 2006. Other months of the field season yielded similar results.

direction, and speeds increased and exceeded 10 m/s by the end of the month. September 2005 winds were westward and increased in speed to greater than 15 m/s. September 2006 winds were westward in direction at 5-10 m/s, except during a storm on September 27, when westward wind speeds exceeded 15 m/s (Figure 22). Winds continued to intensify in early October when wind speeds were often greater than 10 m/s, peaking during storm events. October 11, 2005, brought a sizeable westward storm with winds in excess of 20 m/s, after which winds were more variable in direction throughout the month, although still predominantly westward. A major storm event on October 9, 2006, included wind speeds of ~25 m/s or more. The intensity of this storm was such that wave heights apparently exceeded one half the wavelength (e.g., the surface waves were no longer consistent with linear theory), resulting in a saturated radar spectrum (Figure 17). Hence the first-order spectrum could not be isolated from the higher-order echoes, and data quality was degraded.

3.2 Ice

The break-up and dispersal of sea ice on the Alaskan Beaufort Sea shelf profoundly influences the regional circulation. At relatively large spatial scales (>12 km), satellite-borne microwave sensors can map the sea ice edge and concentration. Sea ice concentrations and the ice edge vary substantially from year-to-year. These differences are illustrated in Figures 23a-d, which compare the location of the ice edge from July through October in both 2005 and 2006. The data were obtained from the Advanced Microwave Scanning Radiometer – Earth Observing System (AMSR-E) microwave sensor, which has a spatial resolution of 12 km.

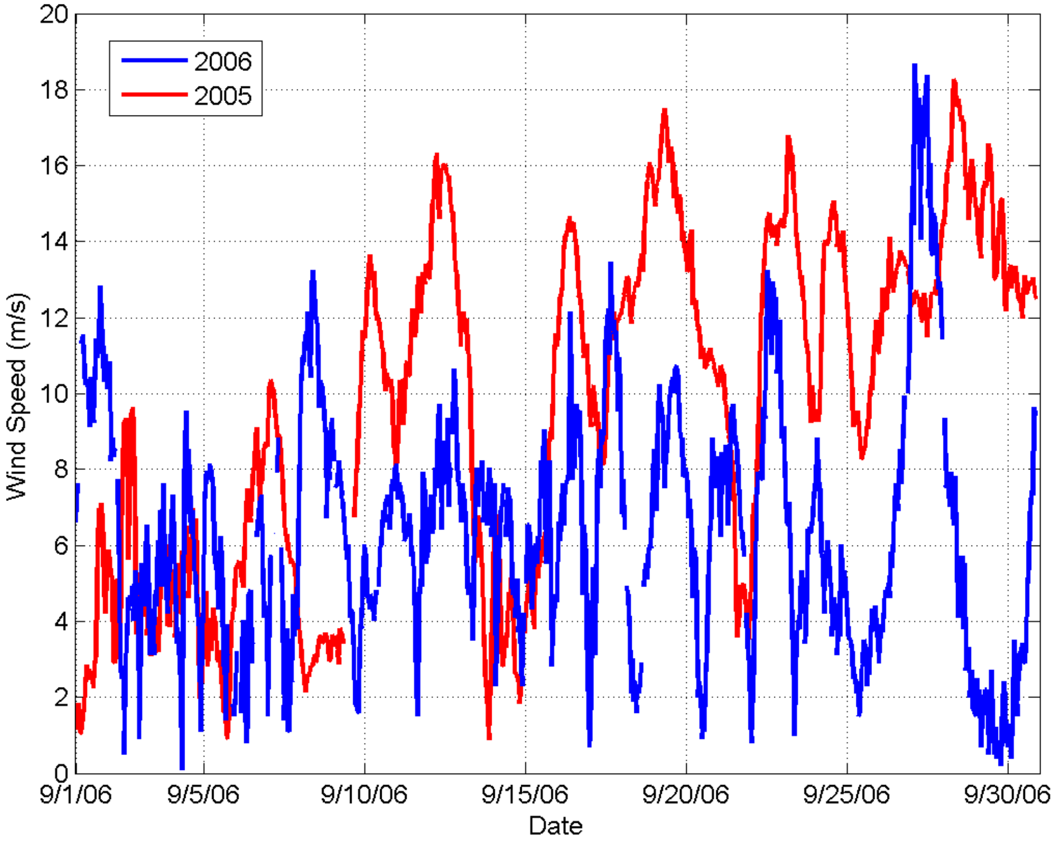

Figure 22. Time series of wind speed for September 2005 (red) and 2006 (blue). Wind speeds in 2005 were greater in magnitude earlier than 2006 winds.

Breakup of the landfast ice began in July of 2005 and 2006, although breakup patterns differed between years. In July 2005 (Figure 23a), open water first appeared to the east of Prudhoe Bay and progressed westward. Very likely this opening was caused by westward spreading of relatively warm waters from the Mackenzie Shelf. In addition, ice receded from the coast creating a narrow band of open water that was largely confined to the region inshore of the barrier islands. Presumably, this nearshore breakup was associated with melting initiated by local river outflow over the landfast ice. The same coastal breakup pattern occurred in July 2006. In August 2005, two tongues of open water developed north-northwest of the study region. The eastern retreat appears to be continuation of the westward propagation of Mackenzie water, whereas ice retreat to the west (along 154^{o}W) likely reflects the influence of relatively warm water from the Chukchi Sea that flowed eastward around Barrow. A narrow (~25 km) band of open water developed along the coast between these two tongues of open water. In August 2006, a similar pattern of ice retreat developed, although the extent of the retreat was considerably less than that in August 2005. An 80 km wide band sea ice remained along the coast to the west of Prudhoe Bay. By September the ice edge had retreated and/or melted far offshore in both years, with open water extending ~ 250 km offshore, well beyond the range of

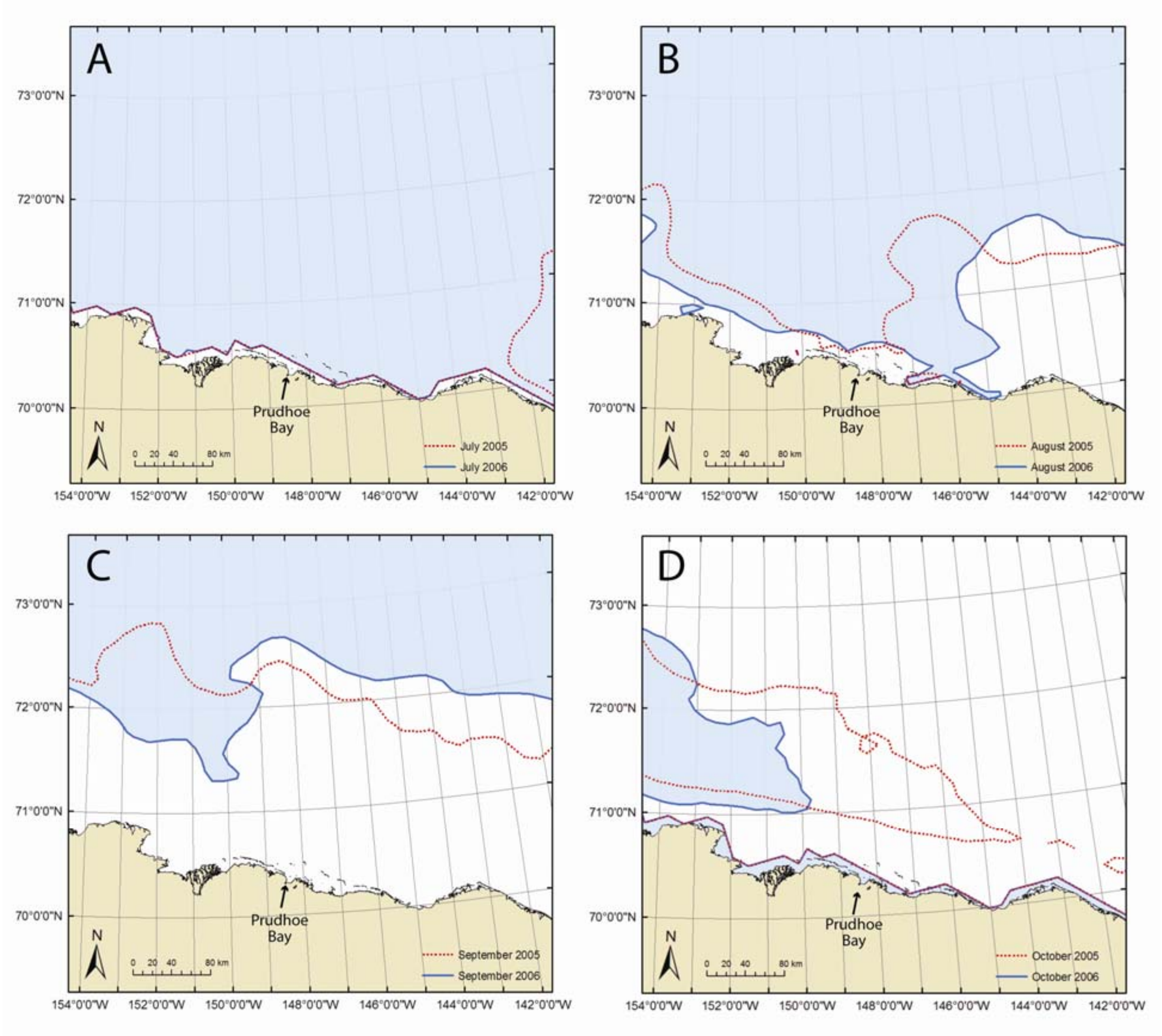

Figure 23. Monthly averages of the ice edge along the North Slope of Alaska from AMSR-E for A) July, B) August, C) September, and D) October 2005 and 2006. The 2005 ice edge is shown in red and dashed, and the 2006 ice edge is shown as a solid, blue line with ice areas shaded. (AMSR-E monthly means were acquired from the Alaska Ocean Observing System)

the radar systems. In October freezing began, the pack ice began to advance from the northeast, and landfast ice began to form along the coast and extend offshore.

The AMSR-E (and other similar) satellite microwave sensor and processing algorithms are useful for large scale assessment of sea ice, but the spatial resolution is much coarser than the one to three kilometer spatial resolution of the HFR. For this reason we used Synthetic Aperture Radar (SAR) data (40 m resolution) for fine scale ice monitoring. (Note, however, that there is not an ice product derived from SAR data but a determination of ice cover based on surface roughness.) SAR data comparisons between 2005 and 2006 reveal even larger differences between the two years than that portrayed by the AMSR-E data set.

SAR imagery (approximately three day temporal resolution) was used to determine ice breakup for July 2005 and 2006. Breakup in 2005 was more gradual than in 2006 and began with overflooding of the ice by river water that spread offshore (between July 6 and 13) about 10 km from the coast prior to landfast ice break up. After breakup of the landfast ice, the ice edge retreated approximately 15 to 20 km offshore between July 16 and August 3. Between August 26 and September 3, a band of ice (5 to 10 km wide and unresolved in the AMSR-E data) was present in the HFR field-of-view just seaward of the barrier islands offshore of Prudhoe Bay. This ice band dissipated in early September leaving relatively ice free waters from September 16 until the beginning of formation of landfast ice in mid-October.

In 2006, SAR imagery suggests that on July 1 the study area was completely ice covered with some overflooding, but by July 5, the landfast ice had broken up and the local ice edge in the HFR field-of-view receded approximately 15 km offshore, although there were some ice floes between the ice edge and shore (Figure 24). This situation persisted until about August 14, at which time the ice began to break up moving the ice edge further away from shore. By August 25 a band of fragmented ice had set up approximately 20 to 30 km offshore (Figure 25a). This was similar to the ice band present in late August 2005 (Figure 25a and 25b). The ice band dissipated by mid-September 2005 (Figure 25c) but persisted until late September in 2006 (Figure 25d), decreasing in width over time. The presence of this ice required an extensive reprocessing effort following the procedures outlined in Section 2 of this report. After the ice band dispersed, the HFR field of view remained relatively ice free until landfast ice formation ended data returns on October 22, 2006.

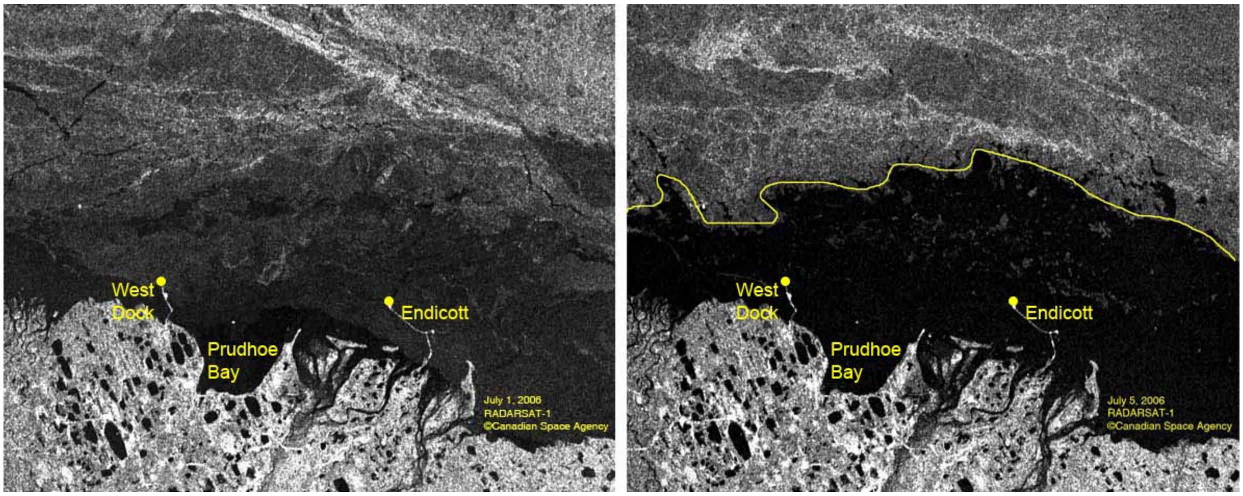

Figure 24. SAR imagery from July 1 (left) and July 5 (right), 2006, depicts the ice conditions near Prudhoe Bay. Both the ice and land appear as shades of white and gray, with the land extending from the bottom of the image, and the ice extending from the top of the image. On July 1 the region is completely ice covered, but by July 5, the local ice edge (shown in yellow) was approximately 15 km offshore.

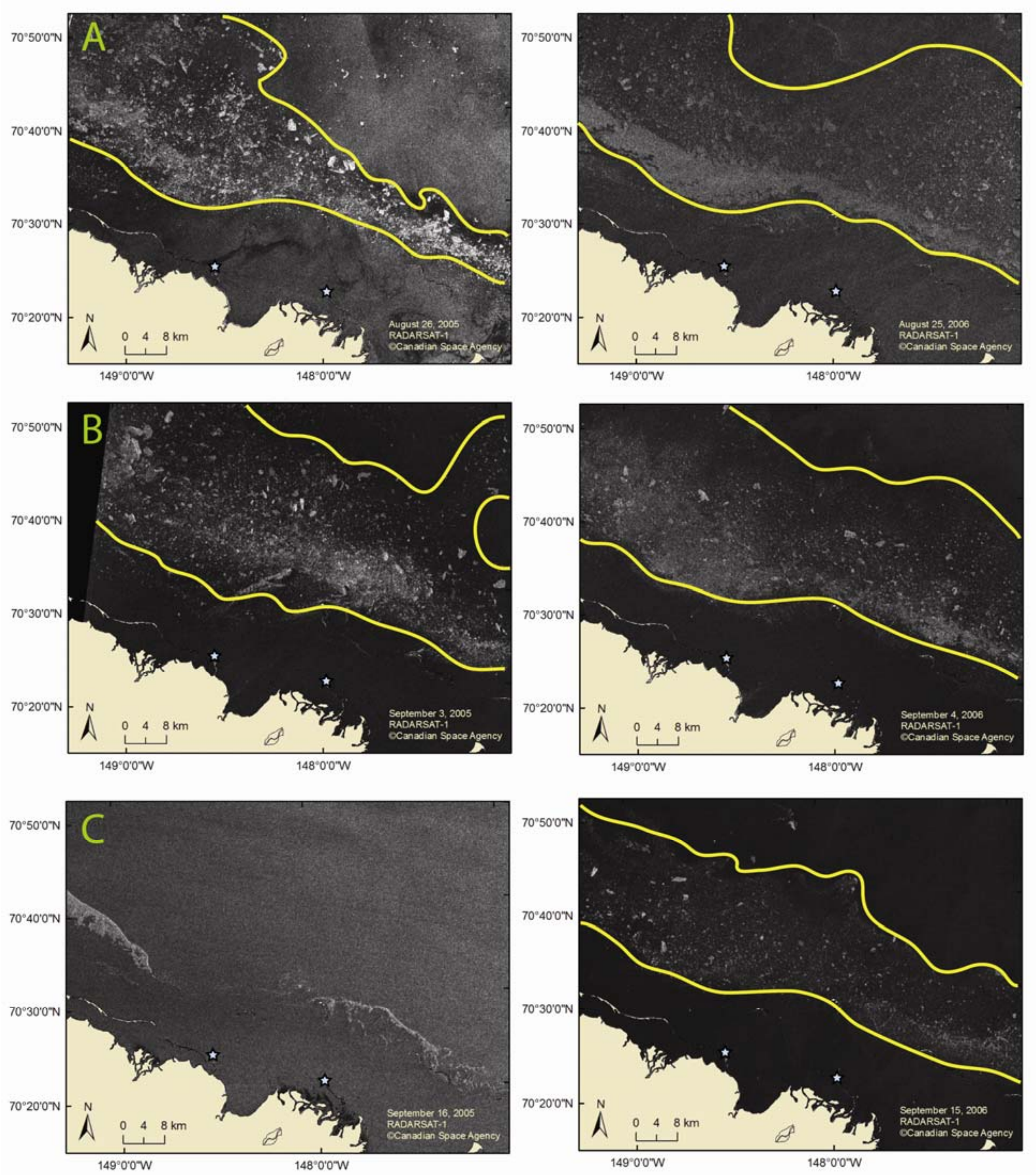

Figure 25 a-c. Bi-weekly SAR imagery from 2005 (left) and 2006 (right). Dates depicted include A) August 26, 2005 and August 25, 2006, B) September 3, 2005 and September 4, 2006, and C) September 16, 2005 and September 15, 2006. West Dock and Endicott field sites are denoted by stars. The yellow lines outline a band of ice located approximately 20-30 km offshore, which dissipated from the 2005 data by September 16 but still existed on September 15 in 2006.

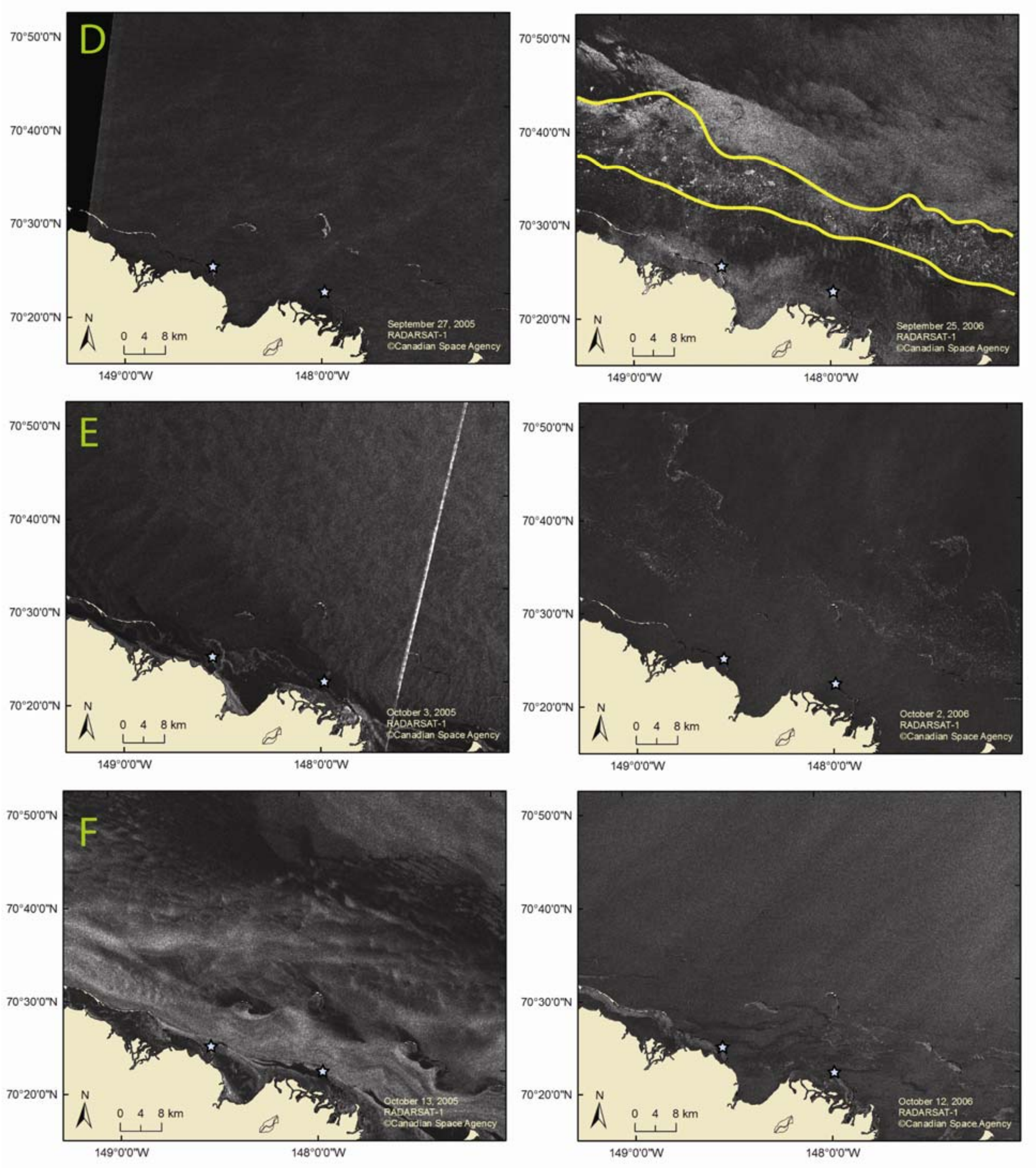

Figure 25 d-f. Bi-weekly SAR imagery from 2005 (left) and 2006 (right). Dates depicted include D) September 27, 2005 and September 25, 2006, E) October 3, 2005 and October 2, 2006, and F) October 13, 2005 and October 12, 2006. West Dock and Endicott field sites are denoted by stars. The yellow lines outline a band of ice located approximately 20-30 km offshore in the September 25, 2006 data, which was not present September 27, 2005, and had dispersed by October 2, 2006. The formation of landfast ice is evident on October 13, 2005, but was not yet present on October 12, 2006.

3.3 Salinity

The offshore propagation of the electromagnetic HFR wave depends on the conductivity of the surface waters as shown in Figure 26 (from Barrick and Long, 2006), with the HFR range generally increasing linearly with increasing salinity. This could be a significant factor in the Beaufort Sea because river runoff and/or ice melt can substantially freshen the surface waters. Although no instances of this were found directly in our dataset, surface salinity variation could influence the radar wave propagation.

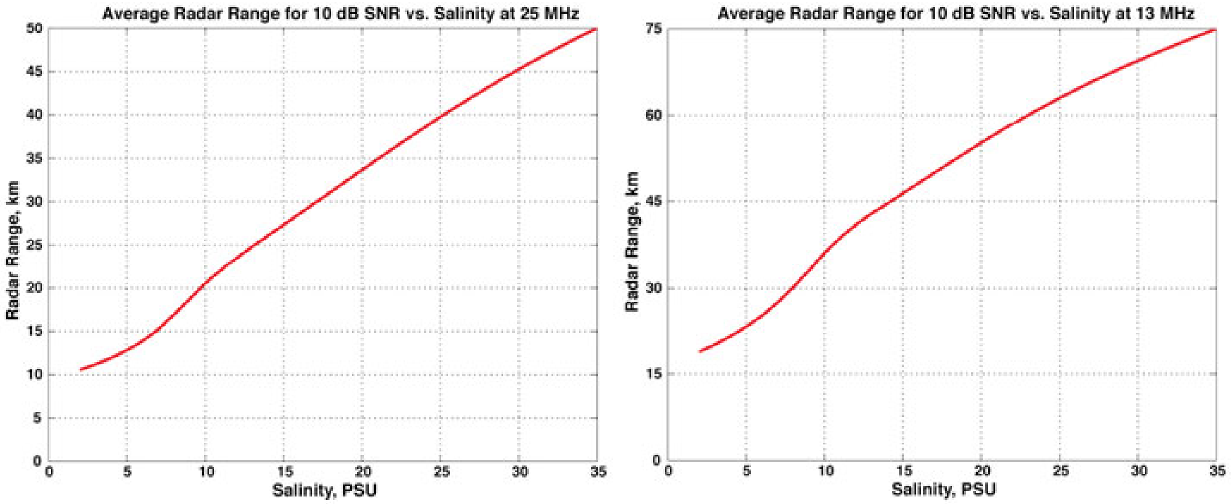

Figure 26. Salinity vs Offshore Radar Range for a 25 MHz (left) and 13 MHz (right) CODAR HFR system (from Barrick and Long 2006). There is a direct relationship between salinity and radar range.

3.4 Currents

Surface current characteristics in the Beaufort Sea can differ with various wind, ice, and salinity conditions. In order to more accurately identify trends in the surface currents and to compare results from one field season to another, the 2005 and 2006 field seasons have been broken into four different physical regimes based on ice cover:

1. Open water within 15 to 20 km of shore with ice covering the rest of the HFR field-of-view (Figure 27). Ice floes were intermittently present in open water areas.
2. Band of fragmented ice floes present 20 to 30 km offshore with open waters shoreward and offshore of the ice band (Figure 28). Ice floes were also intermittently present in open water areas on/offshore of the ice band.
3. Ice-Free waters, with ice floes intermittently present
4. Early landfast ice formation (Figure 29)

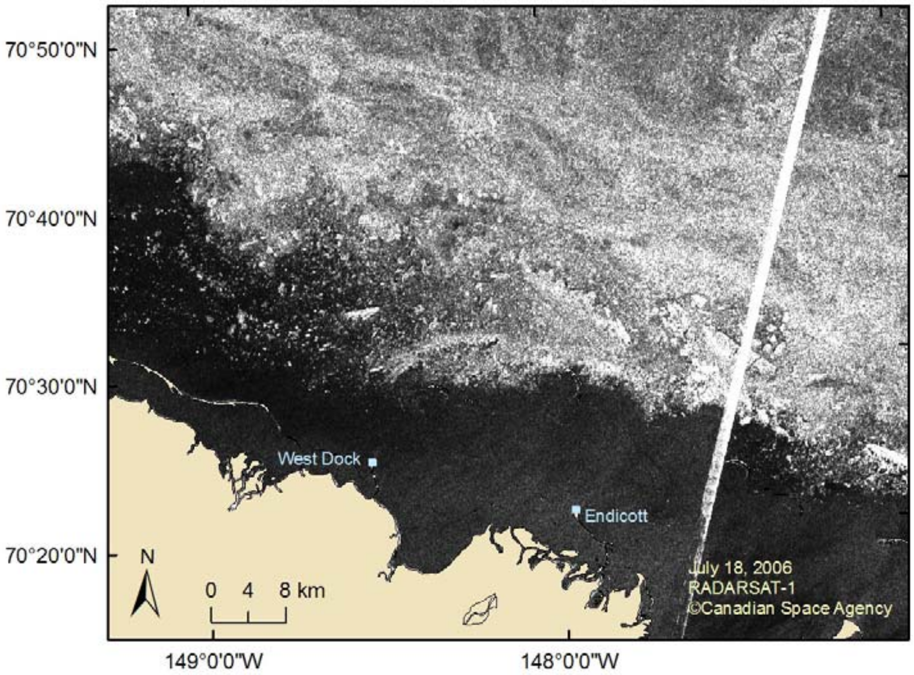

Figure 27. SAR imagery from July 18, 2006, shows an example of Regime One, when open water was within 15 to 20 km of shore and ice covered the rest of the HFR field-of-view. The tan area denotes land, the black open water, and gray symbolizes ice.

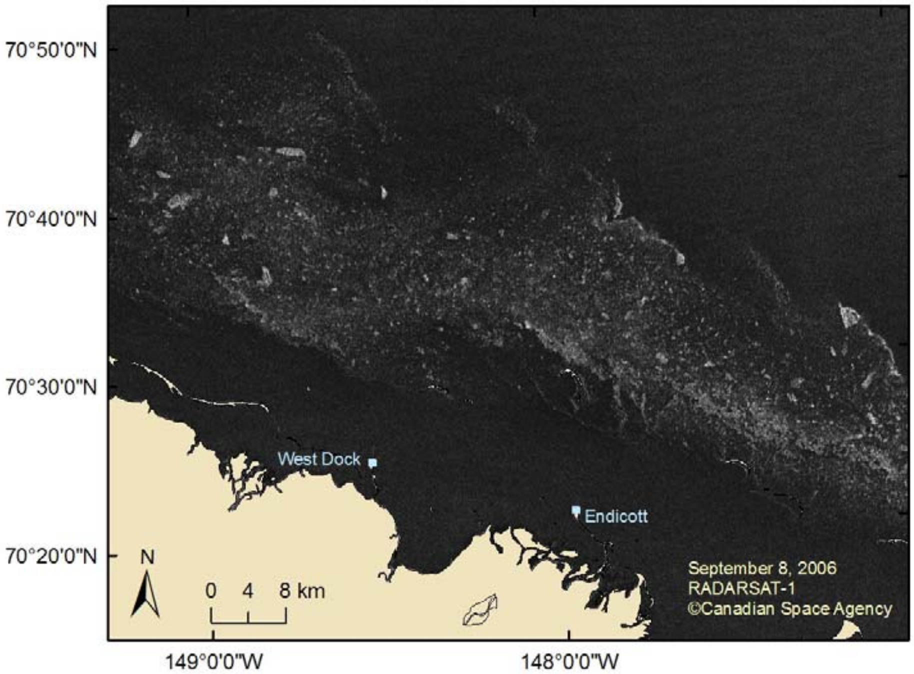

Figure 28. SAR imagery from September 8, 2006, shows an example of Regime Two, when there was a persistent band of fragmented ice 20 to 30 km offshore. The tan area denotes land, the black open water, and gray symbolizes ice.

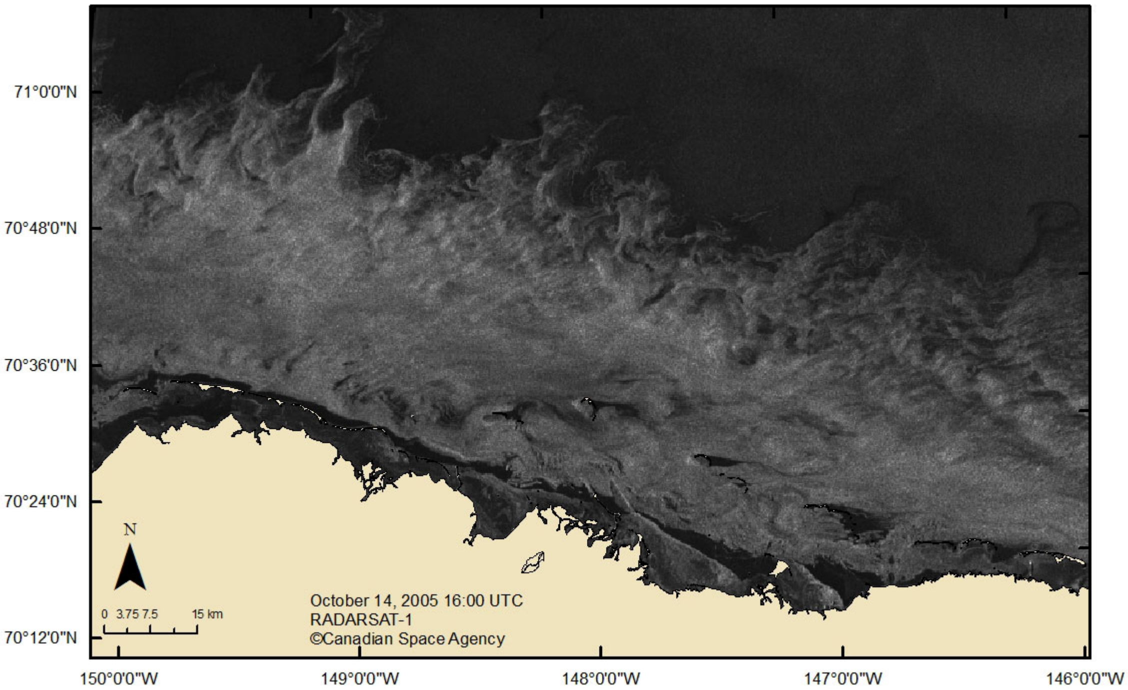

Figure 29. SAR imagery from October 14, 2005, shows an example of Regime Four, when landfast ice was beginning to form from the shoreline seaward. The tan area denotes land, the black open water, and whitish-gray symbolizes ice. Landfast ice is present nearshore out to the barrier islands in darker gray/black, with grease ice in lighter gray.

Waters were completely ice covered until July 6 in 2005 and July 1 in 2006. The first regime as defined above was present from July 16 – August 3, 2005, and July 5 – August 14, 2006. Regime two lasted from August 26 – September 3, 2005, and August 25 – September 25, 2006. The third regime is defined by relatively ice-free waters in the HFR field-of-view and was present from September 16 – October 10 in 2005, and from October 2 – October 20 in 2006. Regime four is defined as early landfast ice formation. Formation of landfast ice entered the HFR area between October 10 and October 13, 2005, and approximately October 19, 2006. Due to the hardware failures outlined in the beginning of this section, interannual comparisons are only available for regimes two and three.

One of the objectives of this project was to determine how well the HFR operates in varying ice conditions. This was examined by overlaying surface currents onto SAR imagery to see where data returns are received when ice is present in the radar field-of-view. Note however, that low surface salinities (<20), which impede signal propagation, typically occur in August (J. Trefey pers. comm.). In addition, surface current data quality and offshore extent depend upon the wave field which is affected by wind speed, duration, and fetch. Naturally, strong winds resulted in a more energetic wave field, which, in turn, resulted in a higher number of HFR returns. In addition, variations in the wind velocity often lead to alterations in ice conditions that can affect radar performance.

3.4.1 Regime One: Open Water out to 15 to 20 km Offshore

Breakup occurred rapidly in 2006. On July 1 there were no HFR returns and SAR imagery showed ice covered waters, except in the very nearshore, south of the radar coverage area, where overflood waters may have hastened the melting of inshore ice. The next available SAR pass on July 5 showed open water out to ~15 km offshore, with intermittent ice floes between the ice edge and shore, and HFR data were obtained in areas of open water without ice floes (Figure 30). Ice remained 15 – 20 km offshore until mid-August. During that time, there was an approximate two week gap in data collection, from July 20 through August 4, at West Dock due to a failed hard drive. Data collection before and after the failure changed greatly with <50 % two-dimensional data returns from July 5 – 19 and >60 % two-dimensional data returns from August 5 – 14 (Figure 31).

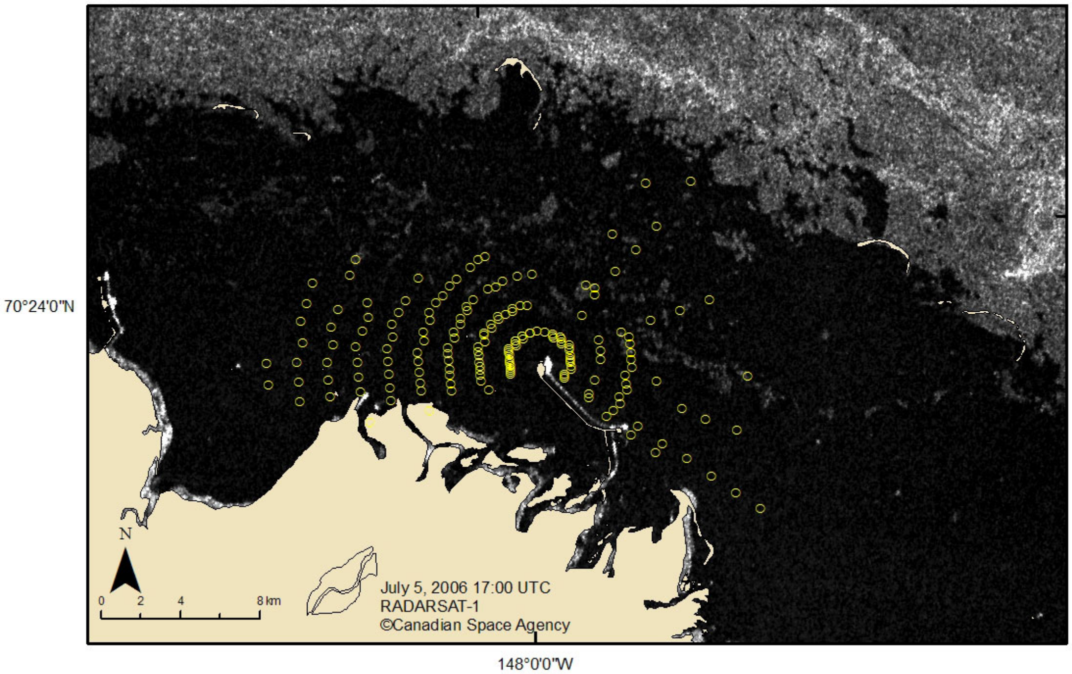

Figure 30. SAR imagery from July 5, 2006. An example of Endicott one-dimensional data return locations (yellow circles) when ice floes were present between shore and the ice edge under westward winds of ~7 m/s.

While all data has been included in our analyses, we note that, in general, currents in regions where the data return is less than 50% may not be representative of the entire time period analyzed. Currents recorded from August 5 – 14 were mainly westward in direction and averaged ~20 cm/s (Figure 32). Winds were also predominantly westward in direction and averaged approximately 4.5 m/s. Vector current time series at each grid point were resolved into their principal component axes. This procedure (based on the eigenvectors of the covariance matrix formed from the east-west and north-south components of the current) determines a new set of orthogonal axes in which the current variance is a maximum along the major axis and a minimum along the minor axis. Once the principal axes are determined, the original surface

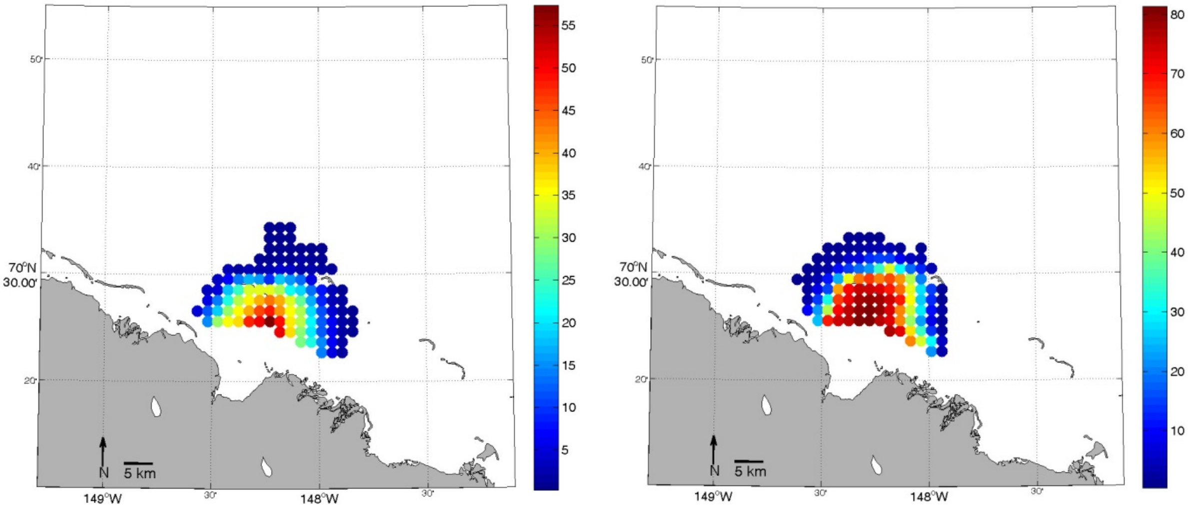

Figure 31. Percent coverage through time of two-dimensional HFR data returns during regime one for July 5-19 (left) and August 5-14 (right), 2006. These times are representative of time periods before and after a hard drive failure at West Dock.

current data are rotated onto this new coordinate system, which is effectively the "natural" coordinate system for the currents at each location.

The major axes for most grid points are parallel to the coast (e.g., along-shore or west-northwest/east-southeast), while the minor axes are perpendicular to the coast (e.g., cross-shore or north-northeast/south-southwest) (Figure 33). For simplicity we refer to the along-shore currents (or those aligned along the major axis) as being either west (negative values) or east (positive values). Similarly, the cross-shore currents are either north (positive values) or south (negative values).

We also examined spatio-temporal variations in the winds and currents by calculating EOFs based on the along-shore current component. Not all grid points had returns throughout the time series, so we used a subset of grid points that had relatively complete time series in the EOF calculation. Temporal data gaps were filled by substituting the mean value before calculating the EOFs. The EOF analysis finds that most (85%) of the along-shore current variance is in mode 1, with all other modes having ~7% or less of the variance and not statistically significant based on North et al. (1982). The mode 1 spatial structure is similar to the principal axes, with the variance primarily along-shore (as defined by our principal axes). The time amplitude function (Figure 34) varies from positive (eastward along-shore currents) and negative (westward along-shore currents). Thus the first mode describes a nearly spatially uniform shelf flow field. The mode 1 time-amplitude function and the along-shore wind time series are significantly correlated with a coefficient of 0.89 with currents lagging the winds by three hours. Thus the first mode represents the rapid response of the surface currents to the wind.

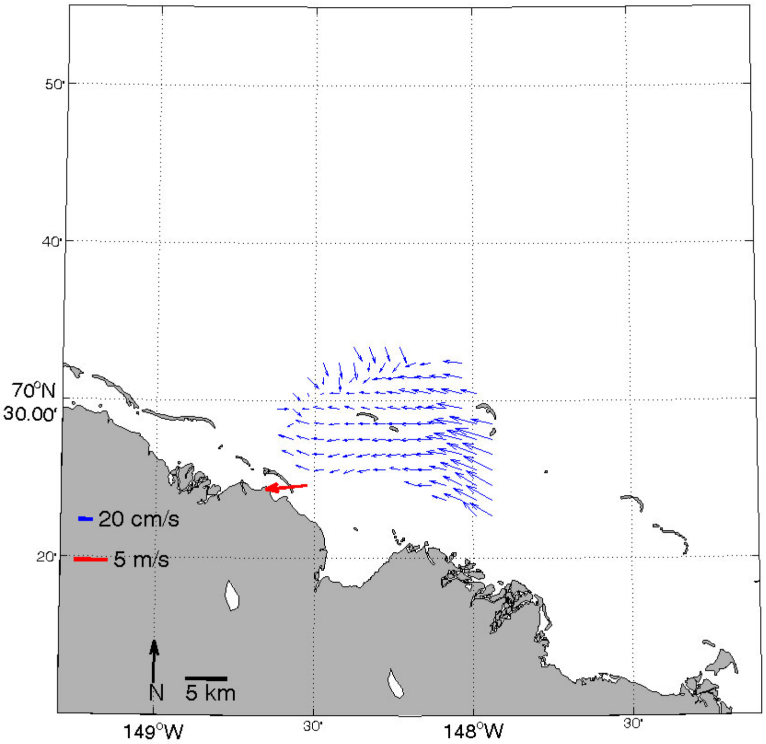

Figure 32. Average current and wind vectors from August 5-14, 2006. Ocean currents are shown in blue, and wind speed is shown in red. The arrowhead indicates direction, and the length of the shaft symbolizes speed. The origin of each velocity measurement is at the base of the arrow shaft.

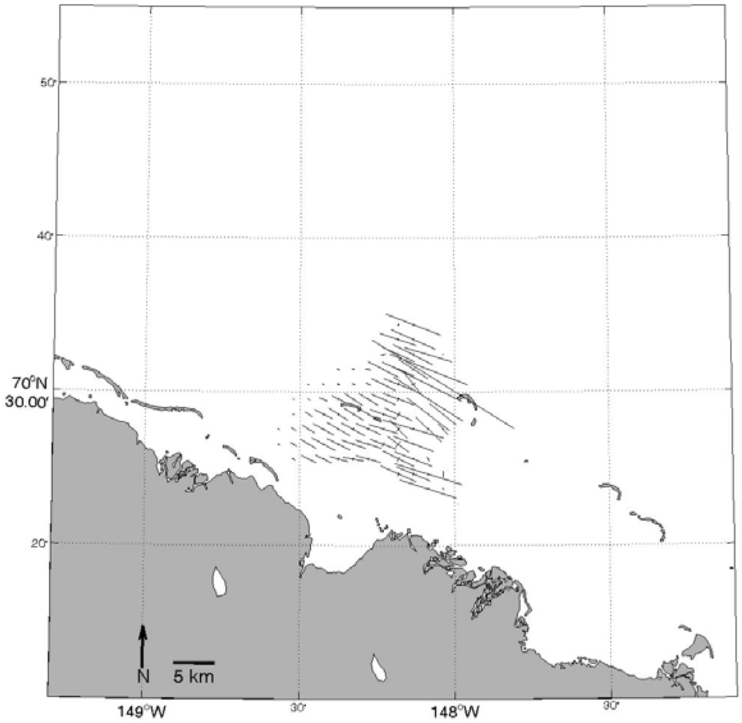

Figure 33. Principal axes for currents measured from August 5-14, 2006. Current variations are predominantly in the along-shore direction with little to no cross-shore flow.

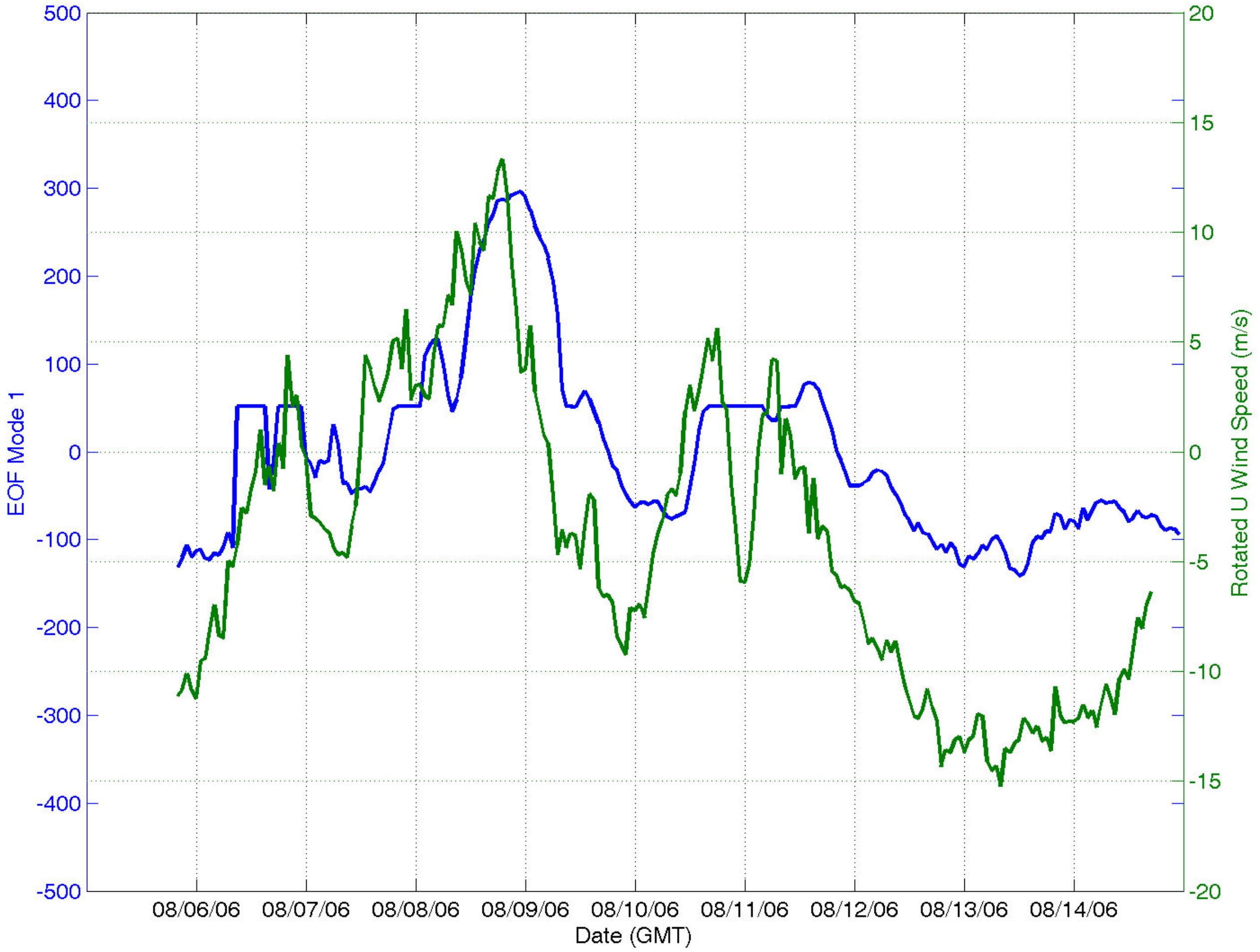

Figure 34. Time series plot of EOF mode 1 (blue) and the along-shore wind speed (green) for August 6 – 14. The two are directly correlated with a coefficient of 0.89. Wind speeds greater than zero indicate an eastward direction, while speeds less than zero indicate a westward direction.

The presence of sea ice affects the wave field by either limiting the fetch or by absorbing wave energy. Waves propagating through sea ice are rapidly damped, although the rate of damping depends upon the wavelength; short waves are damped more rapidly than long waves. When the surface waters are completely ice covered, there is no wave field and hence no radar returns. As the ice break up and through much of regime one conditions, the 25 MHz operating frequency of each radar site, combined with the environmental conditions, was unable to achieve a range of ~40 km, meaning the one-dimensional radial returns from each site did not overlap. Hence, to evaluate system performance at this time, the location of one-dimensional returns from each site were used rather than the two-dimensional currents.

Radial returns from the Endicott radar on July 5, 2006, were patchy with good coverage west of the causeway, but returns were more sparse in the northern and eastern portions of the radar mask where ice floes were present (Figure 30). At the time winds were steadily westward at ~7 m/s. By July 8, the ice floes had dispersed and the wind speeds were ~5 m/s (Figure 35). Ice appears to have impeded returns northwest of West Dock, and returns increased in number over most of the area. However, even when there was little ice present, returns can be variable. For example, on July 15, 2006, data returns were sparse (Figure 36) although no ice floes were apparent between the ice edge and the shoreline. Winds at the time were variable in direction and weak (<4 m/s), suggesting relatively calm conditions.

Differences in data returns also happen on shorter time scales. Figures 37 and 38 are only a day apart, and although the ice environment had not changed much from one day to the next, the data returns were quite different, with more returns on August 8 than on August 7. Winds on August 7 were southward in direction at speeds less than 5 m/s. In contrast, winds on August 8 were eastward between 5 and 10 m/s.

Data from August 7 and 8 also shows the overlap of radials from West Dock and Endicott, which allowed creation of two-dimensional surface currents over a small portion of the coverage area. Overlaying these currents onto SAR imagery shows that the difference in the number of radial returns is reciprocated in the two-dimensional currents (Figures 39 and 40), e.g., the returns on August 7 were significantly fewer than those on August 8. Currents on August 7 are along-shore and westward at ~20 cm/s, while those on August 8 are along-shore and eastward at ~40 cm/s.

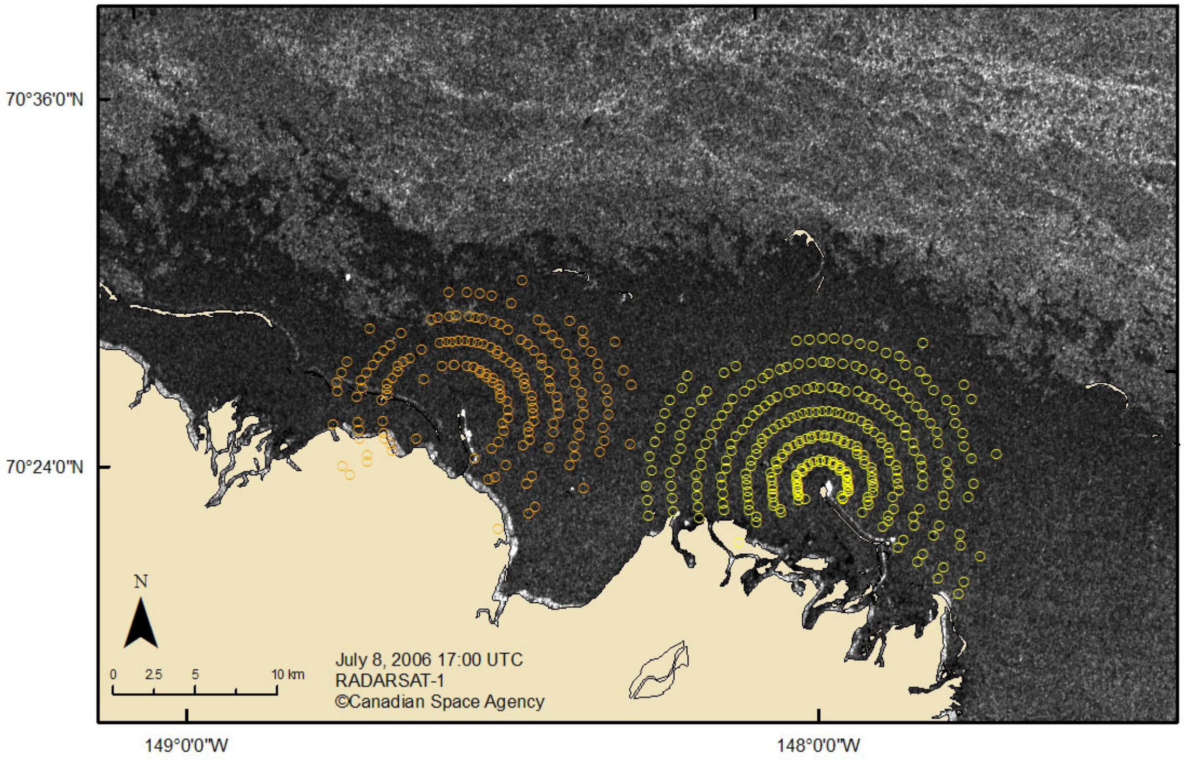

Figure 35. July 8, 2006, one-dimensional HFR returns (West Dock, orange; Endicott, yellow) overlaid on SAR imagery. Winds were westward in direction and sustained at 5 m/s or greater.

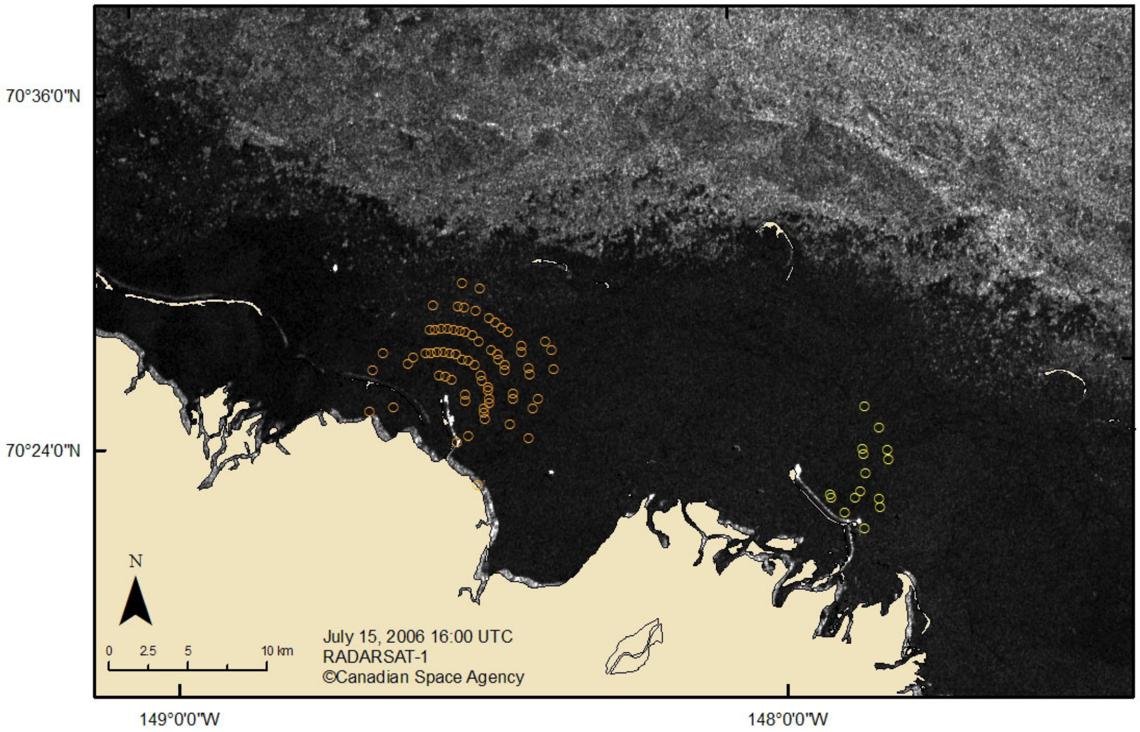

Figure 36. **July 15, 2006, one-dimensional HFR returns (West Dock, orange; Endicott, yellow) overlaid on SAR imagery. Winds were variable in direction and less than 4 m/s.**

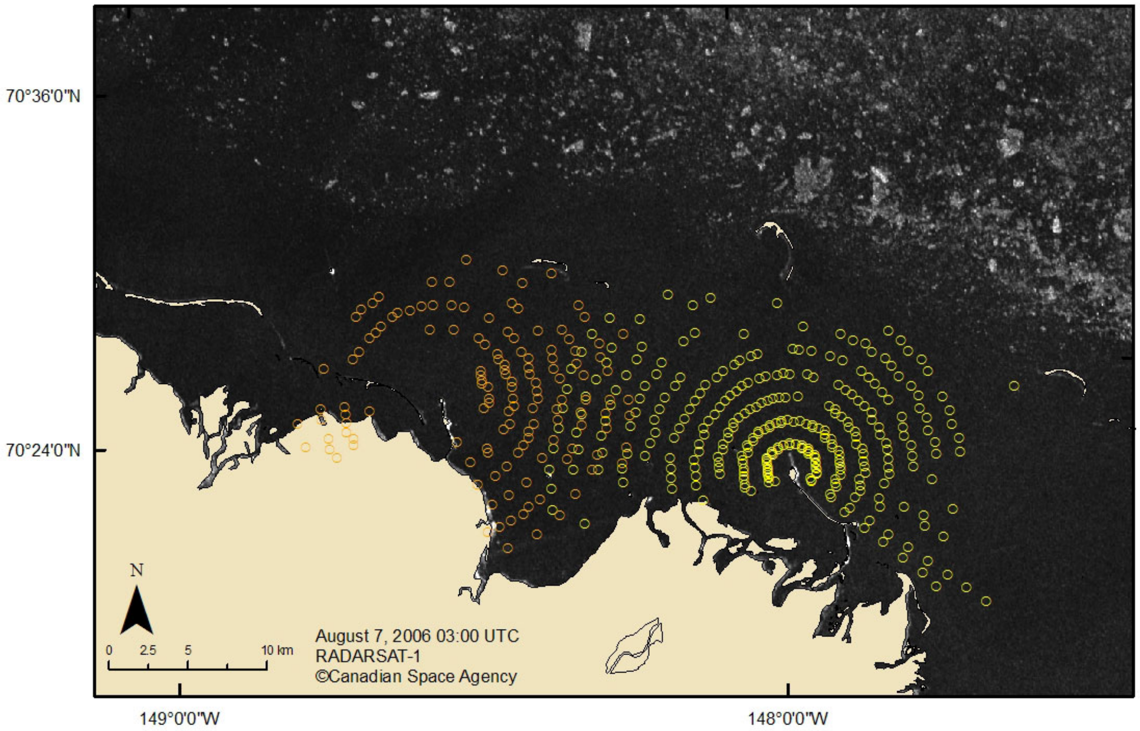

Figure 37. **August 7, 2006, one-dimensional HFR returns (West Dock, orange; Endicott, yellow) overlaid on SAR imagery. Winds were southward at speeds less than 5 m/s.**

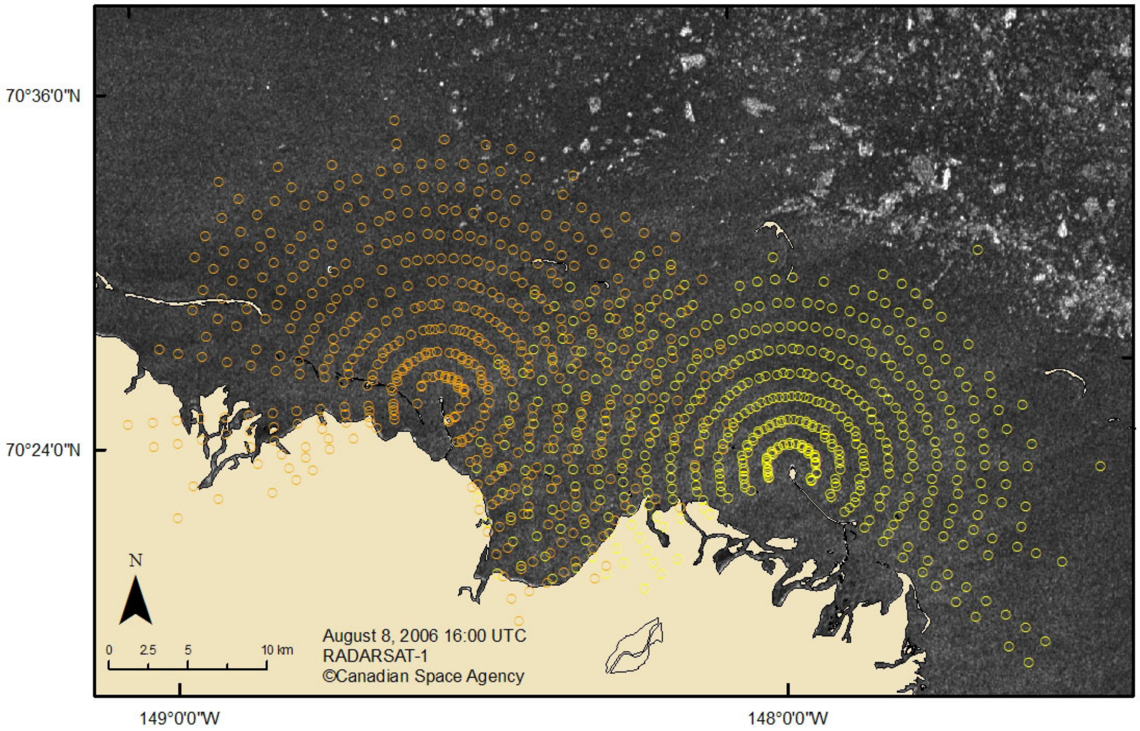

Figure 38. August 8, 2006, one-dimensional HFR returns (West Dock, orange; Endicott, yellow) overlaid on SAR imagery. Winds were sustained to the east at 5 to 10 m/s.

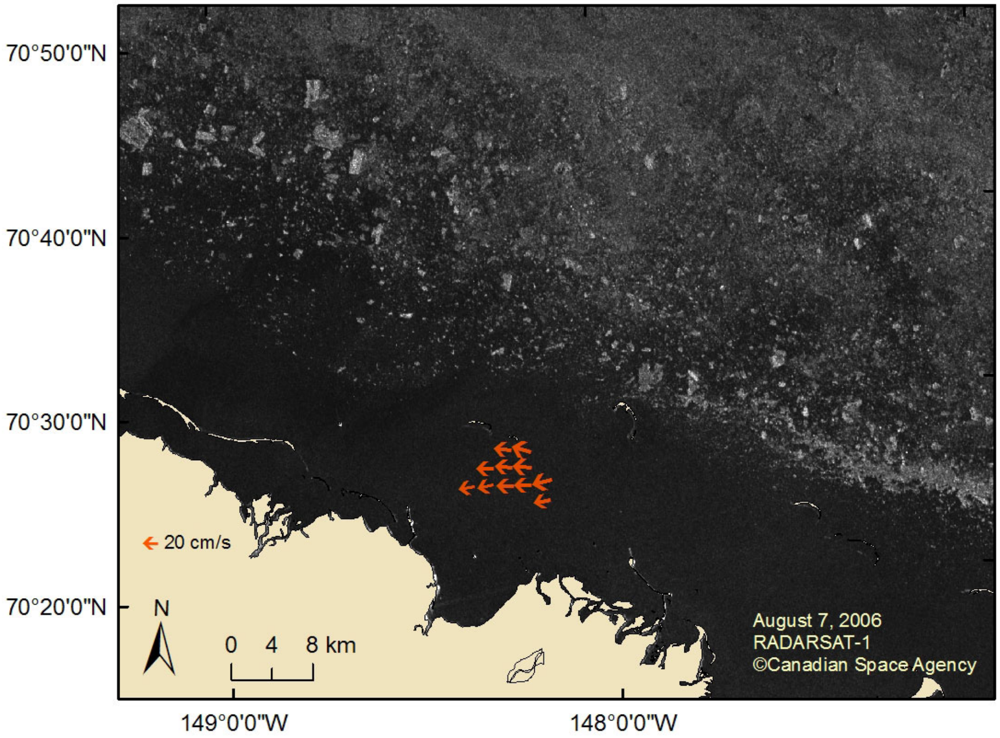

Figure 39. August 7, 2006, two-dimensional HFR returns overlaid on SAR imagery. Currents were ~ 20 cm/s, and winds were from north to south, less than 5 m/s.

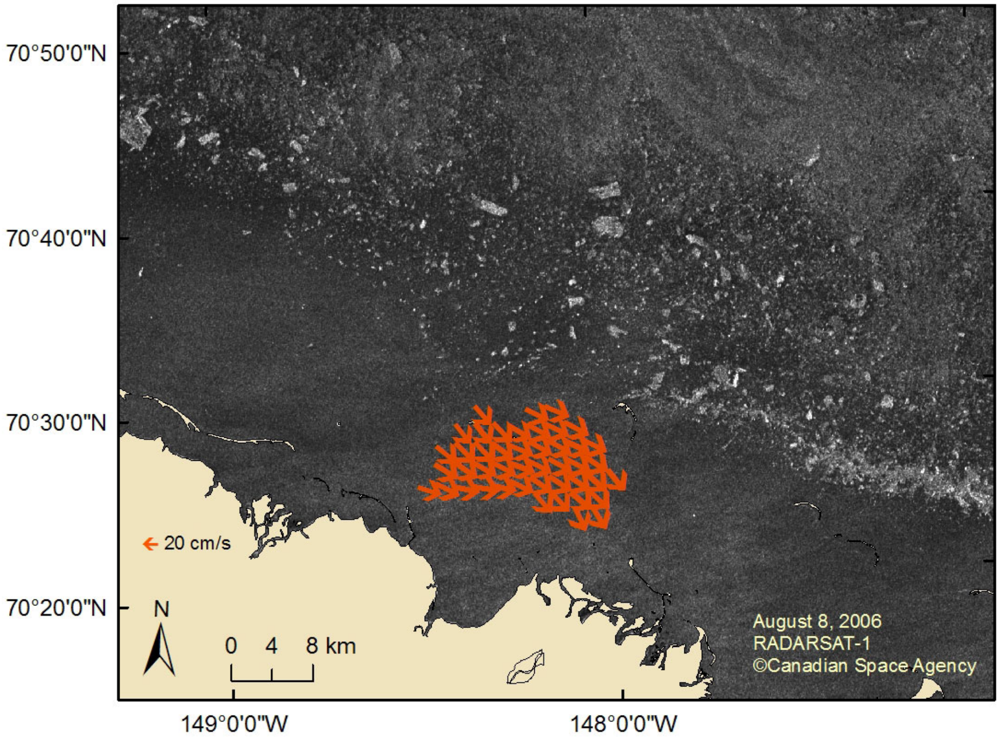

Figure 40. August 8, 2006, two-dimensional HFR returns overlaid on SAR imagery. Currents were ~40 cm/s, and winds were sustained to the east at 5 to 10 m/s.

3.4.2 Regime Two: Band of Fragmented Ice 20 to 30 km Offshore

A band of fragmented ice (Figure 28) was present 20 to 30 km offshore in the HFR coverage area with open water shoreward and offshore of the band from August 26 through September 3 in 2005 and from August 25 to September 25 in 2006. The radar signal was able to propagate over the ice band, making data collection possible both nearshore and offshore of the ice band; however most of the radar returns were between the shore and the ice band rather than offshore of the ice band as shown by the data density distribution in Figure 41. Both temporally and spatially, returns in 2006 were higher in number than those in 2005. In 2005 data returns were recorded >50% of the time inshore of the ice band, but <10% of the returns were obtained offshore of the ice band. In 2006, the radar collected data >50% of the time inshore of the ice band and ~30% of the time offshore of the ice band.

Mean surface current velocities when the band of ice was present were 14.4 cm/s westward, with southward mean winds of ~5.0 m/s, in 2005, and a predominant westward along-shore flow of ~8.3 cm/s was forced by a mean westward wind speed of ~6.0 m/s in 2006 (Figure 42). Current speeds for 2005 varied greatly from onshore to offshore due to the spatial distribution of the data. Nearshore currents in 2005 were smaller than in 2006, while currents offshore of the ice band appeared stronger in 2005 than in 2006. However, a meaningful comparison of the currents offshore of the ice band between the two years is inhibited because of the few offshore data returns obtained in 2005.

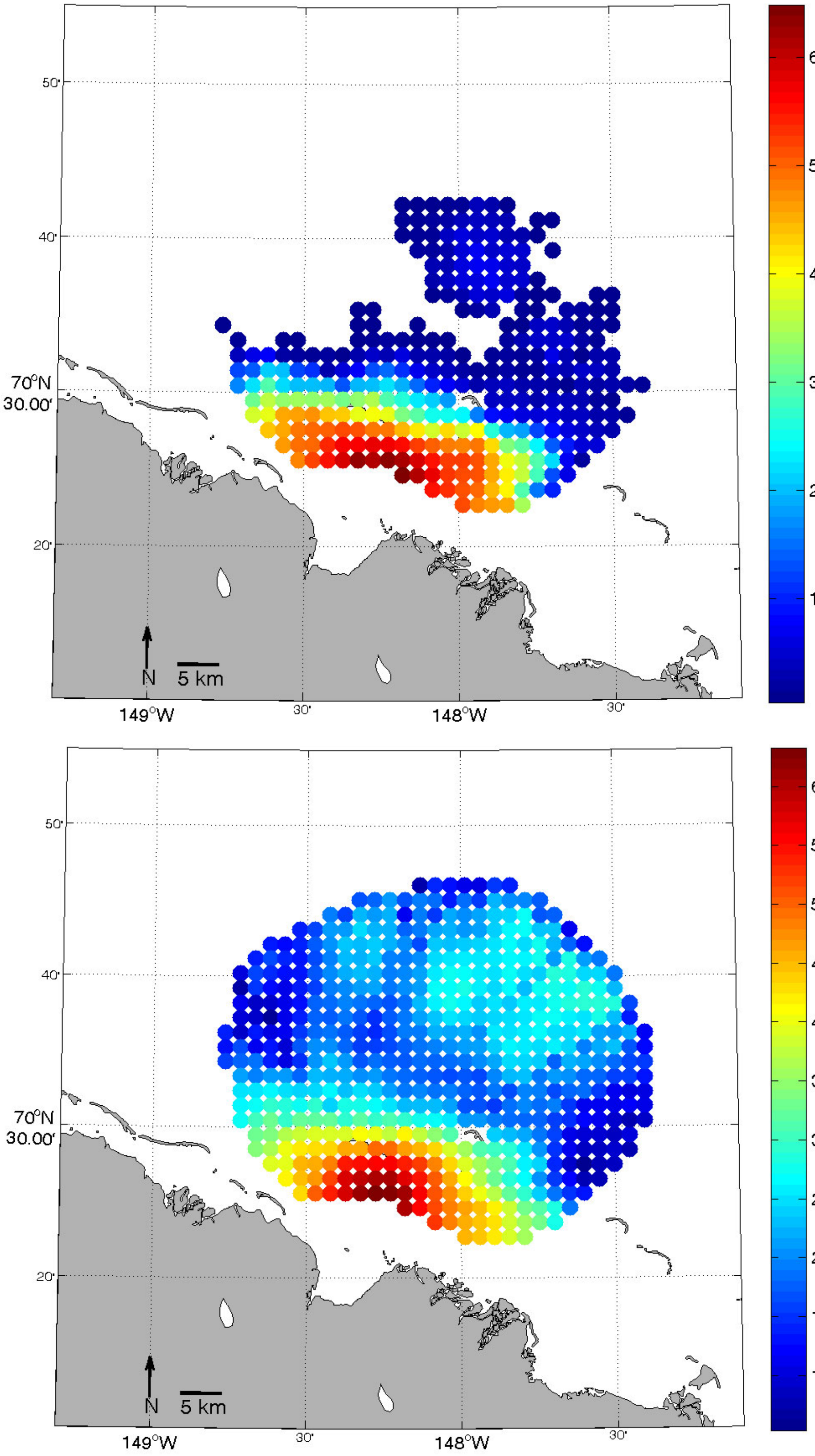

Figure 41. Percent coverage through time of two-dimensional HFR current returns from August 26 – September 3, 2005 (top), and August 25 – September 26, 2006 (bottom).

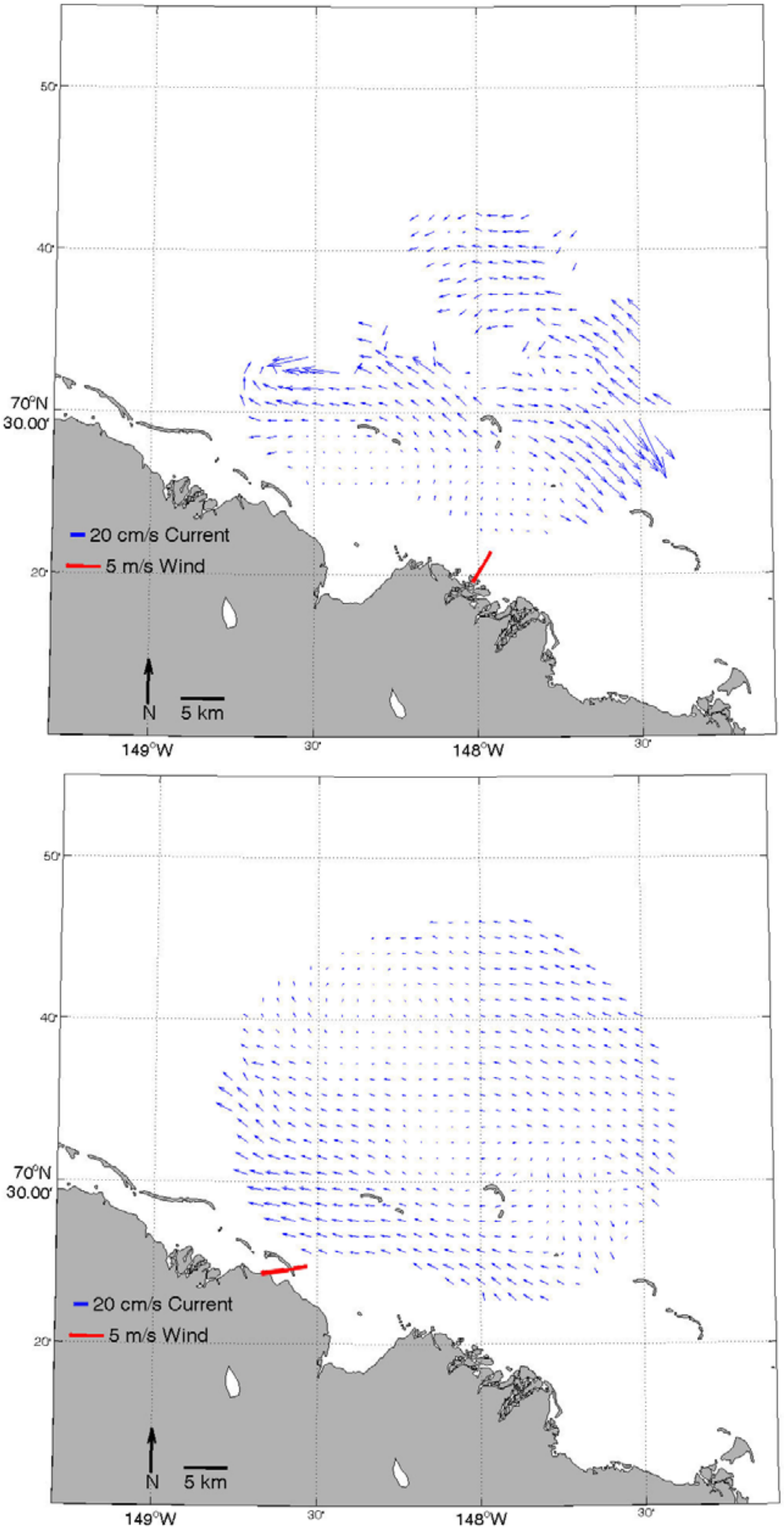

Figure 42. **Mean currents and wind speeds from August 26 – September 3, 2005 (top), and August 25 – September 26, 2006 (bottom)**.

Vector current time series were also resolved into their principal component axes (Figure 43). The analysis for both 2005 and 2006 resulted in major axes that are aligned along-shore and which account for 93% of the current variance in 2005 and 84% of the current variance in 2006. Because most of the variance is in the along-shore component, an EOF analysis on the along-shore current shows finds that most of the variance in 2005 (88%) and 2006 (77%) is in mode 1, with all other modes having 7 – 8% or less of the variance (not statistically significant). In 2005 mode 1 was correlated with the along-shore winds (0.81) with a one hour time lag (Figure 44). In 2006 the maximum correlation was 0.73 with a five hour lag. The EOF and correlation results are consistent with the first mode representing the direct response of the currents to the wind.

We overlaid two-dimensional surface currents onto SAR imagery when the ice band was present. The effort proved useful, although results were diverse due to variations in wind speed, duration, and fetch, as discussed with respect to regime one. Higher winds resulted in a more energetic wave field, which, in turn, resulted in a higher percentage of HFR returns. Higher wind speeds also meant that the properties of the ice band had greater potential to change. At times, the radar signal was able to propagate over the ice band and collect data from both the nearshore and offshore sides of the ice; other times, that was not the case.

The ice band was less persistent in 2005 than 2006, so there were fewer opportunities in 2005 for overlap between the SAR imagery and data returns. Indeed, only occasionally were there offshore returns (Figure 41), and there were no dates of coincident SAR imagery with returns both nearshore and offshore of the ice band. Currents obtained on August 26, 2005, were minimal, with only one two-dimensional current vector calculated and southward (onshore) winds less than 5 m/s (Figure 45), suggesting a fetch-limited, minimal wave field that resulted in few useful radar returns. However, three days later on August 29, winds were westward (along-shore) at ~10 m/s, and sufficient data was obtained within the nearshore side of the ice band. Currents at this time were downwind; however no returns were recorded offshore of the ice band (Figure 46). One day later, the currents and winds shifted direction to the east, with returns again limited to the nearshore side of the ice band and winds were westward at 5 - 10 m/s (Figure 47). Currents were still directed eastward along-shore on September 3 with eastward winds ~5 m/s (Figure 48).

In 2006, when returns offshore increased compared to 2005, the radar signal was able to propagate across the ice band and collect two-dimensional data from both the nearshore and offshore sides of the ice (Figure 49c) at times coincident with SAR imagery. Interestingly, on September 8, only data inshore of the ice band was collected (Figure 49a), whereas on September 11 data returns were only offshore of the ice band (Figure 49b). Winds on September 8 were sustained to the west at ~10 m/s and on September 11 were to the southeast at 5 - 10 m/s. On September 17 (Figure 49c) there were returns from both on- and offshore of the ice band as the winds were blowing to the southeast at ~5 m/s. Four days later on September 21 (Figure 49d), winds averaged 5 - 10 m/s to the southeast, and current returns covered the entire radar field-of-view.

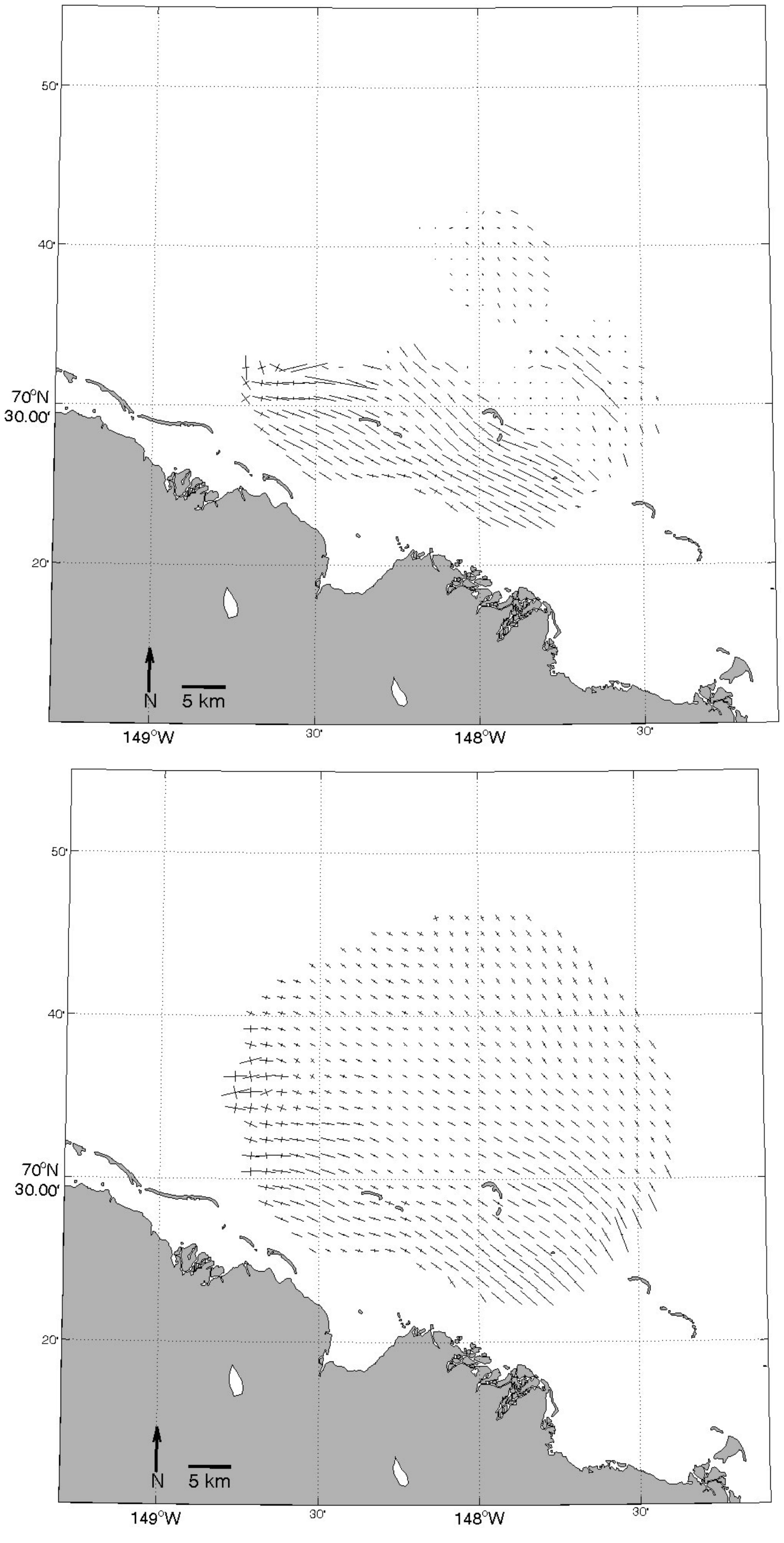

Figure 43. Principal axes from August 26 – September 3, 2005 (top), and August 25 – September 26, 2006 (bottom).

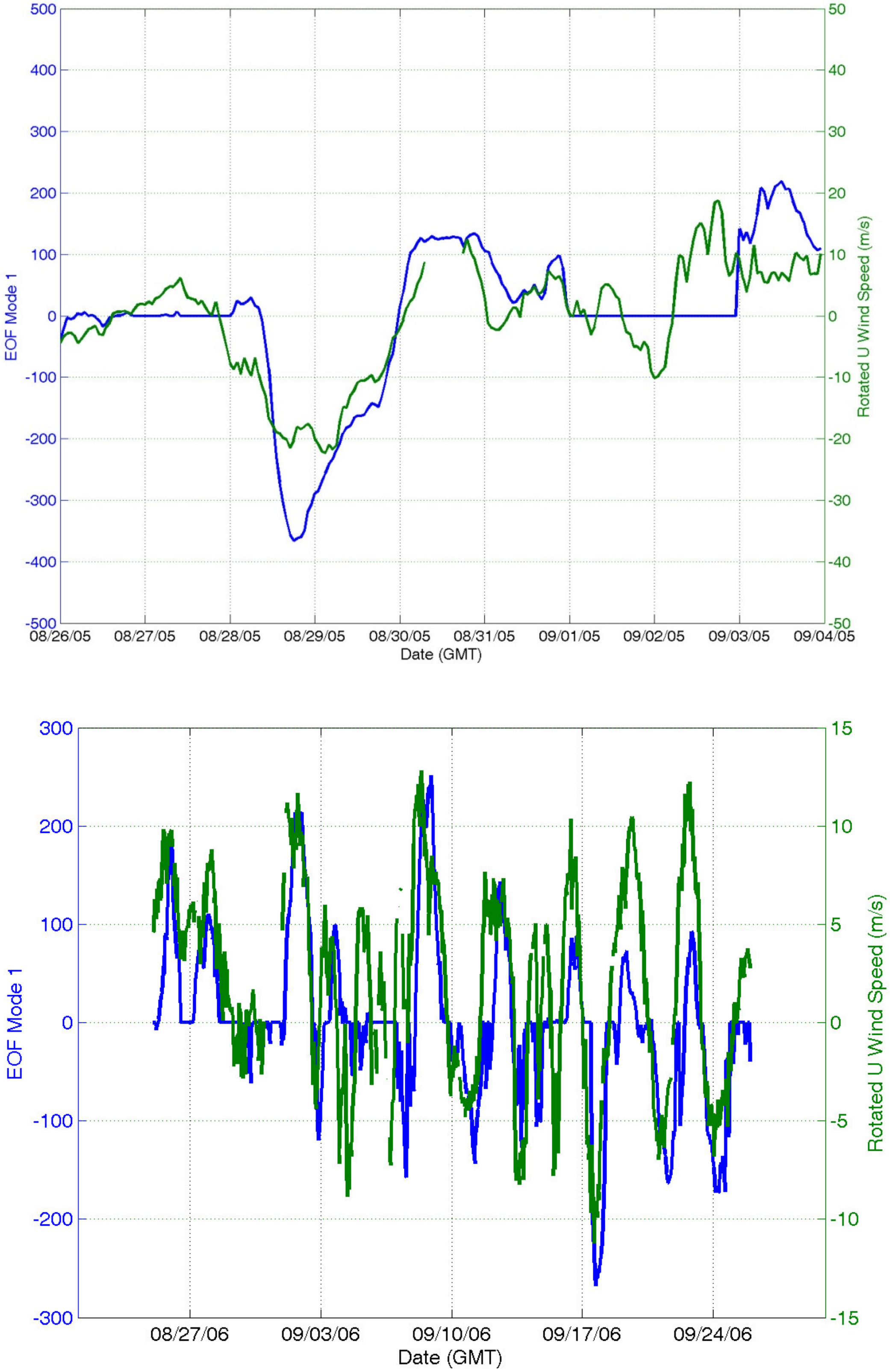

Figure 44. Time series of EOF mode 1 and wind speed from August 26 – September 3, 2005 (top), and August 25 – September 26, 2006 (bottom).

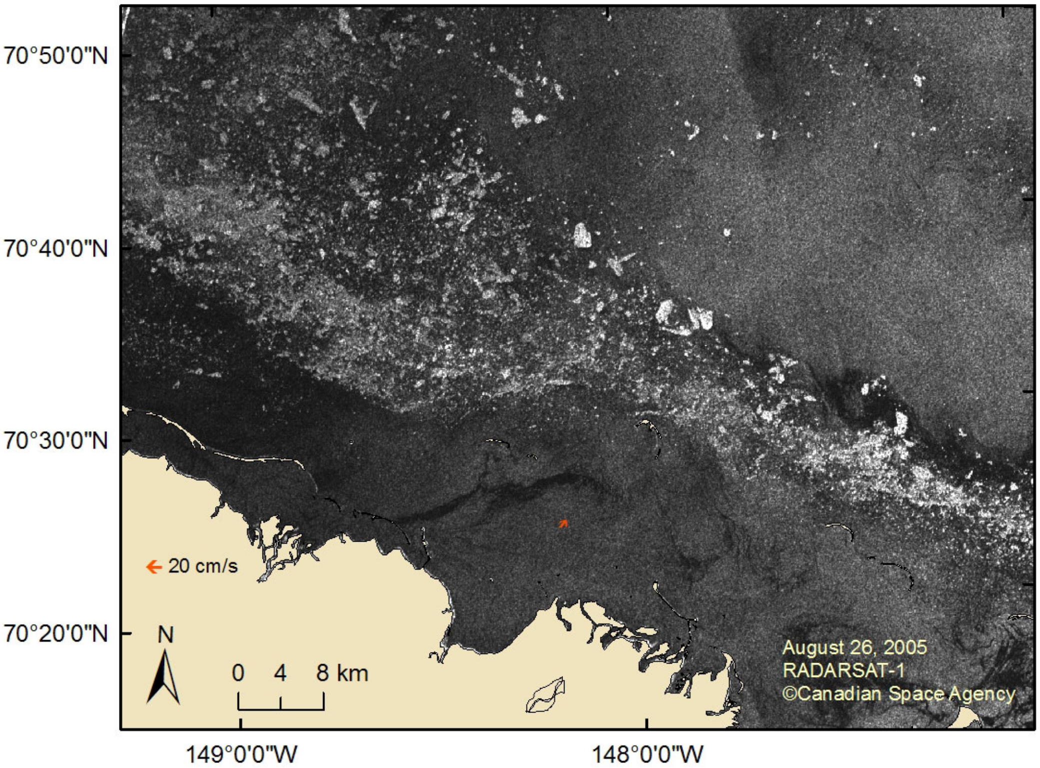

Figure 45. August 26, 2005, two-dimensional HFR returns overlaid on SAR imagery. Winds were southward and <5 m/s.

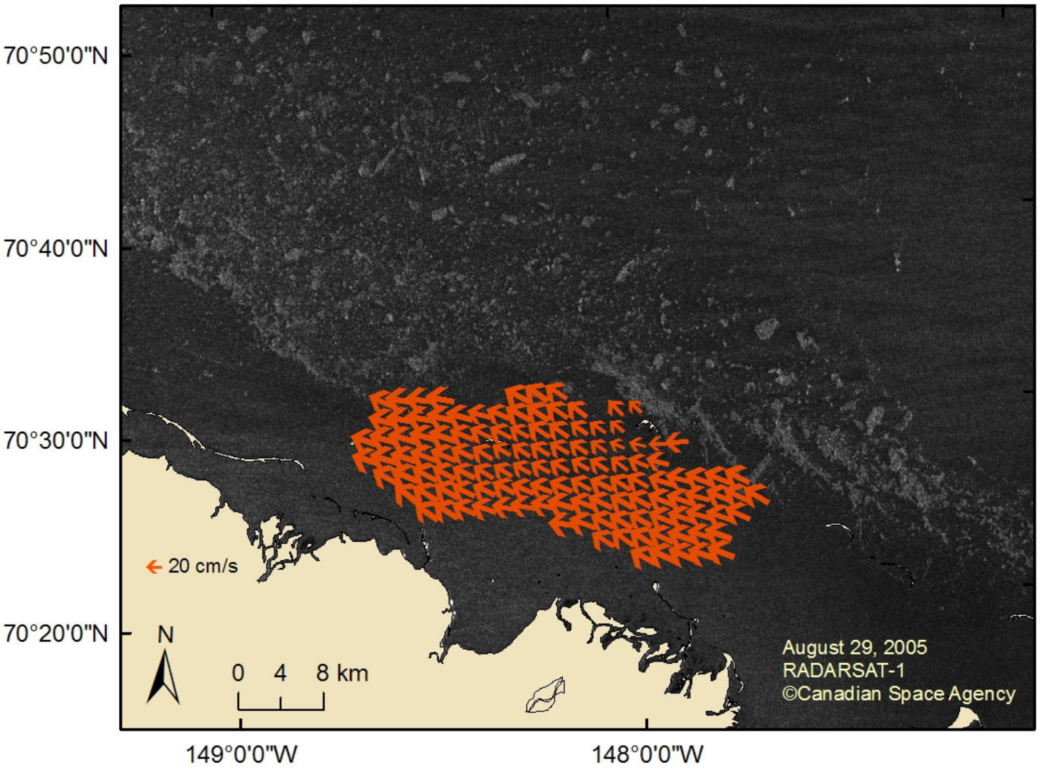

Figure 46. August 29, 2005, two-dimensional HFR returns overlaid on SAR imagery. Winds were to the west at ~10 m/s.

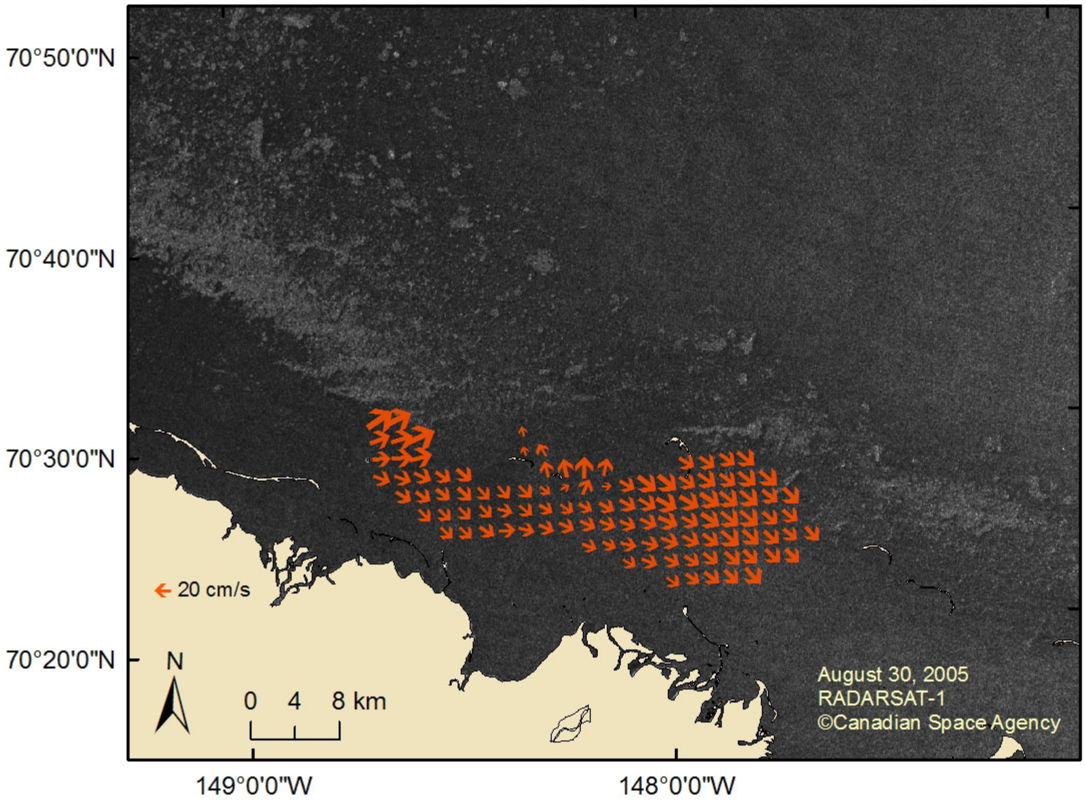

Figure 47. August 30, 2005, two-dimensional HFR returns overlaid on SAR imagery. Winds were eastward at 5 - 10 m/s.

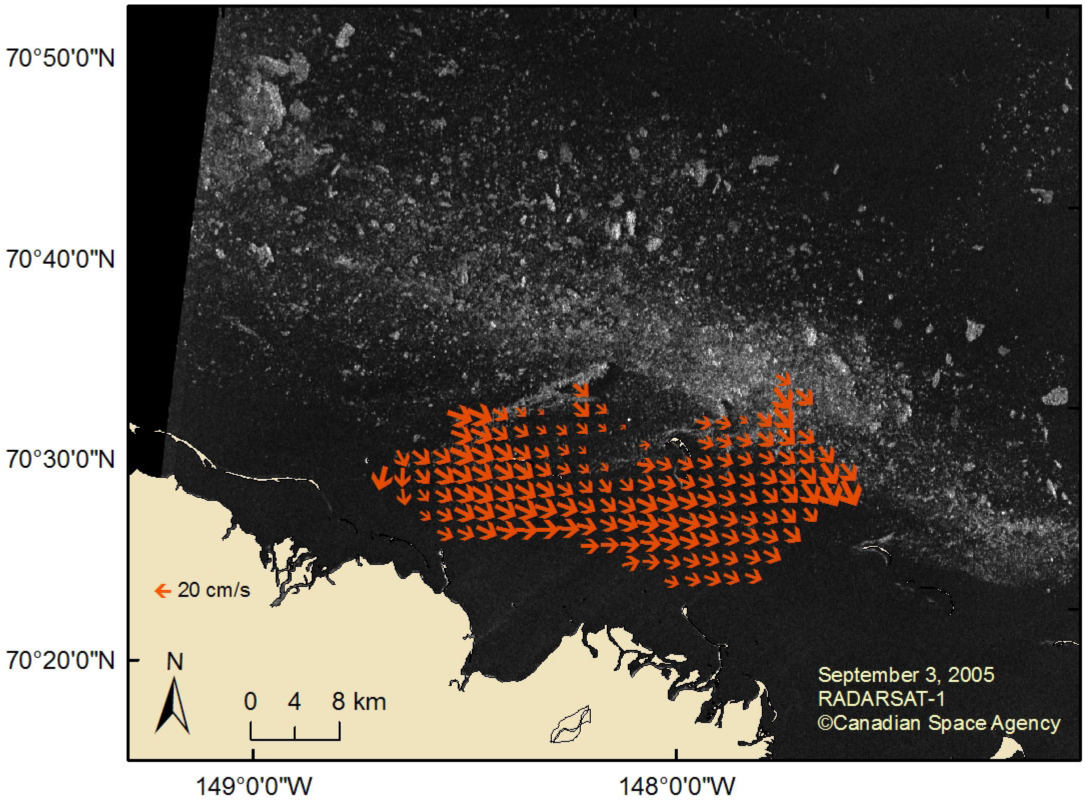

Figure 48. September 3, 2005, two-dimensional HFR returns overlaid on SAR imagery. Winds were eastward at ~5 m/s.

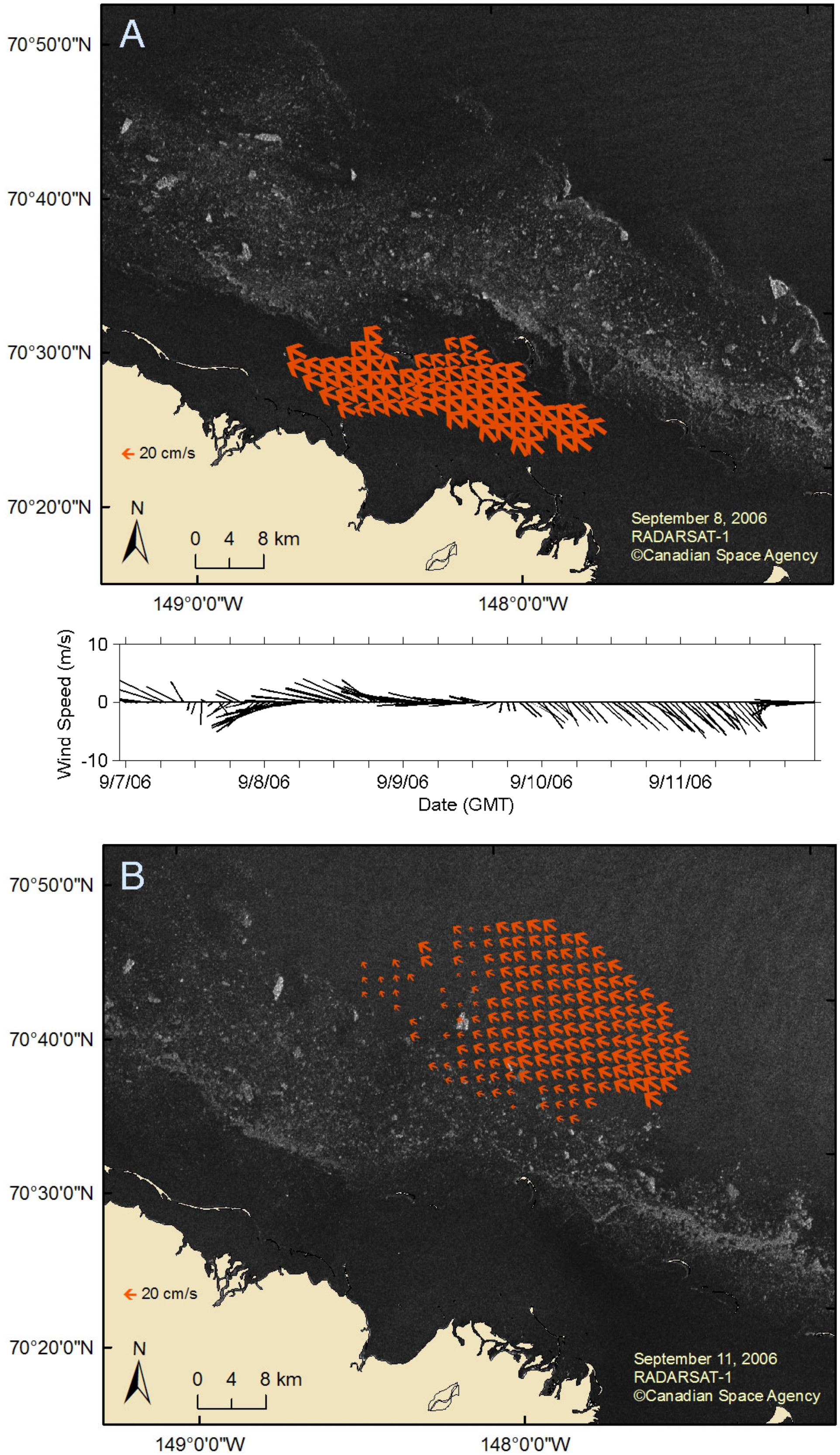

Figure 49 a-b. Two-dimensional surface currents overlaid on SAR imagery for a) September 8, 2006 and b) September 11, 2006. Time series of wind direction and magnitude for September 7 – 11 is shown as a stick plot.

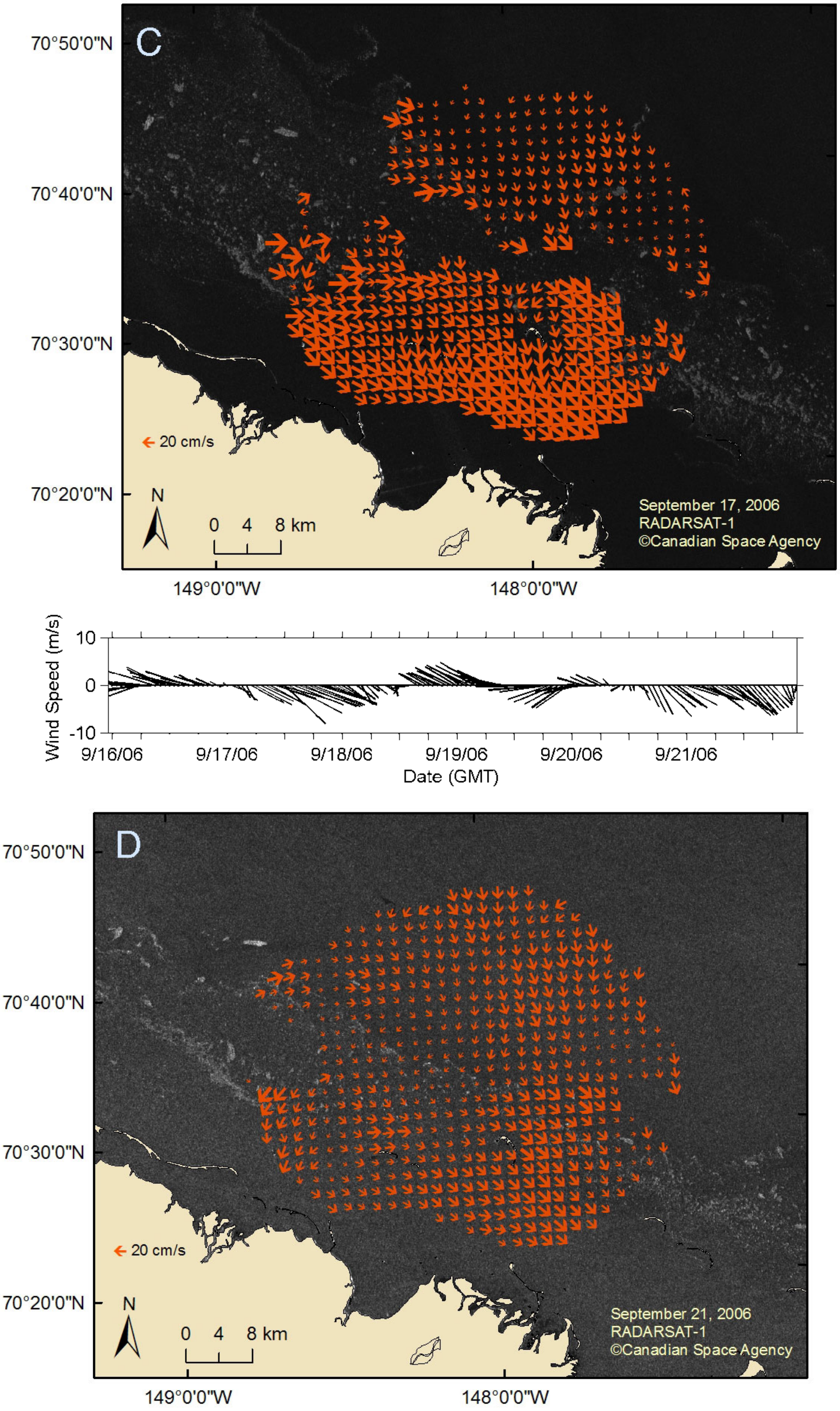

Figure 49 c-d. Two-dimensional surface currents overlaid on SAR imagery for c) September 17, 2006, and d) September 21, 2006. Time series of wind direction and magnitude for September 16 – 22 is shown as a stick plot.

3.4.3 Regime Three: Ice-Free Waters

After storm activity dispersed the ice band present in regime two, waters in the HFR coverage area remained relatively ice-free with only intermittent floes until landfast ice formation. The third regime was present from September 16 – October 10, 2005, and from October 2 – October 20, 2006. During these periods, there were hardware problems, which led to spatial gaps in the data. In 2005 consistent data were obtained only in the southwest region of the HFR field-of-view because the system ran at 25 MHz through September 29 when it was switched to 13 MHz for the duration of the field season. In 2006, there was a wedge of reduced spatial coverage due to a hardware failure in the West Dock Receive antenna (Figure 50).

Mean surface current velocities for the ice free period for both field seasons show a predominant westward along-shore flow, ~30 cm/s in 2005 and 23 cm/s in 2006 (Figure 51), which was forced by a mean westward wind speed of approximately 10 m/s in 2005 and 7 m/s in 2006. The differences between the means in both years reflect differences in wind velocity variations discussed below.

Vector current time series at each grid point were resolved into their principal component axes and show that the major axes for most of grid points are along-shore (Figure 52). This orientation is typical for wind-forced currents on shallow shelves. Major axes in 2005 are more east/west, whereas in 2006 the axes are approximately west-northwest/east-southeast. The principal axes of variance indicate that for both 2005 and 2006 ~90% of the current variability is in the along-shore direction and ~10% in the cross-shore direction. Note that the length of the principal axes is larger in 2006 than in 2005. This is due to the larger variability in along-shore wind velocity in 2006 compared to 2005. In the southeast portion of the HFR field-of-view for 2006, there was considerably more variability in the cross-direction than elsewhere with the major axis accounting for 65% of variance. The change in orientation here may reflect the influence of the offshore/onshore channel that cuts between the barrier islands.

EOF analysis of the along-shore current components finds that most of the along-shore current variance is in mode 1 (75% in 2005; 84% in 2006), with all other modes having significantly less variance (14% or less in 2005; 5% or less in 2006). The mode 1 time-amplitude function and the along-shore wind time series are significantly correlated (Figure 53), with the maximum correlation in 2005 being 0.72 with the currents lagging the winds by one hour. In 2006, the maximum correlation was 0.89 with a six hour lag between the wind and the currents. The results are consistent with the first mode representing the response of the currents to the wind. In comparison, the remaining modes are not statistically significant from one another.

A correlation between the along-shore winds and currents (Figure 54) corroborates the EOF wind correlation results (e.g., the maximum correlation coefficient is 0.85 with the currents lagging the winds by six hours). During the ice-free period of 2006, there were five reversals in wind direction; however, winds were westward approximately 80% of the time, and the westward wind events had significantly higher wind speeds than the eastward wind events. In 2005 there were only two wind reversals, so that nearly 100% of the time the winds were westward and blew with significantly higher wind speeds than the eastward wind events. For this reason, we use the 2006 data to look into more detail of how the currents change with changes in wind.

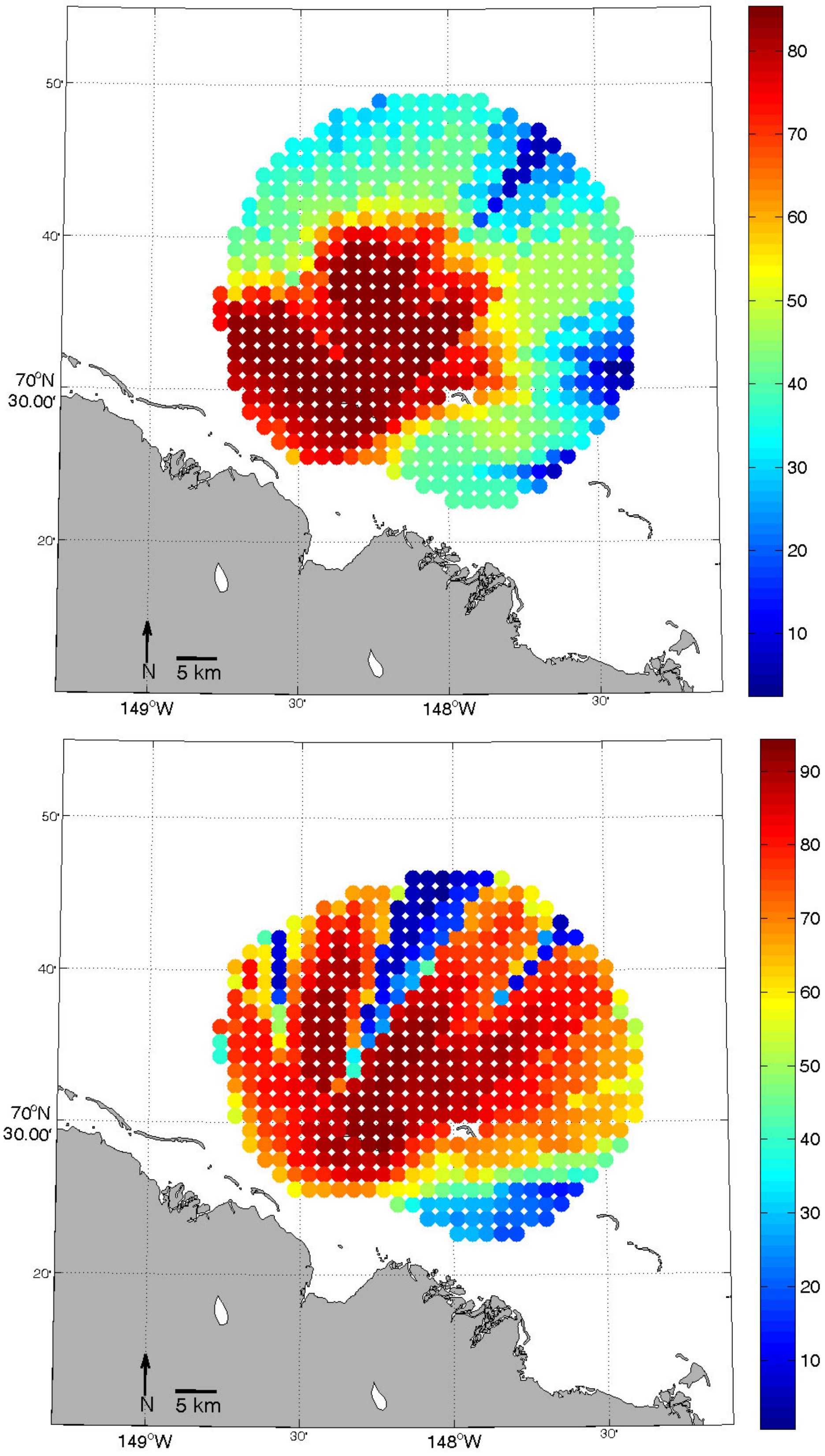

Figure 50. Percent coverage through time of two-dimensional HFR current returns from September 16 – October 10, 2005 (top), and October 2 – 20, 2006 (bottom).

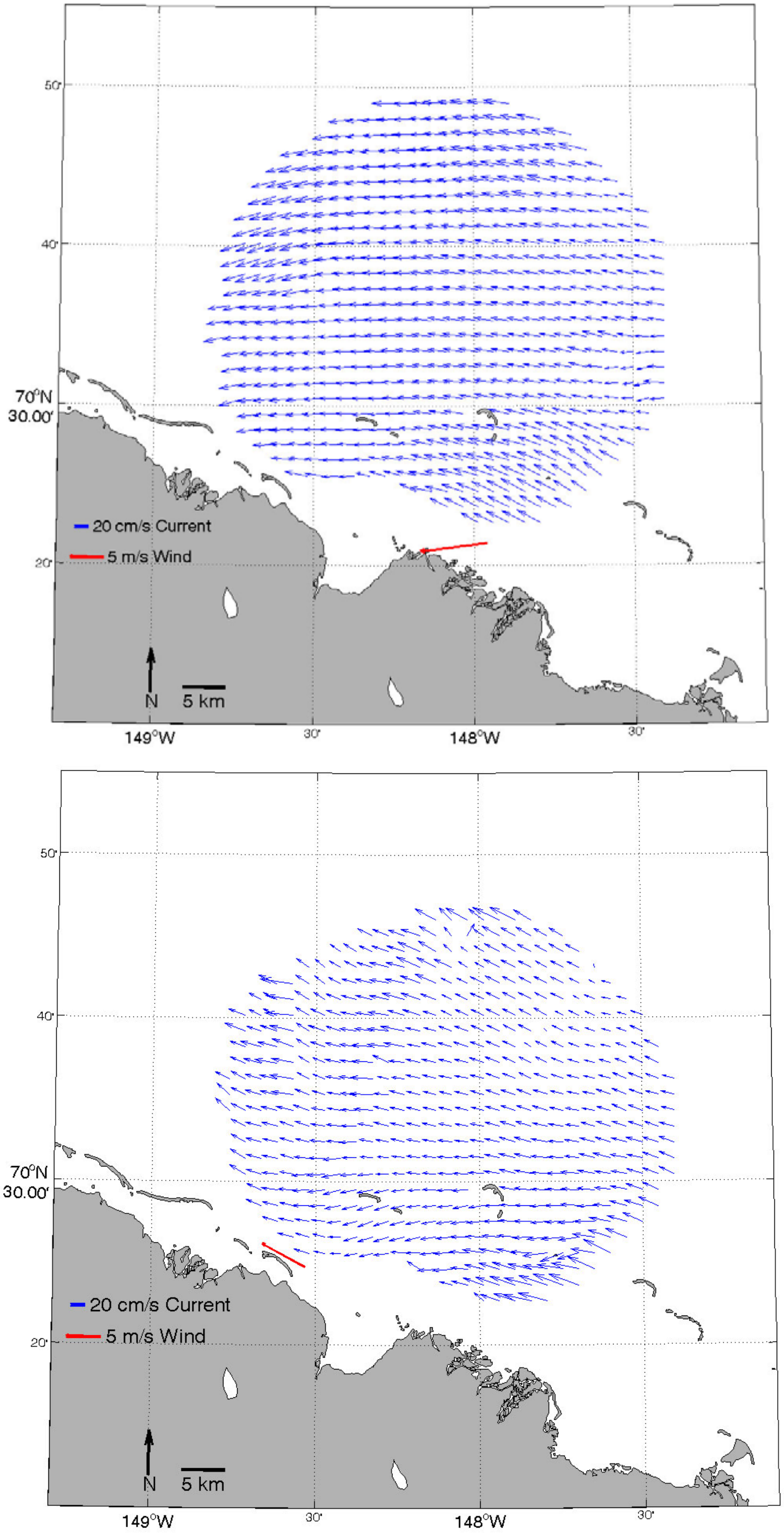

Figure 51. Mean current and wind speeds from September 16 – October 10, 2005 (top), and October 2 – 20, 2006 (bottom).

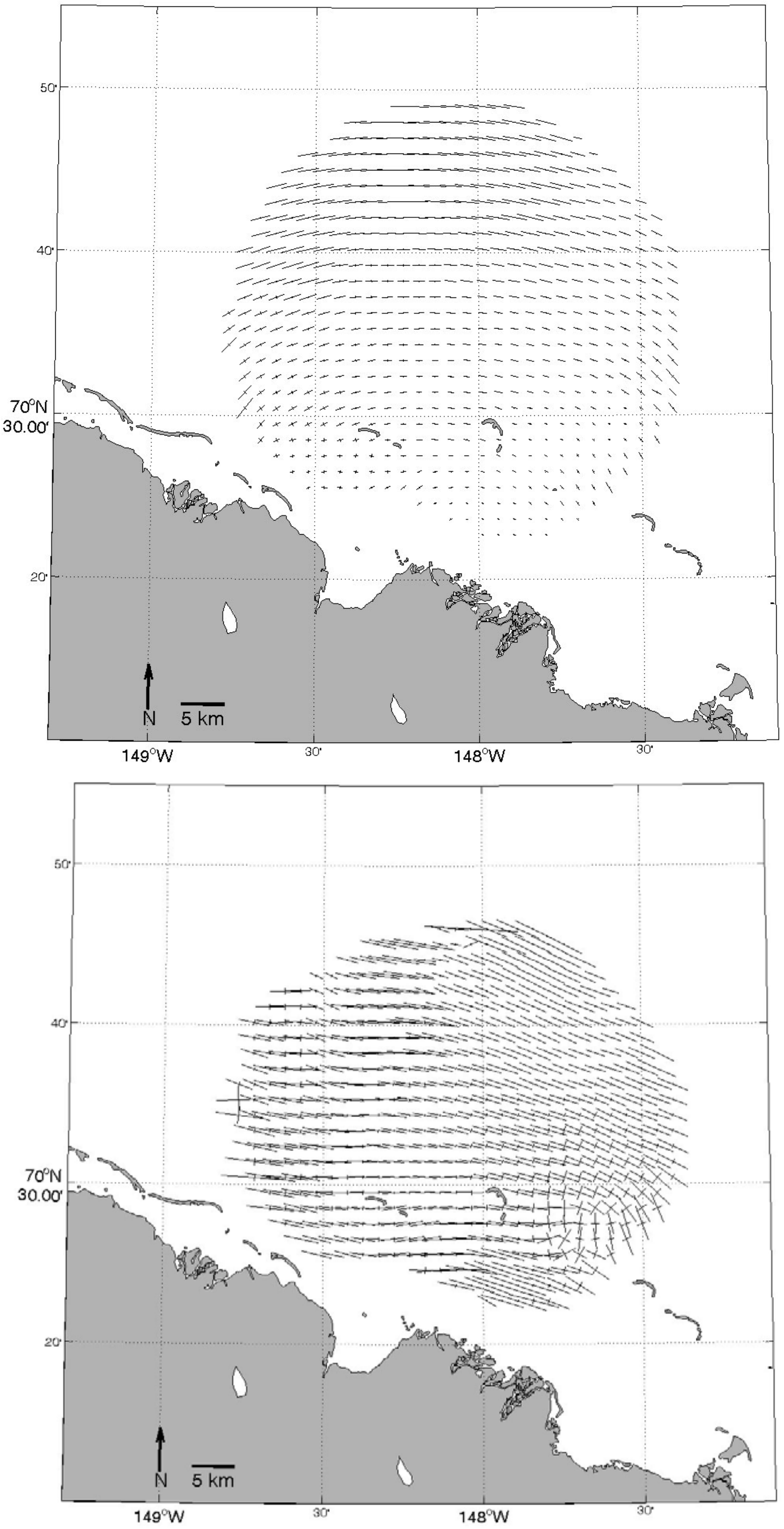

Figure 52. Principal axes from September 16 – October 10, 2005 (top), and October 2 – 20, 2006 (bottom).

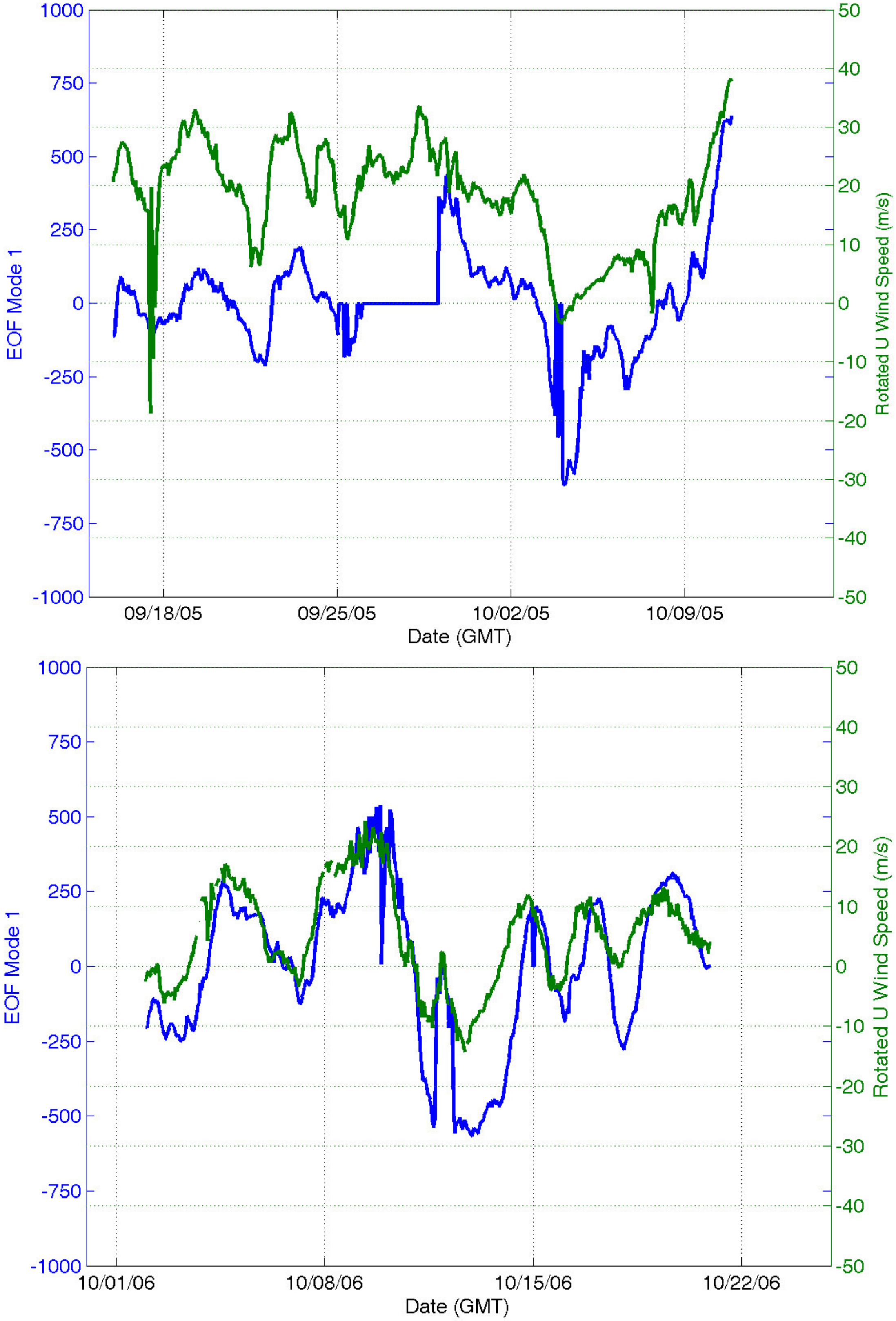

Figure 53. Time series of EOF mode 1 and wind speed from September 16 – October 10, 2005 (top), and October 2 – 20, 2006 (bottom).

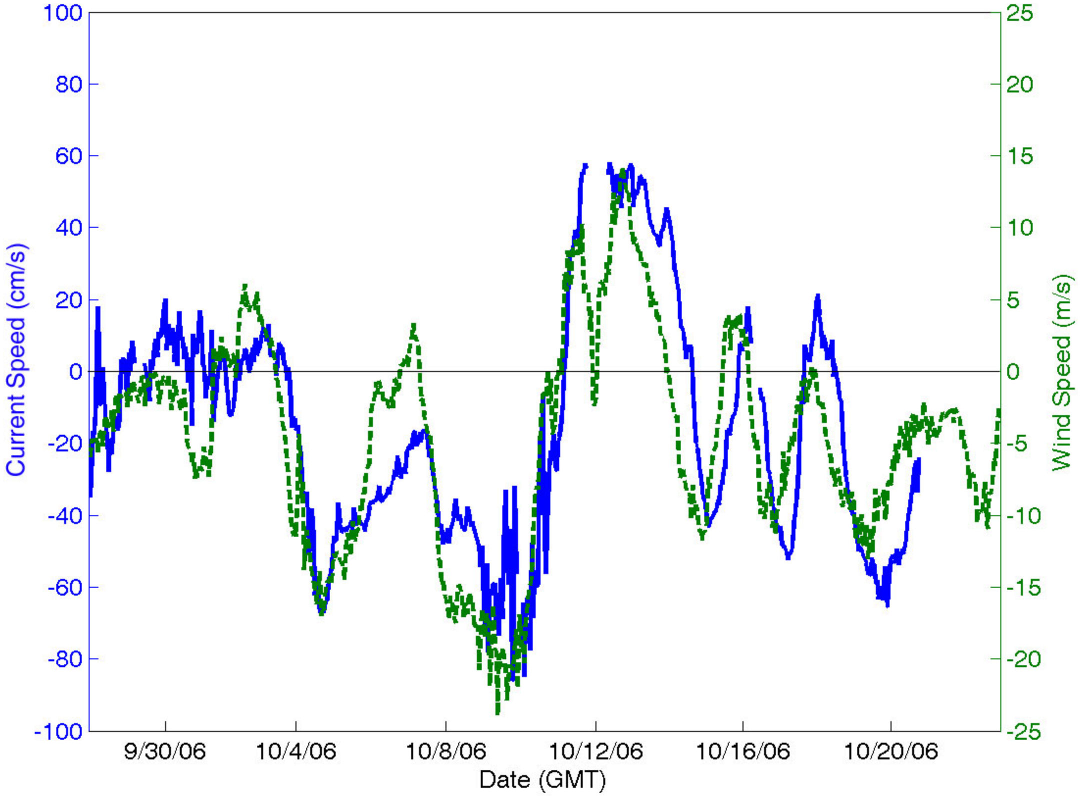

Figure 54. Time series of along-shore surface currents (solid blue line) and winds (dashed green line). Values greater than zero indicate eastward flow/direction, and values less than zero indicate westward flow/direction.

Comparing the individual east/west and north/south components of the surface currents and winds shows higher variation and magnitudes of both the currents and winds in the east/west direction when compared with the north/south components (Figure 55). East/west components show velocities greater than 50 cm/s (currents) and 15 m/s (winds), whereas north/south components never exceeded 25 cm/s (currents) or 15 m/s (winds) respectively. Winds contained a westward component ~75% of the time and a northward component 80% of the time.

As a final illustration of the data, we prepared maps of the mean weekly currents and principal axes components, along with hourly wind vectors for regime three in 2006. From September 24 through 30, current variations were spatially uniform in the along-shore direction with little to no cross-shore component (Figure 56). On September 24, winds were eastward and on average <5 m/s. Winds began changing direction on September 25, maintaining the same speeds, rotating in a clockwise direction from east to west through mid-day September 26, at which point winds were sustained in a westward alongshore direction, peaking at ~10 m/s at 00:00 GMT September 27 and decreasing to ~2 m/s through September 29. Winds remained relatively calm until September 30, when they again picked up to the northwest. Average current speeds from September 24 through September 29 averaged 15 cm/s and were along-shore and to the west.

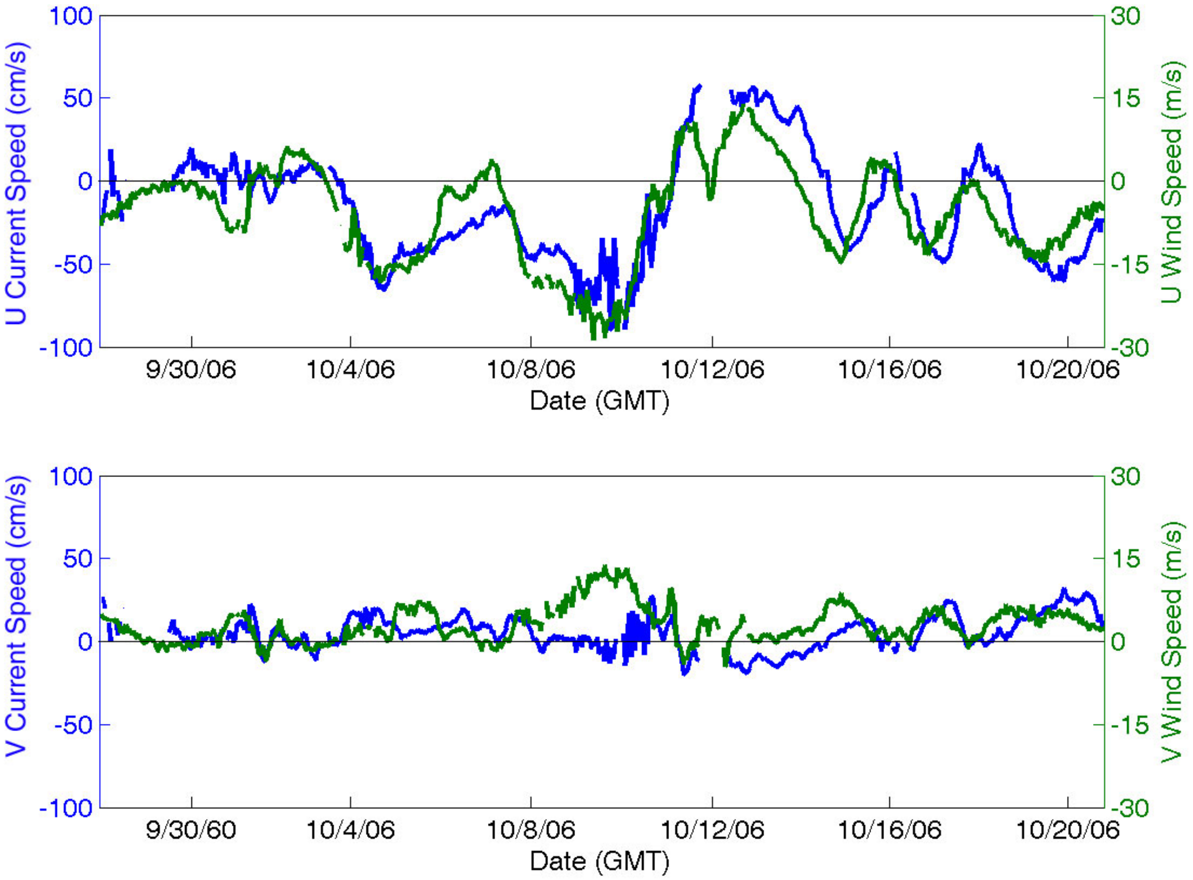

Figure 55. Time series of the u and v components of surface currents (blue) and wind speeds (green). Values greater than zero indicate eastward flow/direction, and values less than zero indicate westward flow/direction.

Principal axes for October 1 - 7 were again in the along-shore direction with little or not cross-shore component (Figure 57). Mean current speeds were 25 cm/s along-shore to the west. Winds varied throughout the week and were highly variable from October 1 through October 2, ranging from northwest to southeast in direction at speeds <5 m/s. On October 3, winds began the day blowing in an eastward direction but abruptly reversed direction to the west. Winds were sustained to the west-northwest at speeds ~10 m/s until October 6, when speeds were reduced to ~2 m/s, varying in direction through October 7, when winds once again increased in speed to the west-northwest.

During the week of October 8 – 14, winds and currents were highly variable, although the principal axes show that most of the variance continued to be in the alongshore direction (Figure 58). Winds were very strong to the northwest from October 8 through October 10 with wind gusts up to 40 m/s; however by midday of October 10, the winds decreased and began to rotate clockwise until the winds became predominantly eastward on October 11. This wind reversal caused a reversal in current direction (Figure 59). The winds changed again on October 14 when they rapidly switched to once again blew toward the northwest, which was followed by a similarly rapid reversal in the surface current direction (Figure 60). These current reversals in response to the winds occur rapidly within hours.

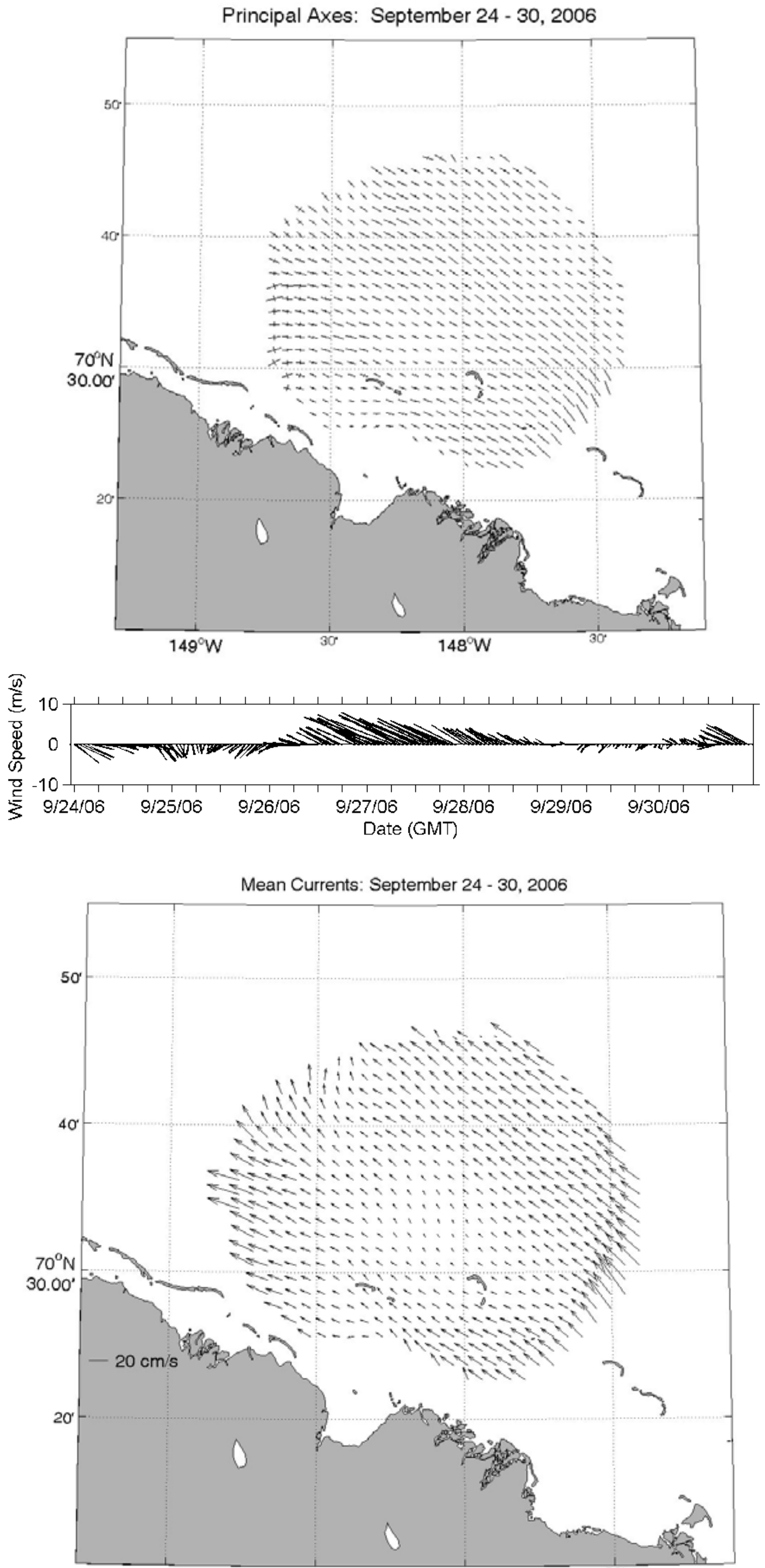

Figure 56. Principal axes (top) for September 24 – 30, with variations predominantly in the along-shore direction. Wind vector time series (center). Averaged surface current vectors (bottom) for the same time frame.

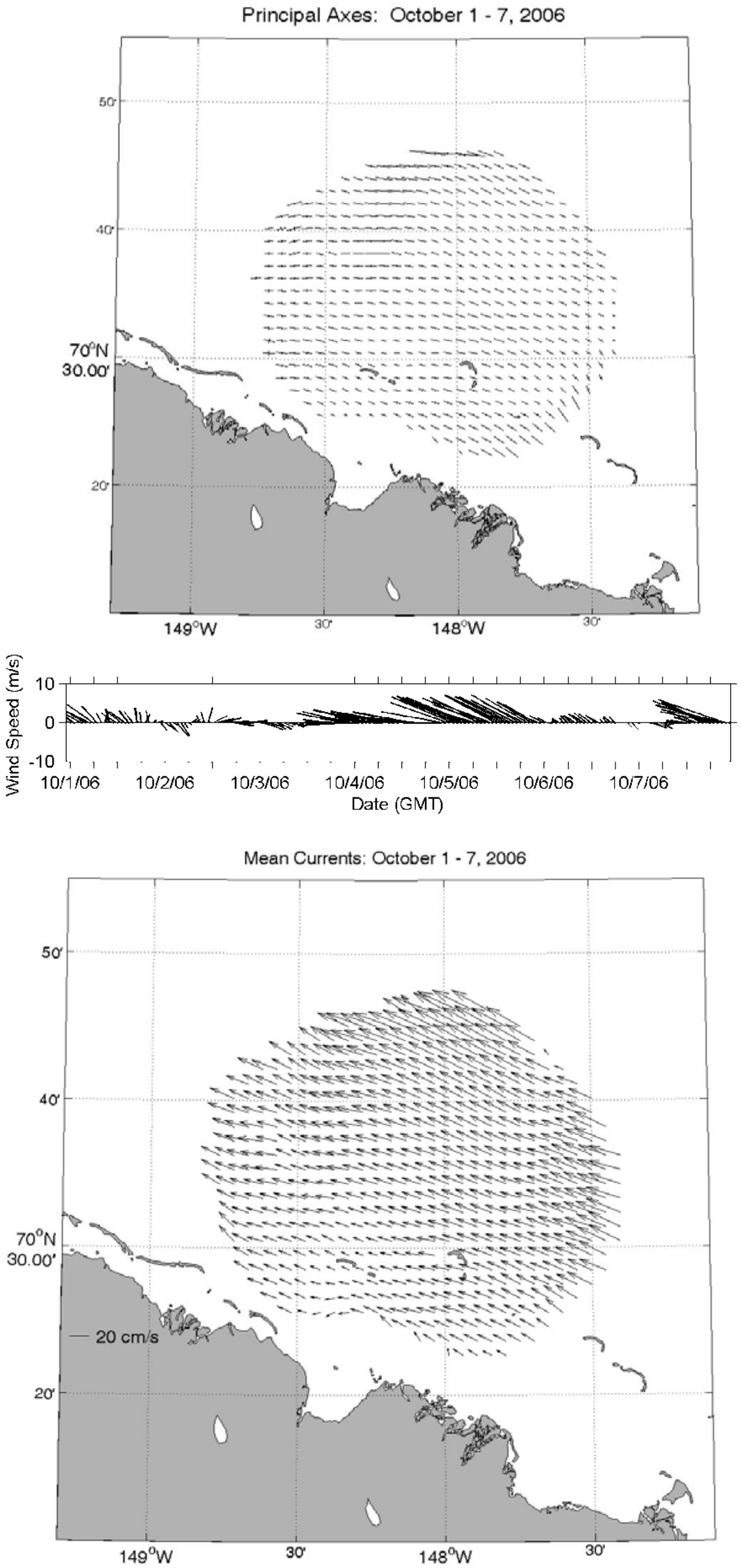

Figure 57. Principal axes (top) for October 1 – 7, with variations predominantly in the along-shore direction. Wind vector time series (center). Averaged surface current vectors (bottom) for the same time frame.

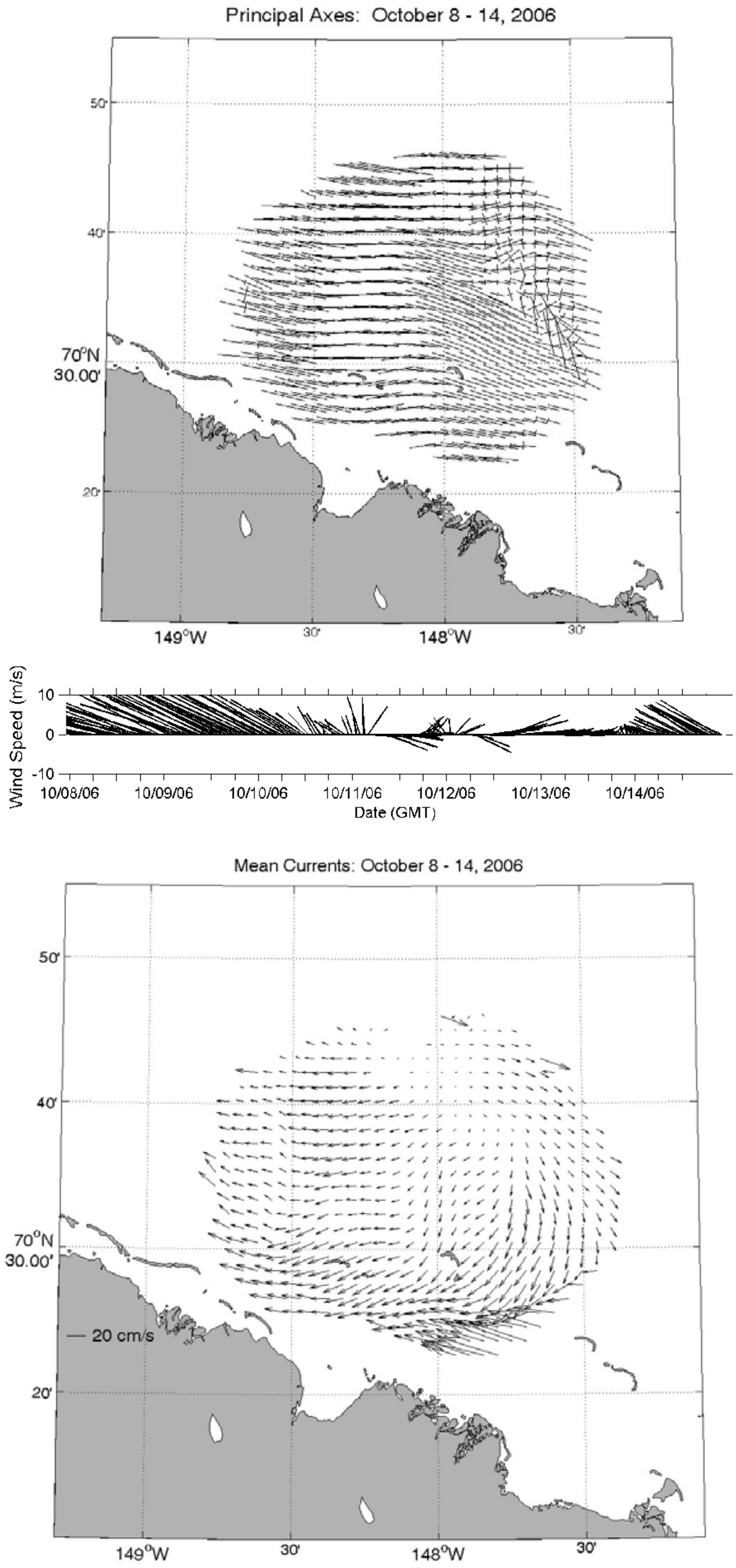

Figure 58. Principal axes (top) for October 8 - 14, with variations predominantly in the along-shore direction. Wind vector time series (center). Averaged surface current vectors (bottom) for the same time frame.

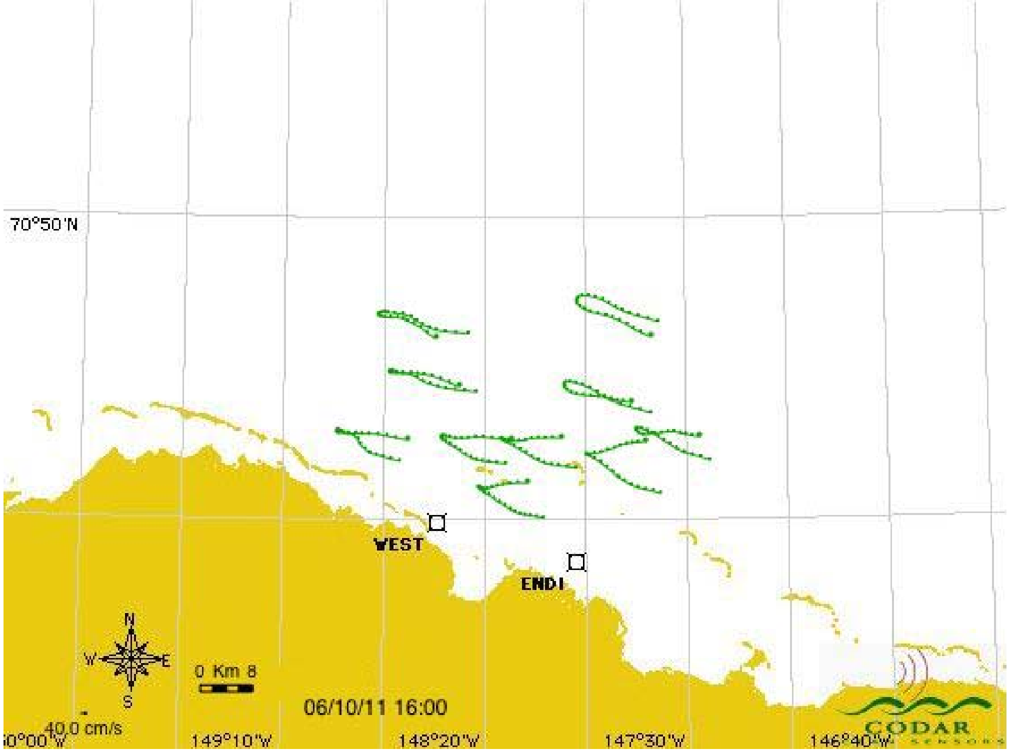

Figure 59. 24-hour surface current trajectories (green) from October 10 – 11, 2006, when winds reversed from blowing to the west to blowing toward the east. Dots on the trajectories depict locations at one hour intervals.

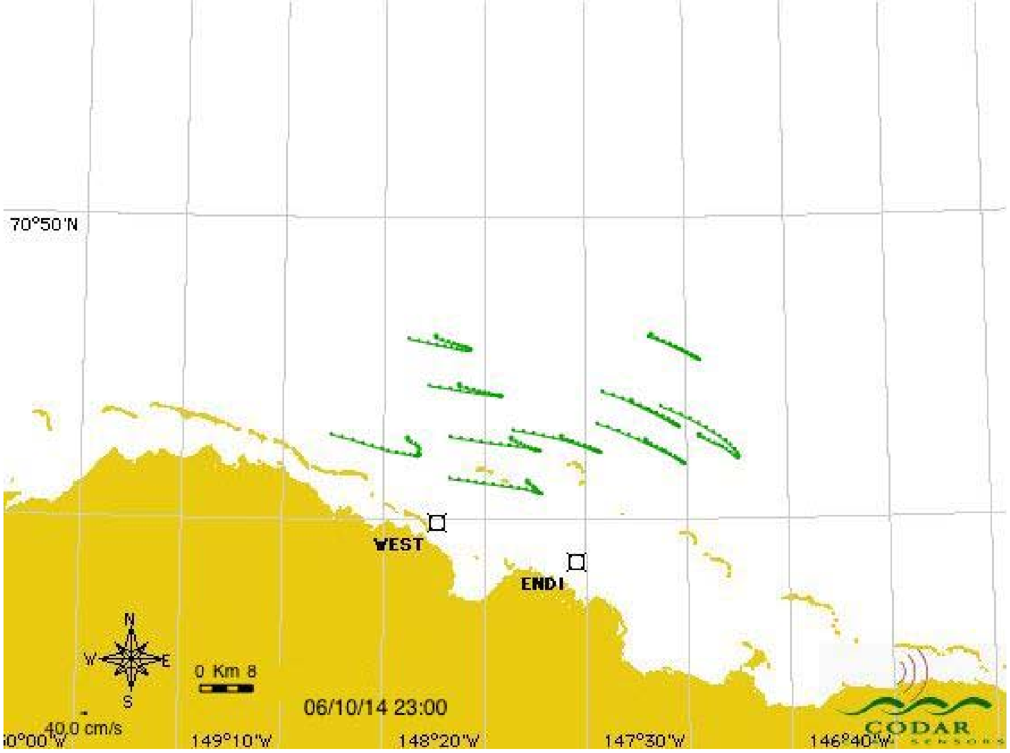

Figure 60. 24-hour surface current trajectories (green) from October 14, 2006. During this time, winds reversed from blowing to the east to blowing toward the west. Dots on the trajectories depict locations at one hour intervals.

3.4.4 Regime Four: Early Landfast Ice Formation

As temperatures dropped to below freezing in mid-October 2005 and 2006, landfast ice began forming at the shoreline of Prudhoe Bay, but the effect on surface current data collection was not evident until the landfast ice entered the HFR field-of-view, ~5 km offshore. As a result, initial landfast ice formation had no effect on the surface current data collected, and it appears that grease ice plays more of a role in hindering HFR returns during freezeup than does landfast ice.

Due to a loss of power at West Dock in 2005, 2006 is the only year when two-dimensional data was collected during landfast ice formation. When compared with regime three, open water, percent coverage of data returns (Figure 49), regime four does not reveal any significant differences offshore of the barrier islands; however there is reduced coverage nearshore in the southwestern portion of the data (Figure 61). Mean currents when ice extended from shore into the HFR mask averaged 48 cm/s, and winds averaged 9.6 m/s (Figure 62). Although the current speeds recorded are greater than those during the open water period, the average direction of current flow and winds remained the same. Mean currents in the southwest portion of the HFR coverage area vary slightly from the rest of the coverage area due to the spatial distribution of the data (Figure 61). Large magnitude winds were sustained west-northwest throughout the period of ice formation from October 18 - 22 (Figure 63).

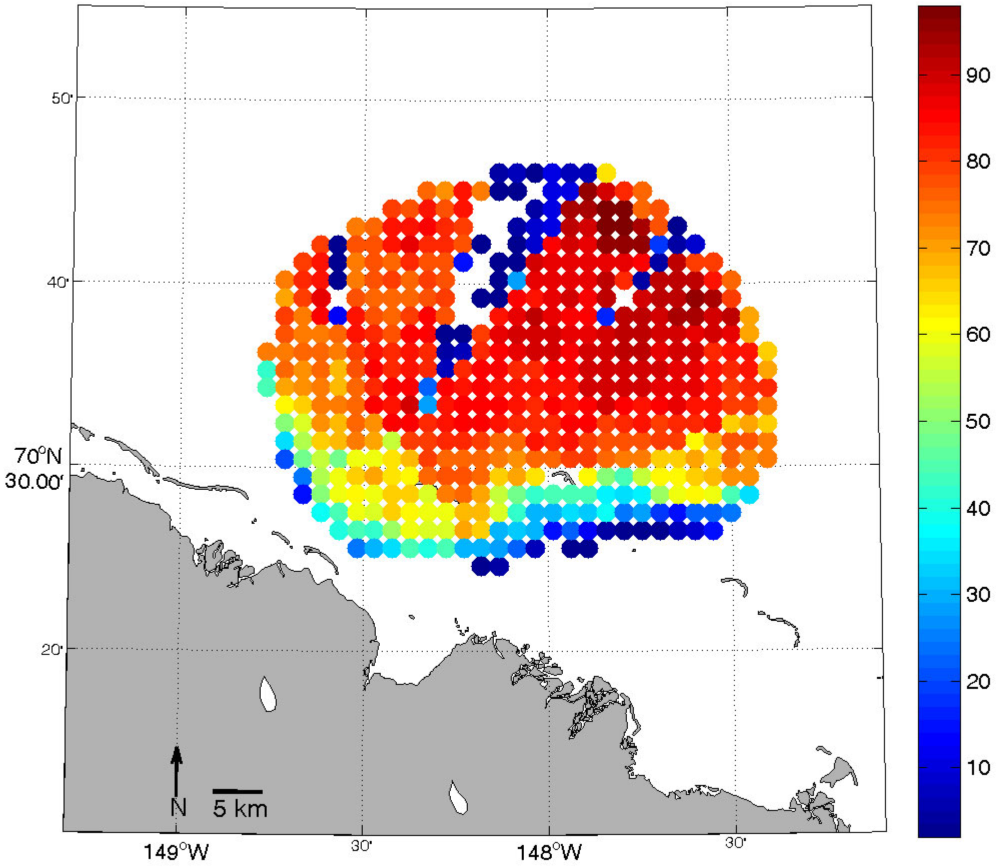

Figure 61. Percent coverage through time of two-dimensional HFR current returns from October 19 – 20, 2006.

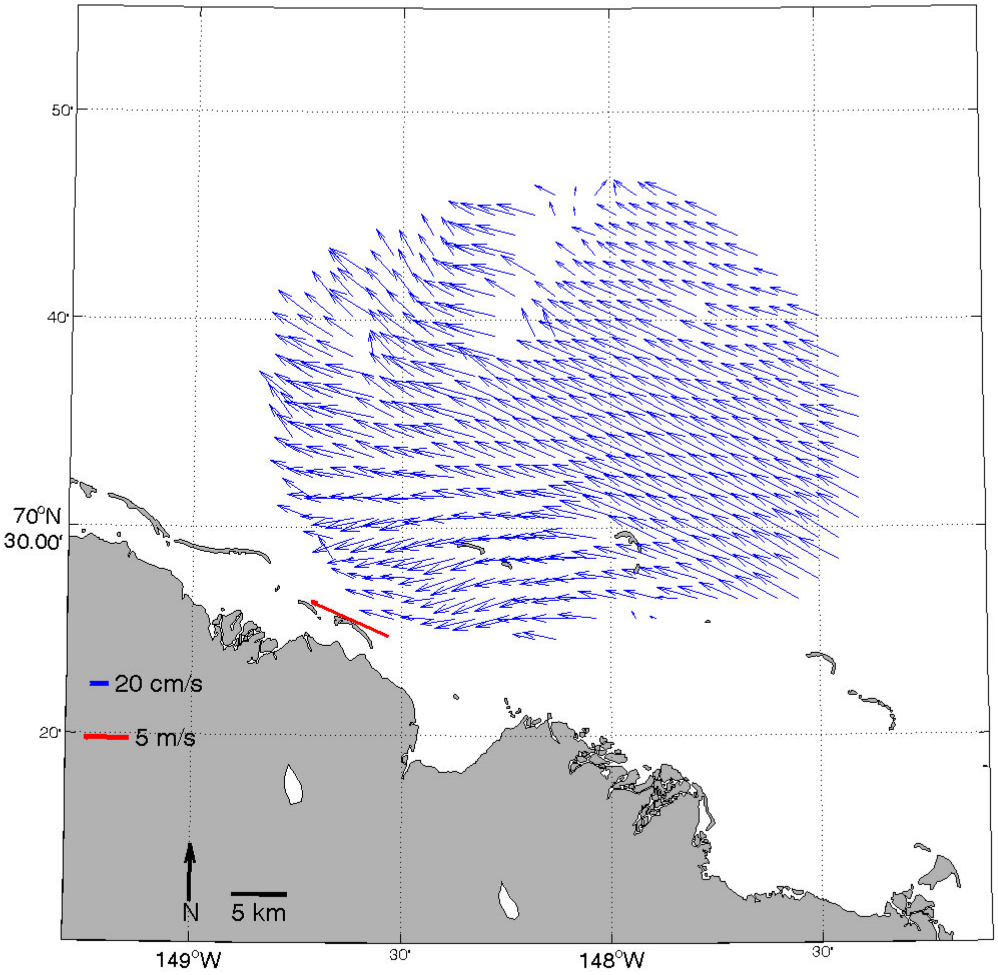

Figure 62. Mean current and wind speeds from October 19 – October 20, 2006.

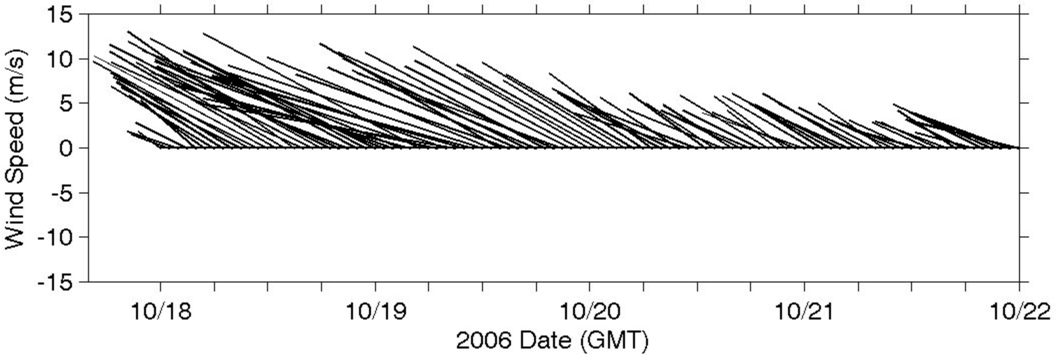

Figure 63. Time series of wind direction and magnitude for October 19 - 20, 2006.

To assess how well the HFR worked while ice was forming in the area, a more detailed view is presented with radial returns overlaid on SAR imagery. Only radials from Endicott are used in this analysis due to a power loss at West Dock in 2005 and failing receive antenna hardware at West Dock in 2006. The failing receive antenna made it impossible to identify data gaps due to hardware failure versus gaps created by the presence of ice.

2005 SAR imagery shows that landfast ice was beginning to form along the shoreline on October 10, but breaking waves hindered ice development. There was full coverage of HFR returns, and winds were ~16 m/s to the west (Figure 64). By the next acquired SAR imagery, October 13, landfast ice had expanded to the HFR baseline, which is defined by a straight line drawn between the two field sites at West Dock and Endicott. (In the baseline region, orthogonality between the radials from each site is not sufficient to create a two-dimensional current (Barrick 2002), so this area does not generate any two-dimensional surface current returns.) Winds were less than 5 m/s, aiding ice formation, as radial returns decreased from 03:00 to 17:00 UTC (Figures 65 and 66). Offshore of the landfast ice edge, grease ice was present in HFR coverage area, with concentrations of ice thickest inside the barrier islands. At 03:00 UTC Returns were recorded in open water beyond the grease ice, as well as near the barrier islands. Fourteen hours later,17:00 UTC, both areas of data return had diminished, likely due to the grease ice becoming dense enough to dampening the local wave field beyond the capability of the HFR. The last 2005 data returns were recorded at 23:00 UTC October 13.

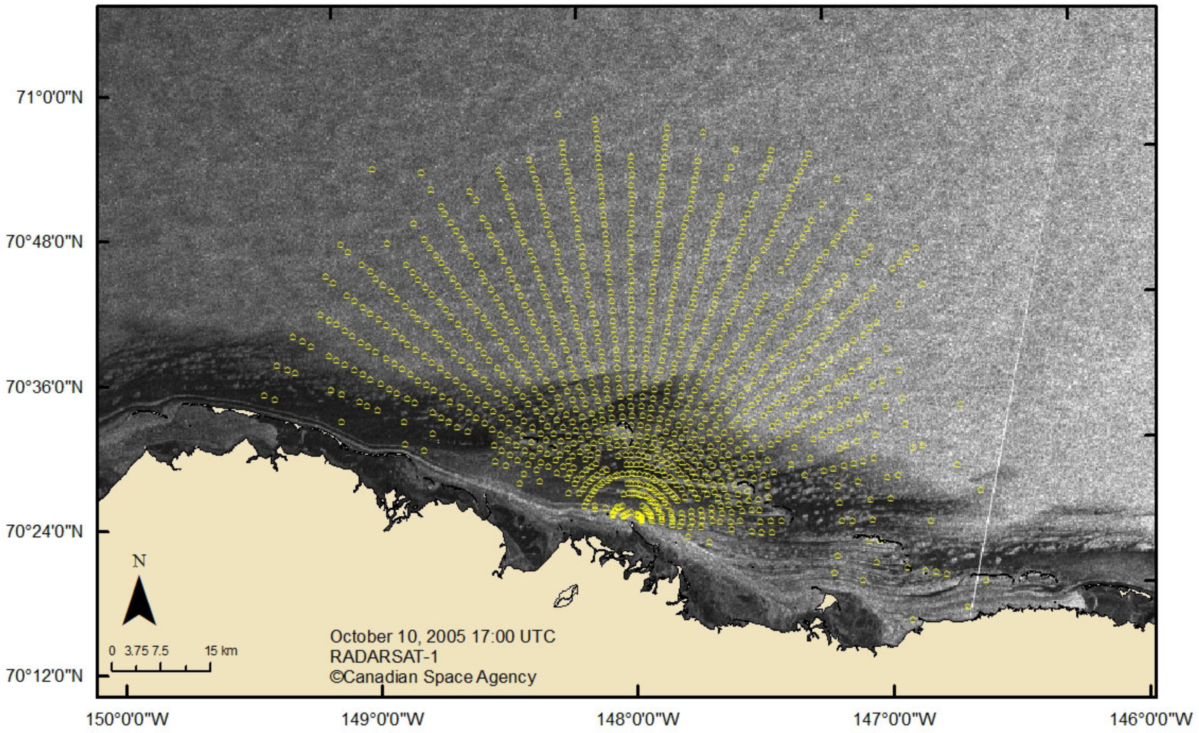

October 10, 2005 17:00 UTC
RADARSAT-1
©Canadian Space Agency

Figure 64. October 10, 2005, SAR image showing open water in the HFR coverage area. Yellow circles represent HFR data returns. Light gray areas near- shore represent both ice and breaking waves (recall from section 3.2 that SAR measures surface roughness). Winds were blowing westward >15 m/s.

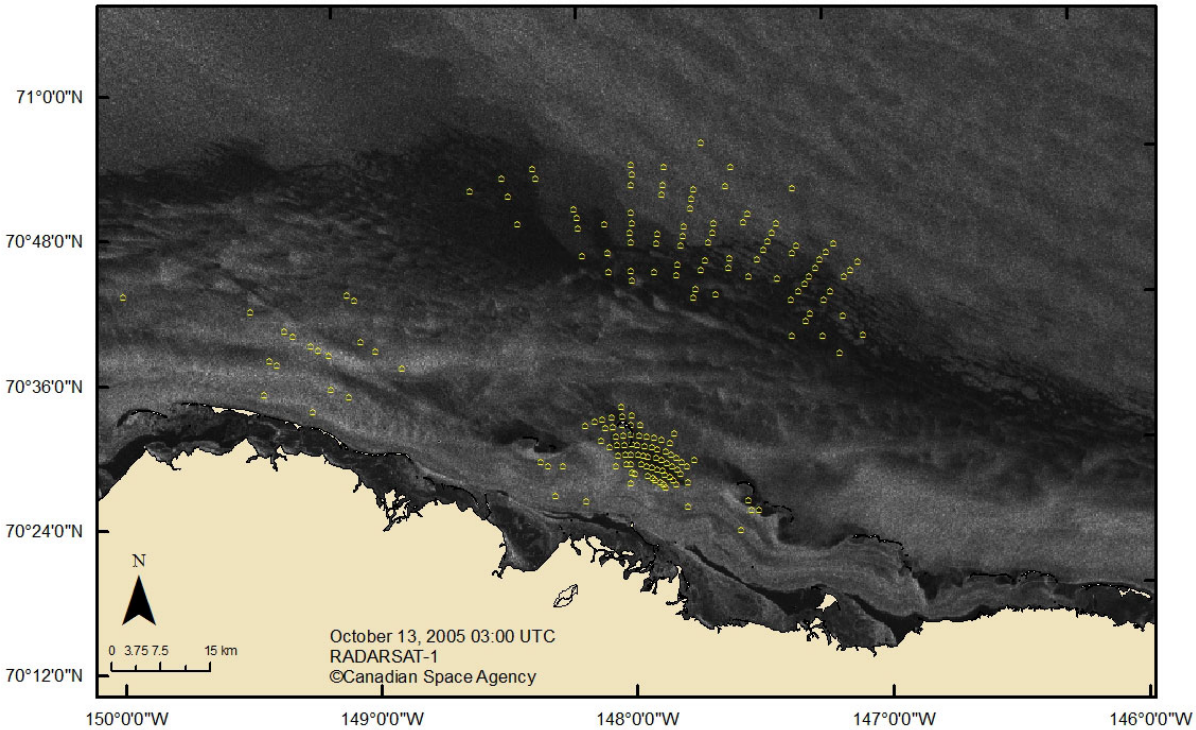

Figure 65. 03:00 UTC, October 13, 2005, SAR image. Yellow circles represent HFR data returns. Winds were blowing offshore ~ 2 m/s. Grease ice in HFR coverage area appears to be thickest shoreward of barrier islands.

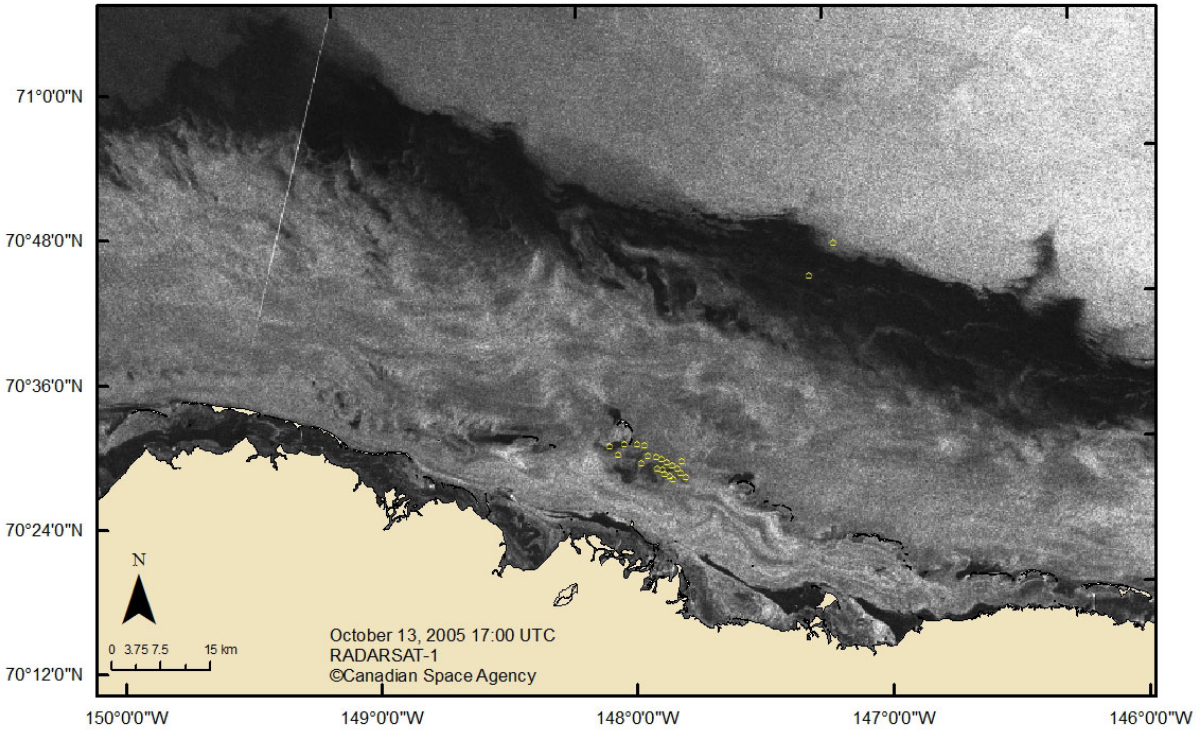

Figure 66. 17:00 UTC, October 13, 2005, SAR image. Yellow circles represent HFR data returns. Winds were blowing eastward at 1-2 m/s. Grease ice in HFR coverage area appears to be thickest shoreward of barrier islands.

Landfast ice formation in 2006 began on approximately October 12, 2006, with grease ice present along barrier island and causeways. These areas were not in the HFR radar mask, so with eastward winds at 12 m/s, full data coverage was returned (Figure 67). By October 15, the next available SAR pass, light winds were rotating clockwise from northwest to the east at ~3 m/s. The nearshore area inside of the barrier islands had been covered with grease ice, which along with light winds, appears to have damped the nearshore wave field beyond the detectable limits of the HFR, reducing the radar returns, but landfast ice had not yet extended into the HFR coverage area (Figure 68). Similar conditions still existed on October 18, when winds were again weak (~2 m/s to the northwest; Figure 69). One day later on October 19, landfast ice began to set up in the HFR field-of-view, but with winds to the northwest at ~13 m/s, ice was not effectively changing the coverage nor range of the HFR any differently than the presence of grease ice (Figure 70). Returns diminished until 00:00 UTC October 21, when no data was recovered, presumable due to the presence of sea ice although no SAR imagery is available for this time. There was a ten hour period on October 22, when northeastward winds increased to ~10 m/s and limited returns were recorded once again at Endicott before ending for the duration of the field season. Although it is known that landfast ice and grease ice were both present in the HFR radar mask on October 22 (Figure 71), without ice thickness measurements, a true determination of the utility of HFR use during landfast ice formation remains unknown.

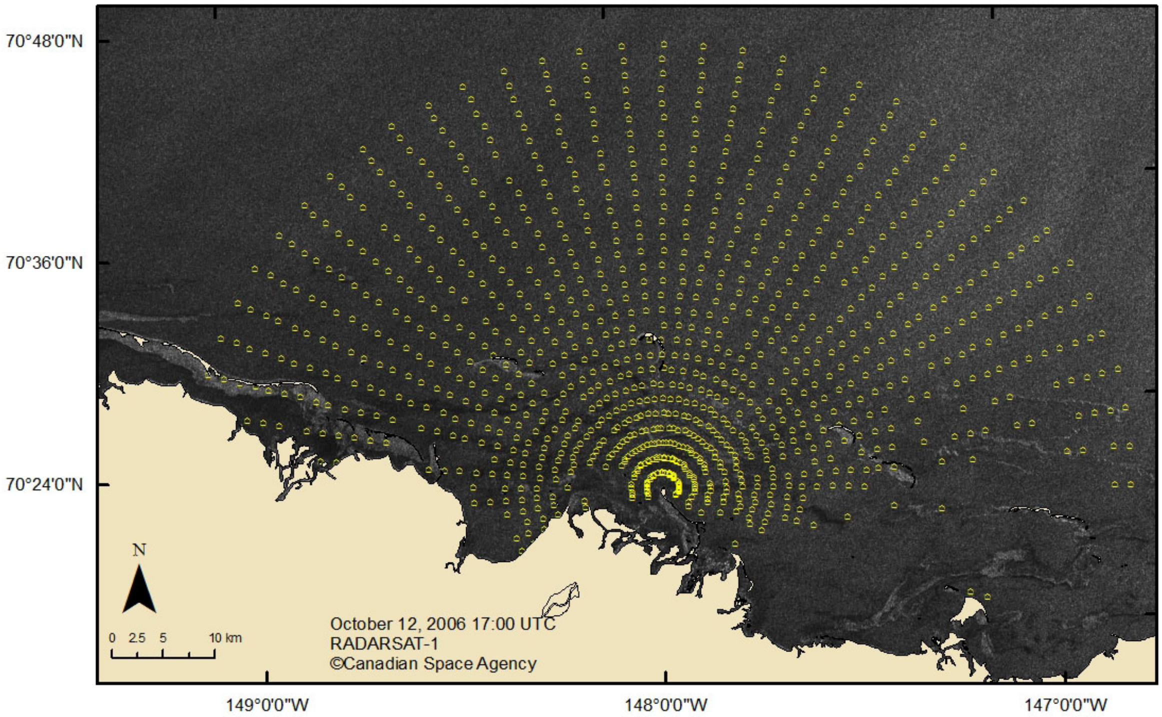

Figure 67. October 12, 2006, SAR image. Yellow circles represent HFR data returns. Grease ice is present along barrier islands and causeways. Winds were from the east at 12 m/s.

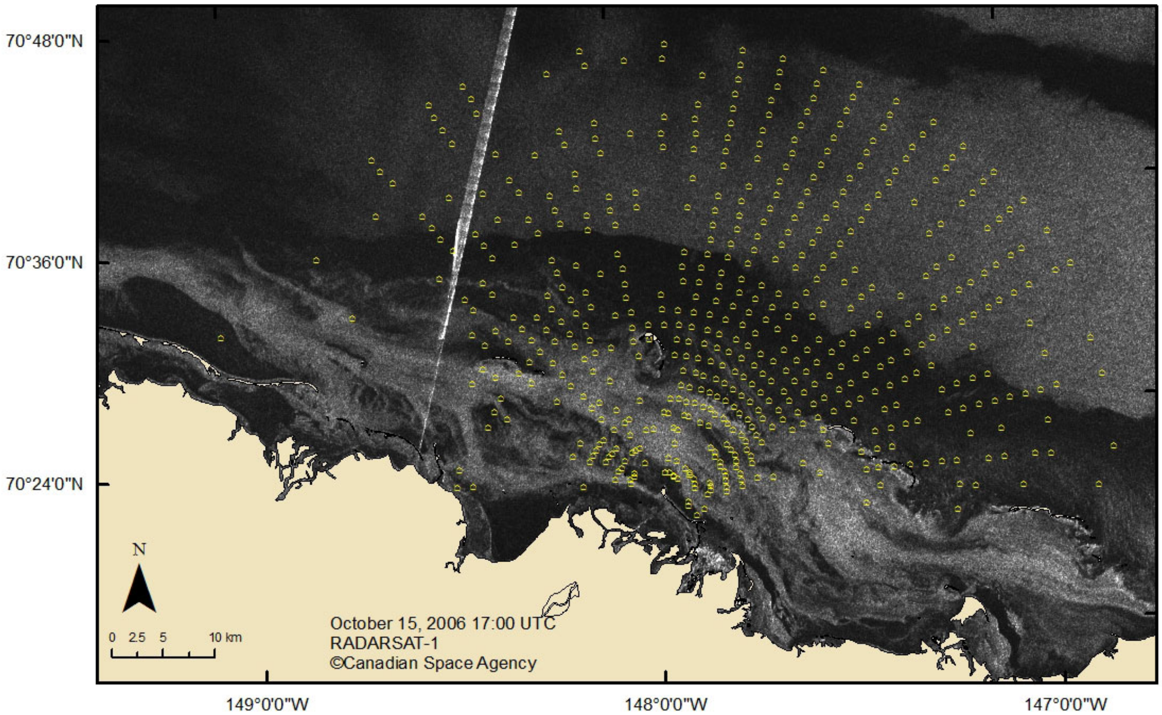

Figure 68. October 15, 2006, SAR image. Yellow circles represent HFR data returns. Winds were rotating clockwise from northwest to east at ~3 m/s. Nearshore area inside of the barrier islands is covered with grease ice. The landfast ice edge has not extended into the HFR coverage area.

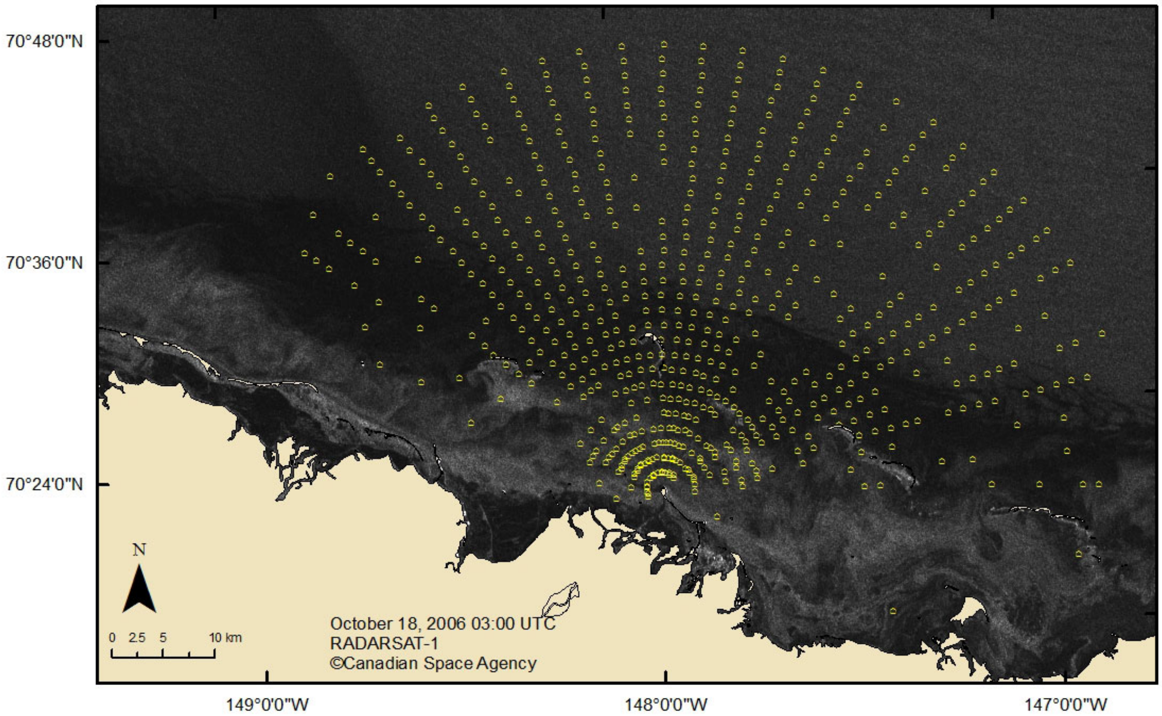

Figure 69. October 18, 2006, SAR image. Yellow circles represent HFR data returns. Winds were northwestward at ~2 m/s. Nearshore area inside of the barrier islands is covered with grease ice. The landfast ice edge has not extended into the HFR coverage area.

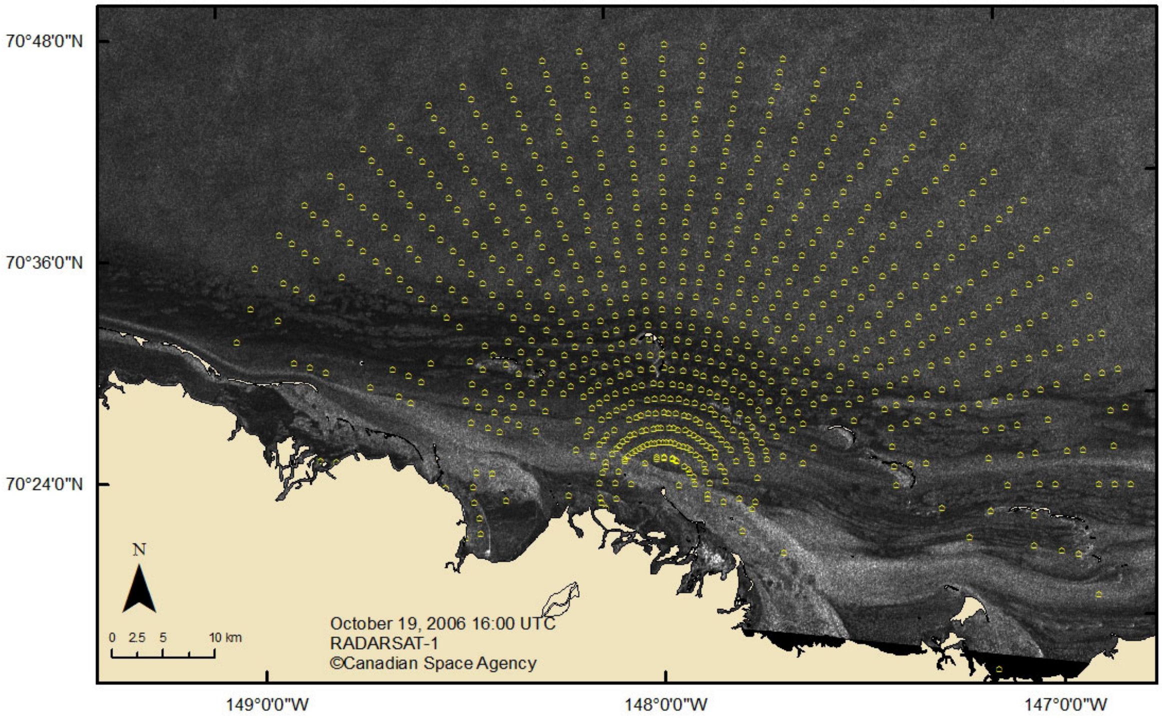

October 19, 2006 16:00 UTC
RADARSAT-1
©Canadian Space Agency

Figure 70. October 19, 2006, SAR image. Yellow circles represent HFR data returns. Winds were northwestward at ~13 m/s. Landfast ice edge has entered the HFR coverage area.

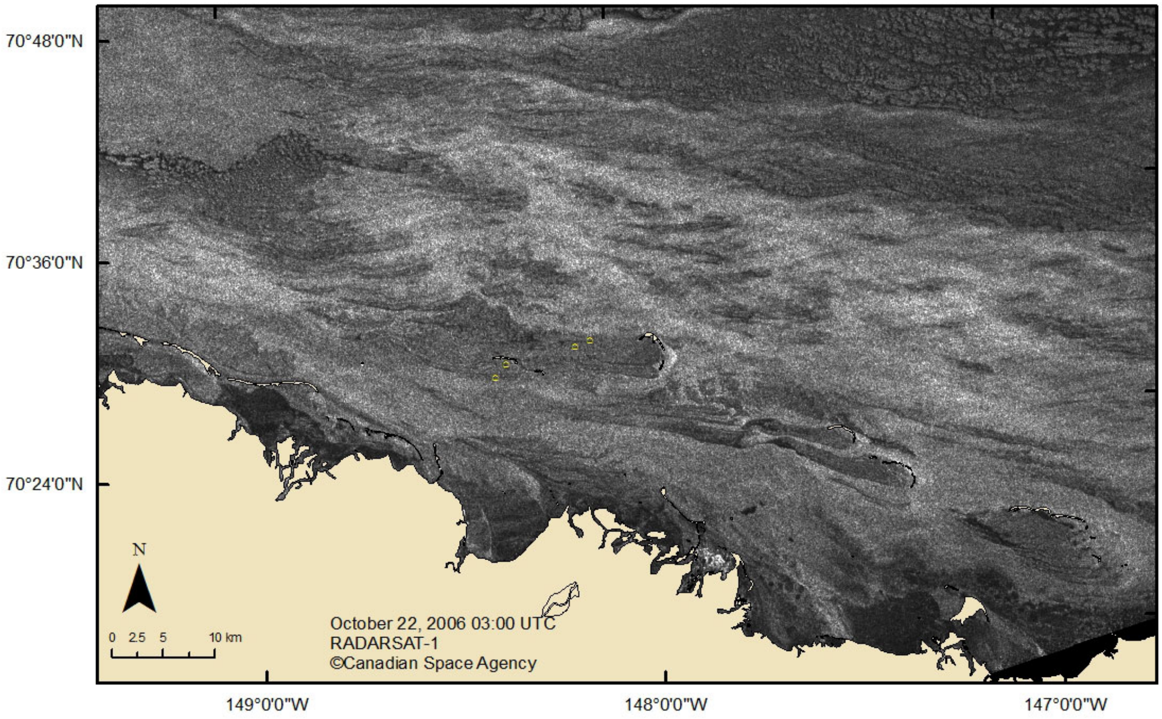

October 22, 2006 03:00 UTC
RADARSAT-1
©Canadian Space Agency

Figure 71. October 22, 2006, SAR image. Yellow circles represent HFR data returns. Winds were to the northwest at ~6 m/s. HFR area is completely ice covered.

3.5 Data Validation

To validate surface currents collected by the HFR, the surface bin of an upward looking Acoustic Doppler Current Profiler (ADCP) deployed near Cross Island (Weingartner et al. 2009) was compared with surface currents collected by the HFR. Both instruments were simultaneously operational from September 29 through October 20, 2006. HFR returns from the grid point nearest the current meter mooring location (Figure 72) were compared to the ADCP data and showed good agreement, apart from the storm event on October 9 when wind gusts reached 40 m/s (Figure 73). Even during this storm event, the along-shore velocities were comparable; however the cross-shore components differed substantially, e.g. the radar-estimated cross-shore currents were onshore at ~60 cm/s, whereas the ADCP cross-shore velocities were offshore at ~20 cm/s. Excluding the data from this storm event, linear regressions between the radar and ADCP along-shore and cross-shore velocities were statistically significant (r^2=0.93 for along-shore components, and r^2=0.70 for the cross-shore components; Figure 74).

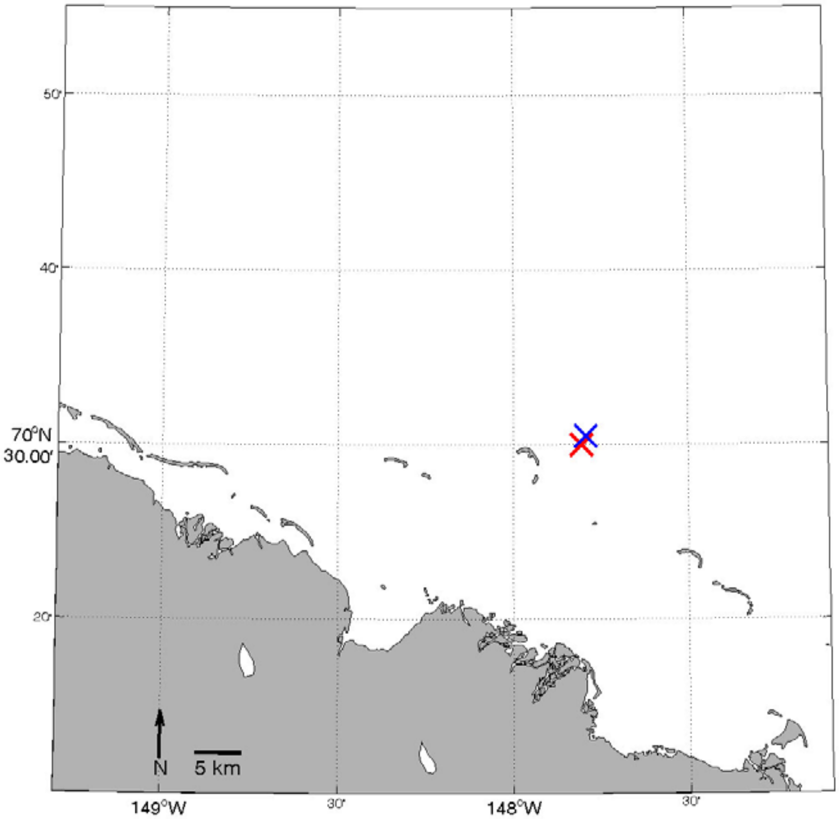

Figure 72. Location of moored upward-looking ADCP (red) and the nearest HFR grid point (blue) which were compared for data validation.

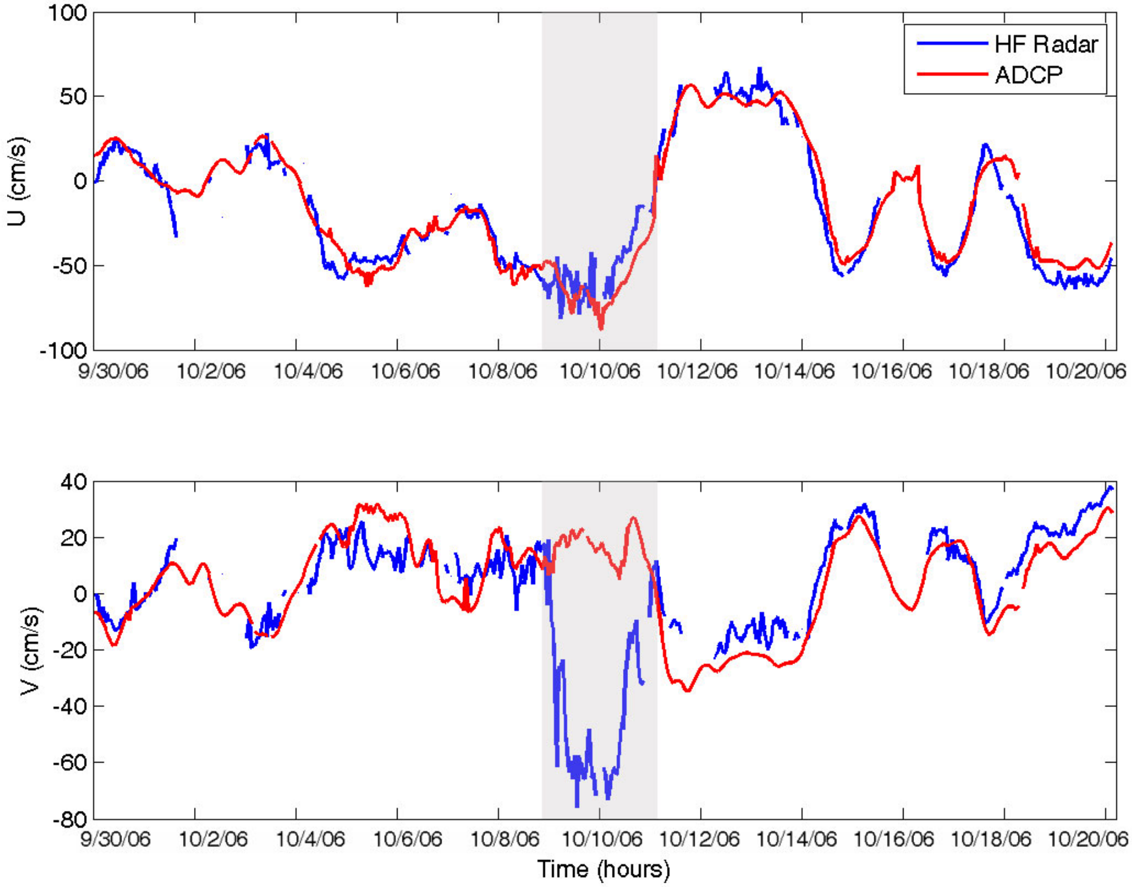

Figure 73. Time series of along-shore (u) and cross-shore (v) current components collected from the HFR (blue) and an upward-looking ADCP (red) located near Cross Island. Gray shaded area represents a storm event with winds gusting up to 40 m/s.

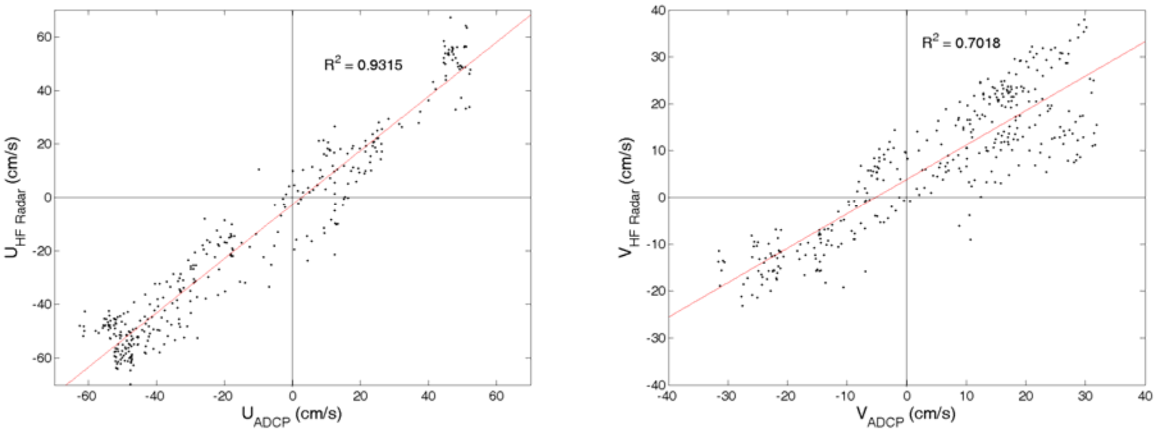

Figure 74. Linear regressions of the along-shore and cross-shore components of the HFR and ADCP, excluding data from the storm on October 9, 2006.

4.0 Discussion

The Beaufort Sea is a unique environment for HFR operations. Even after breakup, changing ice cover causes changing fetch conditions, affecting both wave generation and decay (via wave damping during passage through the ice). For example, open water bounded on all sides by land or ice, as occurs in regime one and inshore of the ice band in regime two, may be fetch-limited from all directions. Thus, the sea state may never fully develop, and remotely generated Bragg waves may not be present; therefore, the "Bragg" detected by radar waves must be generated by local winds. In such cases the wave field may quickly decay after the winds relax. In contrast, open ocean, fetch-unlimited conditions often support a consistent robust wave field because the wave field includes both locally and remotely-generated waves.

Comparisons between radar-derived current velocity components and those from the nearest surface bin of a bottom-mounted ADCP are in good overall agreement, proving the validity of HFR for applications in the Beaufort Sea. However, during the storm event on October 9, 2006, there were substantial discrepancies between the cross-shore velocity components estimated by the ADCP and radar. There are two possible reasons for this discrepancy. During storms and periods of high waves, signal to noise in the radar frequency spectrum decreases, making it difficult to separate the current from the wave speed. In addition, the HFR processing is based on small-amplitude, deep water wave theory. Under strong winds this assumption may fail, since the waves can be of large amplitude (non-linear), and if the water is sufficiently shallow, wave propagation may feel the bottom.

Radar data returns in the presence of ice were variable. Ice in the field-of-view directly impacted the HFR data, for the ice splits the first order peaks and, in the case of the ice band in regime two and when landfast or grease ice is present nearshore as in regime four, the frequency emitted from the transmit antenna potentially would not propagate as far offshore because ice attenuates the transmitted radar signal (Gurgel 2000). When ice was within 20 to 30 km of the shoreline as in regime one, HFR returns could extend to the edge of the ice if wind speeds were ≥5 m/s and had a significant along-shore component in direction. Returns were reduced in range when winds were cross-shore, variable, or <5 m/s. When the winds are cross-shore there is a fetch limited condition from the north due to ice cover and from the south due to land. Variable winds and/or winds less than 5 m/s do not appear sufficient to support the nearshore wave field necessary for HFR operations if ice is nearshore.

Similar results were found when the ice band was present (regime two). In 2005, data was collected on the offshore side of the ice band less than 10% of the time, which resulted in an insufficient sample to properly assess what environmental conditions were conducive to offshore returns. However, in 2006, data collection offshore of the ice band was more successful with 30% data returns. On September 8, only data inshore of the ice band was collected. While the reasons for this are not completely known, the width of the ice band likely hindered propagation of the radar signal; therefore only currents inshore of the band were detected. Winds prior to September 8 were weaker and variable (5 to 10 m/s), but on the 8th and 9th, sustained westward winds of ~10 m/s occurred. We speculate that this wind event compacted the ice band in width and allowed the radar signal to transmit across the ice; so that, in contrast to September 8, data returns on September 11 came only from offshore of the ice band. At the time, winds were blowing onshore (≤5 m/s), resulting in fetch limited conditions for waters inshore of the ice band. This resulted in no data returns in the nearshore range cells. On September 17 there were returns both on- and offshore of the ice band, and by September 21 returns covered the entire radar field-of-view. At this time the ice band was beginning to disperse and was thinning enough that the ice was incapable of suppressing the waves. In both 2005 and 2006, the ice band disappeared following storm events where wind speeds were in excess of 15 m/s.

Although our measurements were of limited duration, they underscore the importance of the winds in forcing the Alaskan Beaufort shelf circulation. Principal axes and EOF analyses show that for all ice regimes and in both 2005 and 2006 most of the current variance (~90%) is along-shore and that these wind-driven currents comprise most (~75%) of the along-shore current variance. This has considerable significance for the Alaskan Beaufort Sea shelf. For example, if we assume regime three conditions when fetch was unrestricted by ice and spatially uniform along-shore winds at 9 m/s for the approximately 25-day period from late September through late October 2006, then a water parcel would be transported westward ~17 km/day. This translates into an along-shore displacement of ~400 km in 25 days, which is a substantial fraction of the 600 km length of the Alaskan Beaufort shelf (between Pt. Barrow and Demarcation Bay). Results also imply that water mass properties on the shelf can be replaced rapidly by strong fall winds. For example, the westward flow documented in fall 2006 very likely advected relatively warm, fresh waters from the Mackenzie shelf into the central Alaskan Beaufort.

The along-shelf mass transport (*U*) across this inner shelf at this time can be estimated from the HFR velocity data as:

$$U = \int_{-h}^{0} \int_{0}^{L_y} u(y)\,dy\,dz \tag{1}$$

where *y* and *z* are the cross-shore and depth coordinates, *u* the surface current velocity determined from the radar (and assumed constant with depth), *h* the water depth (~20 m), and L_y is the width of the section between the coast and the offshore edge of the radar mask (~40 km). We estimate the transport to be ~160,000 m^3/s for late September-late October 2006. This estimate can be compared to a theoretical transport, assuming steady, spatially-invariant winds and the absence of an along-shore pressure gradient:

$$U = \int_{-h}^{0} \int_{0}^{L_y} u(y,z)\,dy\,dz = \frac{h\tau^x}{\rho r_b} L_y \tag{2}$$

where τ^x is the along-shore wind stress, ρ the seawater density, and r_b the linear bottom friction coefficient. Our data allow us to estimate r_b. For ρ = 1022 kg/m^3 and τ^x= 0.21 Nt/m^2, U = 160,000 m^3/s, if $r_b = 10^{-3}$ m/s. Typical values of r_b range between 10^{-4} m/s and 10^{-3} m/s, with the higher values associated with shallow waters. Hence theoretical and radar-derived transport estimates are in good agreement.

Reversals in wind direction are followed by rapid (within ~4 hours), reversals in surface current direction. Cross-shore currents are small in comparison to along-shore currents, and rapid wind reversals generally results in smaller cross-shore currents in comparison to more gradual wind reversals.

5.0 Future Work

HFR is a useful tool for measuring surface currents in coastal seas. While there were occasional problems with hardware, power supply, and EM interference with our HFR systems, the work here has extended the utility of this instrument to high-latitude, partially ice-covered seas. Most of the hardware problems were associated with developing corrections to the switchable frequency system. These problems were not anticipated but have been subsequently corrected; hence, they should not be future issues of concern.

Our ability to define the parameter space (e.g., the combination of ice cover and wave field) that permits HFR sampling within partially ice-covered portions of the radar mask was not fully resolved. To do so will require additional measurements of the wave field within and offshore of the ice-covered region, along with estimates of ice thickness, ice extent, fetch, and wind velocity. While relatively straightforward to do in principle, some luck is required since the "right" ice conditions need to exist within the HFR mask. Ice conditions vary tremendously from year-to-year, so it is hard to plan an experiment given this uncertainty.

Nevertheless, we believe that HFR operations in the Beaufort should, in general, include measurements of the ambient wave field in order to better understand variations in HFR performance. Historical wave measurements in the Beaufort have typically ended by mid-September, although the strongest storms occur later in the fall. Thus late fall wave measurements are useful not only for understanding HFR performance but in defining the wave climate of this shelf.

In addition, salinity measurements within the HFR field of view should be part of the additional suite of measurements made in the Beaufort Sea. As shown earlier the HFR is sensitive to surface salinities, and these can vary from 10 – 31 at the surface on seasonal and synoptic time-scales. Vertical salinity variations affect the stratification, which changes both seasonally and with wind direction. The surface current response is expected to vary with the stratification (Weingartner et al. 2009).

This project benefited enormously from the ability to power the HFR from oil field installations. Yet, this same benefit created problems (occasional power disconnects, variable EM interference due to vehicle and construction activities, and site selection limitations). Since this effort was completed, we attempted a subsequent HFR installation near Oliktok Point with funding provided by the National Ocean Partnership Program (NOPP). At the last minute this deployment had to be cancelled because the oil industry erected a large drill rig near the site. These problems can be avoided by developing autonomous power supply modules that would allow HFR deployments at optimal coastal locations, free of potential time-varying EM interference issues.

In summary, HFR has tremendous potential for use in the Beaufort Sea both for measuring the circulation and, in the event of an oil spill, as a real-time aid in guiding oil spill cleanup.

CHAPTER TWO - Cook Inlet

This study was designed to collect and map surface currents utilizing High Frequency Radar (HFR) in both the Arctic Beaufort Sea, where ice was present in varying concentrations, and in Cook Inlet, where very strong tides were an important environmental factor in the collection and analysis of surface currents. HFR data provides a real-time synoptic view of surface currents, rather than point source data available subsequent to recovery of oceanographic instrumentation, such as that provided by a mooring. Having high temporal resolution surface current data is critical for successful forecasting of contaminant spill trajectories and conducting search and rescue operations.

Chapter two of this report addresses the November 2006 through November 2007 deployment of HFR field sites in lower Cook Inlet under the U.S. Minerals Management Service Outer Continental Shelf program Contract #1435-01-04-CT-35579, Surface Circulation Radar Mapping in Alaskan Coastal Waters: Beaufort Sea and Cook Inlet including 1. introduction with regional setting; 2. methods; 3. results, including tidal variability; 4. discussion of the data; and 5. final conclusions. Beaufort Sea data from 2005 and 2006 are covered in chapter one. This study is the result of a U.S. Minerals Management Service research sponsorship meeting conducted under Contract #1435-01-02-CT-31150.

1.0 Introduction

The first Alaska deployment of an HFR system for mapping surface currents took place in Cook Inlet in July 1977 by NOAA Environmental Research Wave Propagation Laboratory (D. Barrick pers. comm.). This was a short-term test and demonstration of the utility of the CODAR HFR to map surface currents in real-time, which could aid in tracking pollutants. The next use of HFR in Cook Inlet was not until December 2002, when UAF researchers successfully measured surface currents in Upper Cook Inlet, south of the Forelands and east of Kalgin Island, through June 2003 (Musgrave and Statscewich 2006). Subsequently, the NOAA National Ocean Service carried out an installation in Lower Cook Inlet in the same location as this study in the summer of 2003. To our knowledge the results of this deployment have not been published. Surface currents collected by HFR in Cook Inlet are an asset to oil-spill risk analysis in Cook Inlet (W. Johnson et al. 2002)

1.1 Cook Inlet Regional Setting

Cook Inlet is located in the northwest corner of the Gulf of Alaska. Its length from the mouth at the tip of the Kenai Peninsula to its head, near Anchorage, is about 275 km (Figure 75). The upper inlet is about 30 km wide and extends northward from Nikiski for 75 km before dividing into Turnagain (southeast) and Knik (northeast) arms, each of which protrudes inland an additional 70 km. Depths in the upper inlet, including both arms, are ~40 m or less. Extensive tidal flats, usually exposed at low tide, border the area. Lower Cook Inlet is nearly 70 km wide and contains a 100 m deep channel along its central axis. The mouth of the inlet opens onto the

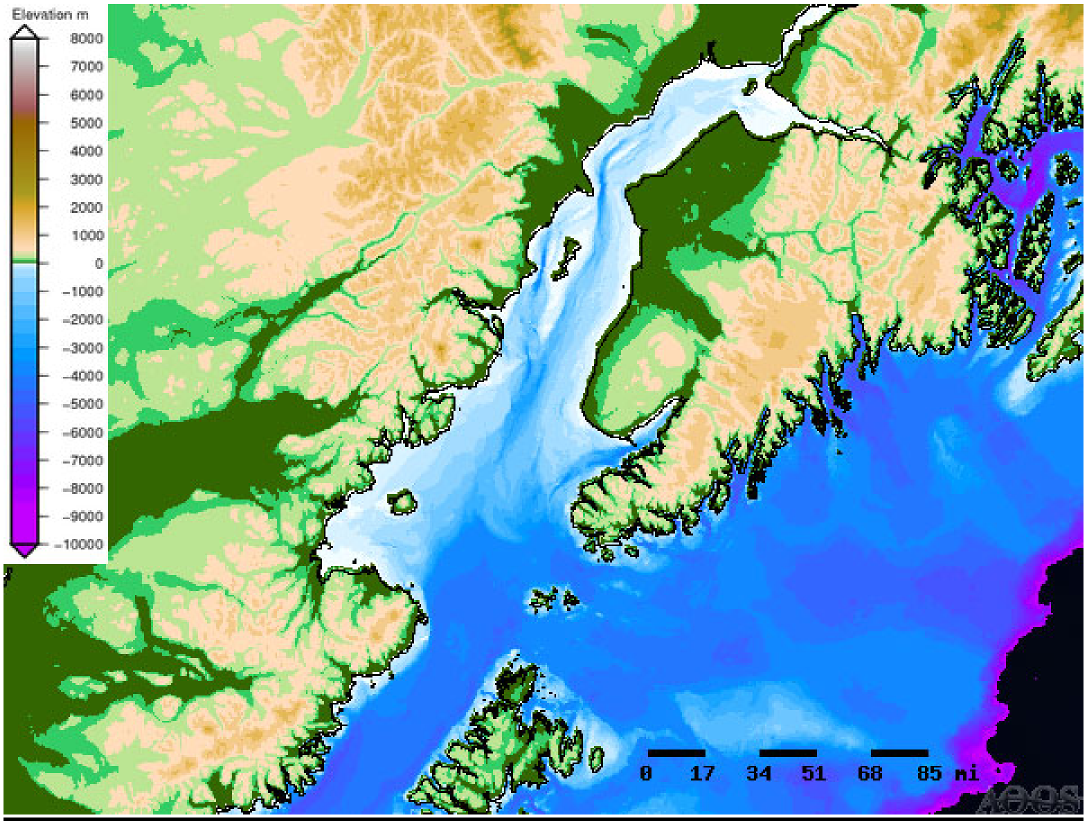

Figure 75. Bathymetric map of Cook Inlet and adjacent Gulf of Alaska.

Gulf of Alaska continental shelf at Kennedy Entrance on its eastern edge and Shelikof Strait to the southwest.

Numerous streams and rivers empty into the inlet, although few are gauged. Figure 76 shows the mean daily discharge curves for the Matanuska, Kenai, and Knik rivers for the period January 1, 2006, through October 31, 2007. Figure 76 also includes the mean monthly runoff from the Susitna River, located just west of the entrance to Knik Arm. The Susitna is the largest river discharging into Cook Inlet but was not gauged during this study. Discharge is minimal from November through April and peaks in late July. More than 85% of the annual discharge occurs from June through September. Seasonally-varying discharge affects circulation by establishing laterally varying water density gradients that can propel currents and establish fronts. Freshwater also affects the vertical stratification and thus the vertical structure of sub-tidal and tidal currents. In the absence of tides and winds, the river outflow will tend to turn to the right upon exiting the river mouth due to the influence of the Earth’s rotation; however, tides and winds can affect dispersal of the river plume waters.

Prevailing southward winds and casual perusal of satellite imagery (ocean color, sea surface temperature, and ice maps) suggest that the bulk of the freshwater outflow is carried southward along the western side of Cook Inlet in a buoyant coastal current (Figure 77). In addition to buoyancy, the regional wind field exerts an important influence on the Inlet’s circulation (Johnson 2008). In general, coastal mountains bordering Cook Inlet exert a channeling effect on the winds, with winds blowing primarily up or down the inlet. Cook Inlet is also seasonally influenced by sea

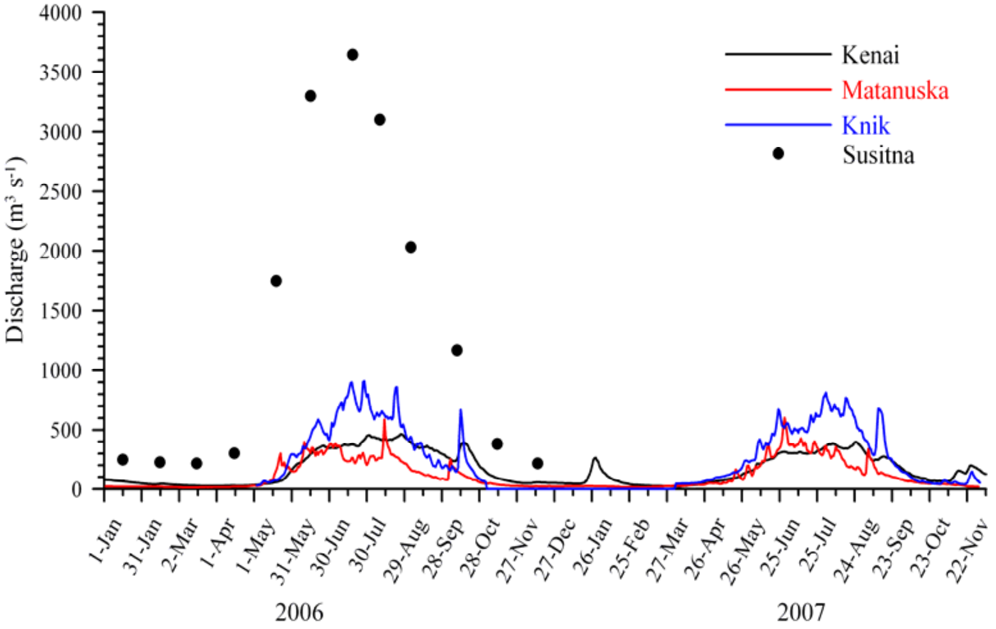

Figure 76. Mean daily discharge (solid lines) from January 1, 2006, through October 31, 2007, for several of the major rivers emptying into Cook Inlet and the mean monthly discharge (filled circles) for the Susitna River at the head of Knik Arm for the period 1975-1993.

Figure 77. May 19, 2007, MODIS visible satellite image. Notice the brown suspended sediment in the Upper Inlet that is transported southward along the western side of the lower Inlet.

ice, which extends southward from the northernmost extents, with the heaviest ice concentrations confined to the western side of the inlet. Ice seldom extends along the entire inlet and is generally confined to north of Ninilchik. However, during unusually cold winters sea ice can extend along the entire length of the inlet.

The Gulf of Alaska shelf exchanges waters with Cook Inlet, primarily via the Alaska Coastal Current (ACC). The ACC has a typical width of 35 km and originates on the British Columbia shelf, although in some months or years it might originate as far south as the Columbia River (Thomson et al. 1989; Royer 1998). A portion of the ACC flows through Prince William Sound with ACC waters entering the sound through Hinchinbrook Entrance and exiting through Montague Strait (Niebauer et al. 1994). The remainder of the current continues across the mouth of Hinchinbrook Entrance, southwestward along Montague Island, and thence westward after rounding the southern tip of Montague. West of Montague Island, this branch of the ACC and the outflow from Montague Strait merge to continue westward along the south coast of the Kenai Peninsula. The ACC apparently splits northeast of Kodiak Island (Stabeno et al. 1995) with some of the current flowing southward along the shelf east of Kodiak Island. However, most of the current curves around the mouth of Cook Inlet before continuing southward through Shelikof Strait (Muench et al. 1978 and Muench et al 1981; Figure 78). As it arcs across the mouth of the inlet, flow-topography interactions induce upwelling and locally strong tides mix salty, nutrient-rich water to the

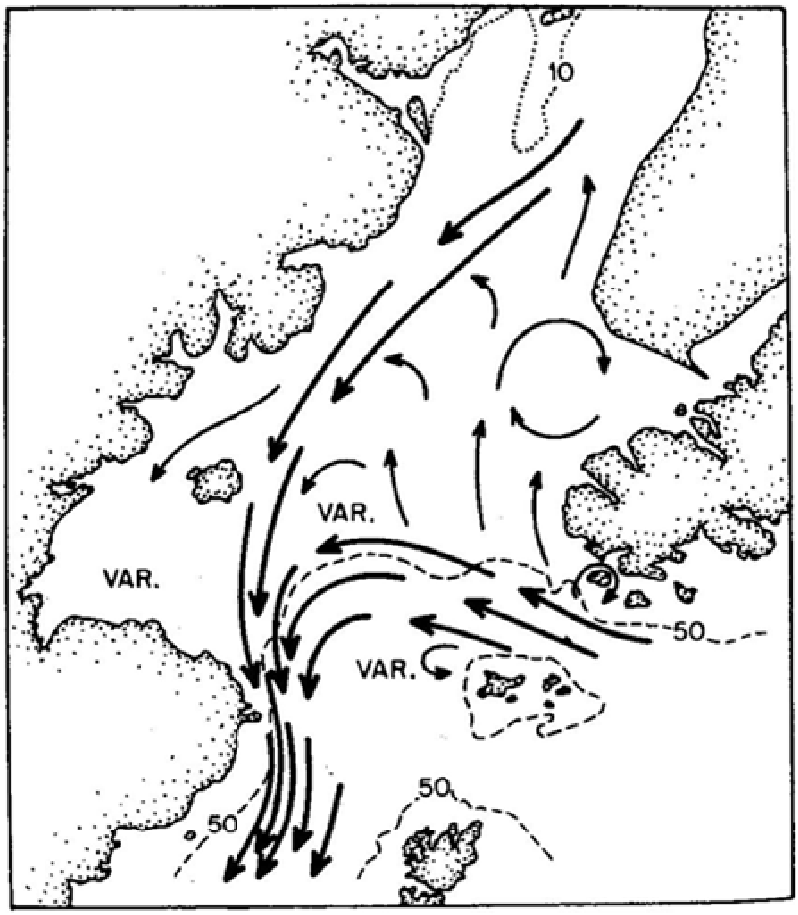

Figure 78. Summer circulation in Lower Cook Inlet (Muench et al. 1978)

surface. Some of this upwelled water flows northward, supplying nutrients and salt (and possibly heat in winter) along the eastern shore of Cook Inlet. This inflow is gradually mixed by tides with freshwater from the rivers that enter along the sides of the inlet to forming a dilute southward flow along the west side of Cook Inlet. The outflow then re-joins the ACC at the head of Shelikof Strait. To the west of Cook Inlet it flows southwestward to Unimak Pass in the western gulf, where it leaves the Gulf of Alaska shelf and enters the Bering Sea (Schumacher et al. 1982; Stabeno et al. 2002). The ACC was the principal vehicle by which oil released from the Tanker Exxon Valdez was transported into Cook Inlet and southward through Shelikof Strait in March 1989 (Royer et al. 1990).

A more extensive view of Cook Inlet's surface circulation can be found in Figure 79 (Burbank 1977). The schematic shows strong rip currents in central Cook Inlet as well as the ACC briefly entering Lower Cook Inlet through Kennedy Entrance and leaving through Shelikof Strait. There are three known rip currents in Cook Inlet, a western rip current, a mid-channel rip current, and an eastern rip current, all of which occur primarily north of Anchor Point, up to the East and West Forelands (Haley et al. 2000), although the mid-channel rip continues as far south as the mouth of the Inlet (Okkonen and Howell 2003).

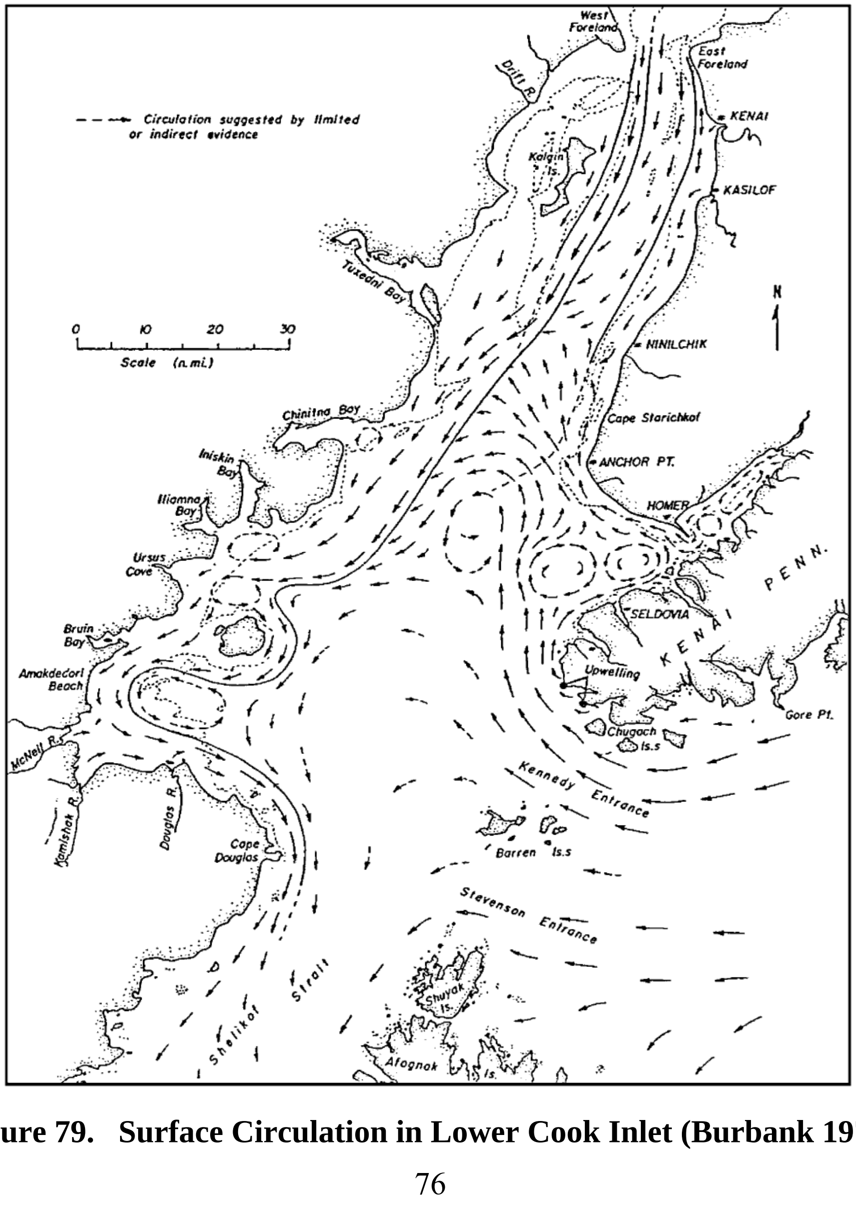

Figure 79. Surface Circulation in Lower Cook Inlet (Burbank 1977).

The bathymetry in Lower Cook Inlet is somewhat complex (Danielson et al 2008; Figure 80), with a deep shipping channel (~100 m) entering from the north at the middle of the inlet, and another deep channel (~100 m), Jakolof Trench, entering from Kachemak Bay on the eastern side. Waters on the west side of the lower Inlet, near and around Augustine Island, are relatively shallow (<40 m), as are the waters in the northeast, near Anchor Point. We have labeled troughs in the center of the Inlet for identification purposes.

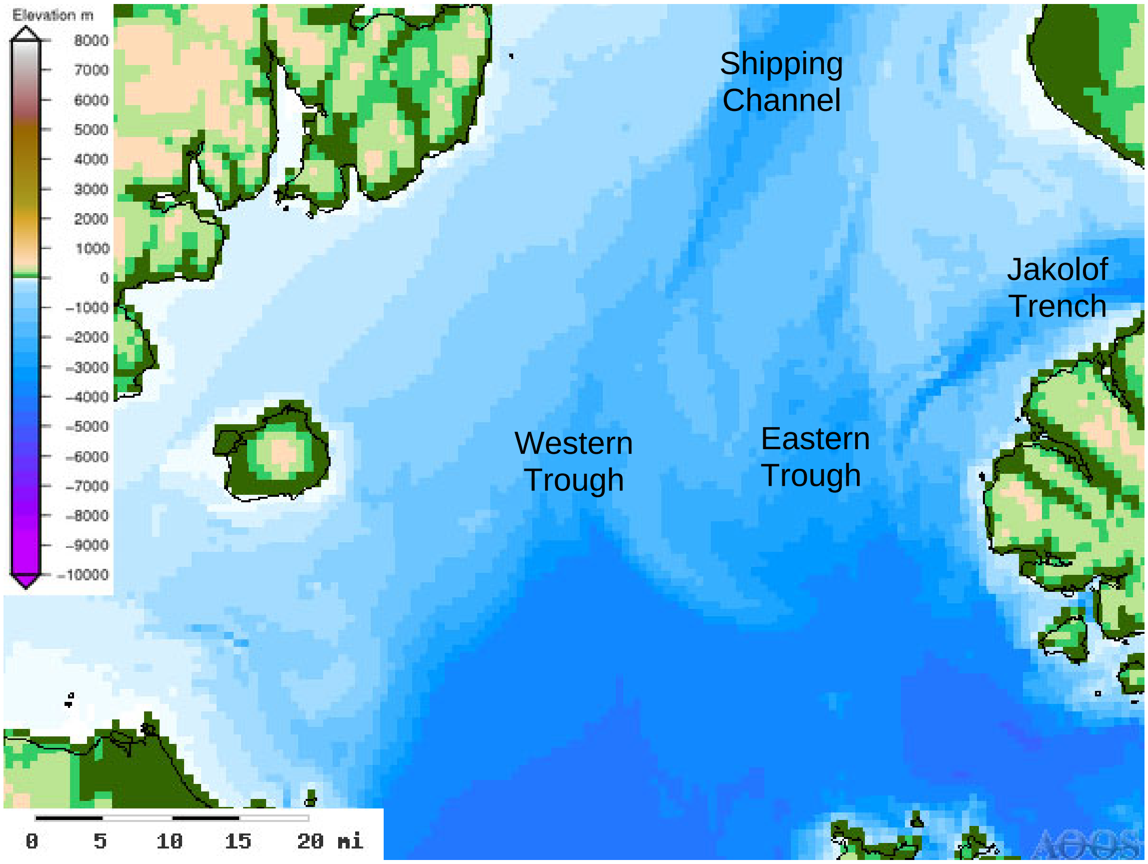

Figure 80. Bathymetric map of Lower Cook Inlet.

2.0 Methods

In November 2006, the two HFR systems from the Beaufort Sea were moved to southern Cook Inlet, more specifically to the community of Anchor Point and the Alutiiq village of Nanwalek (Figure 81), for a 12-month deployment to measure real-time ocean surface currents at high spatial and temporal resolution. Each site consisted of a transmit antenna, receive antenna, receive/transmit electronics, and backup battery power. The electronics were housed in existing onsite structures (Figure 82), and each site had dedicated internet communications: DSL in Anchor Point and village wireless in Nanwalek.

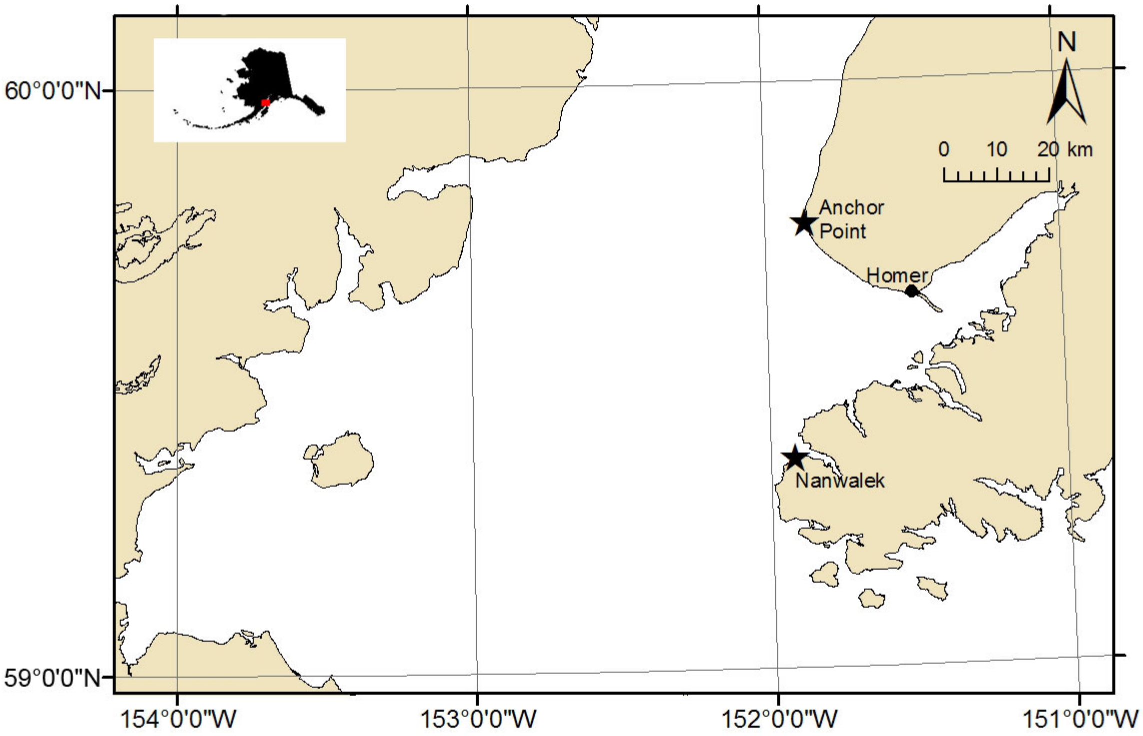

Figure 81. Black stars show locations of the HFR sites in Cook Inlet, Alaska. The northern site was located in Anchor Point, and the southern site was located in the Alaska Native village of Nanwalek.

Figure 82. Onsite housing for electronics at Anchor Point. The Kyllonen cabin was wired for both electricity and DSL internet.

The two 13 MHz HFR field sites were separated by a distance of approximately 50 km and operated from November 12, 2006, through November 10, 2007. The ~60 km offshore coverage of Cook Inlet at 13 MHz radar spans the width of the inlet at the latitude of Anchor Point and to Augustine Island at the latitude of Nanwalek (Figure 83). These distances are dependent on environmental conditions such as wind, wave field, sea surface salinity, presence of sea ice, and ambient radio noise sources.

2.1 Defining Cook Inlet Spectra

Raw cross spectra from Cook Inlet were processed using the same methods as those of the Beaufort Sea (Chapter One Section 2.1 and 2.2). There were instances where first order peaks were split due to high current shear within a range cell, and ice extent in the winter of 2006/2007 extended south of Anchor Point, necessitating further evaluation of the spectra files. In the case of high current shear, the first order peak may split due to the large discrepancy of current speeds within a single range cell. One peak defines the higher magnitude current, while the other equally valid peak defines the lower magnitude current.

Figure 83. Typical two-dimensional coverage of the HFR in Lower Cook Inlet at 13 MHz.

2.2 Antenna Pattern Measurement

Antenna pattern measurements to calibrate the HFR system were conducted in Cook Inlet in the same manner as the Beaufort Sea (Chapter 1 Section 2.3). In Cook Inlet there was a rather clean environment which returned loops with minor interference (Figure 84).

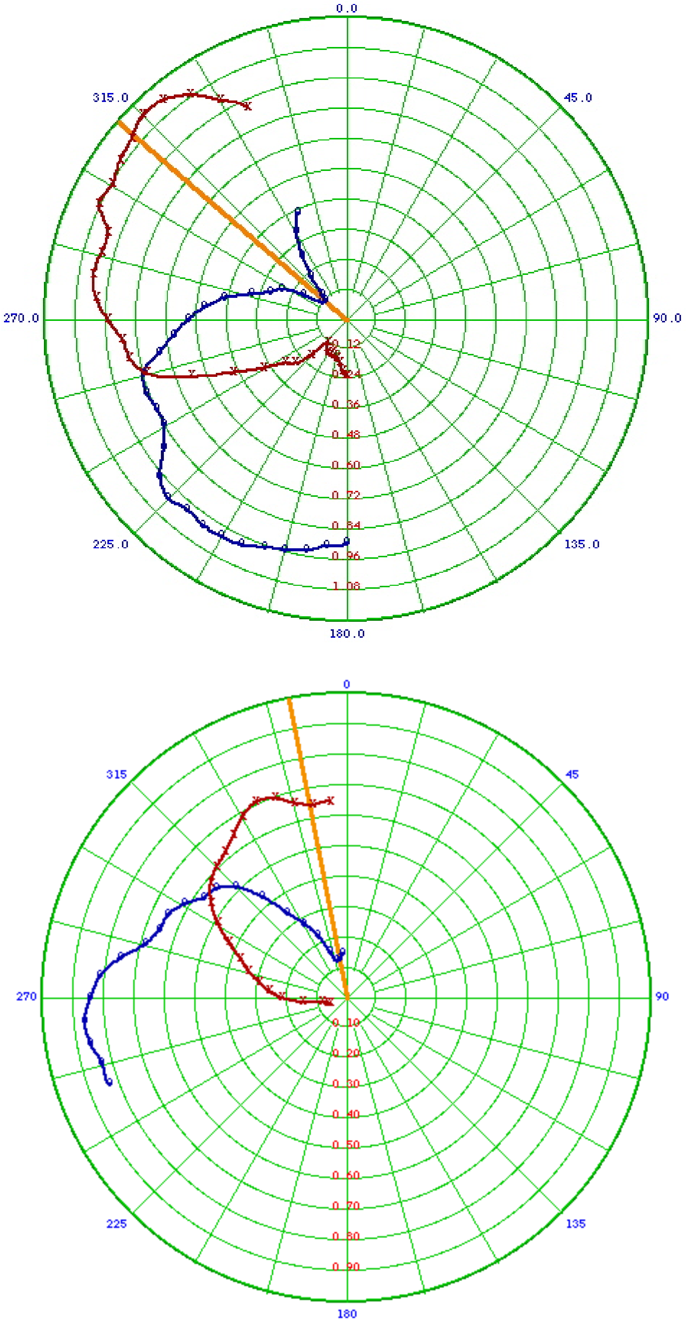

Figure 84. Results of the 13 MHz antenna pattern measurements performed in Cook Inlet for Anchor Point (top) and Nanwalek (bottom).

This does not mean that Cook Inlet data was free of interference from outside sources. In mid-March 2007 a persistent periodic noise source developed in the Nanwalek spectra. Data each day from approximately 00:00 through 06:00 UTC was contaminated by radio frequency interference. We tried transmitting at several different nearby frequencies to try to isolate the noise source, but the interference persisted. After further investigation, hardware malfunction was also ruled out as a cause. The noise persisted at the same time every day through mid-September, and although the source was never identified, we believe that it came from an external source, such as broadcasts, on or near the same frequency, of such high power that the transmissions were interfering with the receive antenna. Don Barrick, CODAR Ocean Sensors, commented that radio noise sources from broadcasters are commonly voice; however the sources are not normally local. The energy gets transmitted by skywave from a thousand kilometers or more away. Such interference is rarely present 24 hours per day, as the broadcasters typically stay on a frequency for 3 to 4 hours maximum; however this varies with location and situation. A second theory is that the interference could have been from the use of marine single side band radios on fishing boats, which operate on the same range of frequencies used on the Nanwalek radar. Many boats have poor radio installations or poor antenna connections, thereby generating significant noise.

3.0 Results

From November 2006 through November 2007, the Nanwalek and Anchor Point field sites were operational 84% and 99% of the time, respectively (Figure 85). After initial installation on November 11-12, 2006, a faulty receive antenna at Anchor Point and problems with high reflected power at both sites became apparent. High reflected power means that most of the power produced by the transmitter was being reflected back to the transmitter rather than radiated seaward. This generates unwanted heat, which can be harmful to the SeaSonde electronics. The high reflected power was corrected by installing a balun, which has two functions: (1) To simulate a transformer at terminals with two different impedances, so that no reflections will occur and (2) to ensure that radiating electric currents do not flow into the system electronics (CODAR Ocean Sensors 2006). These issues were resolved by November 26, 2006.

Additional downtime at Anchor Point was minimal and caused by internet connectivity issues that could not send data from Anchor Point to Fairbanks. Nanwalek downtimes consisted of two problems with the SeaSonde hardware, which were subsequently rectified. The first was in February 2007, when the receive electronics were no longer being recognized by the software due to the system DC power dropping out when the transmitter was turned on. The second, in late September 2007, was an issue with the software on the Nanwalek computer that resulted in the laptop needing to be completely erased, reinstalled, and configured to rectify the problem.

Data density within the HFR grid mask shows a majority of the returns (>60%) in the eastern portion of Cook Inlet, surrounding the mouth of Kachemak Bay. Returns from the northwestern region of the mask decrease to <10% nearing the western shoreline, and to the west toward Augustine Island (Figure 86).

Anchor Point Operational Timeline

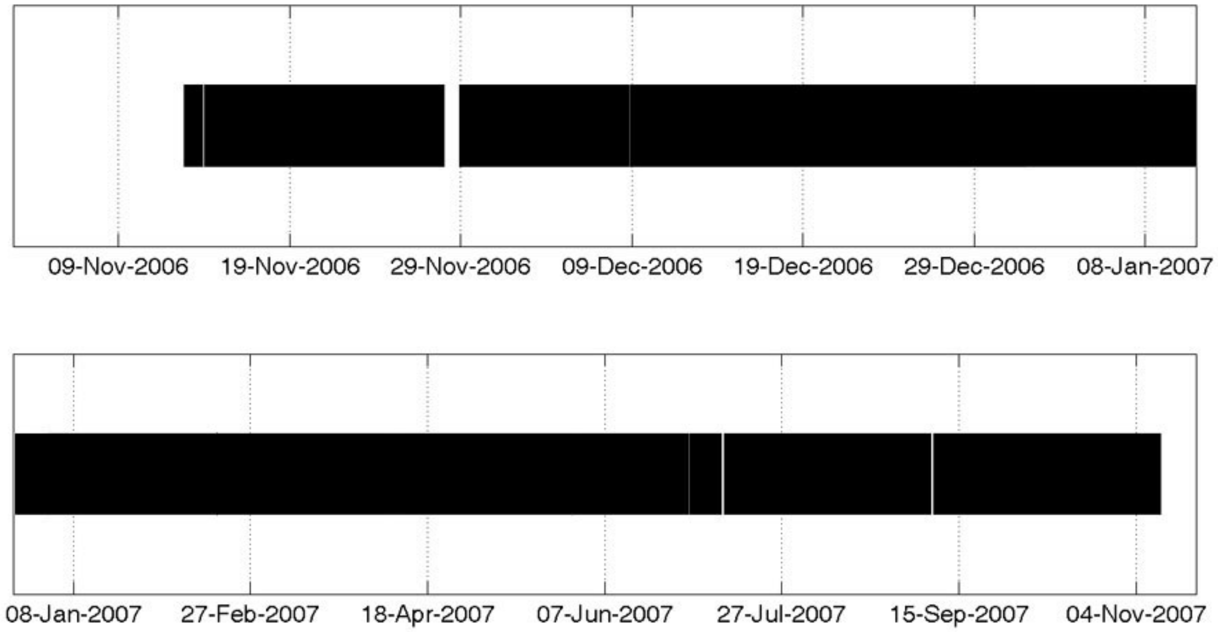

Nanwalek Operational Timeline

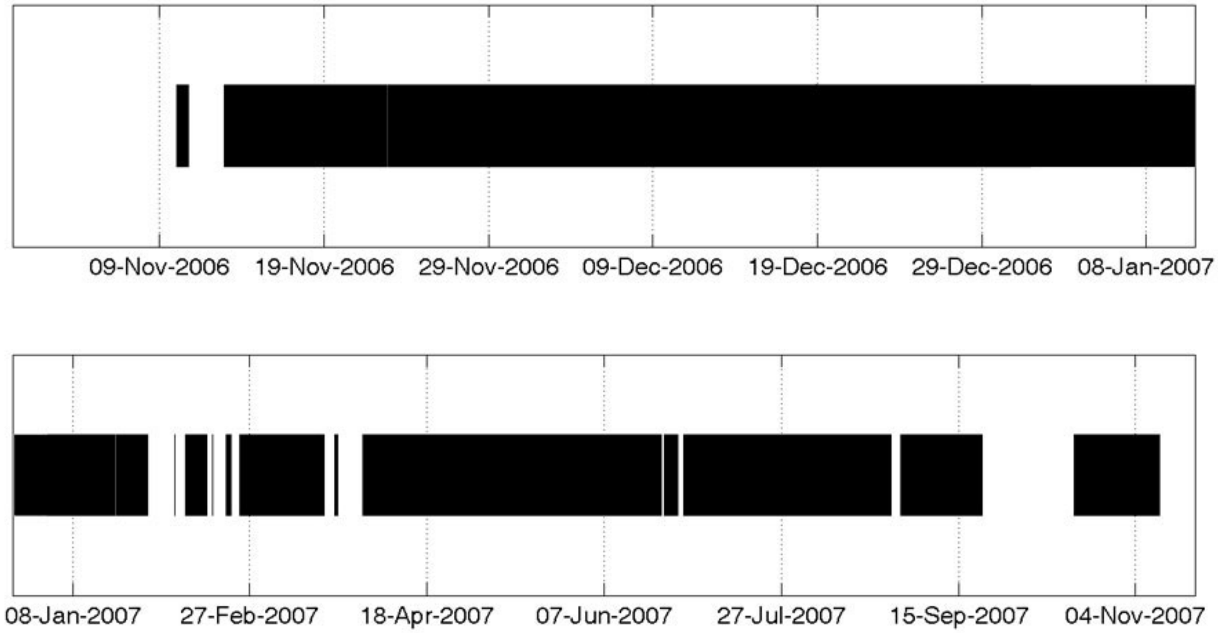

Figure 85. Operational timelines for Anchor Point (top) and Nanwalek (bottom) field sites. Where the black bar is filled, systems were operational, and where there are gaps, the system was not operational.

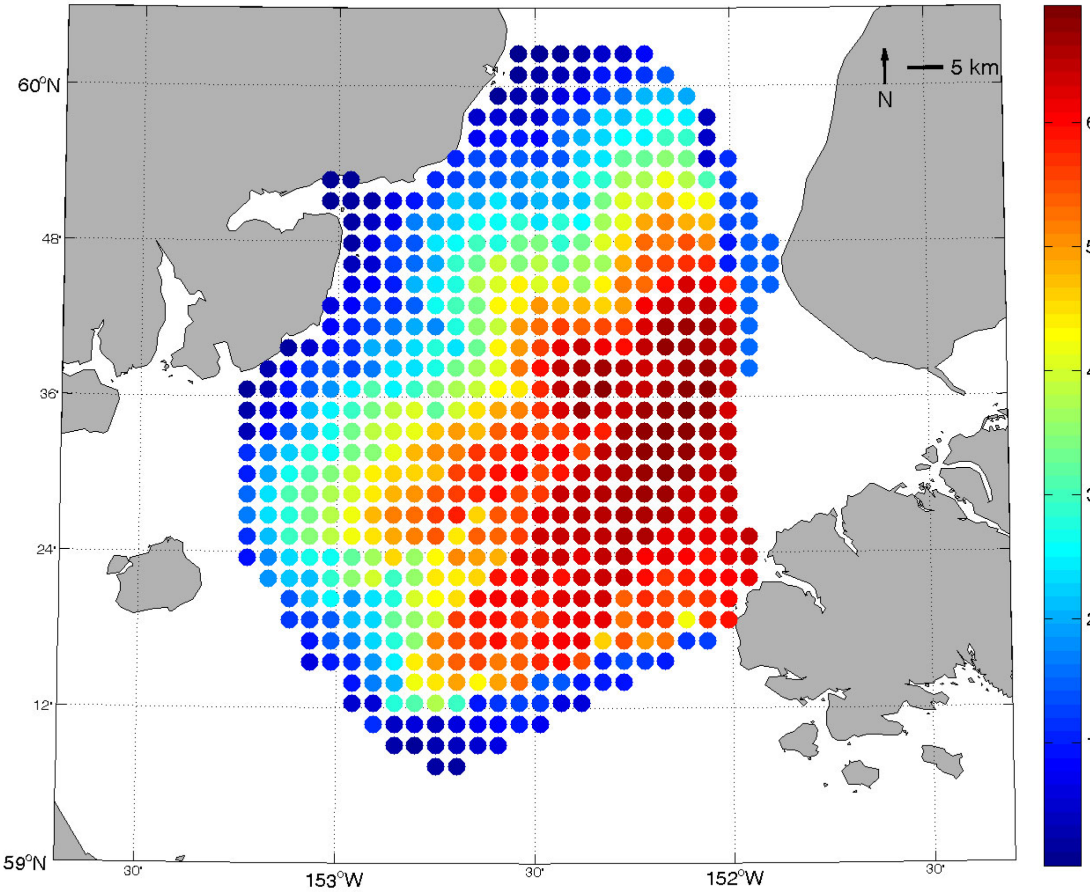

Figure 86. Percent coverage through time of two-dimensional HFR current returns from November 12, 2006, through November 10, 2007.

3.1 Winds

Based on a review of Quick Scatterometer mean weekly wind fields for the period October 2006 through October 2007, we find that near the mouth of the Inlet 73% of winds are southeastward from October through March; 20% of the winds are to the southwest, and 7% of the winds are southward. Typical wind speeds are about 10 m/s. Winds are weaker and more variable from April through September. Westward winds blow ~40% of the time, while northward and eastward winds occur 31% and 20% of the time respectively. Southward and southeastward winds account for the remaining 11%. Meterological stations on Augustine and Flat Islands, operated by the National Data Buoy Center, show similar results and are used in Section 3.5.

3.2 Ice

On March 1, 2007, sea ice entered the coverage area of the HFR current returns from the northwest and persisted through April 1 (Figure 87). The ice is likely grease ice, similar to that which formed in the HFR coverage area in the Beaufort Sea as the landfast ice set up (Chapter 1 Section 3.4.4). Ice resided on the western side of Lower Cook Inlet, although varied somewhat

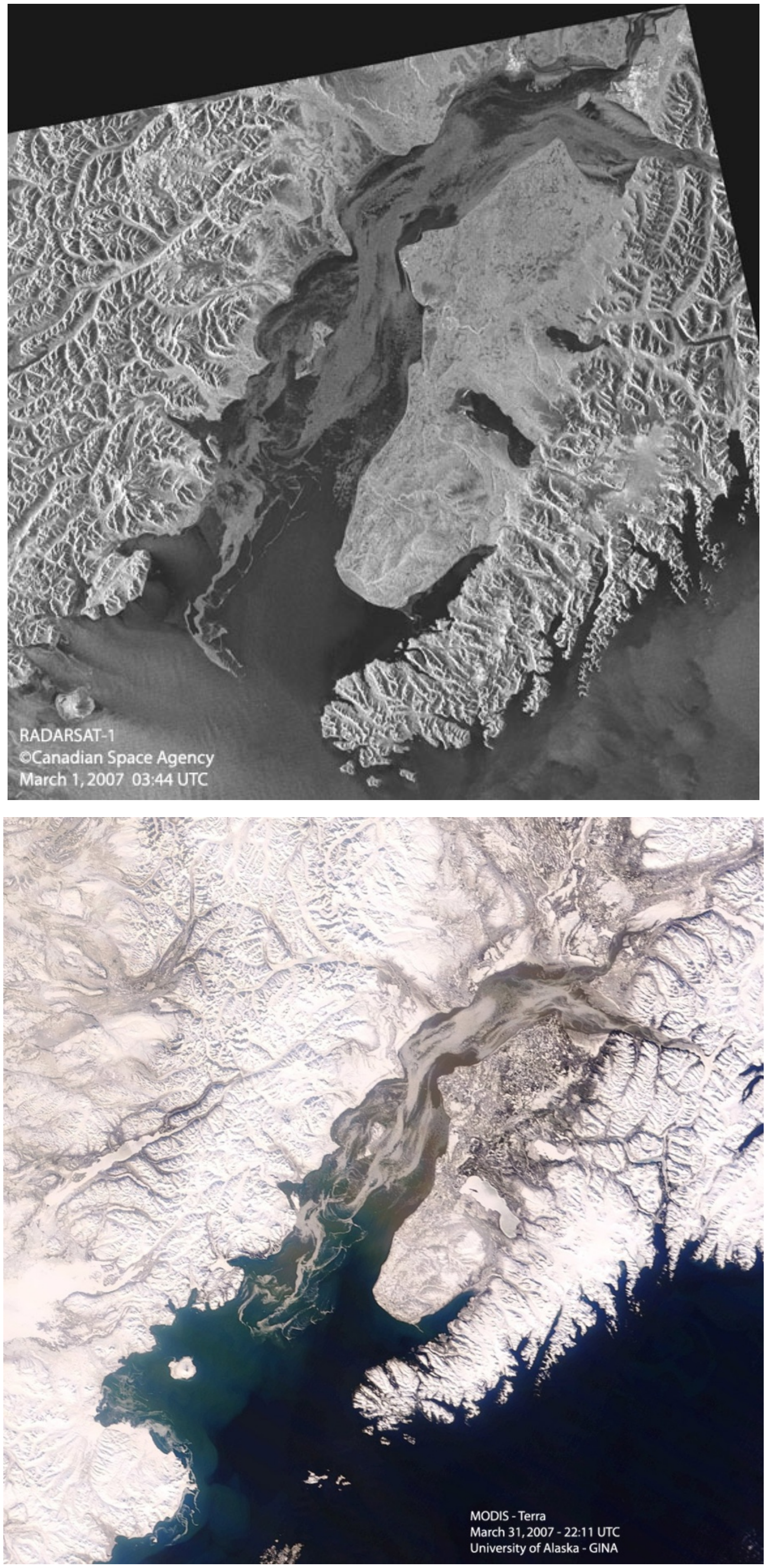

RADARSAT-1
©Canadian Space Agency
March 1, 2007 03:44 UTC

MODIS - Terra
March 31, 2007 - 22:11 UTC
University of Alaska - GINA

Figure 87. Satellite imagery from March 2007 showing grease ice presence in Lower Cook Inlet. The top image is a SAR image from March 1 showing a tongue of ice propagating southward along the mid-channel rip. The bottom image is a visible MODIS image showing ice along the western side of the lower Inlet, opposite Anchor Point.

through time. The ice appears to gather most frequently along the mid-channel rip, suggesting this is an important mode of transport for the ice from the Upper Inlet.

Fortunately, the presence of ice in the HFR field-of-view was brief and had minimal impact on radar returns. Although there were short periods of time when the presence of grease ice reduced data returns in the northwest region of the coverage area, for the most part there was no significant impact, as the grease ice did not dampen the wave field enough to significantly affect HFR operations.

3.4 Tidal Variability

Cook Inlet has one of the largest ranges of tidal height in the world (second to the Bay of Fundy in Newfoundland, Canada), and our data set permits analyses of the tidal constituents currents (Godin 1972) from grid points having >50 % coverage over the field season using “t_tide” (Pawlowicz et al. 2002). The M_2 (semidiurnal) tide is the dominant tidal constituent over the entire domain (Figure 88) and S_2 (semidiurnal) was the second most important constituent (Figure 89). The third most important constituent varied spatially. For grid points in the center of the Inlet the diurnal K_1 dominated (Figure 90) while in shallower waters near Anchor Point the semidurnal L_2 tide was more energetic than the K_1 tide. Of lesser importance are the semidiurnal species K_2 and N_2. Tidal ellipses for all five constituents are strongly polarized such that the dominant tidal current component is oriented approximately north-south, along the channel axis. Tidal properties for the seven largest constituents within various grid cells (Figure 91) of the HFR mask are listed in Table 1. Although not shown in the table, several of the smaller, but non-negligible, tidal components were associated with non-linear interactions among the semi-diurnal components.

Table 2 summarizes the variances associated with the tidal and non-tidal motion for the seven grid points. Tides account for more than 2/3 of the variance at all locations and over the central portion of the lower Inlet account for more than 86% of the variance. As expected, given the orientation of the Inlet, most of the tidal variance is associated with the north-south velocity component.

3.5 Subtidal Variability

After detiding the data, mean annual and weekly maps of the (subtidal) surface currents were constructed. Over most of the region the mean surface currents are southwestward except northwest of the mouth of Kachemak Bay where the mean flow is northward (Figure 92). A cyclonic circulation cell is also suggested at the mouth of the Inlet in line with the findings of Muench et al. (1978 and 1981) and Burbank (1977) (Figures 78 and 79). Although the radar mask does not extend far enough southward to capture the ACC entering Cook Inlet; the annual mean currents indicate westward flow at the mouth of the Inlet (and along the southern boundary of the radar mask), which may be a portion of the ACC

Detided current vector time series were resolved into their principal component axes (Figure 93). Major axes are aligned in a north-south direction following the axis of the Inlet, with some

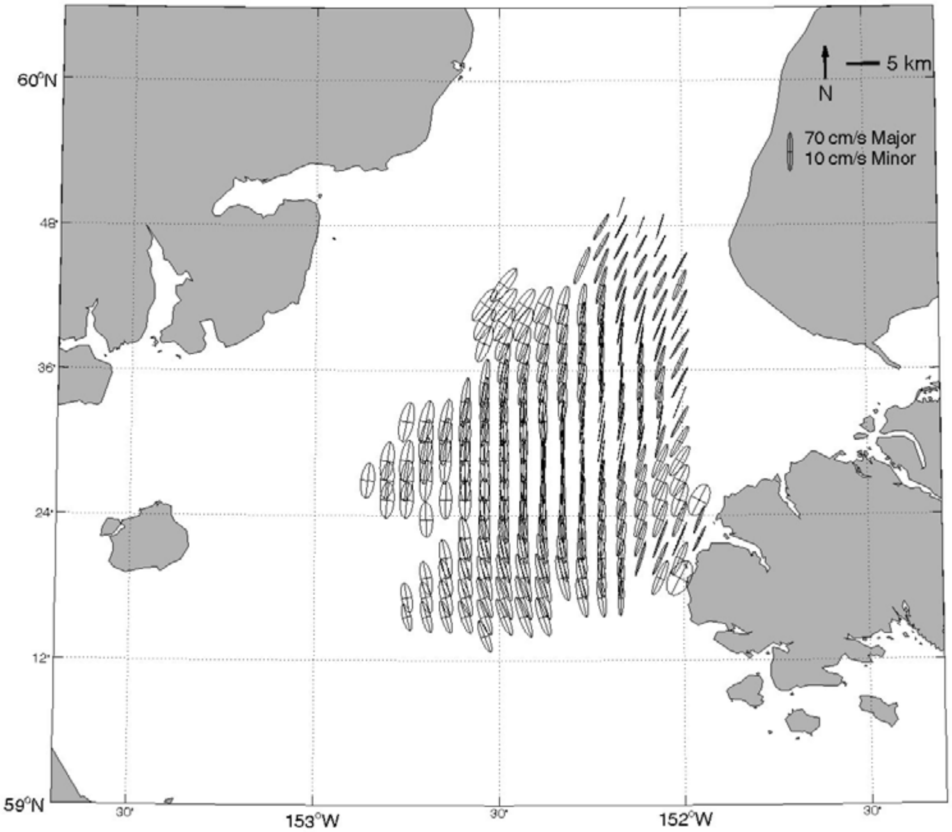

Figure 88. M$_2$ tidal ellipses for points with >50% data coverage.

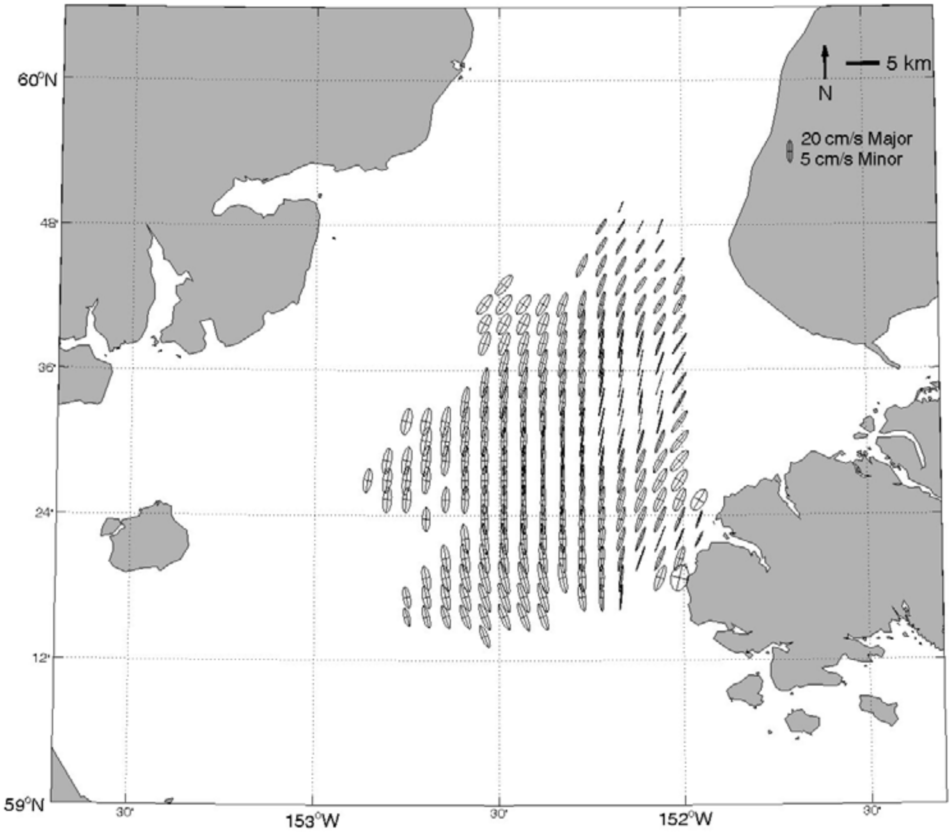

Figure 89. S$_2$ tidal ellipses for points with >50% data coverage.

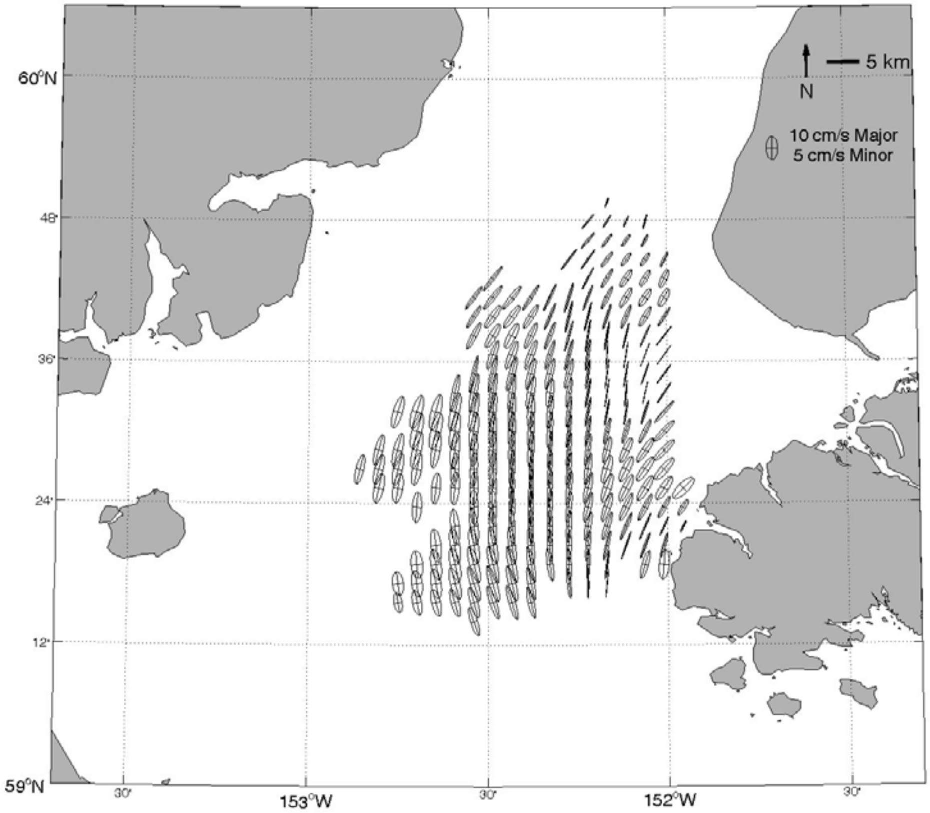

Figure 90. K_1 tidal ellipses for points with >50% data coverage.

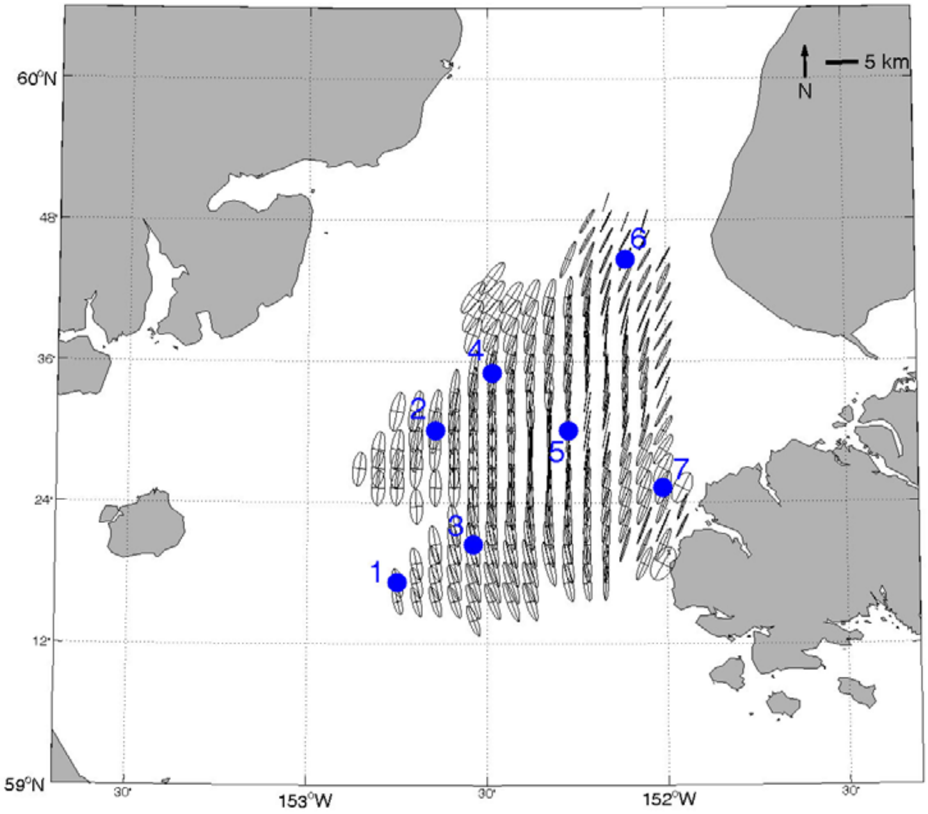

Figure 91. Representative locations displayed in Tables 1 and 2 (p. 88 and 89) overlaid on M_2 tidal ellipses.

Table 1. Tidal ellipse hodograph properties for locations shown in Figure 91. *M* and *m* are the semi-major and semi-minor axes of the tidal ellipses. The angle of inclination is taken from east. The tidal velocity vector rotates cyclonically (counterclockwise) if m > 0 and anticyclonically (clockwise) if m is < 0.

Tidal Constituent	Period (hours)	*M* (cm/s)	*m* (cm/s)	Inclination (degrees)	Phase (degrees)
M_2	12.422	1: 48	1: -15	1: 104	1: 301
		2: 85	2: -20	2: 82	2: 302
		3: 82	3: -18	3: 102	3: 286
		4: 87	4: -11	4: 83	4: 305
		5: 80	5: -0.1	5: 84	5: 285
		6: 47	6: -5	6: 62	6: 303
		7: 64	7: -21	7: 70	7: 288
S_2	12.005	1: 16	1: -5	1: 103	1: 319
		2: 28	2: -7	2: 80	2: 314
		3: 28	3: -6	3: 100	3: 300
		4: 29	4: -4	4: 79	4: 315
		5: 8	5: -1	5: 82	5: 299
		6: 14	6: -3	6: 53	6: 307
		7: 22	7: -7	7: 66	7: 299
K_1	23.923	1: 9	1: -4	1: 100	1: 209
		2: 16	2: -4	2: 76	2: 213
		3: 15	3: -8	3: 100	3: 194
		4: 16	4: -2	4: 77	4: 214
		5: 14	5: -1	5: 82	5: 192
		6: 7	6: -2	6: 53	6: 195
		7: 12	7: -4	7: 55	7: 203
K_2	11.96172	1: 7	1: -2	1: 101	1: 301
		2: 22	2: -2	2: 76	2: 307
		3: 11	3: -3	3: 99	3: 286
		4: 12	4: -1	4: 75	4: 302
		5: 11	5: 0	5: 82	5: 280
		6: 5	6: 0	6: 48	6: 298
		7: 10	7: -3	7: 66	7: 289
N_2	12.658	1: 6	1: -2	1: 99	1: 288
		2: 11	2: -3	2: 80	2: 279
		3: 12	3: -3	3: 101	3: 268
		4: 13	4: -2	4: 84	4: 275
		5: 12	5: 1	5: 83	5: 254
		6: 5	6: -1	6: 37	6: 271
		7: 9	7: -2	7: 65	7: 265

Table 2. Tidal, non-tidal, and total current variances for the east-west and north-south current components at the seven grid points shown in Figure 91. Quantities in parentheses are the percentage of the total variance due to tidal and non-tidal currents.

Grid Point	Non-tidal (east-west)	Tidal (east-west)	Non-tidal (north-south)	Tidal (north-south)	Total
1	178 (44)	229 (56)	304 (19)	1316 (81)	2027
2	140 (28)	355 (72)	515 (11)	4142 (89)	5152
3	137 (28)	354 (72)	506 (12)	3848 (88)	4845
4	97 (36)	176 (64)	472 (10)	4344 (90)	5089
5	68 (56)	54 (44)	379 (9)	3734 (91)	4235
6	101 (24)	324 (76)	567 (36)	1004 (64)	1996
7	184 (24)	580 (76)	240 (10)	2106 (90)	3110

variability near the mouth of Kachemak Bay showing east-west exchange with waters in and out of the Bay.

Subtidal variability is further defined via weekly mean maps of HFR derived surface currents and winds (Augustine and Flat Islands), beginning with November 26, 2006 (Figure 94). The week of November 26, winds were 5 - 10 m/s to the southwest, and currents were similar to the annual mean with a mean southwestward flow, strongest along the western edge of the HFR radar returns. There was northward flow northwest of the mouth of Kachemak Bay and westward outflow at the mouth of Kachemak Bay. Minimal flow was recorded over the eastern trough in the center of the eddy evident in the annual means. The week of December 3-9 was similar although there is a suggestion of the westward-flowing ACC at the mouth of the inlet (Figure 95).

For December 10 - 16, winds decreased to 0 - 5 m/s and shifted to the southeast. Current directions showed little to no response to the wind change (Figure 96), although there was an overall decrease in current magnitude. Cyclonic circulation at the entrance to Kachemak Bay, as is seen in the subtidal mean, developed, and the westward ACC flow along the southwestern boundary was still present. From December 17 - 23, currents were predominantly southward (Figure 97). Cyclonic circulation, elongated in a north-south direction, persisted at the mouth of the Bay, and currents on the western side of the Inlet were substantially greater than those on the eastern side. Winds at this time were ~5 m/s to the southeast.

During the last week in December, winds continued toward the southeast at ~5 m/s and currents over the southern end of the Inlet south to southeastward (Figure 98). There is the suggestion that much of the lower Inlet was involved in a cyclonic circulation pattern centered at the mouth of Kachemak Bay. By the week of December 31 - January 6 winds were ~5 m/s to the east-

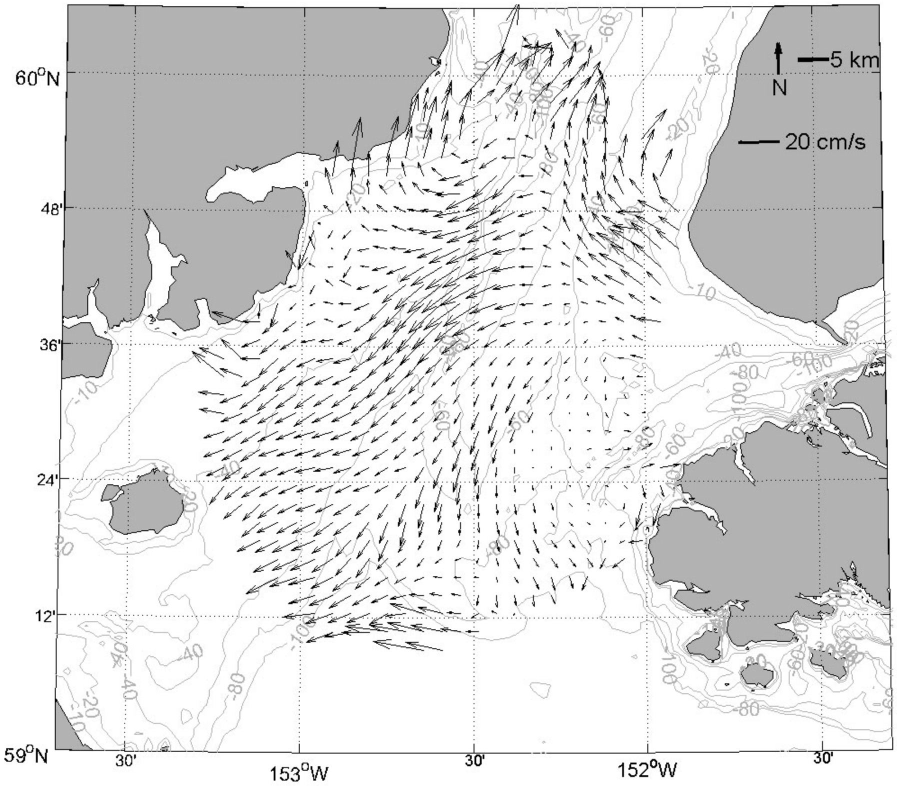

Figure 92. Subtidal mean currents derived from HFR in Lower Cook Inlet from November 12, 2006, through November 10, 2007, overlaid on bathymetry contours (m).

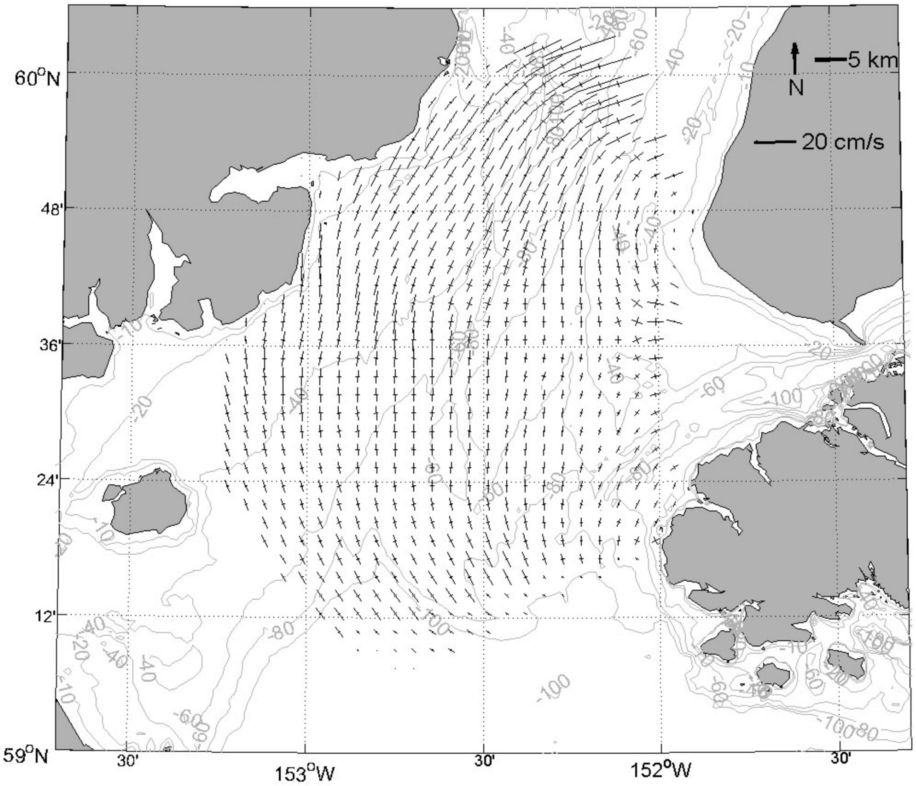

Figure 93. Subtidal principle axes derived from HFR in Lower Cook Inlet from November 12, 2006, through November 10, 2007, overlaid on bathymetry contours (m).

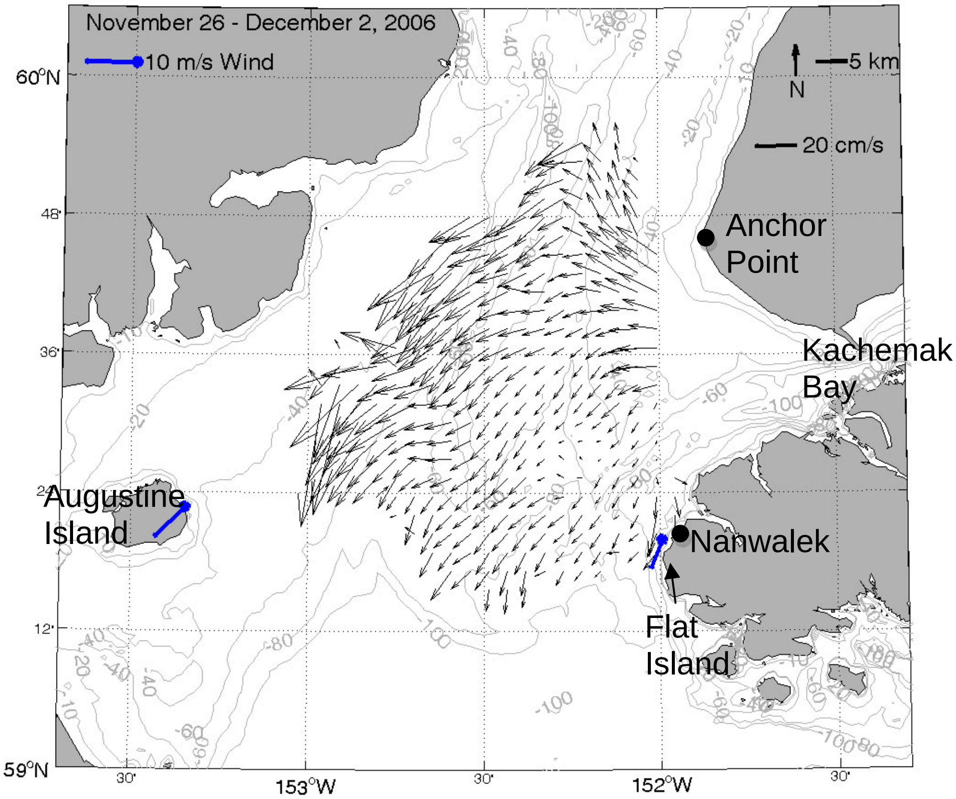

Figure 94. Weekly mean current (black) and wind (blue) vectors overlaid on bathymetry contours (meters) for November 26 - December 2, 2006, with placenames.

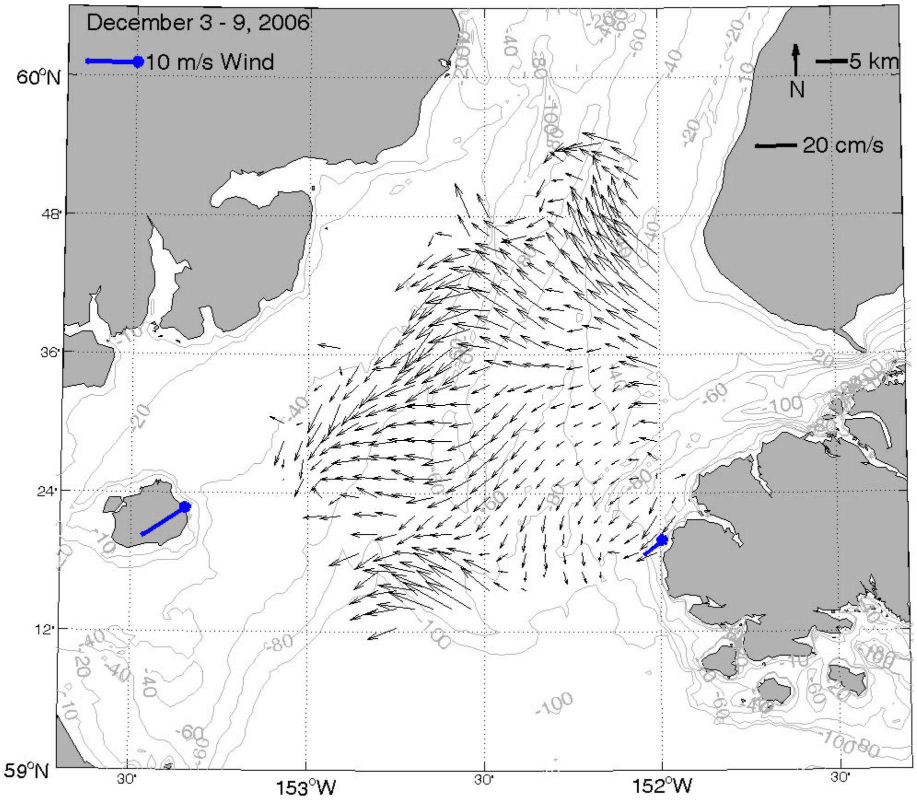

Figure 95. Weekly mean current (black) and wind (blue) vectors overlaid on bathymetry contours (meters) for December 3 - 9, 2006.

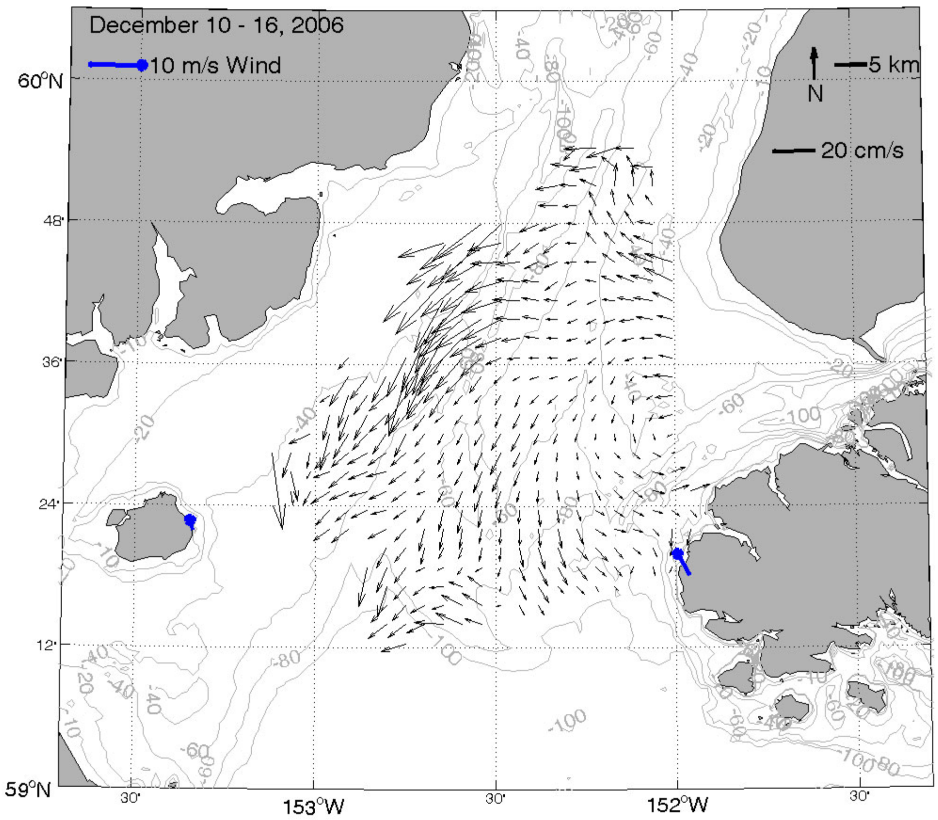

Figure 96. Weekly mean current (black) and wind (blue) vectors overlaid on bathymetry contours (meters) for December 10 - 16, 2006.

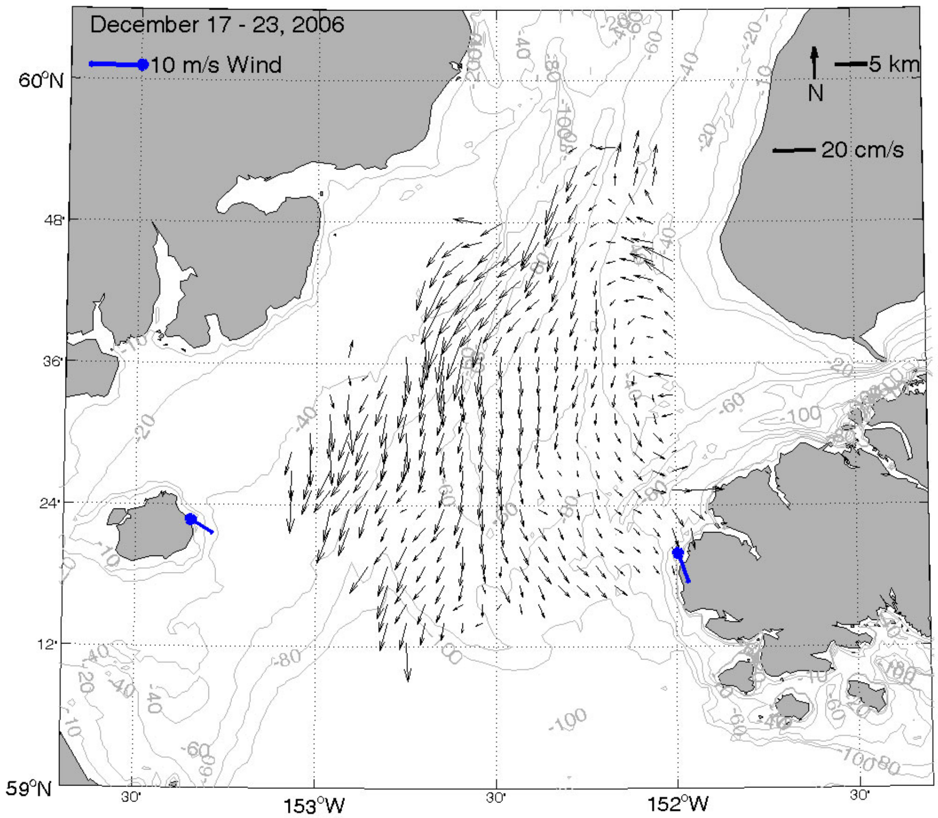

Figure 97. Weekly mean current (black) and wind (blue) vectors overlaid on bathymetry contours (meters) for December 17 - 23, 2006.

southeast (Figure 99). Strong southwestward flow developed over the western portion of the radar mask, and there was a relatively strong eastward flow into Kachemak Bay.

Winds and currents diminished during the week of January 7, with light southward winds overall. Currents reversed direction from the previous week and were to the northeast off the coast of Nanwalek and to the northwest near Anchor Point. However, strong southwest flow continued along the western boundary, and westward flow reappeared at the south end of the Inlet (Figure 100). By January 14 – 20 winds were ~5 m/s to the south, a cyclonic circulation re-appeared at the mouth of Kachemak Bay, currents offshore of Nanwalek reversed to the south-southeast, and a southward jet formed along the eastern edge of the western trough (Figure 101).

Winds for the week of January 21 (Figure 102) varied between Augustine and Flat Islands; they were ~5 m/s to the southwest on Augustine Island, and weak southeastward winds (<2 m/s) were present at Flat Island. Whereas current speeds decreased overall, the jet over the trough, strong currents in the western Inlet, northwest flow offshore Anchor Point, and the cyclonic circulation cell at the mouth of Kachemak Bay persisted. Largely the same current structure occurred but strengthened during the following week (Figure 103) when winds were approximately westward at ~5 m/s.

For the week of February 4 – 10 winds were to the southwest at 5 - 10 m/s. Currents were southward throughout the HFR domain, except for westward flow at the southern boundary of the HFR mask and a few westward returns offshore of Anchor Point (Figure 104). This current pattern persisted through February 11 - 17 (Figure 105).

During the week of February 18 (Figure 106) winds were 5 - 10 m/s to the east on Augustine Island and ~10 m/s to the south on Flat Island. While currents were still flowing westward along the mouth of Kachemak Bay, strong northward currents developed offshore of Anchor Point on the eastern side of the Inlet. South and west of Anchor Point the currents were to the west while currents in the southern region were southward. By the following week (Figure 107) winds on Augustine Island were light (~2 m/s) and to the southeast but ~10 m/s southward on Flat Island. The westward flow of the previous week had vanished, and the majority of the currents were southward, except for the northwestward and northward flow offshore of Anchor Point. This circulation pattern persisted through March 10 (Figure 108).

Winds were to the south-southeast at ~5 m/s on Augustine Island and ~10 m/s on Flat Island during the week of March 11-17 (Figure 109). Currents over the southern region flowed to the southeast, while currents in the northeastern region flowed northward offshore of Anchor Point. Maps for the weeks of March 18 and March 25 were erratic due to gaps in data returns from the Nanwalek site and thus are not presented.

Results from April 1 - 7 were very similar to the subtidal mean with currents northward off the shore of Anchor Point and strong flow west-southwest along the western edge of returns. A southwest jet was present over the western trough, and current returns at the mouth of Kachemak Bay were westward. Flow was minimal over the eastern trough, and winds were southwest in direction, ~10 m/s on Augustine Island and <5 m/s on Flat Island (Figure 110). Similar patterns were seen a week later, although the jet over the western trough had strengthened, and returns in the southeastern portion of the radar mask had diminished (Figure 111). Winds were light (~2 m/s) and toward the southwest.

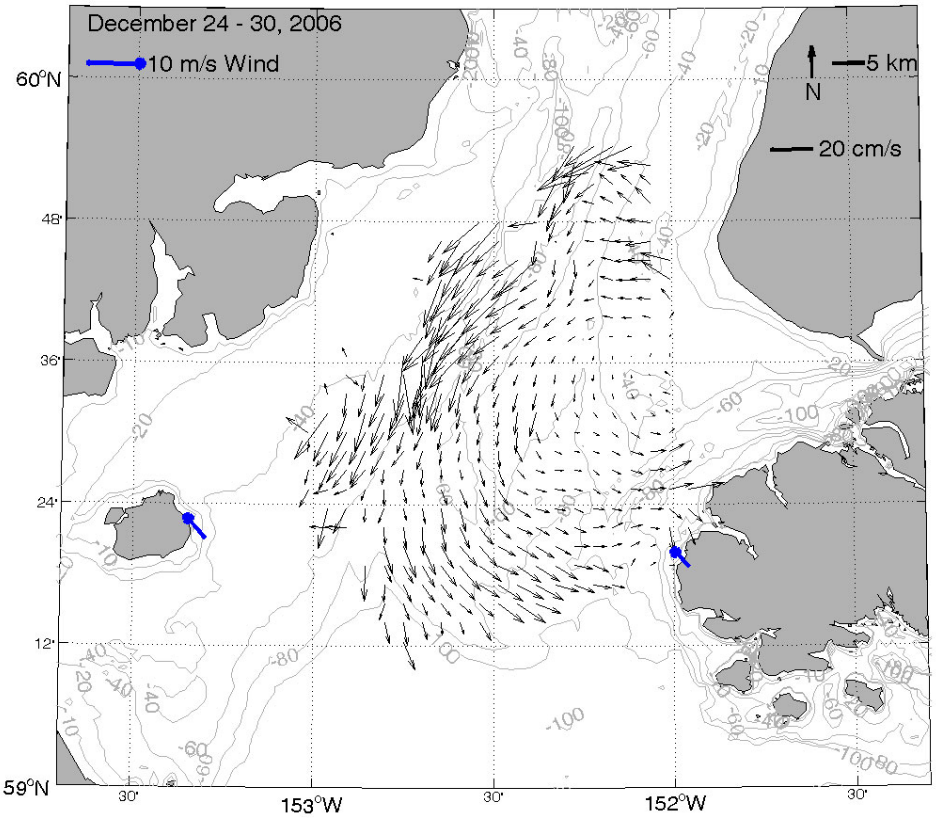

Figure 98. Weekly mean current (black) and wind (blue) vectors overlaid on bathymetry contours (meters) for December 24 - 30, 2006.

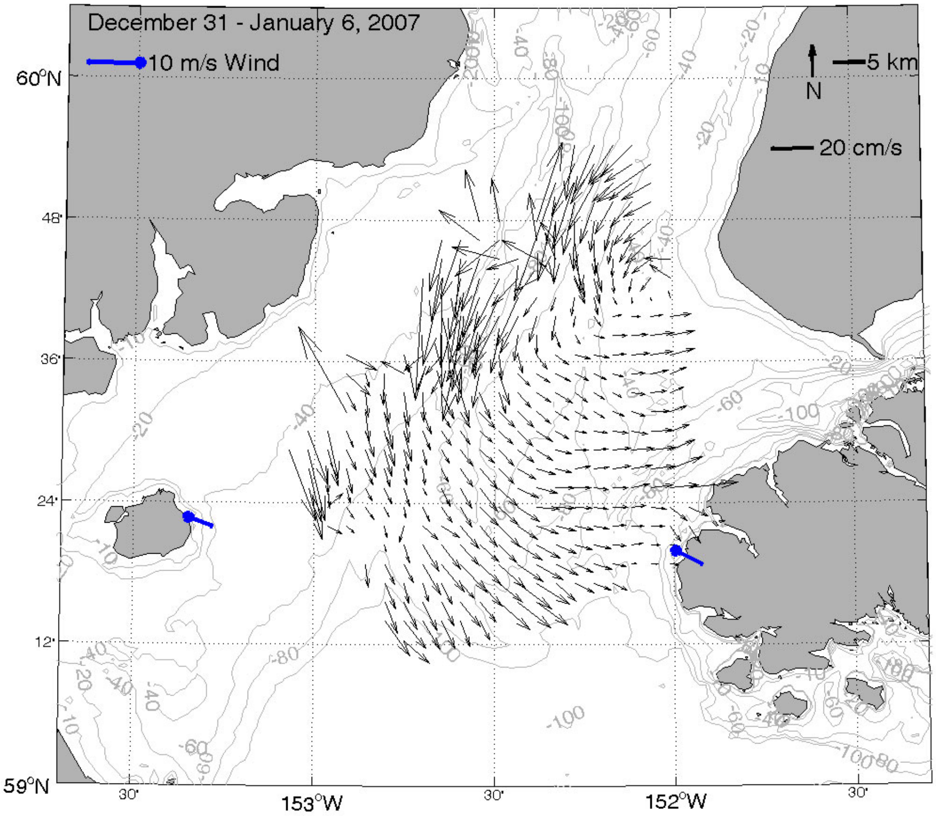

Figure 99. Weekly mean current (black) and wind (blue) vectors overlaid on bathymetry contours (meters) for December 31 - January 6, 2007.

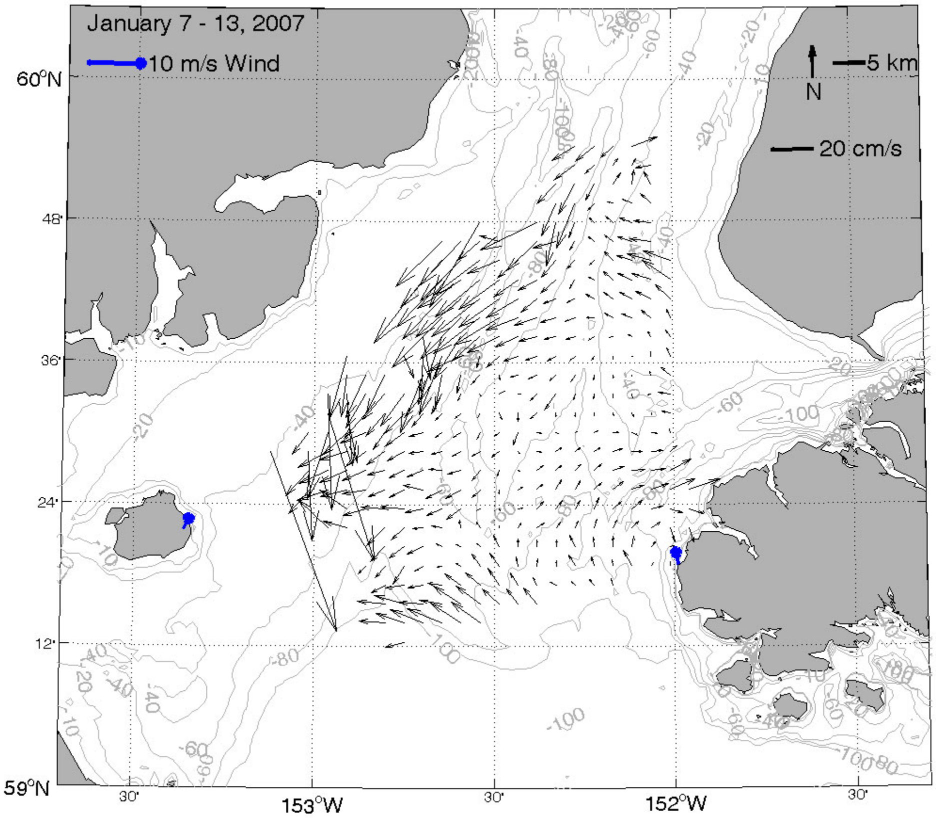

Figure 100. Weekly mean current (black) and wind (blue) vectors overlaid on bathymetry contours (meters) for January 7 - 13, 2007.

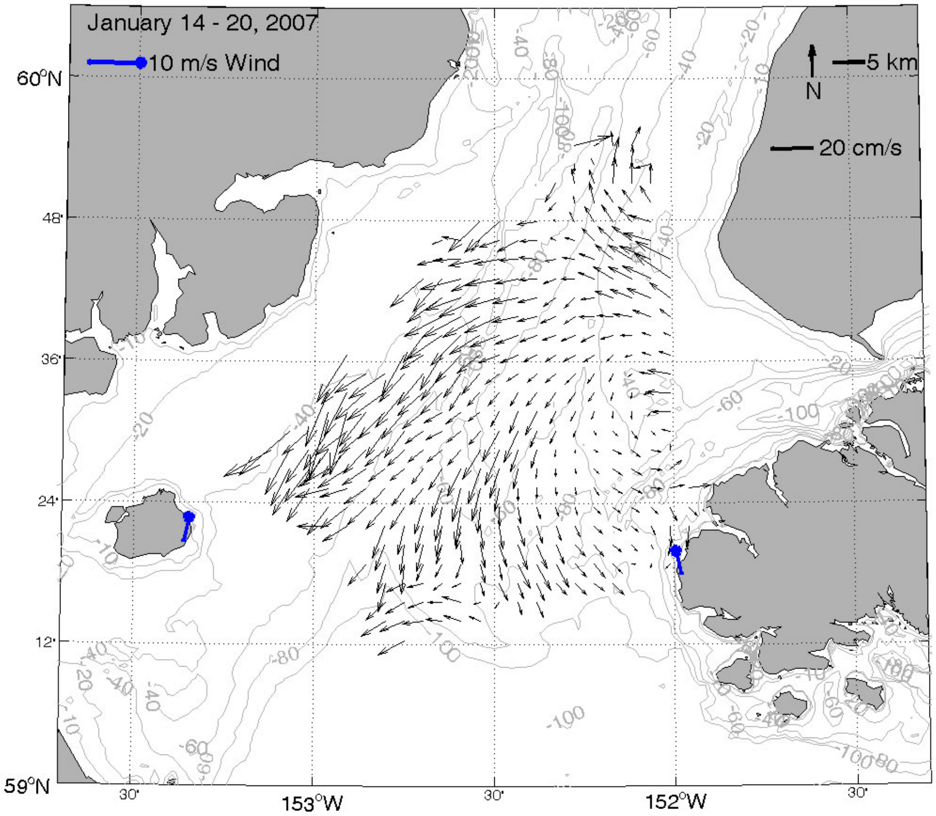

Figure 101. Weekly mean current (black) and wind (blue) vectors overlaid on bathymetry contours (meters) for January 14 - 20, 2007.

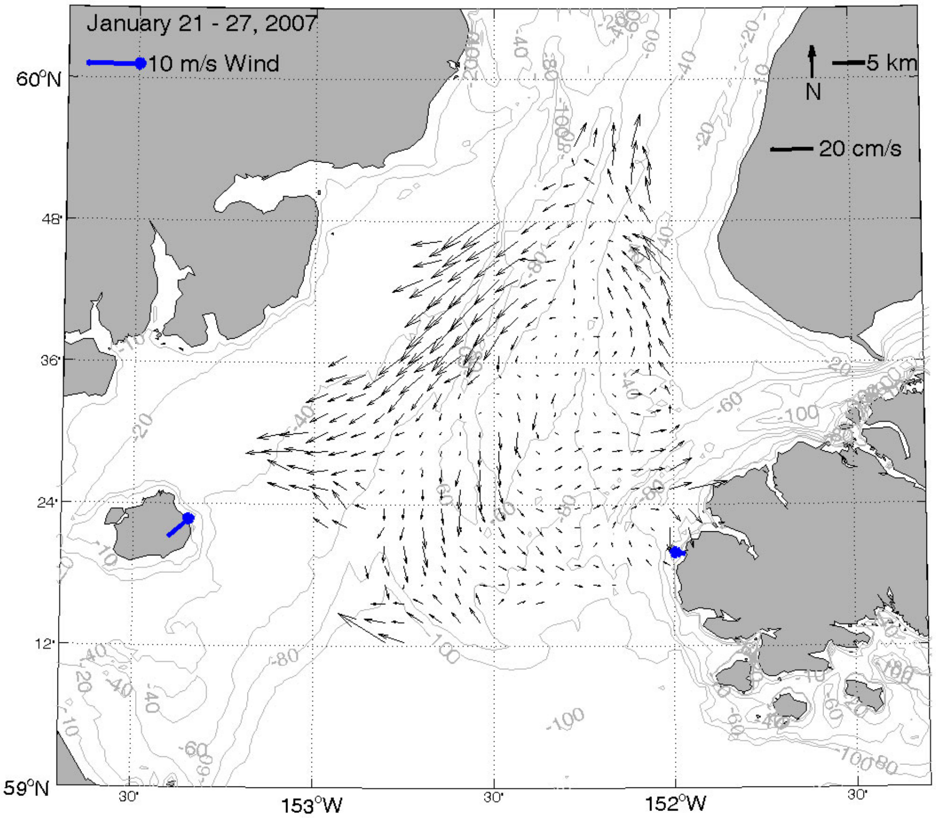

Figure 102. Weekly mean current (black) and wind (blue) vectors overlaid on bathymetry contours (meters) for January 21 - 27, 2007.

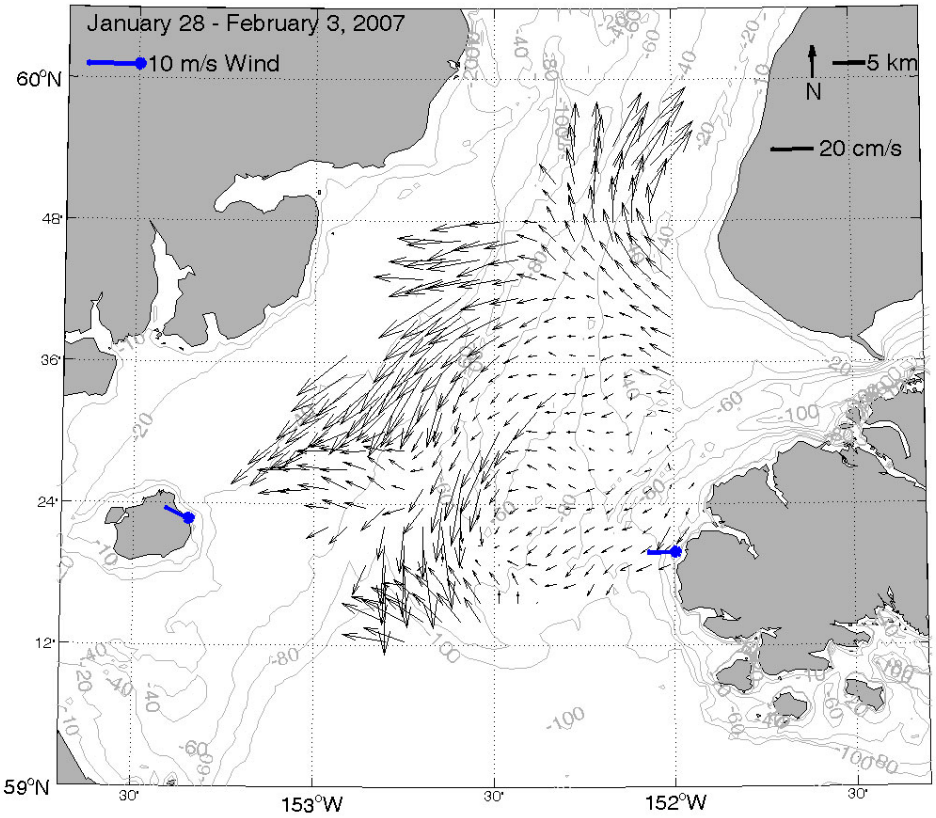

Figure 103. Weekly mean current (black) and wind (blue) vectors overlaid on bathymetry contours (meters) for January 28 - February 3, 2007.

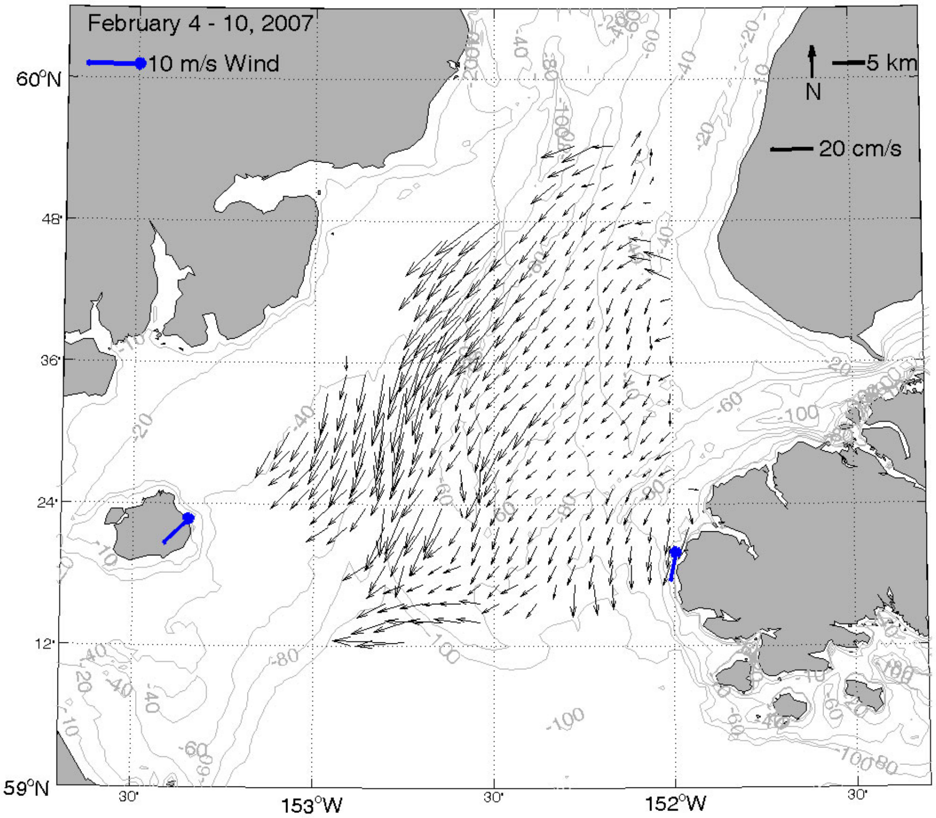

Figure 104. Weekly mean current (black) and wind (blue) vectors overlaid on bathymetry contours (meters) for February 4 - 10, 2007.

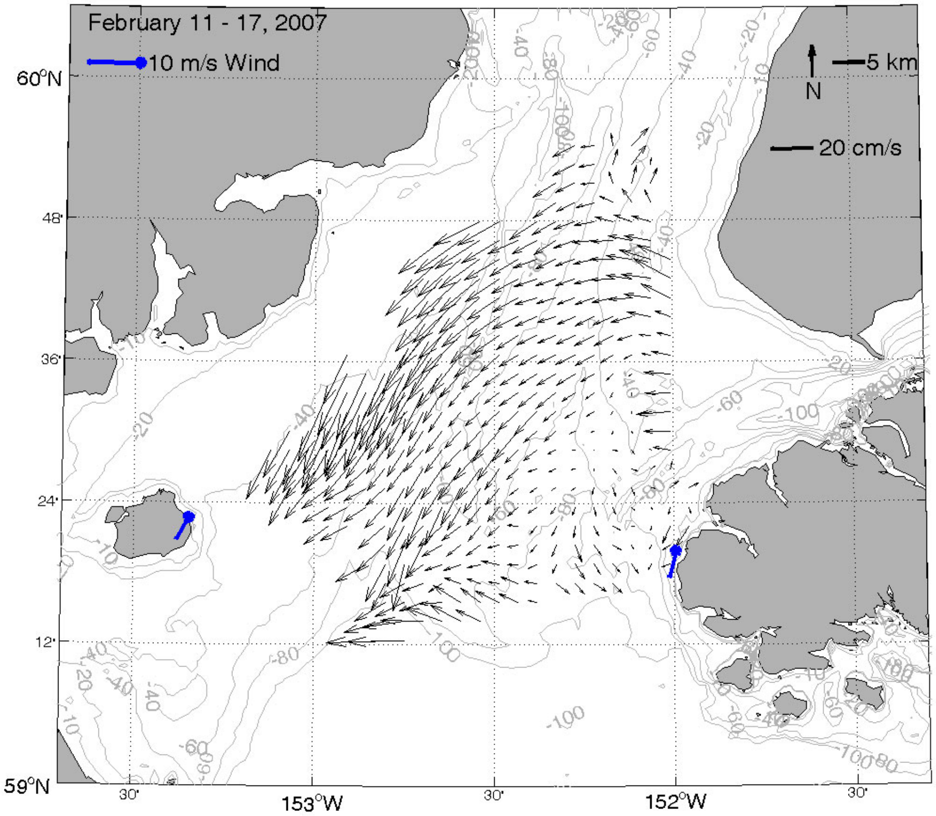

Figure 105. Weekly mean current (black) and wind (blue) vectors overlaid on bathymetry contours (meters) for February 11 - 17, 2007.

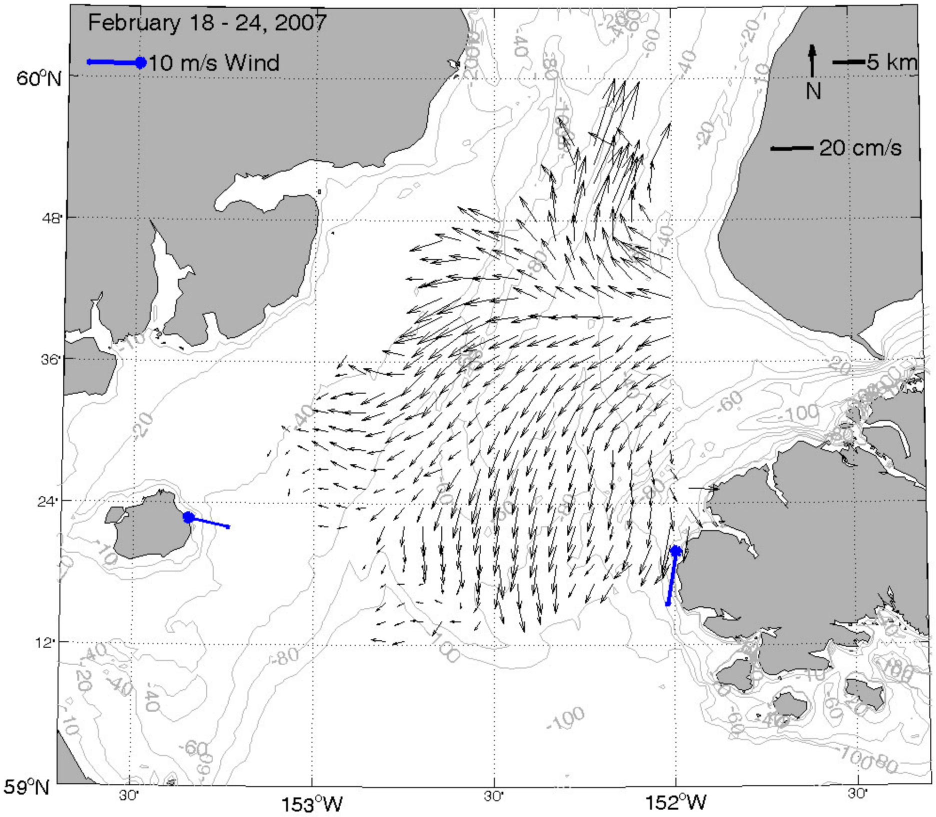

Figure 106. Weekly mean current (black) and wind (blue) vectors overlaid on bathymetry contours (meters) for February 18 - 24, 2007.

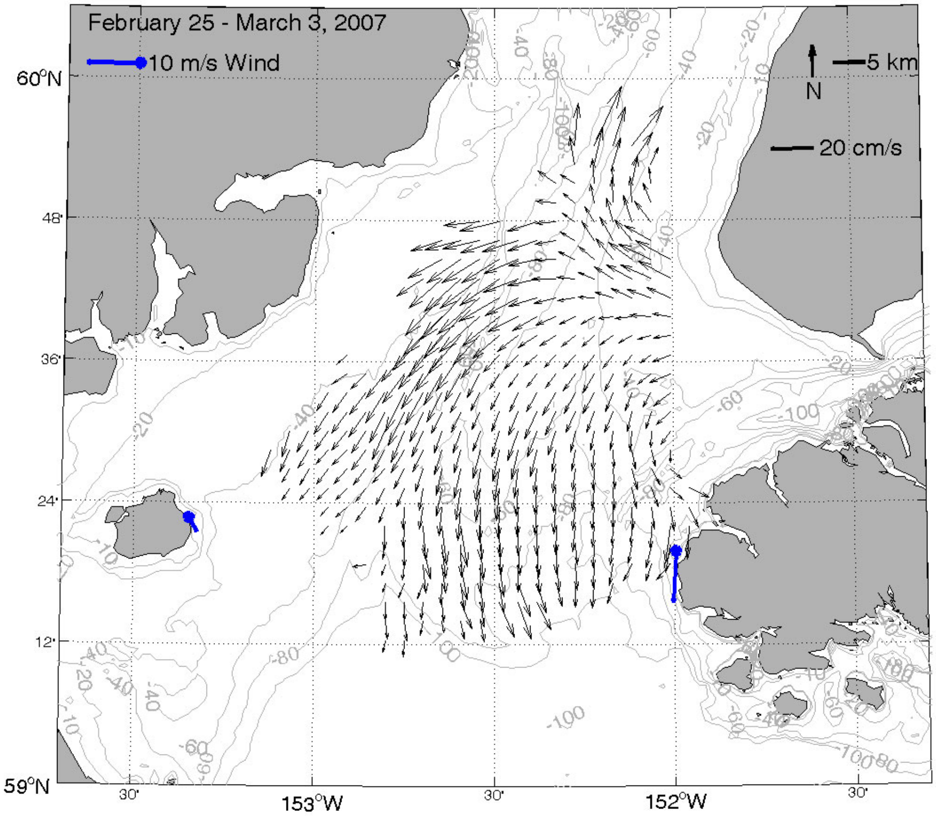

Figure 107. Weekly mean current (black) and wind (blue) vectors overlaid on bathymetry contours (meters) for February 25 - March 3, 2007.

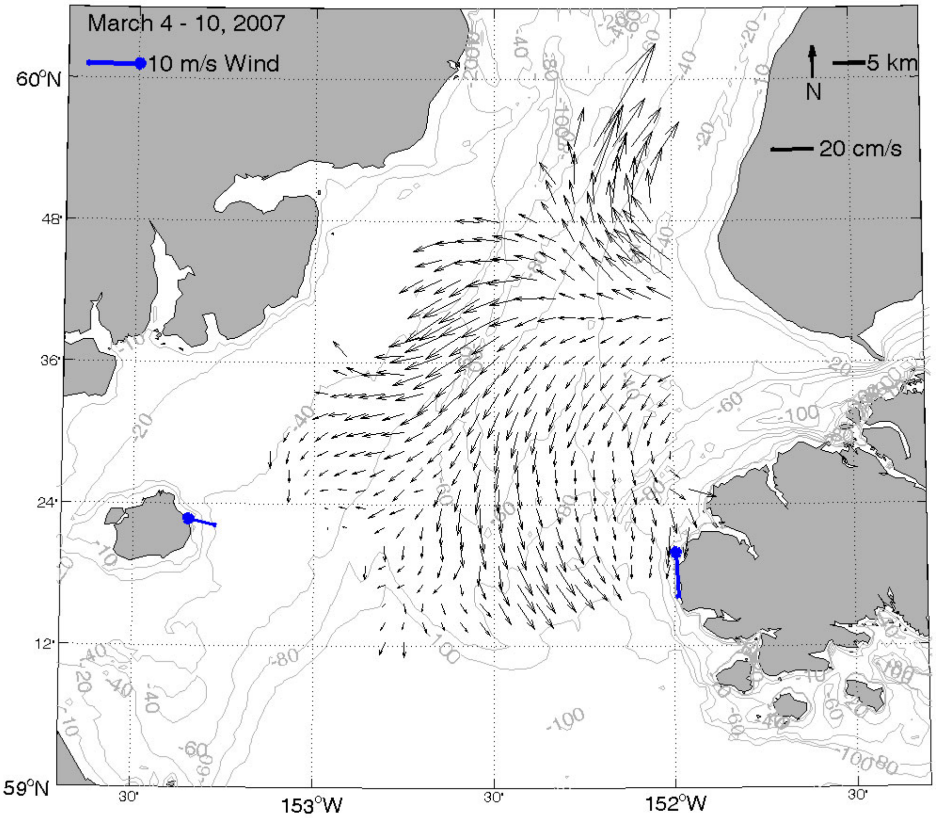

Figure 108. **Weekly mean current (black) and wind (blue) vectors overlaid on bathymetry contours (meters) for March 4 - 10, 2007.**

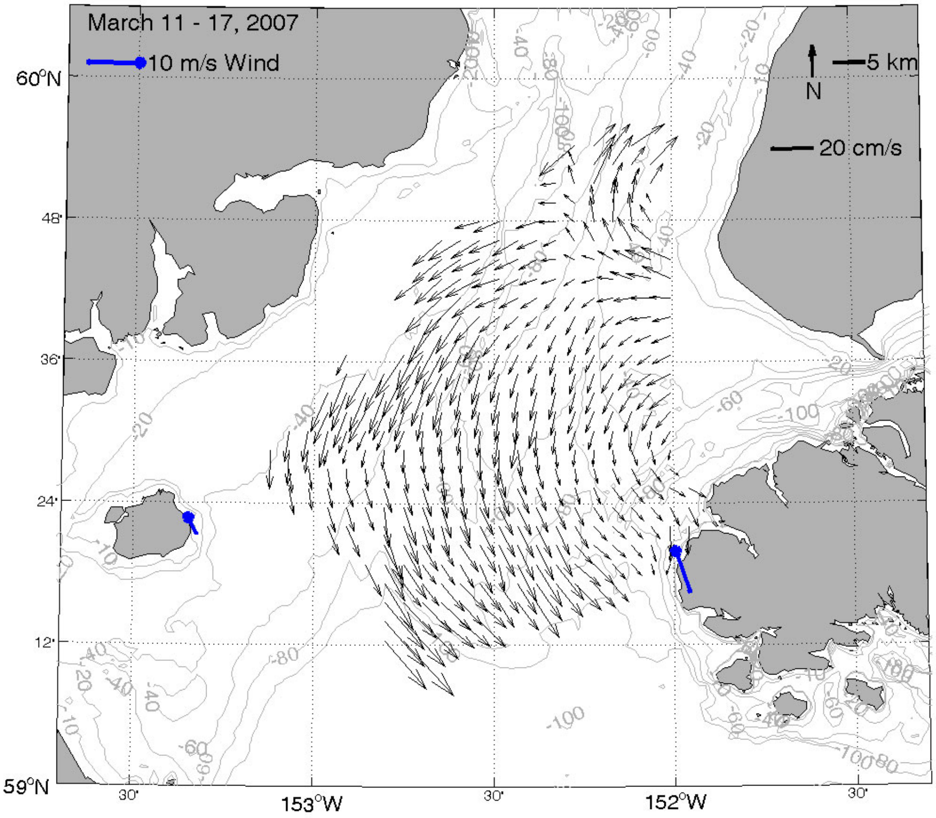

Figure 109. **Weekly mean current (black) and wind (blue) vectors overlaid on bathymetry contours (meters) for March 11 - 17, 2007.**

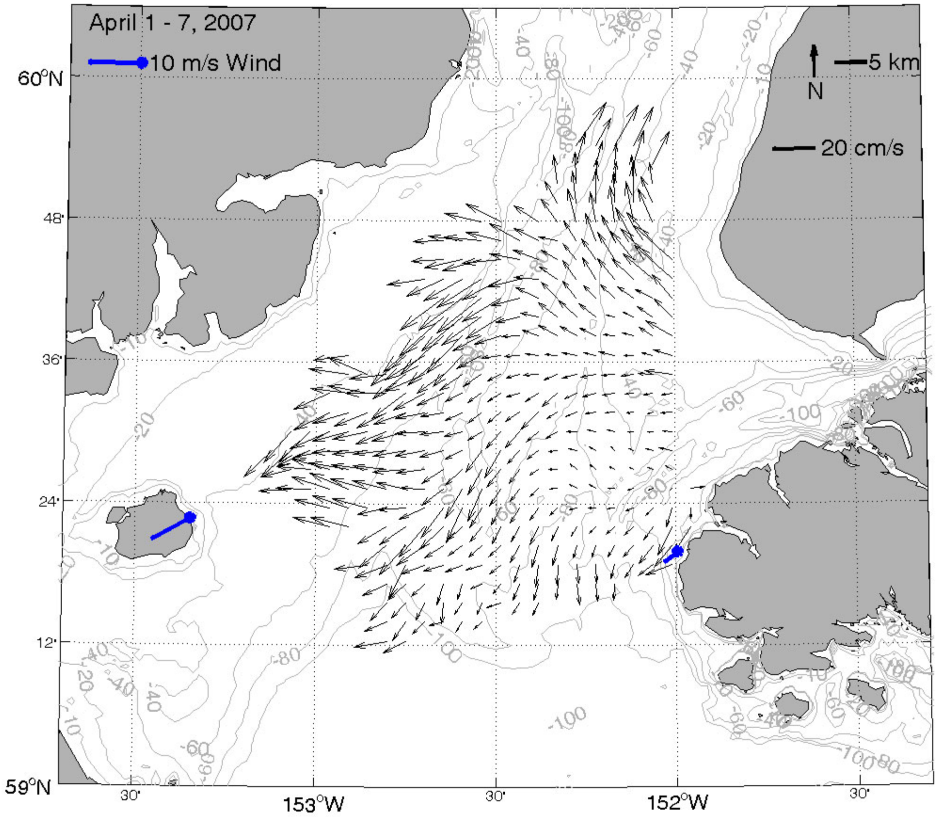

Figure 110. Weekly mean current (black) and wind (blue) vectors overlaid on bathymetry contours (meters) for April 1 - 7, 2007.

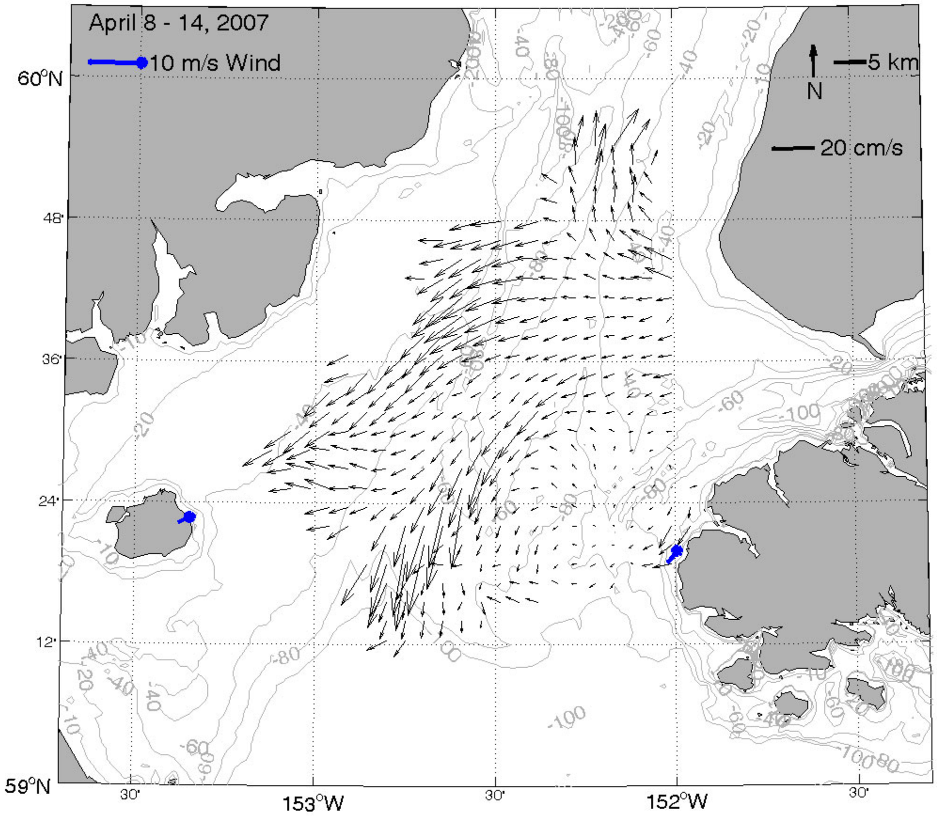

Figure 111. Weekly mean current (black) and wind (blue) vectors overlaid on bathymetry contours (meters) for April 8 - 14, 2007.

By the week of April 15 - 21 winds on Augustine Island increased to ~10 m/s to the southwest, and Flat Island winds were <5 m/s to the southwest (Figure 112). Current speeds increased in magnitude over much of the domain, and the strong horizontal current shear over the western trough began to decrease. The shear gradient decayed further from April 22 – 28 when winds on Augustine island decreased to <5 m/s southwest (Figure 113). Currents in the eastern portion of the HFR mask decreased in magnitude, and the northward currents in the northern region near Anchor Point became more westward. This current pattern persisted through May 5 (Figure 114).

During the week of May 6 winds were <5 m/s (Figure 115). Currents offshore of Anchor Point flowed northward again and the cyclonic circulation developed near the mouth of Kachemak Bay. The mean flow over much of the region was southward. The week of May 13 - 19, returns in the western region of the domain were westward toward Augustine Island. Cyclonic circulation at the mouth of Kachemak Bay had broken down, although currents at the south of the entrance were still eastward, into the Bay (Figure 116). By the following week, the eastward flow into the Bay reversed to the west (Figure 117). Winds were still light (<5 m/s), and currents over the western domain were flowing southwestward, and the northward flow offshore of Anchor Point rotated to be west-southwest. By May 27 - June 2, winds continued to be weak (<5 m/s; Figure 118). Currents were southwestward in the western portion of the HFR mask and southward near the mouth of the Inlet. Weak flows developed over much of the eastern domain, and northward flow was evident offshore of Anchor Point. This pattern continued through the next week, except currents offshore of Nanwalek shifted westward (Figure 119).

In the second week of June (Figure 120), winds on Flat Island were northward at <5 m/s while Augustine Island recorded eastward winds of <5 m/s. Currents were highly variable in direction and magnitude, and two separate patterns of flow developed. Offshore of Nanwalek, in the southern half of the HFR returns, currents were northward in the eastern trough and then veered eastward into Kachemak Bay and also westward and then southward through the western trough. In the northern half of the domain waters near Anchor Point flowed northward and then turned to the southwest along the western edge of the radar mask. During the following week a similar circulation occurred over the southern half of the domain (Figure 121). However, currents north of Nanwalek flowed northward into the Inlet shipping channel, while the flow along the western edge of the radar mask varied in direction, suggesting mesoscale circulations along the western boundary of the Inlet.

Currents increased in magnitude by June 24 – 30 (Figure 122) and were similar to the annual mean, with westward currents along the southern edge of the radar mask and minimal flow over the eastern trough. Currents during the first week of July were similar, but flow at the southern edge of the returns were southward (Figure 123). Winds during these two weeks were light (<5 m/s) and variable. The overall current pattern of mean flow to the south-southwest continued into the second week of July, but all currents at the mouth of Kachemak Bay were eastward (into the Bay), while returns in the west near Augustine Island were west-northwest (Figure 124) under light winds. During the week of July 15 - 21, currents again resembled the subtidal mean; however, at the southern end of the HFR mask the flow was southward, and circulation near the mouth of Kachemak Bay was predominantly to the west (Figure 125). During the last week of July, currents offshore of Nanwalek were to the north and diverted toward the mouth of Kachemak Bay (Figure 126). Currents in the northern portion were westward before veering to the southwest along the western edge of the radar mask. Over the southern entrance to the Inlet, westward flow converged with a southwest jet over the western trough.

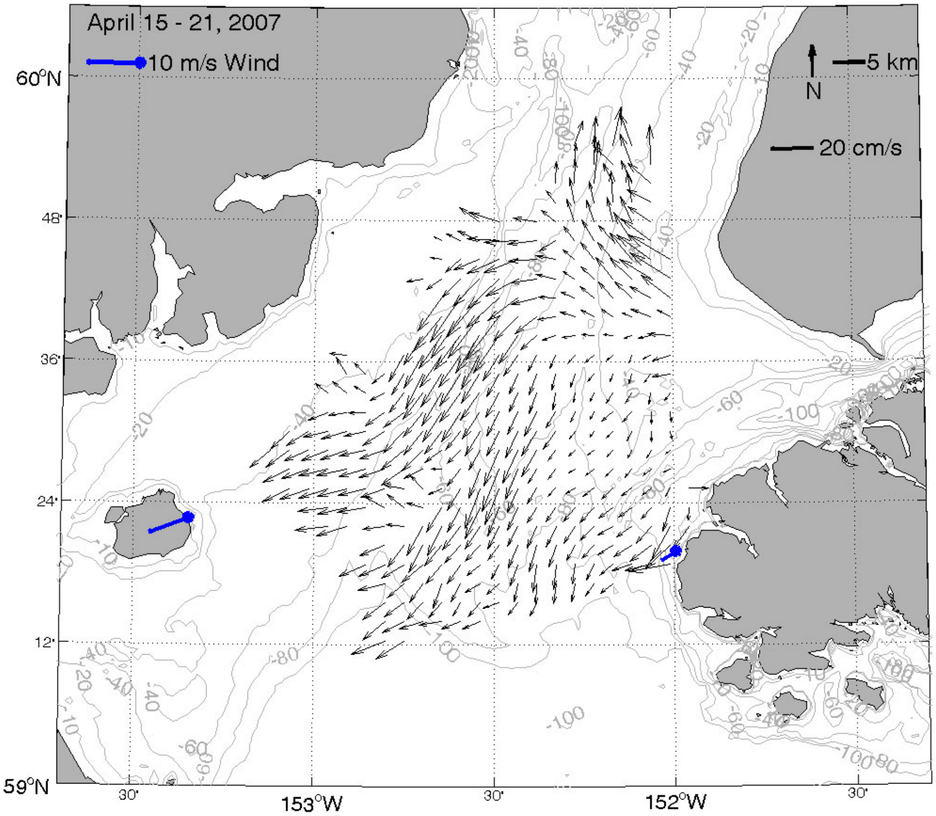

Figure 112. Weekly mean current (black) and wind (blue) vectors overlaid on bathymetry contours (meters) for April 15 - 21, 2007.

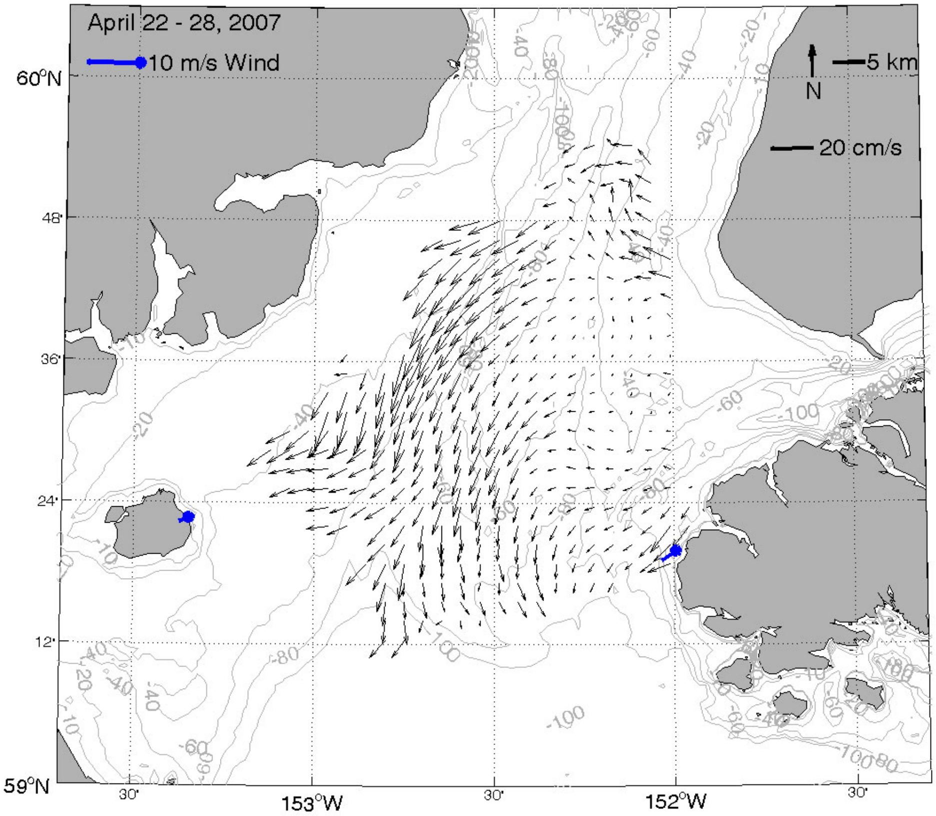

Figure 113. Weekly mean current (black) and wind (blue) vectors overlaid on bathymetry contours (meters) for April 22 - 28, 2007.

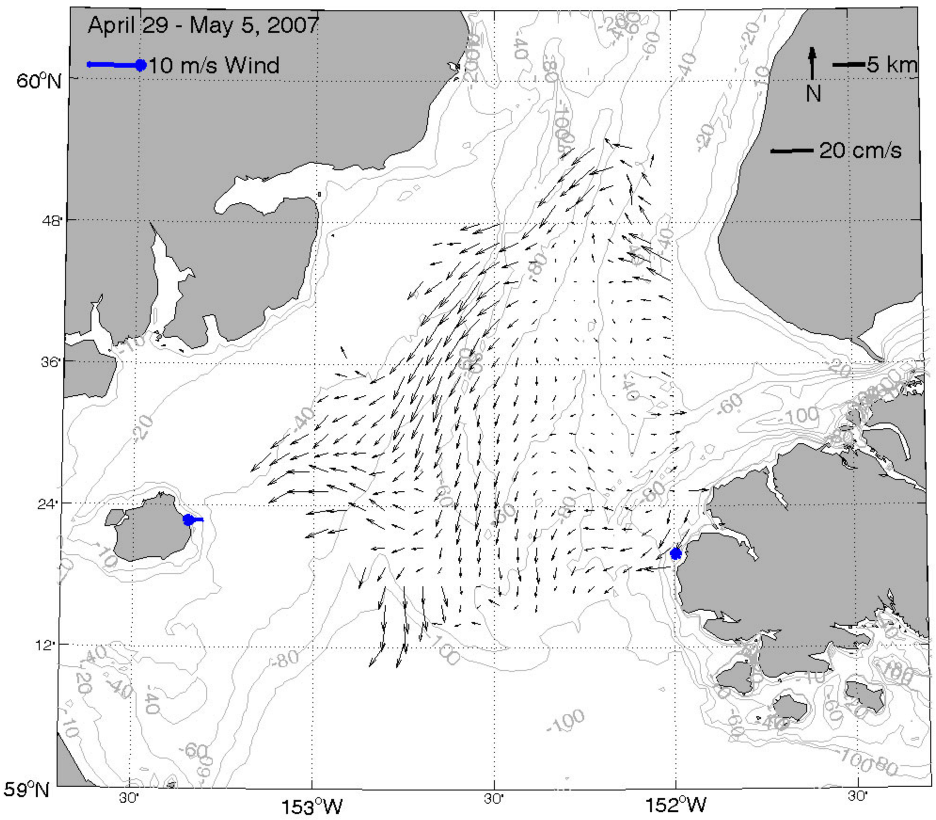

Figure 114. Weekly mean current (black) and wind (blue) vectors overlaid on bathymetry contours (meters) for April 29 - May 5, 2007.

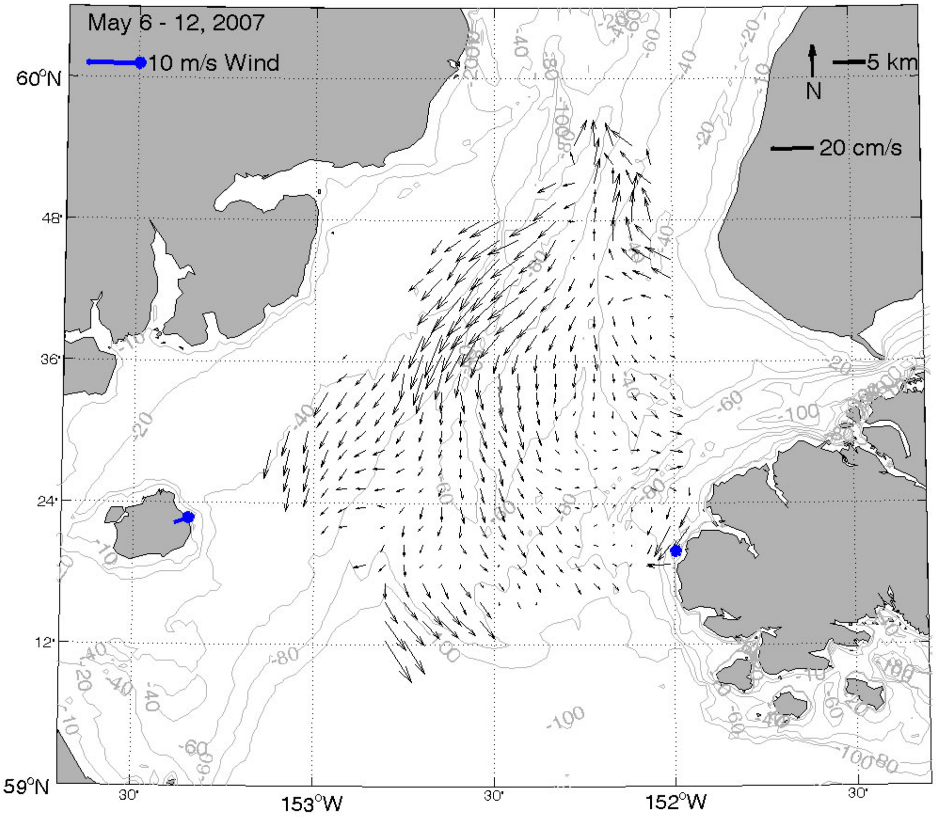

Figure 115. Weekly mean current (black) and wind (blue) vectors overlaid on bathymetry contours (meters) for May 6 - 12, 2007.

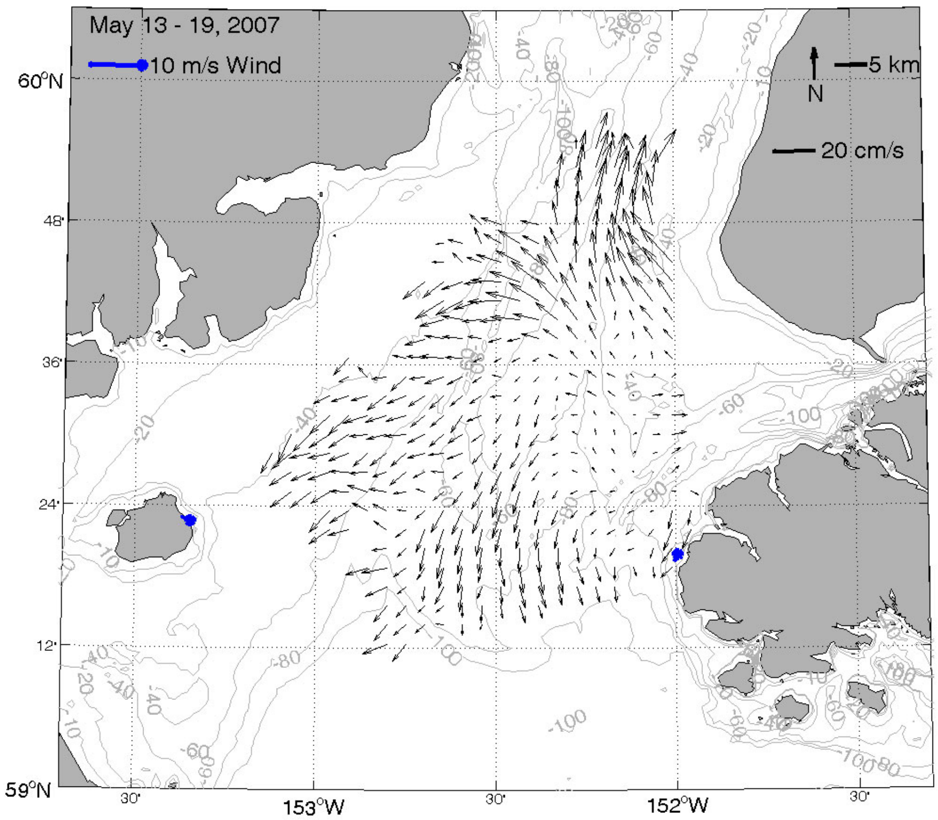

Figure 116. Weekly mean current (black) and wind (blue) vectors overlaid on bathymetry contours (meters) for May 13 - 19, 2007.

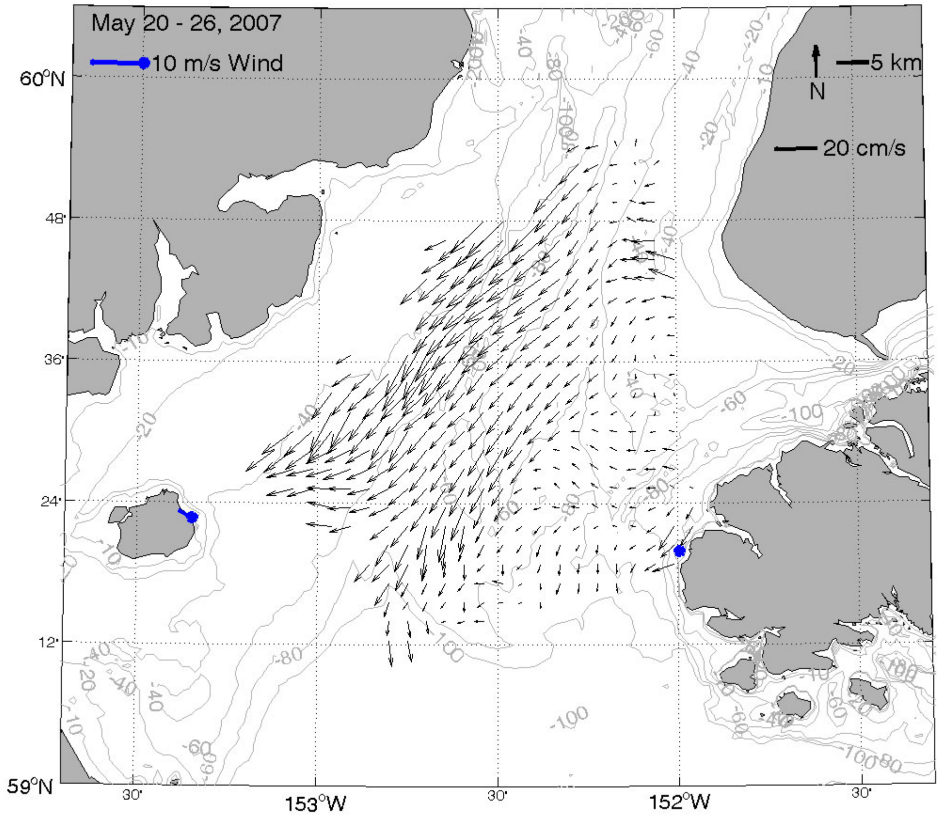

Figure 117. Weekly mean current (black) and wind (blue) vectors overlaid on bathymetry contours (meters) for May 20 - 26, 2007.

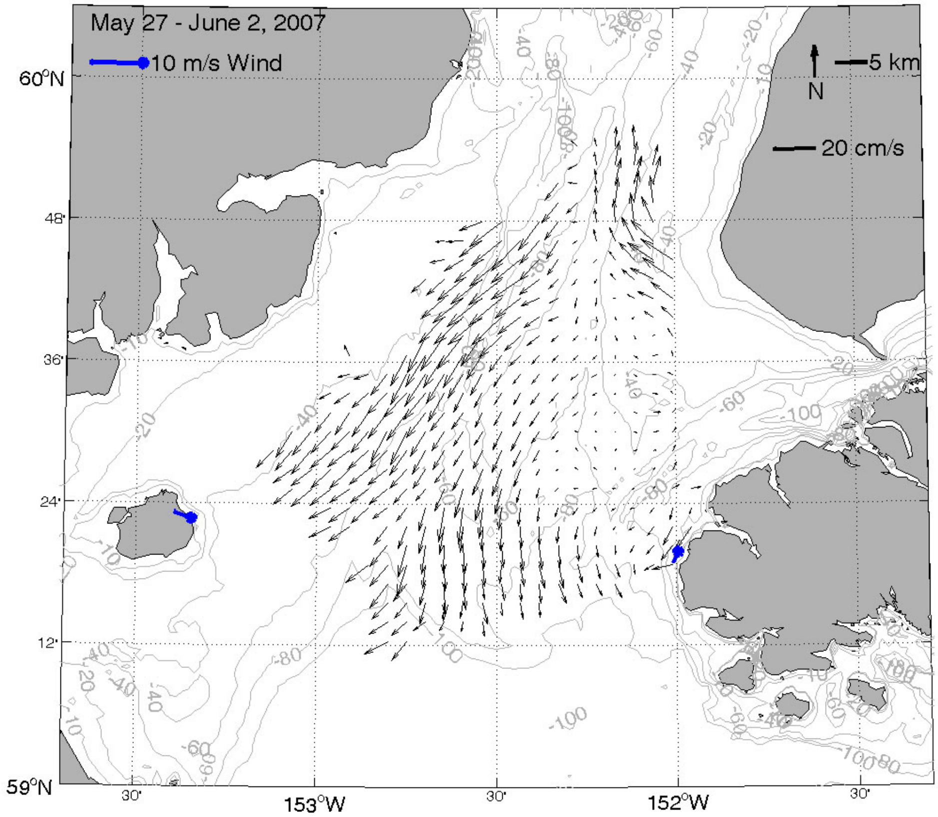

Figure 118. Weekly mean current (black) and wind (blue) vectors overlaid on bathymetry contours (meters) for May 27 - June 2, 2007.

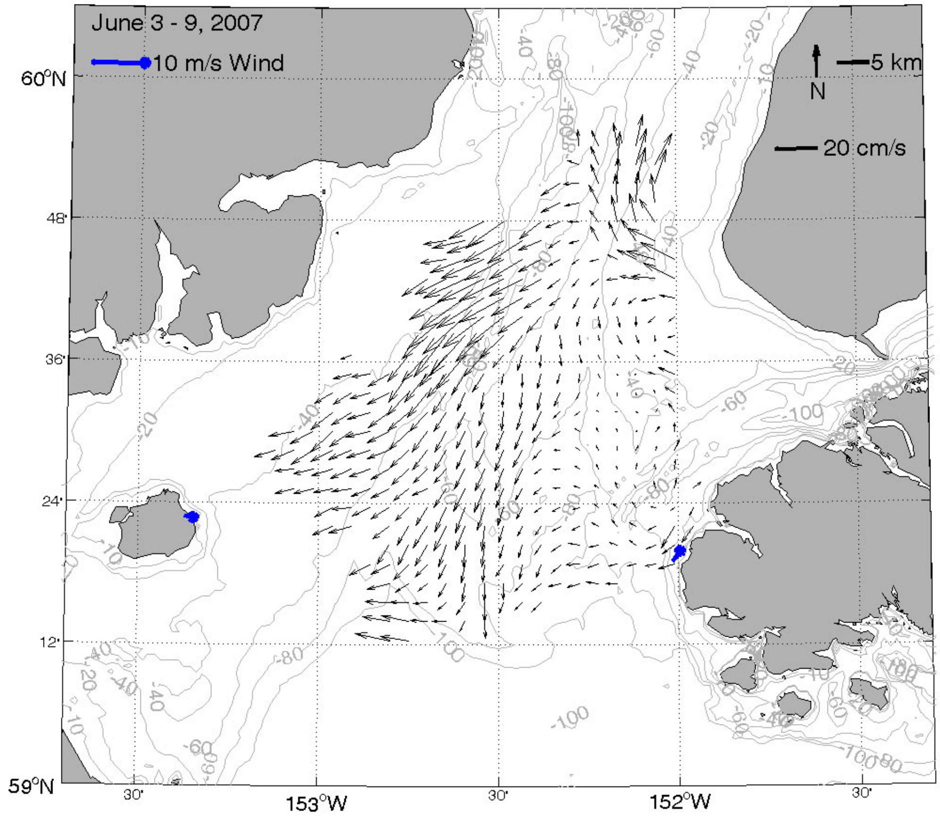

Figure 119. Weekly mean current (black) and wind (blue) vectors overlaid on bathymetry contours (meters) for June 3 - 9, 2007.

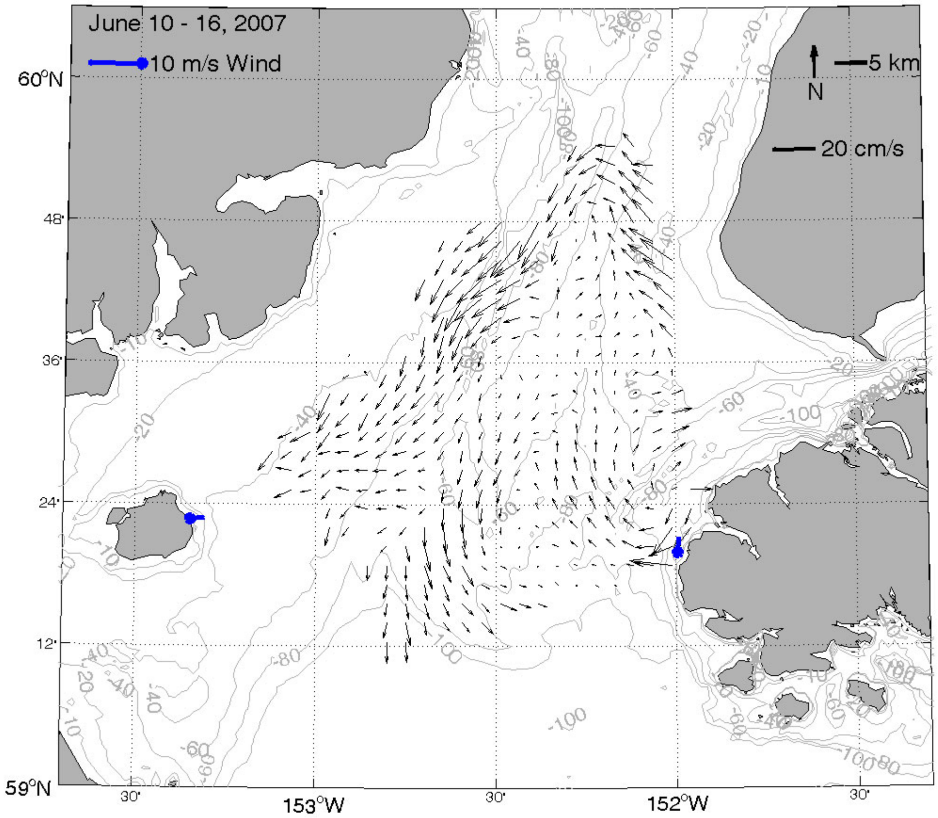

Figure 120. Weekly mean current (black) and wind (blue) vectors overlaid on bathymetry contours (meters) for June 10 - 16, 2007.

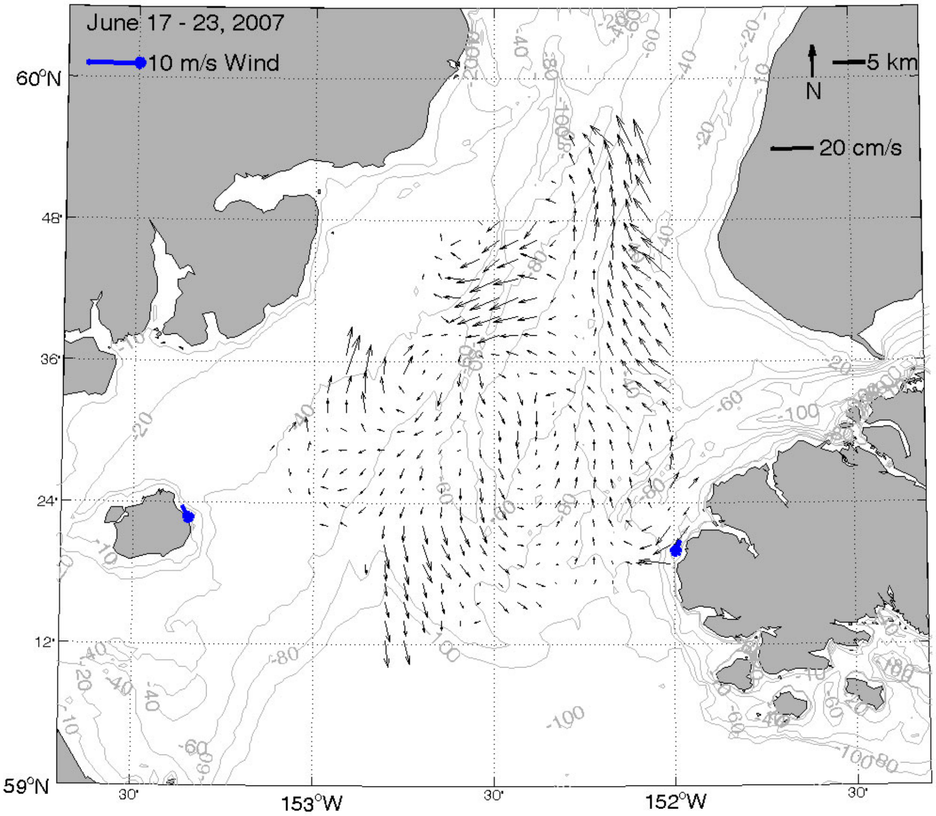

Figure 121. Weekly mean current (black) and wind (blue) vectors overlaid on bathymetry contours (meters) for June 17 - 23, 2007.

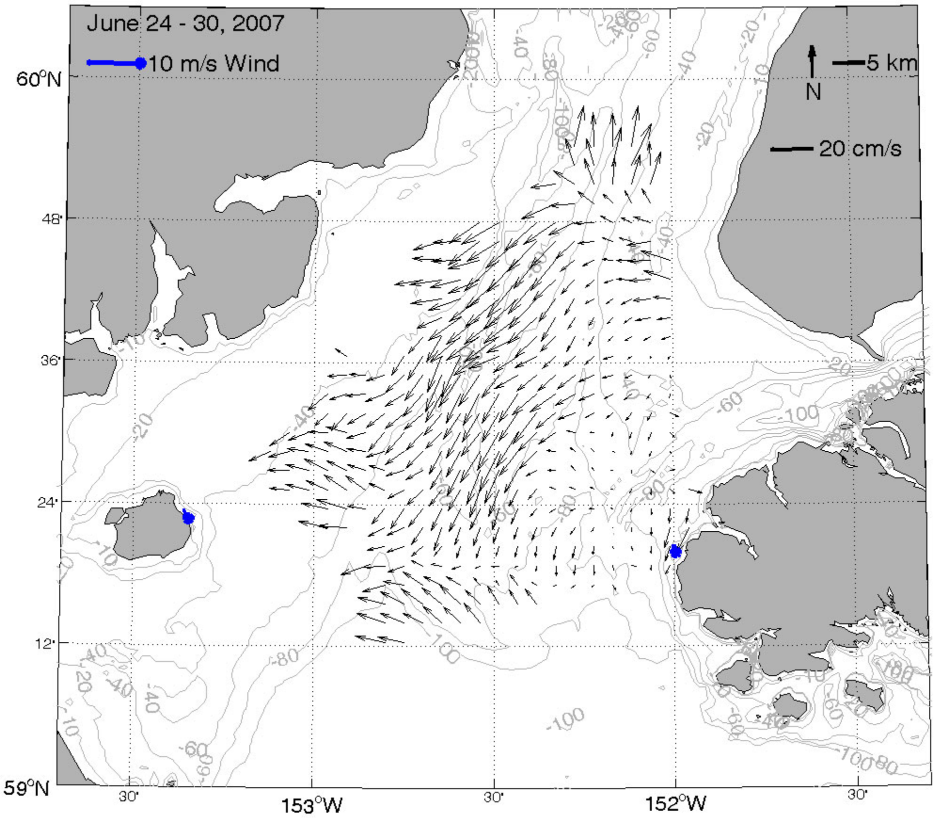

Figure 122. Weekly mean current (black) and wind (blue) vectors overlaid on bathymetry contours (meters) for June 24 - 30, 2007.

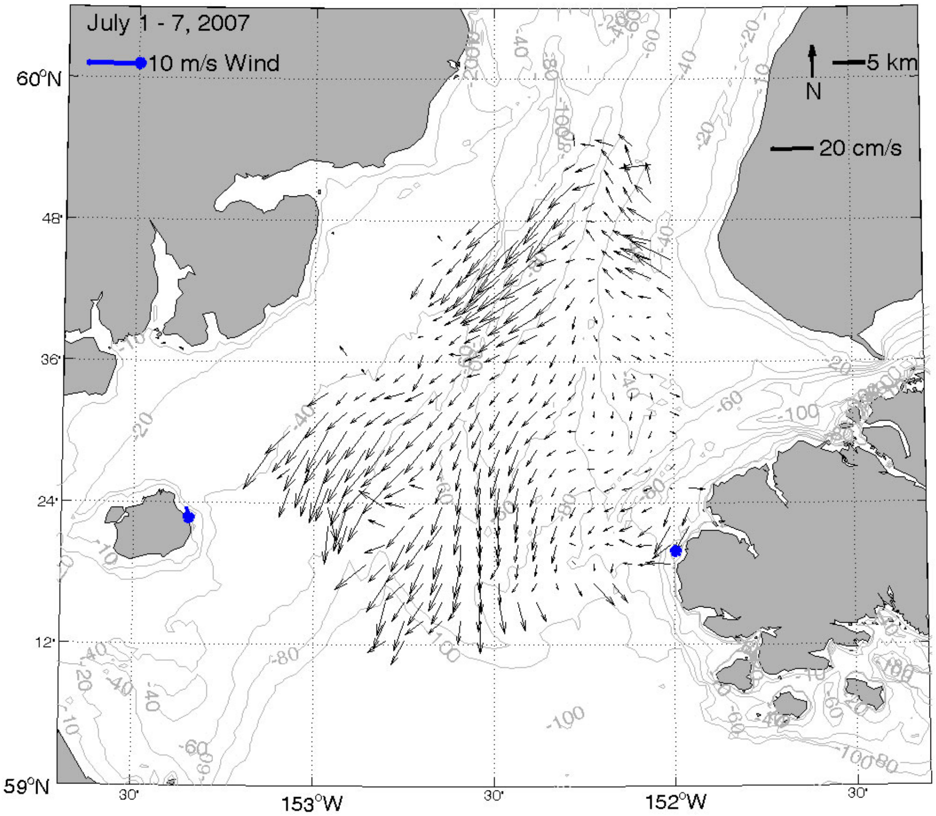

Figure 123. Weekly mean current (black) and wind (blue) vectors overlaid on bathymetry contours (meters) for July 1 - 7, 2007.

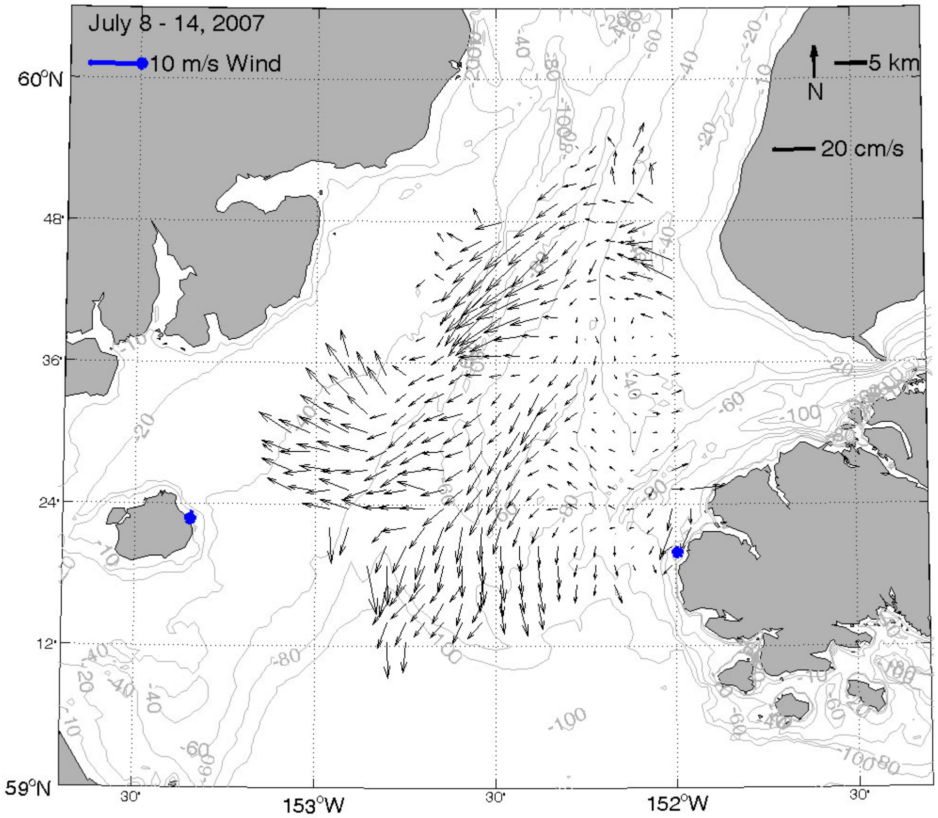

Figure 124. Weekly mean current (black) and wind (blue) vectors overlaid on bathymetry contours (meters) for July 8 - 14, 2007.

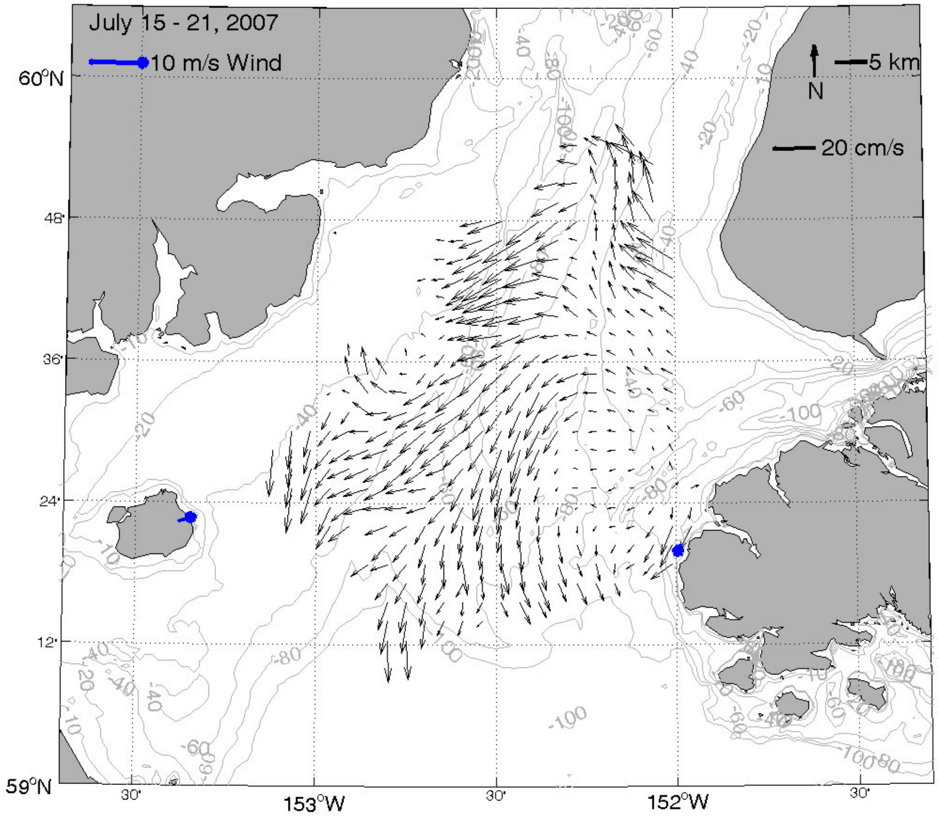

Figure 125. Weekly mean current (black) and wind (blue) vectors overlaid on bathymetry contours (meters) for July 15 - 21, 2007.

Currents became more variable in direction and magnitude from July 29 - August 4 (Figure 127). Cyclonic circulation was recorded near the mouth of Kachemak Bay with currents to the north offshore of Anchor Point and to the west in the northwest portion of data returns. Currents near Augustine Island were northwest in direction, while currents in the southern portion of the radar mask were predominantly southward in direction, although there was westward flow recorded into the southwest portion of the returns. Winds were consistently light and variable. By the next week, August 5 - 11, cyclonic circulation at the mouth of Kachemak Bay was no longer existent, and currents in the northern portion of the HFR mask deflected to the west-southwest along the shipping channel (Figure 128). Currents along the western boundary decreased in magnitude, and currents in the southern region remained predominantly southward in direction. The following week, eastward flow was recorded along the axis of the mouth of Kachemak Bay and northward flow was once again recorded offshore of Anchor Point (Figure 129). Currents along the western boundary were southward, as was the jet from the eastern to western trough, while currents over the eastern trough were minimal. Currents in the southern portion remained southward in direction, other than the westward flow at the southwest edge of radar returns.

By the week of August 19 – 25 (Figure 130), currents increased in magnitude, and a prominent cyclonic circulation cell developed in the southern portion of the mask, suggesting upwelling of waters from depth to the surface. The northwestern portion of the mask showed strong southwestern currents with a westward flow toward Augustine Island. Currents offshore of Anchor Point flowed northward, while currents at the mouth of Kachemak Bay were eastward. A small area of westward flow persisted in the southwest area of returns. By the following week, the cyclonic circulation that dominated the southern inlet had dissipated, resulting in weak flow over the eastern trough and southward flow over the western trough. However, a cyclonic circulation was evident at the mouth of Kachemak Bay (Figure 131). Flow in the west was toward the Augustine Island, and currents near Anchor Point were northward. Winds remained lights and variable.

During the first week in September, westward flow at the southern edge of the radar mask was very prominent, suggesting a greater influence of the ACC on waters in Lower Cook Inlet (Figure 132). Currents offshore of Nanwalek were southward, while waters offshore of Anchor Point were northward. Along the eastern edge of the mask, the flow was westward into the center of the Inlet, while in the west, currents were westward in the shallower areas and southwest in the western trough. The flow was similar during the week of September 9 - 15 except offshore of Nanwalek where the southern flow reversed to northward and then veered eastward into outer Kachemak Bay (Figure 133).

From September 16 - 22, currents were southward over much of the domain (Figure 134). Cyclonic circulation dominated flow near the mouth of Kachemak Bay with westward flow north of the mouth and eastward flow in the south. Currents were more variable in direction from September 23 - 29 (Figure 135). Then, flow offshore of Anchor Point was northward, and currents in the west were southwestward, while currents in the south were southward. Offshore of Nanwalek the flow was eastward into Kachemak Bay. A week later eastward winds with speeds of ~5 m/s developed. Currents in the southeastern area of the mask were eastward, while in the western region currents were southwestward (Figure 136). Currents offshore of Anchor Point continued flowing to the northwest.

Mean winds for October 7 - 13 were ~5 m/s to the south-southeast, and although current speeds were greater, the current pattern closely resembled the annual mean, and included cyclonic

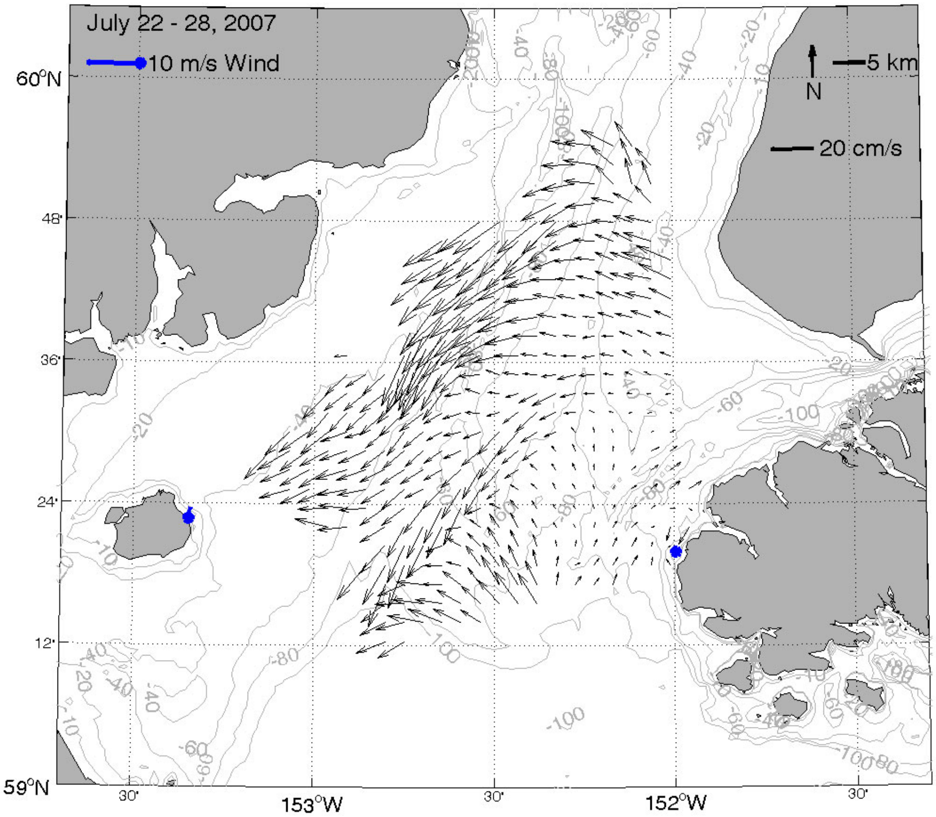

Figure 126. Weekly mean current (black) and wind (blue) vectors overlaid on bathymetry contours (meters) for July 22 - 28, 2007.

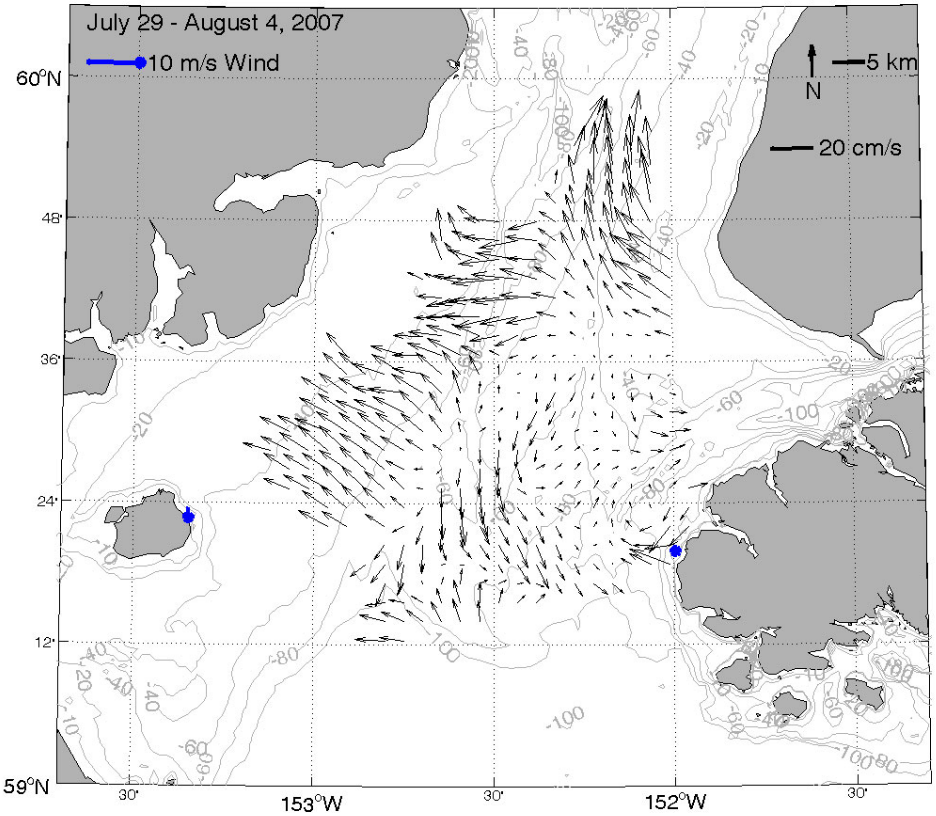

Figure 127. Weekly mean current (black) and wind (blue) vectors overlaid on bathymetry contours (meters) for July 29 - August 4, 2007.

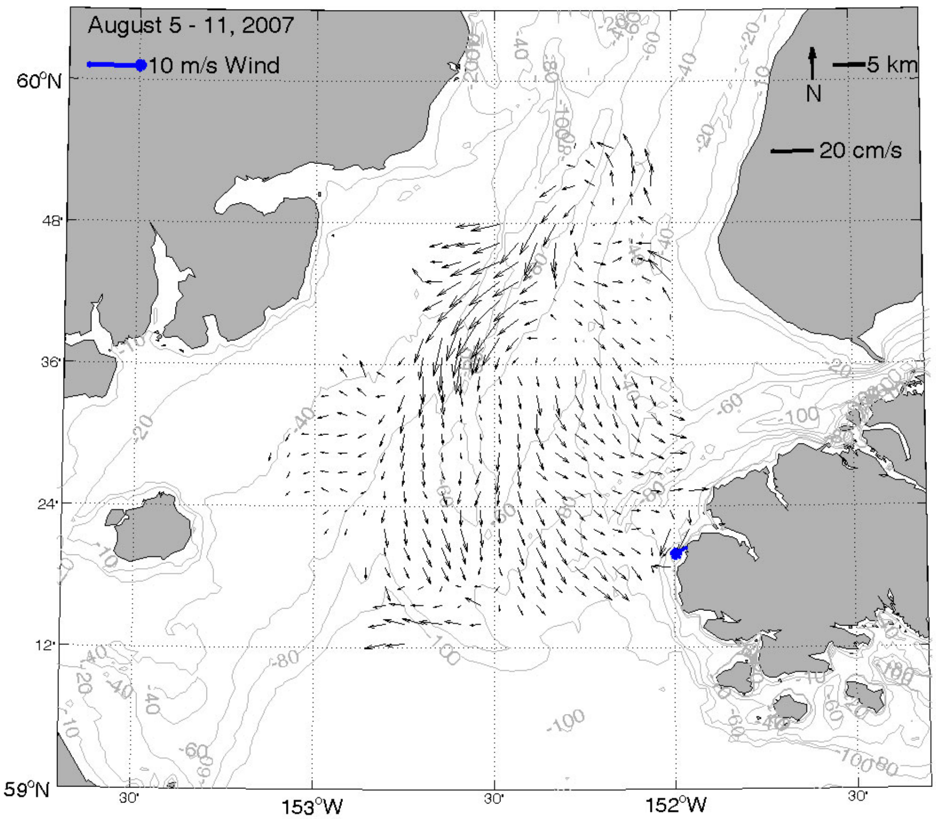

Figure 128. Weekly mean current (black) and wind (blue) vectors overlaid on bathymetry contours (meters) for August 5 - 11, 2007.

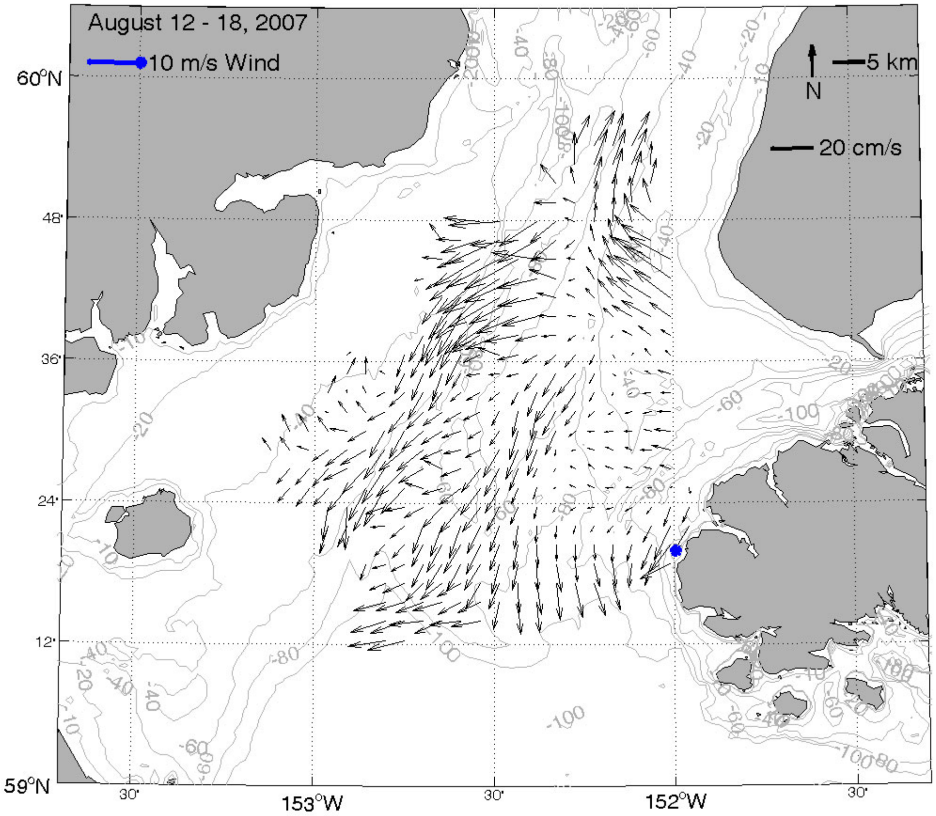

Figure 129. Weekly mean current (black) and wind (blue) vectors overlaid on bathymetry contours (meters) for August 12 - 18, 2007.

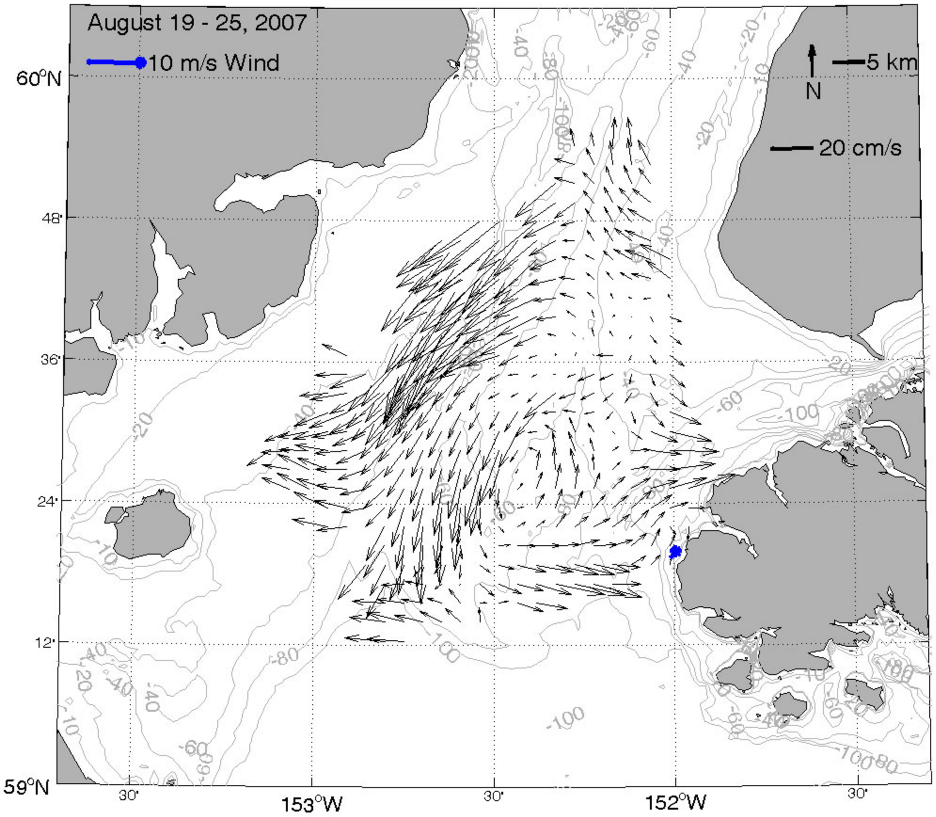

Figure 130. Weekly mean current (black) and wind (blue) vectors overlaid on bathymetry contours (meters) for August 19 - 25, 2007.

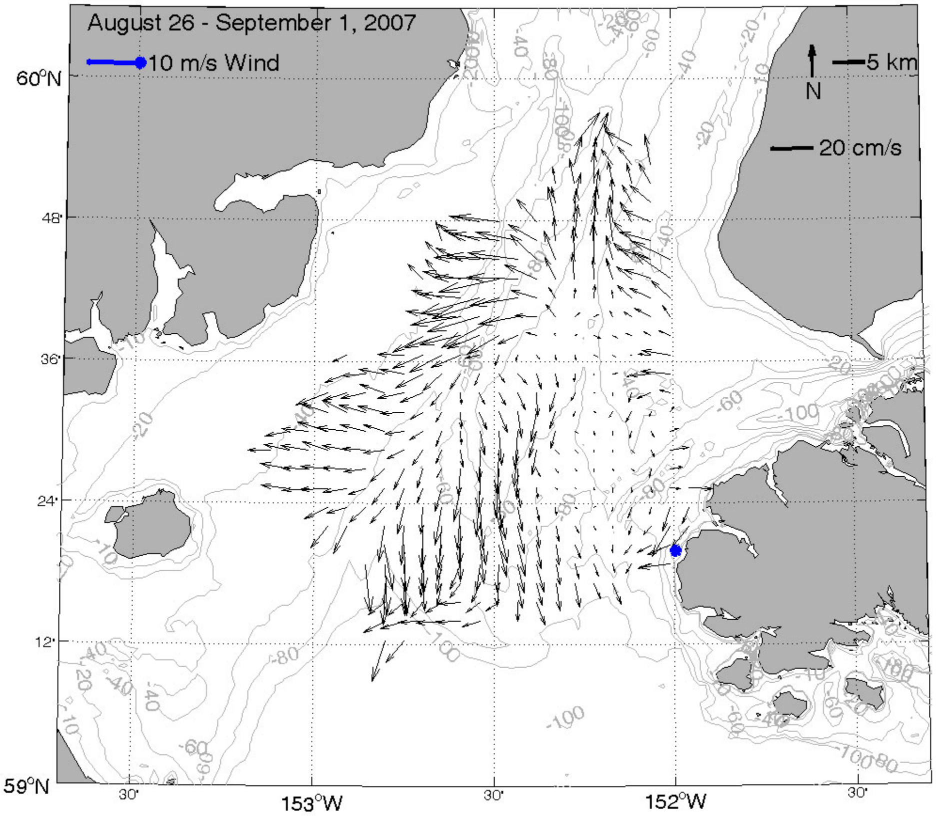

Figure 131. Weekly mean current (black) and wind (blue) vectors overlaid on bathymetry contours (meters) for August 26 - September 1, 2007.

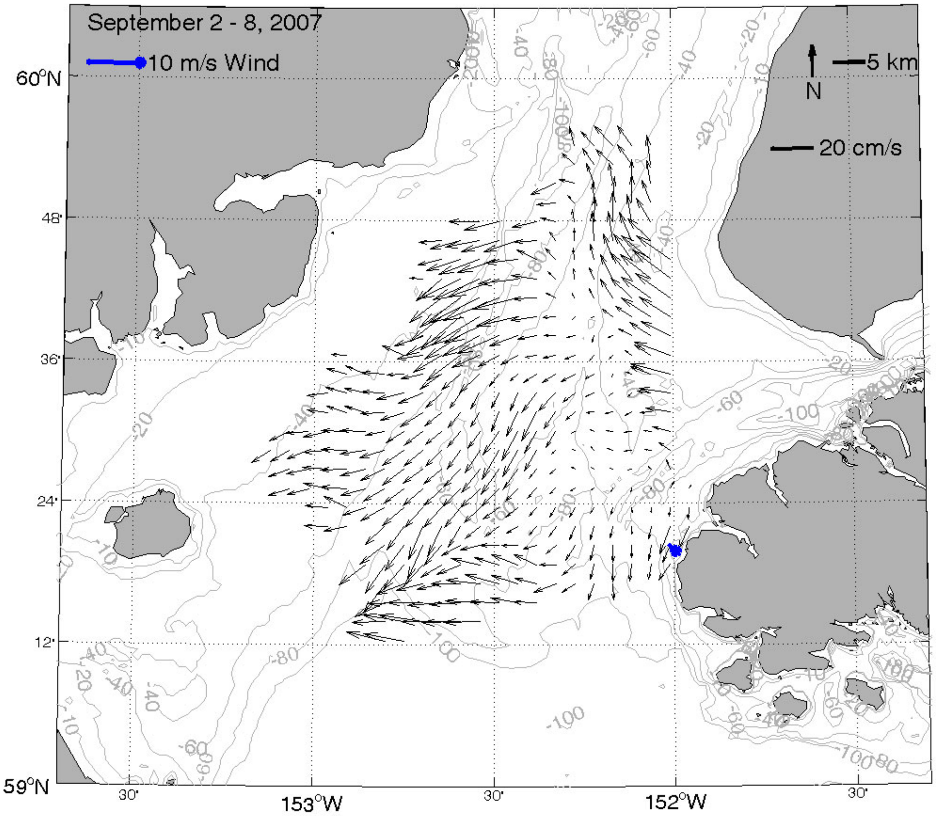

Figure 132. Weekly mean current (black) and wind (blue) vectors overlaid on bathymetry contours (meters) for September 2 - 8, 2007.

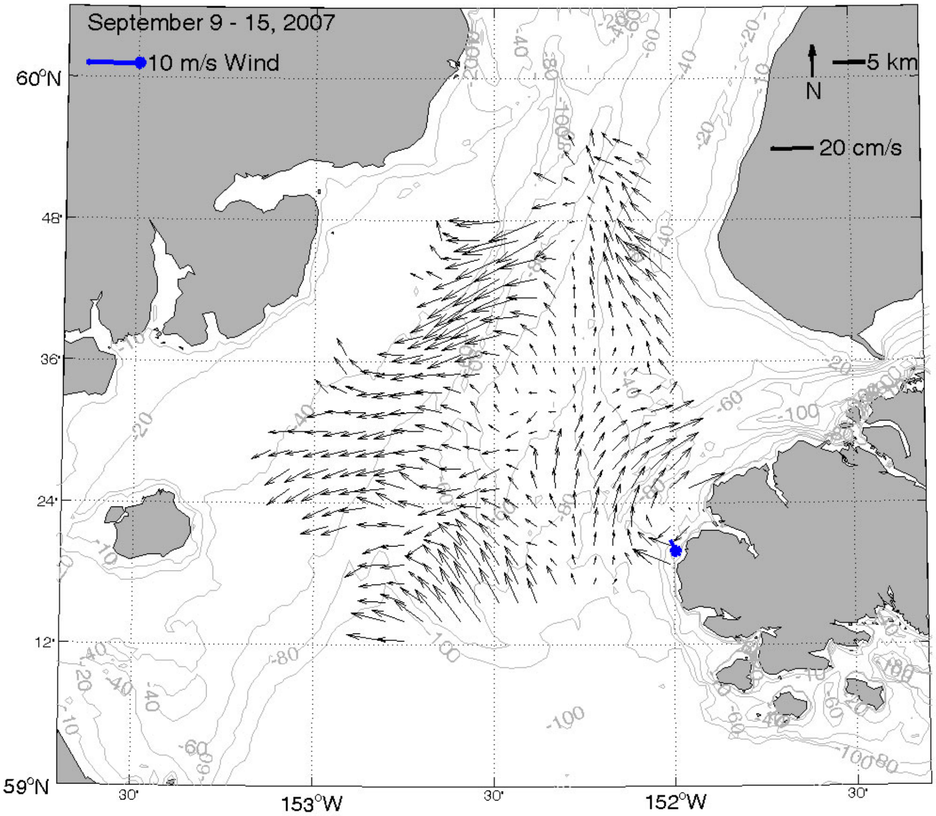

Figure 133. Weekly mean current (black) and wind (blue) vectors overlaid on bathymetry contours (meters) for September 9 - 15, 2007.

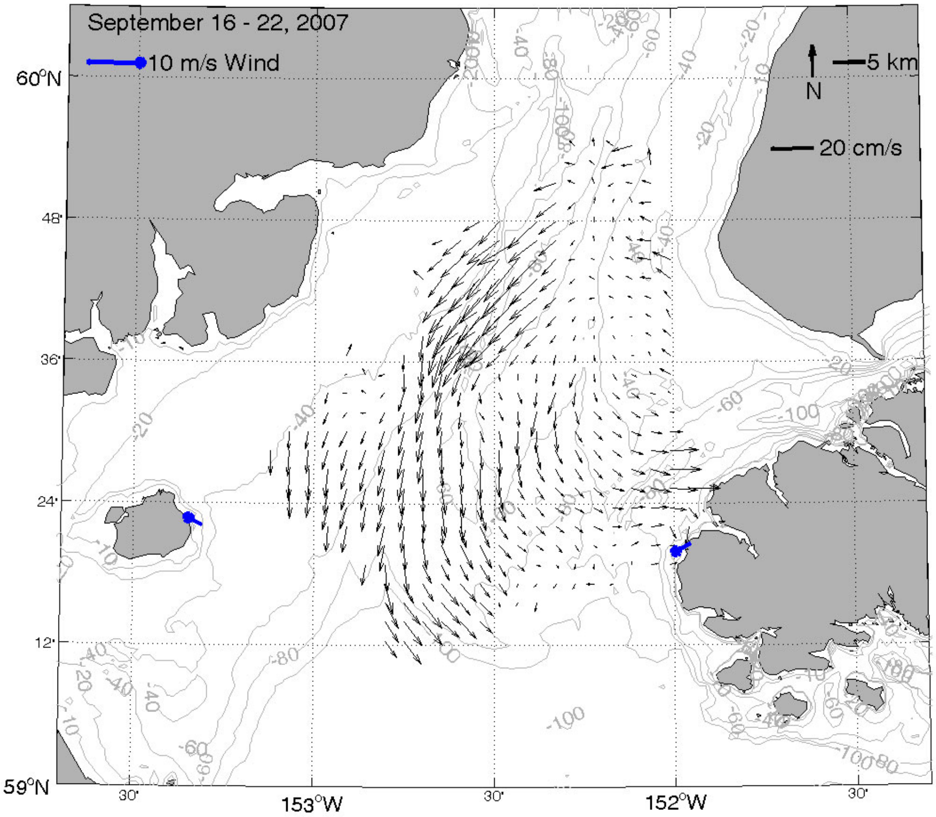

Figure 134. Weekly mean current (black) and wind (blue) vectors overlaid on bathymetry contours (meters) for September 16 - 22, 2007.

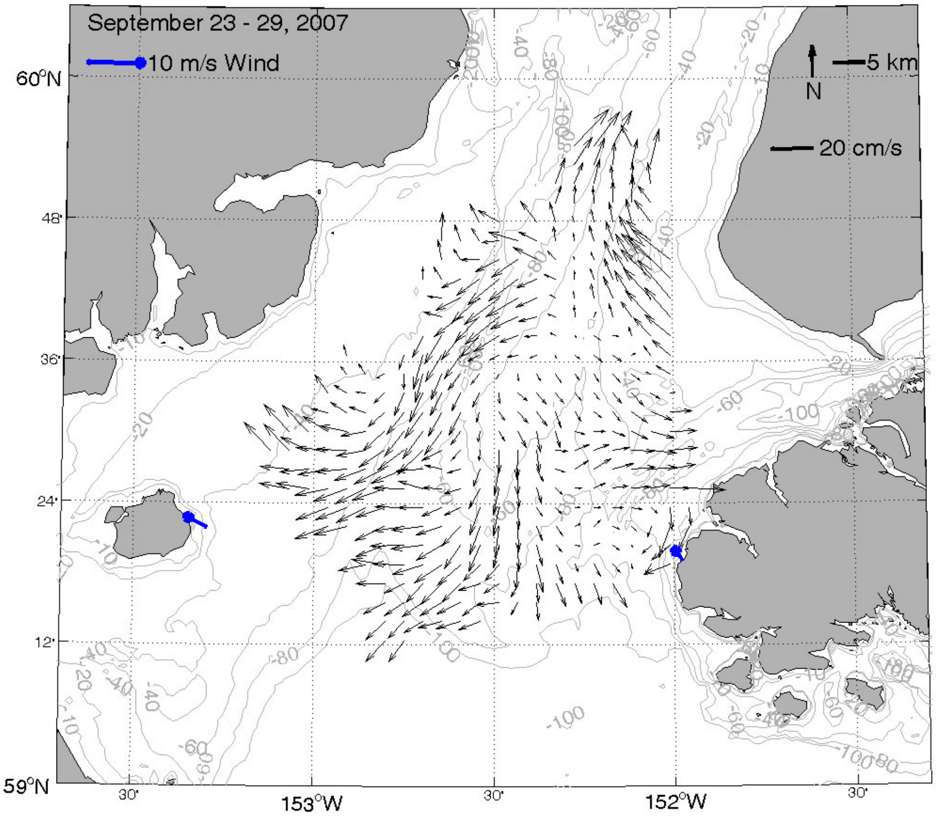

Figure 135. Weekly mean current (black) and wind (blue) vectors overlaid on bathymetry contours (meters) for September 23 - 29, 2007.

circulation near the mouth of Kachemak Bay and westward ACC flow along the southern edge of the radar mask (Figure 137). By the following week, winds decreased, and a cyclonic circulation set up over the entire domain of Lower Cook Inlet (Figure 138). This feature persisted through October 27. However, by the end of the week of October 21, currents in the west shifted from south to westward and the flow offshore of Anchor Point was northward (Figure 139). By the week of October 28, currents returned to the annual mean pattern when winds were weak and variable (Figure 140). During the last week of sampling, currents increased under westward winds (Figure 141). Near the Inlet mouth the flow was northward and near Augustine Island the flow was westward. Offshore of Anchor Point, currents flowed northward into the middle of Cook Inlet.

4.0 Discussion

Tidal currents dominate the circulation variability in Lower Cook Inlet accounting for at least 67% the current variability and, in many locations, more than 85% of the variance. The dominant tidal constituents are the M_2 and S_2 semi-diurnal tides, followed by the N_2, L_2, and K_1 constituents, all with similar magnitudes. The predominance of the semi-diurnal tides is due to the geometry of Cook Inlet, which promotes tidal resonance at about the semi-diurnal period.

The major axes of the tidal constituents are influenced by the bathymetry. These axes are aligned north/south in the center of Lower Cook Inlet, but, closer to the mouth of Kachemak Bay, the axes are aligned north-northeast/south-southwest and thus suggest surface water exchange between the Inlet and the Bay. Although not presented, non-linear tidal constituents also add to the current variance in some of the shallower areas within the tidal mask, such as offshore of Anchor Point.

The mean non-tidal surface current circulation includes:

1. westward flow along the southern portion of the Inlet;
2. southward flow, which is swiftest along the western edge of the radar mask and over the steep topography along the western side of the Western Basin;
3. northward flow north and offshore of Anchor Point; and
4. a weak cyclonic eddy over Lower Cook Inlet offshore of Nanwalek.

The westward flow at the mouth of Lower Cook Inlet is presumably the ACC flowing westward through Kennedy Entrance, thence along the southern mouth of Cook Inlet before turning south into Shelikof Strait. (Note however, that occasionally ACC waters flow northward offshore of Nanwalek and then appear to enter outer Kachemak Bay). The swift southerly outflow along the western portion of the radar mask presumably reflects the influence of dilute waters associated with river inflows in Upper Cook Inlet. Hence this portion of the current field is likley a coastal-trapped buoyancy-influenced current that extends along the length of western Cook Inlet. All of these outflows ultimately join the ACC and continue southward into Shelikof Strait. The northward flow near Anchor Point appears to be fed by Kachemak Bay waters and probably consists of another buoyancy-influenced coastal current fed by freshwater discharges along the periphery of the Bay.

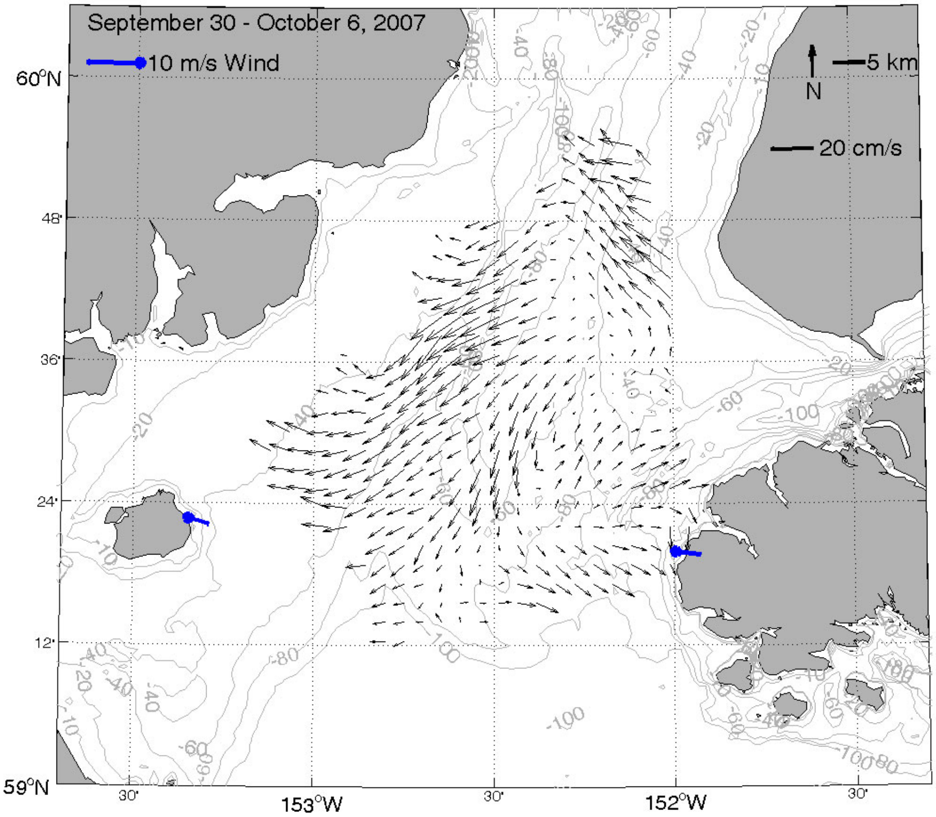

Figure 136. Weekly mean current (black) and wind (blue) vectors overlaid on bathymetry contours (meters) for September 30 - October 6, 2007.

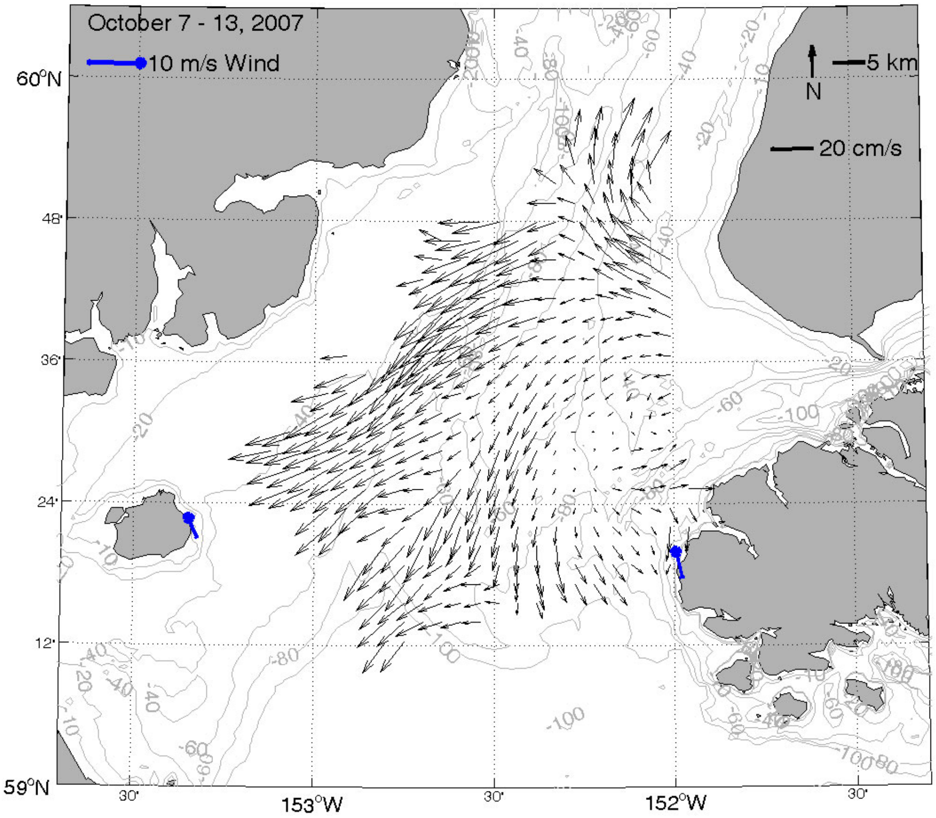

Figure 137. Weekly mean current (black) and wind (blue) vectors overlaid on bathymetry contours (meters) for October 7 - 13, 2007.

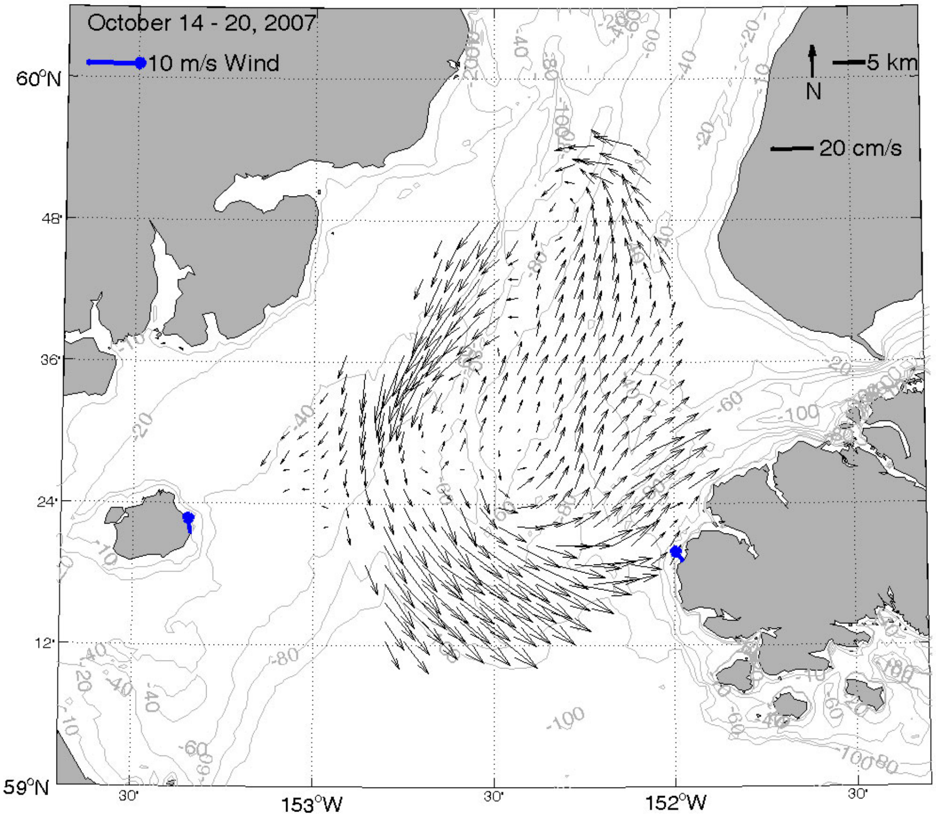

Figure 138. Weekly mean current (black) and wind (blue) vectors overlaid on bathymetry contours (meters) for October 14 - 20, 2007.

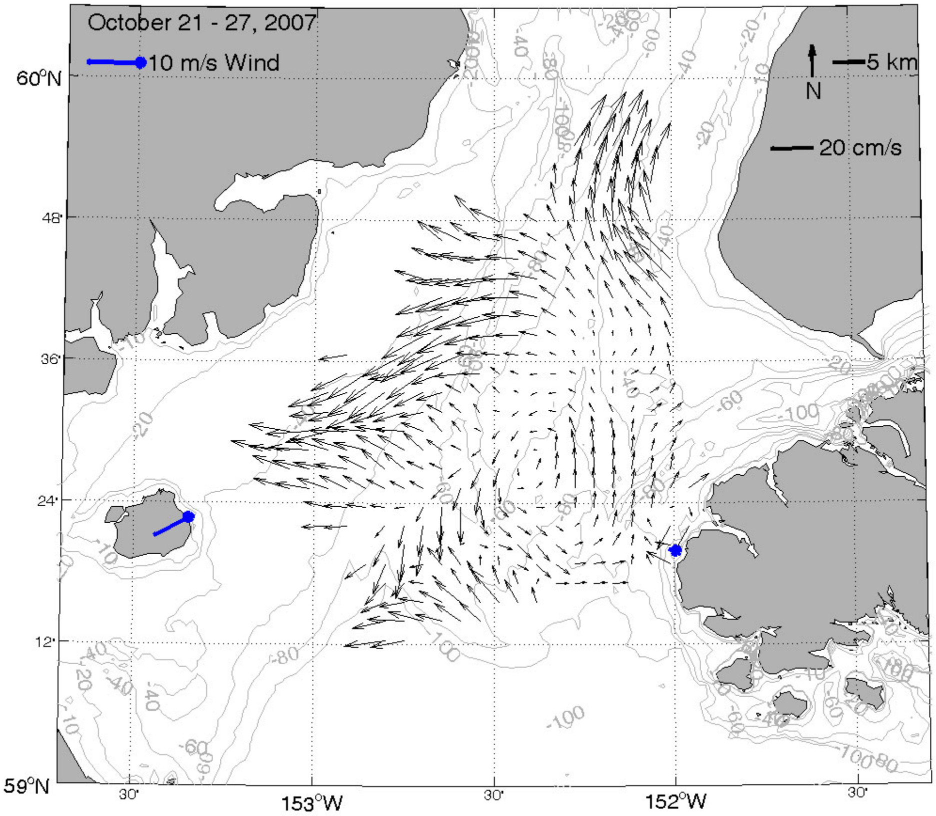

Figure 139. Weekly mean current (black) and wind (blue) vectors overlaid on bathymetry contours (meters) for October 21 - 27, 2007.

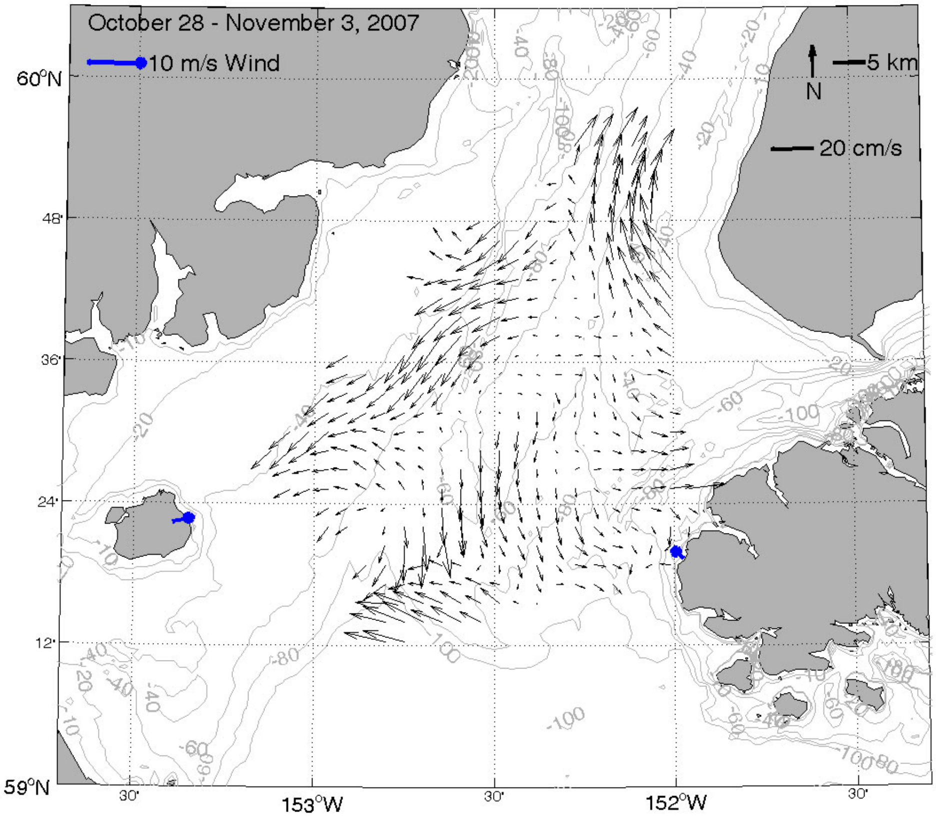

Figure 140. Weekly mean current (black) and wind (blue) vectors overlaid on bathymetry contours (meters) for October 28 - November 3, 2007.

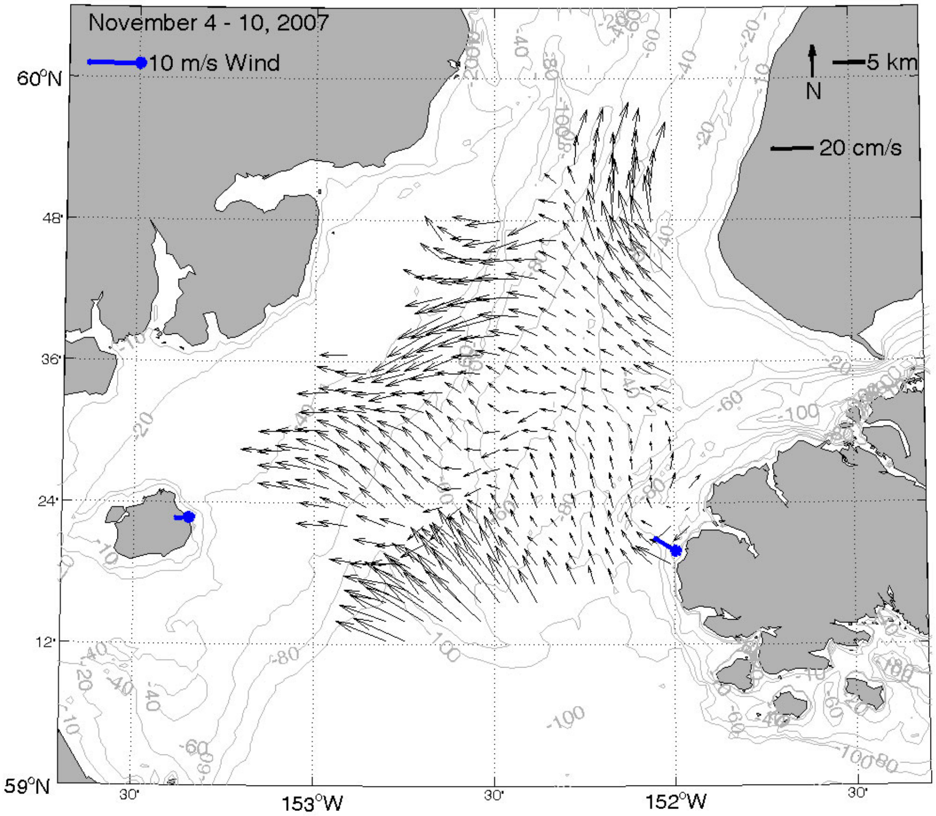

Figure 141. Weekly mean current (black) and wind (blue) vectors overlaid on bathymetry contours (meters) for November 4 - 10, 2007.

In aggregate the net surface flow in Lower Cook Inlet is southward. Mass balance implies this outflow be balanced by river inflows and a deeper inflow. Indeed a deep inflow was observed by Muench et al. (1978 and 1981), and it is probable that it is steered into the Western and Eastern basins of Lower Cook Inlet. From there it may flow up-inlet via an estuarine-type (entrainment) circulation processes and/or upwelled into the surface waters by the eddy in Lower Cook. The latter may be a particularly effective mechanism for introducing more nutrient-rich waters into the surface layer to support biological production.

The non-tidal circulation appears to be only weakly coupled with the wind field. We performed monthly correlations between the winds and non-tidal velocities and found no significant correlation between winds (at either Augustine Island or Flat Island) and the along-inlet velocity component. Cross-inlet velocities and winds are only weakly correlated in general and at best explain about 30% of the non-tidal variance. This may be an artifact of the wind products used in the analyses, since topographic effects may influence the wind measurements at both Augustine and Flat Islands. On the other hand, much of the variability may be related to forcing associated with fronts and the bathymetry and/or processes originating on the continental shelf.

5.0 Future Work

Due to unanticipated costs associated with other aspects of this project, the data obtained from this study of Lower Cook Inlet has not been exhaustively analyzed. In addition, there are now several other data sets from Cook Inlet, which while not collected coincidentally with one another, should be reviewed and analyzed in aggregate. These include previous HFR measurements in the middle of the Inlet (Musgrave and Statscewich 2006) and a temporary HFR deployment in the same area in spring/summer of 2009 in response to the Mt. Redoubt eruption. These data should be combined with the present data set to better define the circulation properties in the Cook Inlet. Specific tasks that could be accomplished in this effort are calculations of tidal energetics and velocities for evaluation of numerical models and the delineation of shear zones associated with tidal rips and/or the non-tidal circulation. In addition, there are numerous CTD profiles gathered during the middle of the decade from both the lower and middle of Cook Inlet (Okkonen and Howell 2003; Okkonen 2005) as well as a number of short-duration (~month-long) current meter moorings collected by NOAA for tidal measurements that should be combined with the HFR data to assess the vertical structure of the currents and hydrography. Moreover, this synthesis activity should permit a better understanding of the estuarine nature of the circulation in Cook Inlet and how that circulation varies seasonally.

The HFR hardware used here did not extend consistently across the entire breadth of Lower Cook Inlet (nor did the system used by Musgrave and Statscewich in Middle Cook Inlet) and so we were unable to measure surface currents on the shallower western side of the Inlet. In the case of middle Cook Inlet this includes the area surrounding the Drift River terminal, and in Lower Cook Inlet the western side of the Inlet includes the probable terminal area for the Pebble Mine, should it be developed. To achieve measurements in these areas will require siting HFRs on the west coast of Cook Inlet. However, power is unavailable along this shoreline so measurements will require an autonomous power supply such as that under development at the University of Alaska (http://www.ims.uaf.edu/artlab/).

Similarly, power availability could prove to be a constraint on allowing adequate sampling of the exchange between Kachemak Bay and Lower Cook Inlet, which was not achieved in this study. An alternative sampling design is required to assess this exchange, and if HFR is desired, the installations will either require multiple (three or more) HFR sites or autonomous power.

List of References

Aagaard, K. 1984. The Beaufort Undercurrent. In: Barnes, P.W., D.M. Schell, and E. Reimnitz, eds. The Alaskan Beaufort Sea: Ecosystems and Environment. New York: Academic Press. p. 47-71.

Aagaard, K. and A.T. Roach. 1990. Arctic ocean-shelf exchange: Measurements in Barrow Canyon. J. Geophys. Res. 95:18163-18175.

Barrick, D.E., B.J. Lipa, and R.D. Crissman. 1985. Mapping Surface Currents with CODAR. Sea Technology 26:43-48.

Barrick, D.E. and B.J. Lipa. 1986. Correcting for Distorted Antenna Patterns in CODAR Ocean Surface Measurements. IEEE J. of Oceanic Engr. OE-11(2):304-309.

Barrick, D.E.. 2002. Geometrical Dilution of Statistical Accuracy (GDOSA) in Multi-Static HF Radar Networks. White Paper.
http://www.codar.com/Manuals/SeaSonde/Docs/Informative/GDOSA_Definition.pdf

Barrick, D.E. and R. Long. 2006. How Salinity Affects Radar Performance: A Case Study of 24 MHz HF Radar Performance in San Francisco Bay During the 2006 New Year Storm Floor. White Paper.

Brower, W.A. Jr., R.G. Baldwin, C.N. Williams Jr., J.L .Wise, and L.D. Leslie. 1988. Climate atlas of the outer continental shelf waters and coastal regions of Alaska, volume III, Chukchi-Beaufort Sea. Asheville: National Climatic Data Center. 497 pp.

Burbank, D. 1977. Circulation studies in Kachemak Bay and lower Cook Inlet, volume III, In: Environmental Studies of Kachemak Bay and Lower Cook Inlet. Marine/Coastal Habitat Management Report, Alaska Dept. Fish and Game, Anchorage, AK.

Carmack, E.C., R.W. Macdonald, and J.E. Papdakis. 1989. Water mass structure and boundaries in the Mackenzie Shelf Estuary. J. Geophys. Res. 94:18043-18055.

CODAR Ocean Sensors. 2002. Defining First-Order Region Boundaries. White Paper. 9 pp. (http://www.codar.com/Manuals/SeaSonde/Docs/Informative/FirstOrder_Settings.pdf)

CODAR Ocean Sensors. 2006. What Goes In Should Come Out... CODAR Currents Newsletter. p. 4-6. (http://www.codar.com/images/news/Newsletter_0906.pdf)

Colonell, J.M. and B.J. Galloway. 1997. Wind-driven transport and dispersion of age-0 arctic ciscoes along the Alaska Beaufort coast. In: Fish Ecology in Arctic North America. American Fisheries Society Symposium 19, Bethesda, MD. p. 90-103.

Danielson, S., M. Johnson, S. Solomon, and W. Perrie. 2008. 1 km Gridded Bathymetric Dataset Based on Ship Soundings: A research tool for the waters of eastern Russia, Alaska & western Canada. 2008 Alaska Marine Science Symposium, Anchorage, Alaska. Poster presentation.

Emery, W.J. and R.E. Thomson. 1997. The Spatial Analyses of Data Fields. In: Data Analysis Methods in Physical Oceanography. New York: Pergamon. p. 305-370.

Fong, D. and W. R. Geyer. 2001. Response of a river plume during an upwelling favorable wind event. J. of Geophys. Res. 106(C1):1067-1084.

Godin, G. 1972. The Analysis of Tides. Toronto: University of Toronto Press. 264 pp.

Guay, C.K. and K.K. Falkner. 1998. A survey of dissolved barium in the estuaries of major Arctic rivers and adjacent seas. Cont. Shelf Res. 8:859-882.

Gurgel, K.W. 1997. Experience with shipborne measurements of surface currents fields by HF Radar. Oceanography 10(2):82-84.

Haley, B., G. Tomlins, O. Smith., W. Wilson, and M. Link. 2000. Mapping Cook Inlet Rip Tides Using Local Knowledge and Remote Sensing. MMS OCS Study 2000-025. Final Report MMS Contract No. 01-98-CT-30906. 67 pp.

Johnson, M. 2008. Water and Ice Dynamics in Cook Inlet. MMS OCS Study 2008-061. Final Report. 106 pp.

Johnson, W.R., C.F. Marshall, and E.M. Lear. 2002. Oil-Spill Risk Analysis: Cook Inlet Planning Area, OCS Lease Sales 191 and 199. MMS OCS Study 2002-074. Final Report. 76 pp.

Kozo, T.L. 1980. Mountain barrier baroclinicity effects on surface winds along the Alaskan Arctic coast. Geophys. Res. Lett. 7:377-380.

Kozo, T.L. 1982a. A mathematical model of sea breezes along the Alaska Beaufort Sea coast. J. Appl. Met. 21:906-924.

Kozo, T.L. 1982b. An observational study of sea breezes along the Alaska Beaufort Sea coast. J. Appl. Met. 21:891-905.

Kozo, T.L. 1984. Mesoscale wind phenomena along the Alaskan Beaufort Sea coast. In: P. Barnes and E. Reimnitz, eds. The Alaskan Beaufort Sea: Ecosystems and Environment. New York: Academic Press. p. 23-45.

Lipa, B.J., R.D. Crissman, and D.E. Barrick. 1986. HF Radar observations of Arctic pack-ice breakup. IEEE J. of Oceanic Engr. OE-11(2):270-275.

Macdonald, R.W., E.C. Carmack, F.A. McLaughlin, K. Iseki, D.M. Macdonald, and M.C. O'Brien. 1989. Composition and Modification of water masses in the Mackenzie Shelf Estuary. J. Geophys. Res. 94:18057-18070.

Macdonald, R.W. and E.C. Carmack. 1991. The role of large-scale under-ice topography in separating estuary and ocean on an arctic shelf. Atmosphere-Ocean 29:37-51.

Macdonald, R.W., E.C. Carmack, F.A. McLaughlin, K.K. Falkner, and J.H. Swift. 1999. Connections among ice, runoff, and atmospheric forcing in the Beaufort Gyre. Geophys. Res. Lett. 26(15):2223-2226.

Macdonald, R.W., E.C. Carmack, and D.W. Paton. 1999. Using the delta ^{18}O composition in landfast ice as a record of arctic estuarine processes. Mar. Chem. 65:3-24.

MBC Applied Environmental Sciences. 2004. Proceedings: U.S. Minerals Management Service Research Sponsorship Meeting to Map Surface Currents in the Beaufort Sea and Cook Inlet from High Frequency Doppler Radar. MMS OCS Study 2004-045. Final Report MMS Contact No. 1435-01-02-CT-31150. 37 pp.

Mountain, D.G., L.K. Coachman, and K. Aagaard. 1976. On the Flow Through Barrow Canyon. J. Phys. Oceanogr. 6(4):461-470.

Muench, R.D., H.O. Mofjeld, and R.L. Charnell. 1978. Oceanographic conditions in Lower Cook Inlet: Spring and Summer 1973. J. Geophys. Res. 83:5090-5098.

Musgrave, D.L. and H. Statscewich. 2006. CODAR in Alaska. MMS OCS Study 2006-032. Final Report. 28 pp.

Niebauer, H.J., T.C. Royer, and T.J. Weingartner. 1994 Circulation of Prince William Sound, Alaska. J. Geophys. Res. 99:14,113 – 14,126.

North, G.R., T.L. Bell, R.F. Cahalan, and F.G. Moeng. 1982. Sampling errors in the estimation of empirical orthogonal functions. Mon. Weath. Rev. 110:699-706.

Okkonen S.R. and S. S. Howell. 2003. Measurements of Temperature, Salinity and Circulation in Cook Inlet, Alaska. MMS OCS Study 2003-036. Final Report. 32 pp.

Okkonen, S. R. 2005. Observations of Hydrography and Currents in Central Cook Inlet, Alaska, During Diurnal and Semidiurnal Tidal Cycles. MMS OCS Study 2004-058. Final Report. 28 pp.

Okkonen, S.R., C.J. Ashjian, R.G. Campbell, W. Maslowski, J.L. Clement-Kinney, and R. Potter. 2009. Intrusion of warm Bering/Chukchi waters onto the shelf in the western Beaufort Sea, J. Geophys. Res. 114:C00A11, doi:10.1029/2008JC004870.

Okkonen, S.R., S. Pegau, and S. Saupe. 2009. Seasonality of Boundary Conditions for Cook Inlet, Alaska. MMS OCS Study 2009-041. Final Report. 64 pp.

Pawlowicz, Rl, B. Beardsley, and S. Lentz, 2002. Classical tidal harmonic analysis including error estimates in MATLAB using T_TIDE. Computers and Geosciences 28:929-937.

Pickart, R.S. 2004. Shelfbreak circulation in the Alaskan Beaufort Sea: Mean structure and variability. J. Geophys. Res. 109:C04024, doi:10.1029/2003JC001912.

Pickart, R.S., T.J. Weingartner, L.J. Pratt, S. Zimmermann, and D.J. Torres. 2005. Flow of winter-transformed Pacific water into the western Arctic. Deep-Sea Res. II 52(24-26):3175-3199.

Royer, T.C. 1998. Coastal Processes in the northern North Pacific. In: The Sea. A.R. Robinson and K. H. Brink (eds.), John Wiley and Sons, NY, p. 395 – 414.

Royer, T.C., J.A. Vermisch, T.J. Weingartner, H.J. Niebauer, and R.D. Muench. 1990. Ocean circulation influencing the Exxon Valdez oil spill. Oceanography 3:3 – 10.

Schumacher, J.D., C.A. Pearson, and R. K. Reed. 1982. An exchange of water between the Gulf of Alaska and the Bering Sea through Unimak Pass. J. Geophys. Res. 87:5785-5795.

Stabeno, P.J., R.K. Reed, and J.M. Napp. 2002. Transport through Unimak Pass, Alaska. Deep-Sea Res. II 49(26):5931 – 5943.

Stabeno, P.J., R.K. Reed and J.D. Schumacher. 1995. The Alaska Coastal Current: continuity of transport and forcing. J. Geophys. Res. 100:2477-2485.

Taylor, K.D., and T.J. Weingartner. 2007. Unpublished data. University of Alaska Fairbanks. Fairbanks, Alaska.

Thomson, R.E., Hickey, and LeBlond. 1989. The Vancouver Island Coastal Current: Fisheries barrier and conduit. In: Effects of ocean variability on recruitment and an evaluation of parameters used in stock assessment models. Canadian Special Publication in Fisheries and Aquatic Sciences, R.J. Beamish and G.A. McFarlane (ed.), p. 265 – 296.

Veltkamp, B. and Wilcox, J.R. 2007. Nearshore Beaufort Sea Meteorological Monitoring and Data Synthesis Project. MMS OCS Study 2007-011. Final Report MMS Contract 1435-01-05-CT-39037. 107 pp.

Weingartner, T.J., K. Aagaard, R. Woodgate, S. Danielson, Y. Sasaki, and D. Cavalieri. 2005. Circulation on the North Central Chukchi Sea Shelf. Deep-Sea Res. II 52(24-26):3150-3174.

Weingartner, T.J., S.L. Danielson, Kasper, J.L., and S.R. Okkonen. 2009. Circulation and Water Property Variations in the Nearshore Alaskan Beaufort Sea. MMS OCS Study 2009-035. Final Report MMS Contract M03PC00015. 167 pp.

Woodgate, R.A., K. Aagaard, and T. Weingartner. 2005. Monthly temperature, salinity, and transport variability of the Bering Strait throughflow. Geophys. Res. Lett. 32(4), doi: 10.1029/2004GL022112.

Acknowledgements

The authors would like to thank the U.S. Minerals Management Service for this funding opportunity, the original principal investigator who secured the funding, David Musgrave, and our COTR, Warren Horowitz. There were many technicians who helped with this project, without whom this study could not have taken place: Hank Statscewich, Tony D'Aoust, Andrew Bray, Jeremy Kasper, David Leech, and David Janka. CODAR Ocean Sensors, especially Belinda Lipa, provided expert help with the analyses, and the MATLAB Toolbox developed by David Caplan further facilitated the analyses. In Prudhoe Bay, we would like to acknowledge both BP and Alaska Clean Seas for their support during the 2006 field season. BP provided power, lodging, meals, and transportation as well as long-distance troubleshooting support, while Alaska Clean Seas provided boat support for the antenna pattern measurement. Seth Danielson processed the Beaufort Sea ADCP data used for validation. In Cook Inlet, we are indebted to Buzz and Susan Kyllonen and the Nanwalek Tribal Council for allowing us the use of their land. James Kvasnikoff was an invaluable resource and excellent addition to our support team in Nanwalek who quickly became a friend. Kachemak Bay Research Reserve provided lodging in Homer Alaska, and Cook Inlet Regional Citizens Advisory Council provided boat support for our antenna pattern measurements in Cook Inlet. Elizabeth Wasserman provided long-distance support for our field site in Anchor Point.

APPENDIX A

Table 3. Field log listing frequency switches, notes, and significant events for the 2005 Endicott field season.

Date	Time(UTC)	Frequency	Event/Observation
6/2/2005	17:40	12.95	First Cross Spectra collected
6/30/2005	18:10	12.95	Power turned off, Rx Antenna is retrofitted with Dual Frequency Antenna
6/30/2005	19:00	12.95	Power turned back on, data collection started
7/11/2005	23:30	25.35	Change frequency
7/14/2005	19:20	12.47	Change frequency
7/14/2005	19:40	13.51	Change frequency
7/14/2005	22:00	13.49	Change frequency
7/14/2005	23:20	13.51	Change frequency, first quality sea echo observed
7/15/2005	0:30	25.35	Change frequency
7/15/2005	0:40	13.51	Change frequency
7/22/2005	22:20	25.35	Change frequency
8/1/2005	23:10	13.51	Change frequency
8/2/2005	21:50	13.51	Data logging stopped, reason unknown, possibly due to power but no evidence that the battery backup engaged
8/14/2005	17:20	13.51	Data logging started, asked Endicott security to reboot laptop
8/21/2005	21:20	13.51	Data logging stopped for APM measurement
8/21/2005	21:58	13.51	APM
8/21/2005	23:52	25.35	APM
8/21/2005	0:44	25.35	Tx APM
8/22/2005	1:10	25.35	Resume data collection, change frequency
9/1/2005	15:50	25.35	Installed 25Mhz pattern in all folders, turned on measured radials,
9/28/2005	23:50	13.51	Change frequency
9/30/2005	3:10	13.51	Changed settings so that 64 range cells are processed
10/13/2005	20:00	13.51	No sea echo detected possibly due to sea ice
10/26/2005	18:10	13.51	Last CSS file produced, system is taken down and winterized

Table 4. Field log listing frequency switches, notes, and significant events for the 2005 West Dock field season.

Date	Time (UTC)	Frequency	Event/Observation
5/25/2005	19:00	13.56	First Cross Spectra collected
5/25/2005	19:10	12.47	Change Frequency
6/7/2005	0:00	12.47	Lost Power switch to Battery Backup
6/9/2005	16:10	12.47	Last CSS file produced, Battery Backup is drained
6/29/2005	18:20	12.47	Power turned back on, data collection started
6/29/2005	18:30	12.47	Laptop is turned off, Data collection is stopped
6/30/2005	21:40	12.47	Power turned back on, data collection started, Rx Antenna is retrofitted with Dual Freq Antenna
7/1/2005	17:00	12.47	Laptop is turned off, data collection is stopped
7/13/2005	23:00	12.47	Laptop power turned back on, data collection started
7/13/2005	23:30	12.47	Data collection stopped
7/14/2005	8:00	25.32	Data collection started, Change frequency
7/14/2005	16:30	25.4	Testing antennas with transponder
7/14/2005	18:40	12.47	Change frequency, testing continued, make internal changes to system
7/14/2005	21:00	13.56	Change frequency, quality sea-echo observed
7/22/2005	21:40	25.35	Change frequency
7/27/2005	19:50	25.35	Stop data collection for APM measurement
7/27/2005	21:00	25.3	APM at 25.3 MHZ
7/27/2005	22:30	13.46	APM at 13.46 MHZ
7/28/2005	0:20	13.46	Tx antenna APM at 13.46 MHZ
7/28/2005	1:30	25.35	Resume normal data collection
7/30/2005	17:22	25.35	Testing switching script
8/1/2005	23:00	13.56	Change Frequency
8/1/2005	23:30	25.35	Change Frequency
8/2/2005	19:00	13.56	Change Frequency
8/2/2005	20:20	13.56	Testing switching script
8/3/2005	18:25	13.56	Observed no seaecho, sent T/R reset , TRCTL 40, TRCTL 0, Atten, refresh
8/5/2005	14:15	13.56	Observed no seaecho, sent T/R reset , TRCTL 40, TRCTL 0, Atten, refresh
8/13/2005	0:20	25.35	Change Frequency
8/21/2005	1:00	25.35	Move Rx Antenna to new location, Testing reveals problem with Tx trap
8/21/2005	16:00	25.35	Stop data collection for APM measurement
8/21/2005	16:40	25.35	APM at 25.3 MHZ
8/21/2005	18:44	13.46	APM at 13.46 MHZ

8/21/2005	19:40	13.46	Resume normal data collection
8/21/2005	20:00	25.35	Change Frequency, Trap problem was causing poor Tx output power
9/29/2005	0:20	25.35	Data collection stopped
9/29/2005	2:30	13.46	Data collection resumed at new frequency, new trap installed
10/10/2005	18:00	13.46	Lost Power, switch to battery backup
10/10/2005	22:40	13.46	Last CSS file produced, Battery Backup is drained
10/25/2005			System is taken down and winterized

Table 5. Field log listing frequency switches, notes, and significant events for the 2006 Endicott field season.

Date	Time (UTC)	Frequency	Event/Observation
6/5/2006			Sea ice had melt water laying on the surface.
6/6/2006		25.30	SeaSonde set up with five 8' whips on the Rx and 2 on the Tx.
6/7/2006			Walking antenna pattern measurement performed at Endicott.
6/8/2006		25.30	Replace the 8' ground plane whips on the Rx antenna with 4' whips.
6/12/2006		25.30	ACS reports that water from various rivers is flowing on to the ice.
6/29/2006		25.30	First radial data collected from ENDI.
7/10/2006	10:00 - 22:00	25.30	Upgraded the software to correct system errors. CrossSpectra were not produced during this time.
7/13/2006	00:00 - 17:00	25.30	Computer hung up on automatic reboot. Until a forced reboot, no cross spectra were collected.
7/15/2006	01:30 06:20	25.30	Ice moved offshore, so changed blanking to range out to 20 km. Spectra were not being collected after blanking range was changed at 01:30. Restarting the system has corrected the problem.
7/17/2006	19:12	25.30	Ice moved further offshore, so changed blanking out to 278 us for a range of 25 kilometers.
7/18/2006			Antenna Pattern Measurement performed for both frequencies
7/22/2006	23:00	25.30	The radials for ENDI go out maybe 8 km and get pretty good spatial coverage.
7/26/2006	0:37	13.51	Switched frequency to achieve better range.
8/18/2006	21:31	13.51	Switch frequency to 13 MHz. Only receiving returns about halfway between shore and ice.
8/24/2006		25.30	No Bragg Energy detected, switch frequency to 25 MHz.
8/25/2006	17:55	13.51	Changed frequency to 13 MHz.
8/28/2006	17:58	25.30	Calm winds. Switched frequency to 25 MHz.
8/29/2006	1:09	13.51	Switched frequency to 13 MHz. No Bragg energy detected. Switched in case this was due to freshwater.
8/31/2006	19:11	25.30	Switched frequency to 25 MHz and are seeing more Bragg energy. Winds are picking up.
9/1/2006	17:44	13.51	Switched frequency to 13 MHz.
9/5/2006	21:17	25.30	Switched frequency to 25 MHz. Bragg peaks were nonexistent at 13 MHz. Winds are ~5 mph out of the SW. Immediately, more Bragg energy was seen at ENDI.

9/6/2006	21:40	13.51	Switched frequency to 13 MHz. No more Bragg energy was seen, but the winds are forecasted to shift directions and increase in magnitude over the next twelve hours, so 13 MHz is assumed to be the more ideal frequency.
9/15/2006	17:34	25.30	Switched frequency to 25 MHz. Winds are coming from the South, and there is not much Bragg energy. It is assumed that we are in a fetch limited situation, so we change to 25 MHz to see if we can increase the Bragg energy.
9/16/2006	2:11	13.51	Switch frequency to 13 MHz. Returns are still low, but the way the forecast looks, 13 MHz is the best way to leave the system. Strong winds are predicted from the east, which always bring us good returns.
10/16/2006	16:00	13.51	Laptop hard drive nearly filled; one radial (16:00) was lost before space could be cleared.
10/21/2006		25.30 13.51	No Bragg energy, so switched frequency to 25 MHz. Still no Bragg energy at the new frequency, so switched back to 13 MHz. Hypothesis: Everything is frozen.
10/25/2006		25.30 13.51	No Bragg energy at 13 MHz, so switched frequency to 25 MHz. No Bragg peaks at 25 MHz either. Switched frequency back to 13 MHz before the system is shut down. Ice cover is prevalent.
10/26/2006	17:17		Turned off system.

Table 6. Field log listing frequency switches, notes, and significant events for the 2006 West Dock field season.

Date	Time (UTC)	Frequency	Event/Observation
6/5/2006			Sea ice had melt water laying on the surface. It appeared that a few of these melt water ponds were rather deep as evidenced by several birds disappearing out of sight into the water and not popping back up right away.
6/8/2006		25.30	SeaSonde set up. Walking Antenna Pattern Measurement performed.
6/12/2006			ACS reports that water from various rivers is flowing on to the ice.
7/3/2006	22:45	13.51	Switched frequency due to lack of Bragg peaks to see if the new frequency will make a difference.
7/5/2006	19:24	25.30	Switched frequency as well as turned off pulse shaping to boost the signal in early range cells.
7/19/2006			Antenna Pattern Measurement is performed at West Dock
7/26/2006	00:28 23:00	13.51	Switched frequency to achieve better range. Salinity was also low at West Dock on Wednesday morning (~11 ppt if I recall correctly). Laptop appears to have hung up on reboot.
7/27/2006		13.51	Can ping WEST, but cannot Timbuktu nor SSH into it. BP Electrician goes out and cycles power on the laptop.
7/28/2006		13.51	Still cannot log in, but there is heavy fog in the area. Interrupted Starband connectivity?
7/31/2006		13.51	Receive reports that the fog has lifted but still cannot contact the site.
8/1/2006		13.51	BP electrician cycled the power to the laptop again, and reported back that the laptop has a folder icon in the center with a smiley face alternating with a ?.
8/3/2006		13.51	CODAR configures backup laptop to swap out with the problem one at WEST.
8/6/2006	16:07		Swap out faulty laptop at WEST due to the hard drive failure.
8/18/2006	21:39	13.51	Switched frequency. Only getting returns about halfway between shore and ice.
8/24/2006		25.30	No Bragg Energy detected, switching frequency.
8/25/2006	17:50	13.51	Switched frequencies.
8/28/2006	17:54	25.30	Calm winds. Switched frequencies.
8/29/2006	1:08	13.51	Switched frequency because no Bragg peaks were detected all day even though there were variable winds.

8/31/2006	19:11	25.30	Switched frequency.
9/1/2006	17:44	13.51	Switched frequency.
9/5/2006	21:16	25.30	Low winds out of the SW. Switched frequency to try and get more Bragg energy.
9/6/2006	21:40	13.51	Switched frequency.
9/15/2006	17:35	25.30	Switched frequency. Winds are coming from the South, so it is assumed that we are currently in a fetch limited situation. Bragg energy has been super low.
9/16/2006	2:11	13.51	Switched frequency in anticipation of high forecasted winds.
9/17/2006	2:11	13.51	Winds have switched to come out of the East. Switched frequency.
10/1/2006	07:00 - 19:00	13.51	No radials or spectra due to a power outage at STP.
10/3/2006		13.51	Started noticing gaps in the radial data from WEST.
10/8/2006	~18:30	13.51	Starband dish and the transmit antenna blew over onto the ground in a storm which generated up to 70 mph.
10/11/2006		13.51	Arrive at WEST and finds one horizontal transmit whip bent but still functional. Green antenna, including trap, seems undamaged. Rx antenna never fell and is intact.
10/21/2006	23:07 23:34	25.30 13.51	No Bragg peaks at 13 MHz, so switched to 25 MHz. No Bragg peaks were seen at that frequency either, so switched the frequency back to 13 MHz. Hypothesis: everything is frozen.
10/23/2006		13.51	CODAR contributes gaps in radial data (see 10/3 above) are likely due to environmental conditions (not conclusive).
10/25/2006	18:27 18:47 21:45	25.30 13.51	No Bragg peaks present. Switched frequency. No Bragg energy detected, so frequency was switched back to 13 MHz. Turned off system.

APPENDIX B

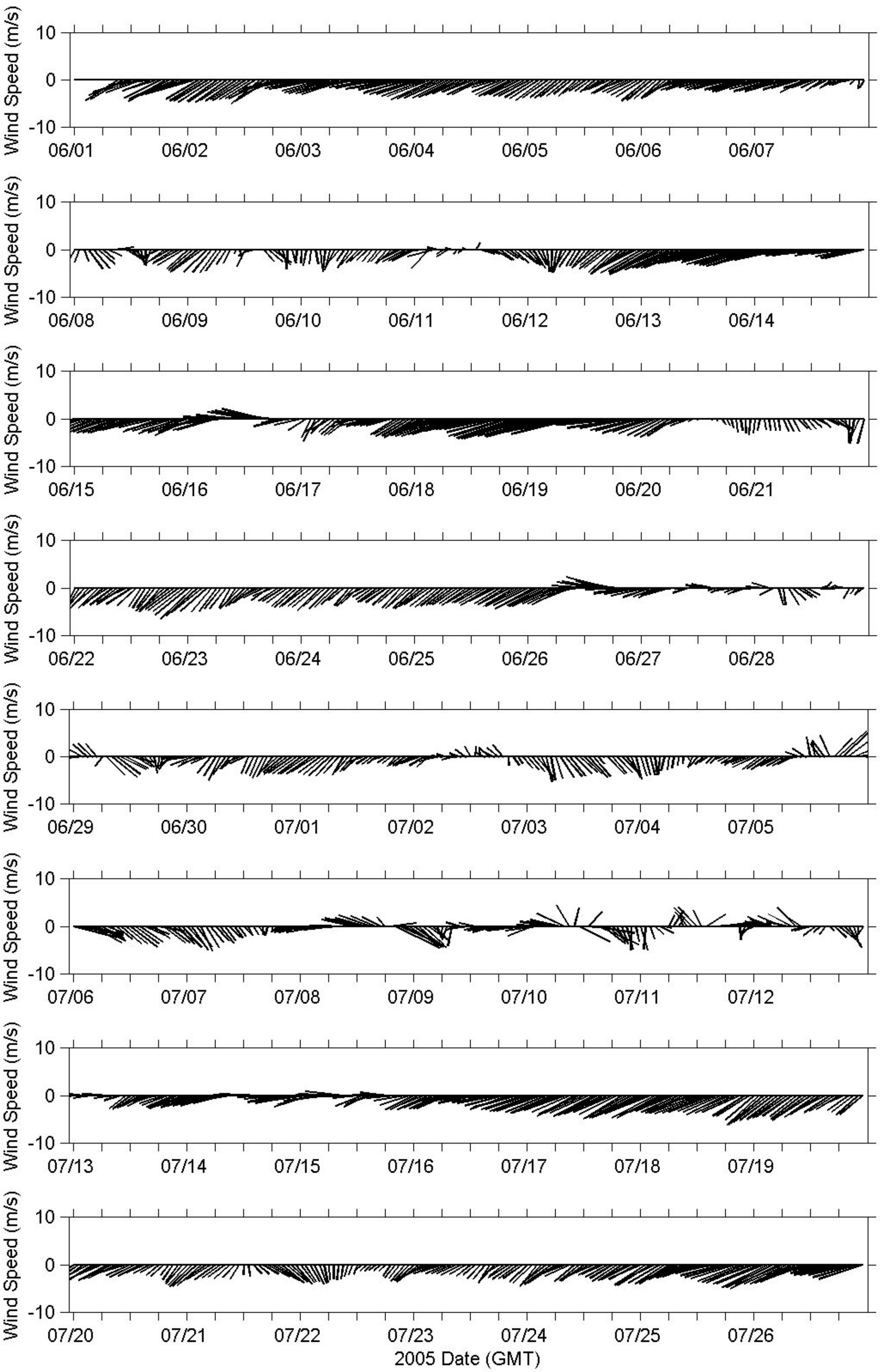
Wind Speed (m/s)
10
0
-10
06/01
06/02
06/03
06/04
06/05
06/06
06/07
06/08
06/09
06/10
06/11
06/12
06/13
06/14
06/15
06/16
06/17
06/18
06/19
06/20
06/21
06/22
06/23
06/24
06/25
06/26
06/27
06/28
06/29
06/30
07/01
07/02
07/03
07/04
07/05
07/06
07/07
07/08
07/09
07/10
07/11
07/12
07/13
07/14
07/15
07/16
07/17
07/18
07/19
07/20
07/21
07/22
07/23
07/24
07/25
07/26
2005 Date (GMT)

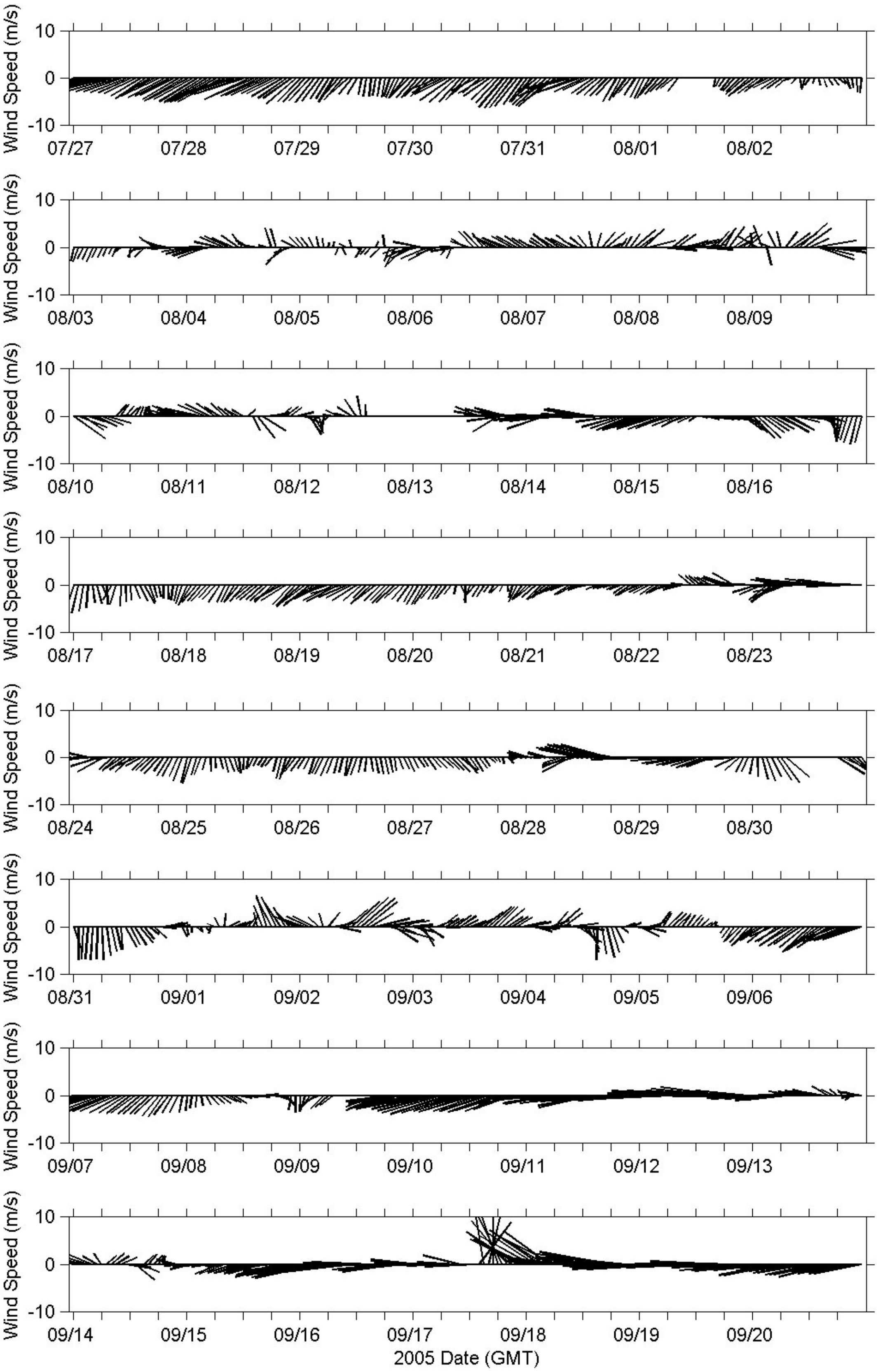
Wind Speed (m/s)
10
0
-10
07/27
07/28
07/29
07/30
07/31
08/01
08/02
08/03
08/04
08/05
08/06
08/07
08/08
08/09
08/10
08/11
08/12
08/13
08/14
08/15
08/16
08/17
08/18
08/19
08/20
08/21
08/22
08/23
08/24
08/25
08/26
08/27
08/28
08/29
08/30
08/31
09/01
09/02
09/03
09/04
09/05
09/06
09/07
09/08
09/09
09/10
09/11
09/12
09/13
09/14
09/15
09/16
09/17
09/18
09/19
09/20
2005 Date (GMT)

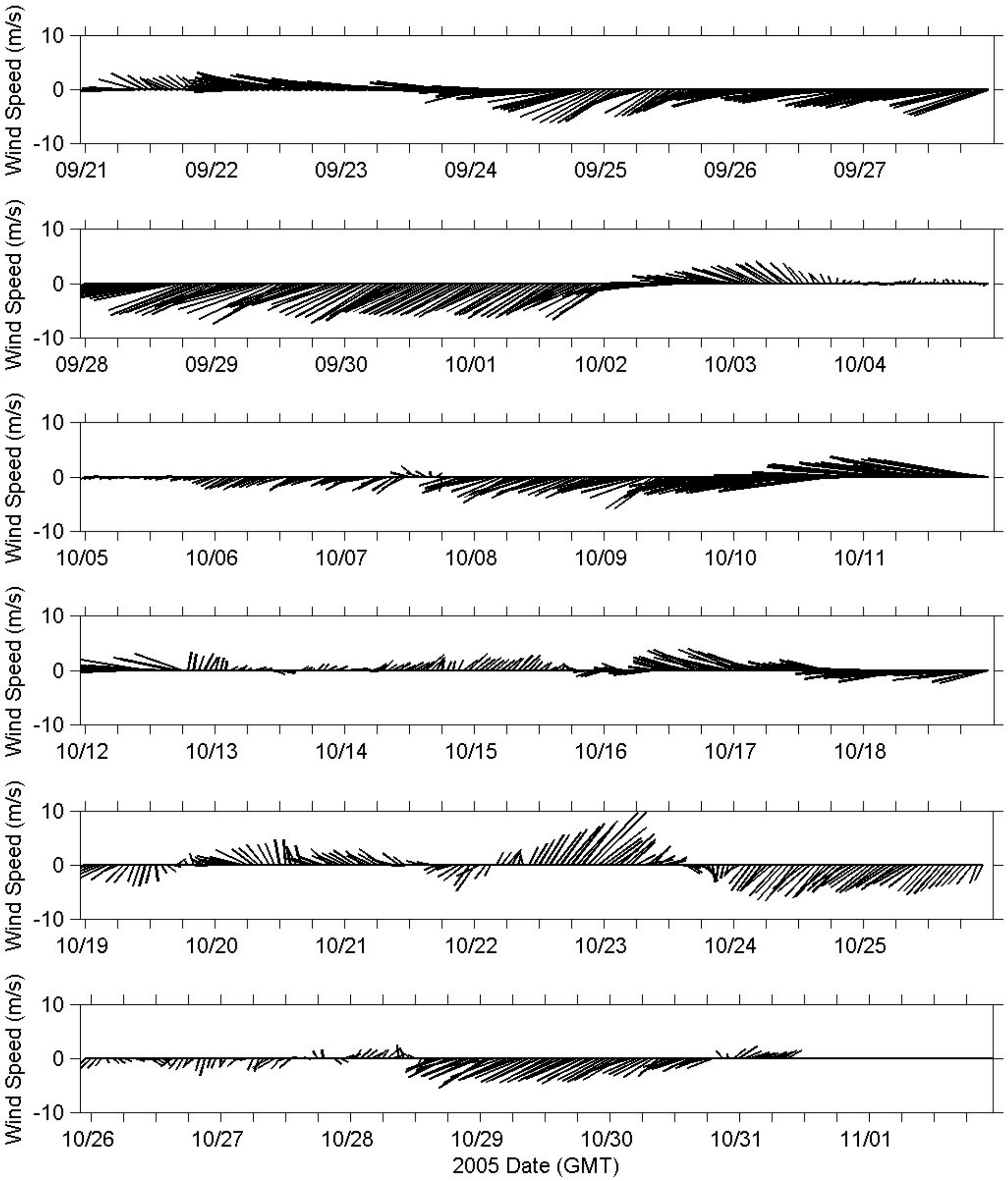
Wind Speed (m/s)
10
0
-10
09/21
09/22
09/23
09/24
09/25
09/26
09/27
09/28
09/29
09/30
10/01
10/02
10/03
10/04
10/05
10/06
10/07
10/08
10/09
10/10
10/11
10/12
10/13
10/14
10/15
10/16
10/17
10/18
10/19
10/20
10/21
10/22
10/23
10/24
10/25
10/26
10/27
10/28
10/29
10/30
10/31
11/01
2005 Date (GMT)

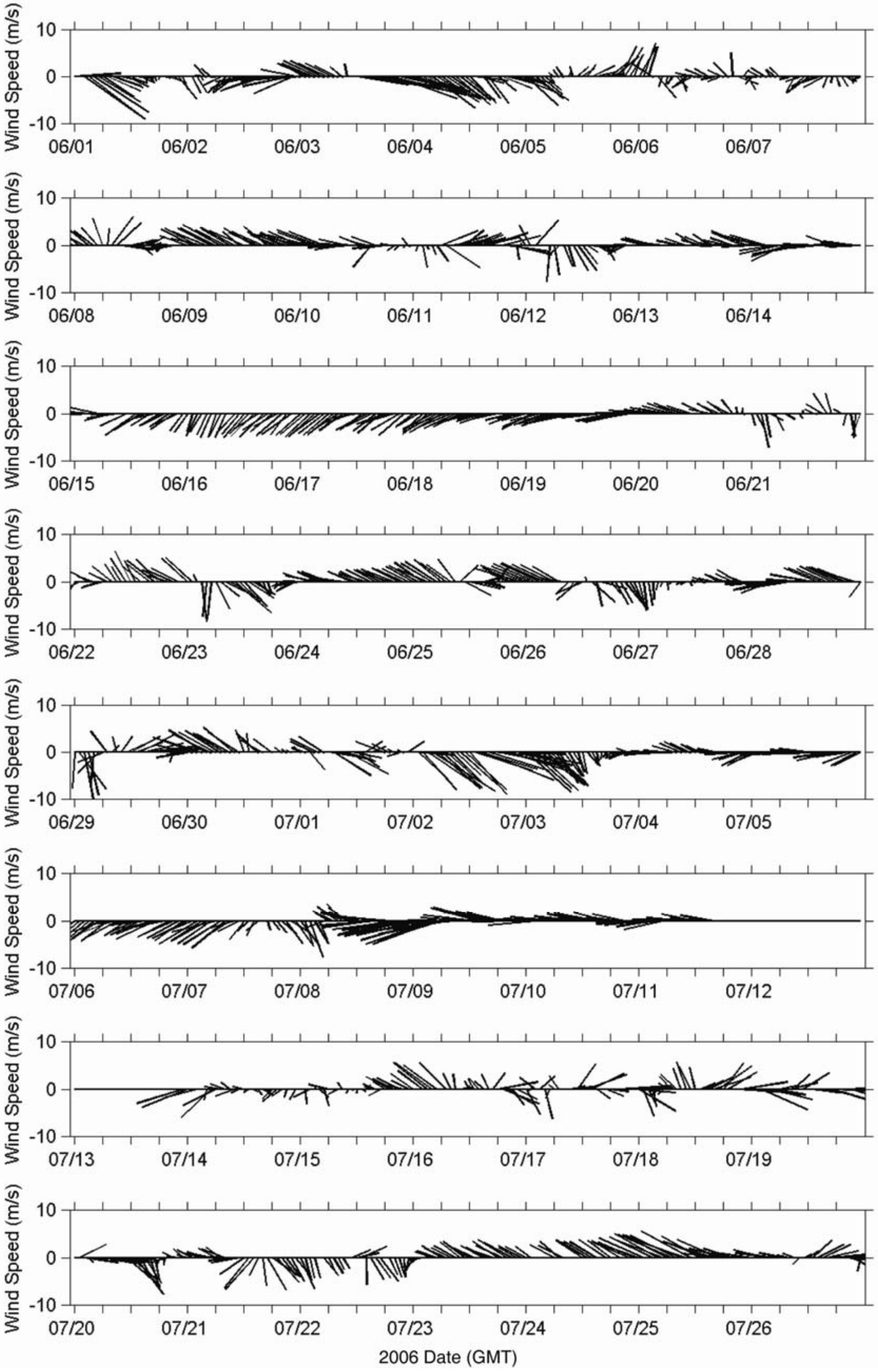
Wind Speed (m/s)
10
0
-10
06/01
06/02
06/03
06/04
06/05
06/06
06/07
06/08
06/09
06/10
06/11
06/12
06/13
06/14
06/15
06/16
06/17
06/18
06/19
06/20
06/21
06/22
06/23
06/24
06/25
06/26
06/27
06/28
06/29
06/30
07/01
07/02
07/03
07/04
07/05
07/06
07/07
07/08
07/09
07/10
07/11
07/12
07/13
07/14
07/15
07/16
07/17
07/18
07/19
07/20
07/21
07/22
07/23
07/24
07/25
07/26
2006 Date (GMT)

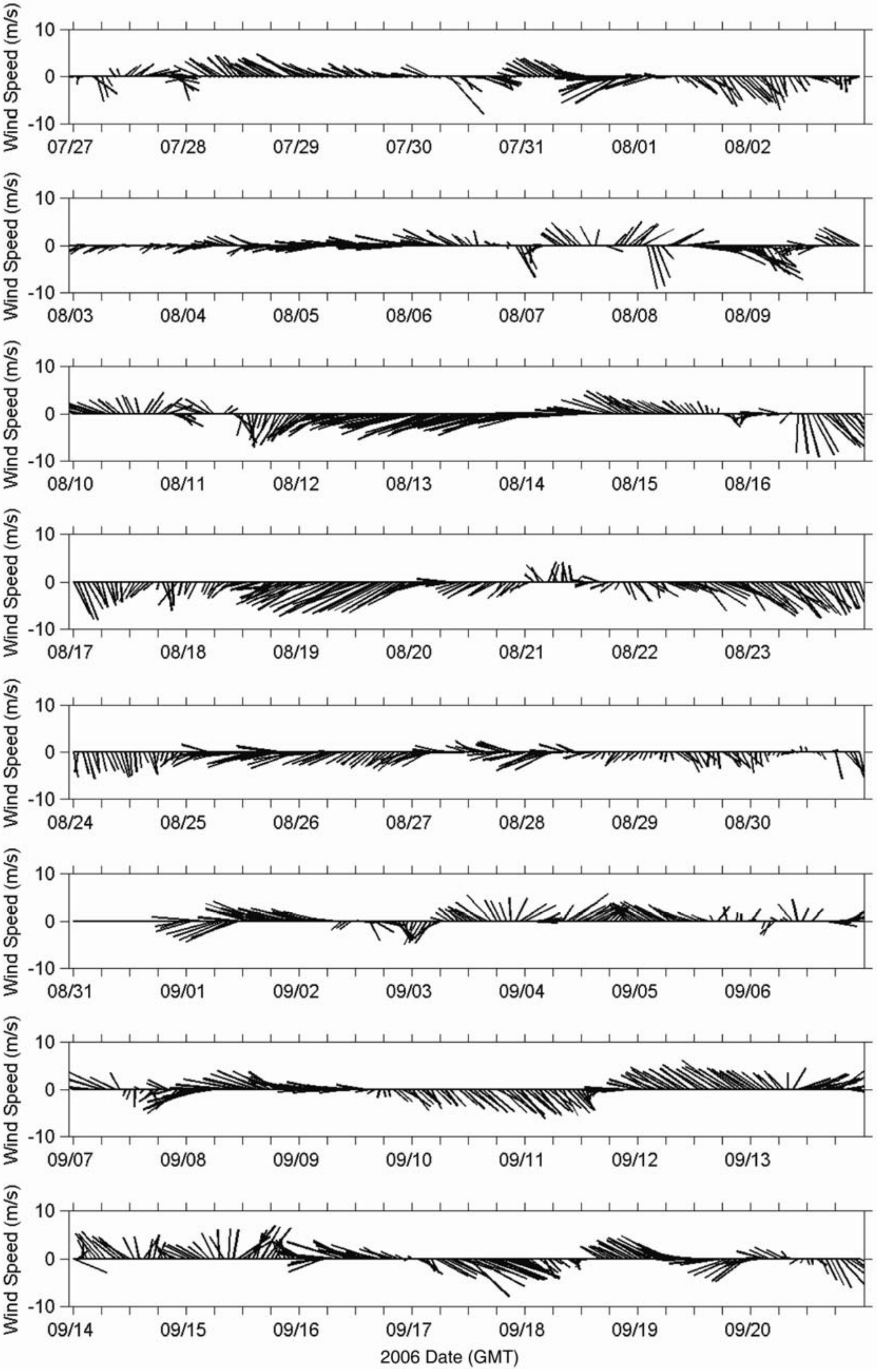
Wind Speed (m/s)
10
0
-10
07/27
07/28
07/29
07/30
07/31
08/01
08/02
08/03
08/04
08/05
08/06
08/07
08/08
08/09
08/10
08/11
08/12
08/13
08/14
08/15
08/16
08/17
08/18
08/19
08/20
08/21
08/22
08/23
08/24
08/25
08/26
08/27
08/28
08/29
08/30
08/31
09/01
09/02
09/03
09/04
09/05
09/06
09/07
09/08
09/09
09/10
09/11
09/12
09/13
09/14
09/15
09/16
09/17
09/18
09/19
09/20
2006 Date (GMT)

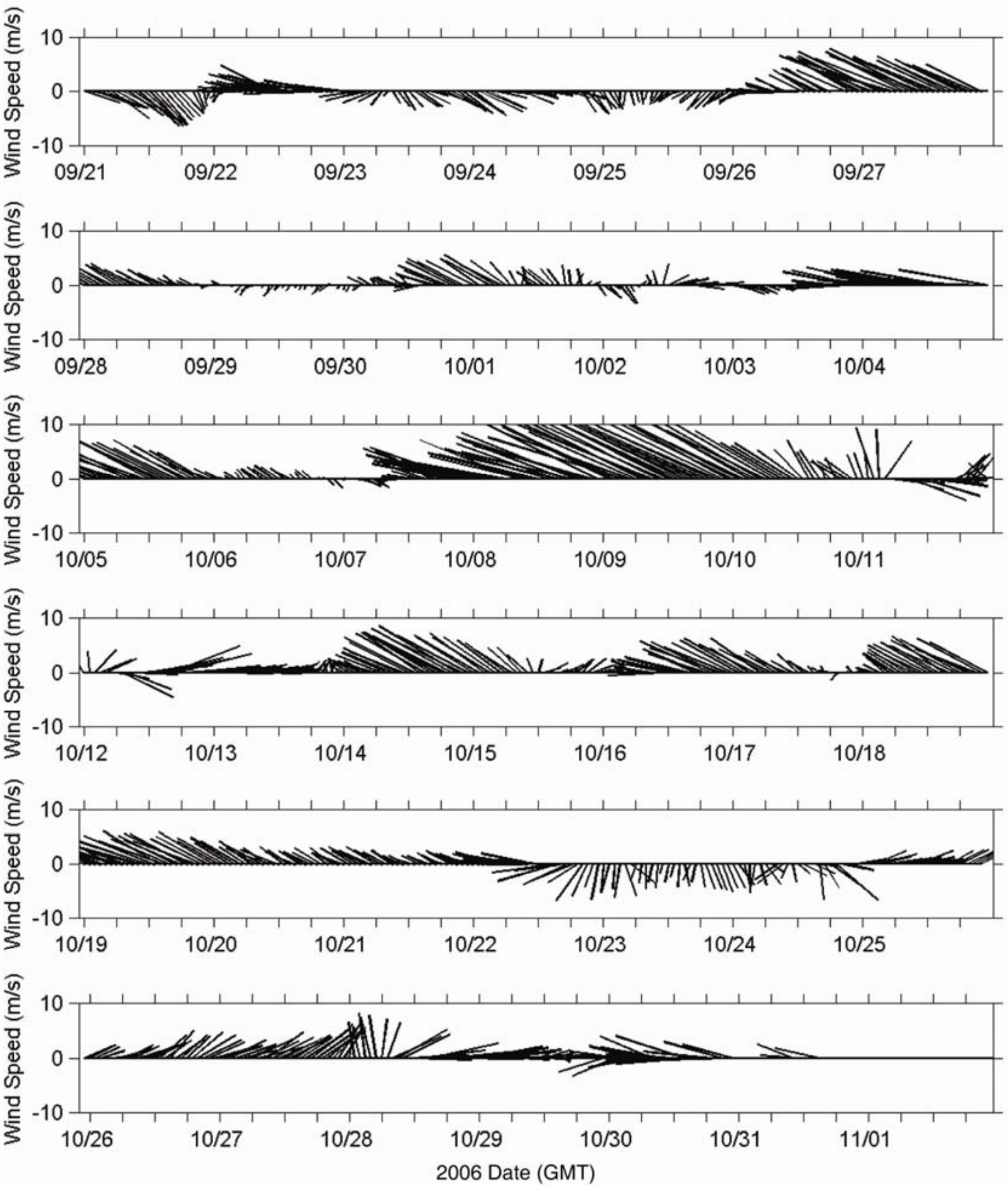
Wind Speed (m/s)
10
0
-10
09/21
09/22
09/23
09/24
09/25
09/26
09/27
09/28
09/29
09/30
10/01
10/02
10/03
10/04
10/05
10/06
10/07
10/08
10/09
10/10
10/11
10/12
10/13
10/14
10/15
10/16
10/17
10/18
10/19
10/20
10/21
10/22
10/23
10/24
10/25
10/26
10/27
10/28
10/29
10/30
10/31
11/01
2006 Date (GMT)